

THE UNIVERSITY OF CHICAGO

SUPERCONDUCTING QUBIT ADVANTAGE FOR DARK MATTER (SQuAD)

A DISSERTATION SUBMITTED TO
THE FACULTY OF THE DIVISION OF THE PHYSICAL SCIENCES
IN CANDIDACY FOR THE DEGREE OF
DOCTOR OF PHILOSOPHY

DEPARTMENT OF PHYSICS

BY
ANKUR AGRAWAL

CHICAGO, ILLINOIS
DECEMBER 2022

Table of Contents

| | |
|---|------|
| List of Figures | vi |
| List of Tables | x |
| Acknowledgments | xi |
| Abstract | xiii |
| 1 Introduction | 1 |
| 1.1 Detecting Dark matter in the lab | 7 |
| 1.2 Thesis Overview | 7 |
| 2 Dark matter and axion cosmology | 9 |
| 2.1 Axion and hidden photons | 9 |
| 2.1.1 Interaction with Axions | 10 |
| 2.1.2 Interaction with hidden photons | 12 |
| 2.1.3 Direction detection of dark matter | 13 |
| 2.1.4 Expected signal due to dark matter | 14 |
| 2.1.5 Detection principle | 15 |
| 2.2 Current Challenges | 16 |
| 2.3 Our Approach | 19 |
| 3 Superconducting devices | 21 |
| 3.1 Introduction | 22 |
| 3.2 Non-linear oscillator | 24 |
| 3.3 Design and Fabrication | 25 |
| 3.4 Coupling transmon with a microwave cavity | 25 |
| 3.5 Coupling to the outside world | 27 |
| 3.5.1 Microwave control electronics | 28 |

| | | |
|-------|---|----|
| 3.5.2 | Amplification chain | 30 |
| 3.6 | Qubit readout and characterization | 32 |
| 3.7 | Cavity state control and measurement | 37 |
| 3.7.1 | Selective-on Number Arbitrary Phase (SNAP) gate | 46 |
| 3.7.2 | Numerical optimisation methods to create quantum states | 49 |
| 3.8 | Josephson Parametric Amplifier | 54 |
| 3.8.1 | principle of operation | 55 |
| 3.8.2 | Design and Fabrication | 56 |
| 3.8.3 | Test and Characterization | 58 |
| 4 | Noise temperature measurement | 61 |
| 4.1 | Sources of noise and their limits | 62 |
| 4.2 | Calibration of noise temperature | 65 |
| 4.2.1 | Y-factor method (Hot-cold load method) | 65 |
| 4.2.2 | Primary thermometer | 67 |
| 4.2.3 | Qubit as a thermometer | 69 |
| 5 | Single Photon Counter | 74 |
| 5.1 | Meet the device | 74 |
| 5.2 | Quantum Non-demolition interaction | 75 |
| 5.3 | Repeated measurement protocol | 77 |
| 5.4 | Hidden Markov Model Analysis | 77 |
| 5.5 | Reconstructing the cavity state | 82 |
| 5.6 | Likelihood test | 83 |
| 5.7 | Testing the HMM with real events | 83 |
| 5.7.1 | No photon in the cavity | 84 |
| 5.7.2 | One photon in the cavity | 84 |
| 5.8 | Detector Characterization | 85 |

| | | |
|--------|---|-----|
| 5.9 | Metrological Gain | 88 |
| 5.10 | Mysterious Background Photons | 90 |
| 5.11 | Hidden Photon Search | 92 |
| 5.11.1 | Search protocol with photon counting | 92 |
| 5.11.2 | Computing the expected signal rate | 93 |
| 5.11.3 | Calculating 90% confidence limit | 95 |
| 5.11.4 | Hidden photon parameter space exclusion | 96 |
| 5.12 | Measurement optimization | 100 |
| 5.12.1 | Josephson Parametric Amplifier | 100 |
| 5.12.2 | Optimal readout shape pulse | 101 |
| 5.12.3 | Linear filter/optimal integration weights | 102 |
| 5.12.4 | Active reset of the qubit | 104 |
| 5.13 | Summary | 105 |
| 6 | Enhancement of weak signal with stimulated emission | 106 |
| 6.1 | Signal Enhancement with Stimulated Emission | 106 |
| 6.1.1 | Treating dark matter wave as a classical drive | 108 |
| 6.2 | Preparing Non-classical States in the Cavity | 110 |
| 6.3 | Stimulated emission protocol | 113 |
| 6.3.1 | HMM for stimulated emission | 116 |
| 6.3.2 | Examples of the HMM in action | 117 |
| 6.3.3 | Signature of enhancement with Fock states | 118 |
| 6.4 | Hidden photon search | 121 |
| 6.4.1 | Kinetic mixing angle exclusion | 124 |
| 6.5 | Summary | 127 |
| 7 | Photonic Bandgap Axion Haloscope | 129 |
| 7.1 | Introduction | 129 |

| | | |
|-------|---|-----|
| 7.1.1 | What is a Photonic Bandgap (PBG)? | 130 |
| 7.1.2 | Why do we need a photonic bandgap? | 131 |
| 7.2 | Computing the bandgap | 132 |
| 7.2.1 | Computational tools | 133 |
| 7.2.2 | Defect as a cavity | 135 |
| 7.3 | Woodpile with an omni-directional bandgap | 136 |
| 7.4 | Bragg Fiber | 142 |
| 7.4.1 | Tapered dielectric shells | 145 |
| 7.4.2 | Conical taper in metal end-caps | 147 |
| 7.5 | Tuning the cavity mode | 154 |
| 7.6 | Preparing for science run | 157 |
| 7.6.1 | Projected sensitivity to axions | 162 |
| 7.6.2 | Axion data collection | 163 |
| 7.7 | Summary | 163 |
| 8 | Future Dark Matter Search | 165 |
| 8.1 | Axion search with qubits | 165 |
| 8.2 | Hidden photon search with a tuner | 166 |
| 8.3 | Rydberg atoms as single photon counter | 167 |
| 9 | Conclusion | 169 |
| | References | 171 |

List of Figures

| | | |
|------|---|----|
| 1.1 | Structure formation in the universe. | 4 |
| 1.2 | Cosmic microwave background. | 5 |
| 1.3 | Galaxy rotation curve. | 6 |
| 2.1 | Principle of axion conversion | 11 |
| 3.1 | Anharmonic quantum oscillator. | 23 |
| 3.2 | Photon number dependent frequency shift. | 27 |
| 3.3 | State dependent frequency shift. | 28 |
| 3.4 | SMA dipole antenna for input-output control. | 29 |
| 3.5 | Wiring diagram inside the dilution refrigerator and the room temperature measurement setup. | 31 |
| 3.6 | QND readout of the transmon state. | 32 |
| 3.7 | Rabi-flopping experiment of a transmon. | 33 |
| 3.8 | Qubit lifetime and dephasing time measurement. | 35 |
| 3.9 | Qubit temperature measurement | 36 |
| 3.10 | QNDness of qubit measurement. | 38 |
| 3.11 | Photon number parity measurement | 40 |
| 3.12 | .Storage lifetime T_1 measurement with a coherent state | 41 |
| 3.13 | Storage lifetime T_1 measurement with a Fock state. | 42 |
| 3.14 | Storage coherence T_2 measurement. | 44 |
| 3.15 | Qubit-cavity dispersive shift measurement. | 45 |
| 3.16 | Cavity Kerr non-linearity measurement. | 46 |
| 3.17 | Examples of SNAP sequences to prepare Fock states in the cavity. | 48 |
| 3.18 | Cavity dynamics under OCT pulses. | 51 |
| 3.19 | Example of an OCT pulse to prepare Fock states. | 52 |
| 3.20 | QNDness of storage cavity measurement. | 54 |

| | |
|---|-----|
| 3.21 Schematic of a JPA circuit | 57 |
| 3.22 JPA in a box. | 58 |
| 3.23 Flux-scan of the JPA resonance frequency | 59 |
| 3.24 Measured gain of the JPA. | 60 |
| | |
| 4.1 Wiring diagram for a Y-factor measurement. | 66 |
| 4.2 Response of a SNT as a function of applied voltage. | 68 |
| 4.3 Qubit Ramsey as a function of the input readout power | 71 |
| 4.4 1-Photon amplitude. | 72 |
| 4.5 SNR improvement with JPA added to the readout chain. | 73 |
| | |
| 5.1 Photon counting device. | 75 |
| 5.2 Spurious parity jumps. | 76 |
| 5.3 Photon counting protocol. | 77 |
| 5.4 State reconstruction scenarios. | 82 |
| 5.5 Zero cavity photon. | 84 |
| 5.6 One cavity photon. | 85 |
| 5.7 Photon counter characterization. | 86 |
| 5.8 Detector efficiency and false positive probability. | 87 |
| 5.9 Histogram of events. | 88 |
| 5.10 Metrological gain literature survey. | 89 |
| 5.11 Microwave lines assembly in a dilution refrigerator. | 91 |
| 5.12 Cumulative probability of hidden photon candidate producing observed signal. . | 97 |
| 5.13 Parity measurement and detector efficiency. | 98 |
| 5.14 Excluded n_{drive} as a function of $\omega_{\gamma'}$ | 99 |
| 5.15 Comparison of readout photon population with different pulse shapes. | 102 |
| 5.16 Temporal response of the readout cavity. | 103 |
| 5.17 Without and with active reset. | 104 |

| | | |
|------|--|-----|
| 6.1 | Phase-space representation of the cavity state before and after the dark matter wave push. | 108 |
| 6.2 | Creation of Fock states in the cavity using GRAPE method. | 112 |
| 6.3 | Decay rate of Fock states. | 113 |
| 6.4 | Stimulated emission protocol. | 114 |
| 6.5 | No stimulated emission. | 118 |
| 6.6 | Stimulated emission. | 119 |
| 6.7 | Signature of enhancement. | 120 |
| 6.8 | Examples of fit to background counts. | 123 |
| 6.9 | Systematic effects on a_0 | 123 |
| 6.10 | Excluded ϵ with $m_{\gamma'}$ | 126 |
| 6.11 | Fock state preparation with non-zero occupation in the cavity. | 127 |
| 7.1 | Natural periodic micro-structures responsible for the iridescent color in stones and feathers. Source: Wikipedia | 130 |
| 7.2 | Empty cylindrical cavity. | 132 |
| 7.3 | Band structure of a Bragg stack. | 134 |
| 7.4 | Defect in a Bragg stack. | 135 |
| 7.5 | Photonic band-structure of a woodpile structure. | 137 |
| 7.6 | Defect cavity inside a woodpile structure. | 139 |
| 7.7 | Woodpile cavity for cryogenic measurements. | 140 |
| 7.8 | Tracking cavity frequency. | 141 |
| 7.9 | Tuning a woodpile defect cavity. | 142 |
| 7.10 | 2D triangular lattice with a defect. | 143 |
| 7.11 | Bragg fiber. | 145 |
| 7.12 | Tapered Bragg fiber. | 146 |
| 7.13 | Bragg fiber with conical end-caps. | 148 |
| 7.14 | Parametric sweep to determine the optimal cone dimensions. | 149 |

| | | |
|------|--|-----|
| 7.15 | Bragg fiber prototype. | 151 |
| 7.16 | Q-factor measurements. | 152 |
| 7.17 | Cavity parameters as a function of magnetic field. | 155 |
| 7.18 | ADMX cavity tuning system. | 156 |
| 7.19 | Breaking the radial symmetry to tune the mode. | 157 |
| 7.20 | Cavity tuning with a tapered rod. | 158 |
| 7.21 | HFSS Simulation of a JPA chip. | 159 |
| 7.22 | JPA operation with magnet on. | 160 |
| 7.23 | Quantum limited amplification. | 161 |
| 7.24 | Sensitivity to axion with quantum limited amplifier. | 162 |
| 7.25 | Axion test data. | 164 |
| 8.1 | Electrical cavity tuning with a Josephson junction. | 167 |

List of Tables

| | | |
|-----|--|-----|
| 3.1 | Cavity state demolition probability | 54 |
| 5.1 | Device parameters. | 81 |
| 5.2 | Metrological gain with qubit based photon counting with multiple samples at different frequencies. | 89 |
| 5.3 | Photon counting experimental parameters. | 95 |
| 6.1 | Fitted parameters. | 122 |
| 6.2 | Stimulated emission experimental parameters. | 125 |
| 7.1 | TM ₀₃₀ Mode Parameters. | 153 |

Acknowledgments

First, and foremost I would like to thank my advisors - Aaron Chou and David Schuster for giving me the opportunity to conduct my doctoral thesis under their guidance. I couldn't have asked for a better combination than this duo. While Aaron always emphasized on the importance of running quick numbers which made sense without blindly trusting computers, Dave always encouraged trying out new ideas and quickly iterating over to understand the underlying physics to build a successful prototype. Together, they provided such an enriching and collaborative environment that I hope to find and contribute to creating in my career ahead. I am really grateful for their unwavering support throughout my PhD and for providing me with ample opportunities to learn and help others in the lab. I would like to thank my labmates - Akash, Tanay, Vatsan, Kevin, Gerwin, Andrew and the rest of the Schuster lab folks for making my ride joyful while I failed and learnt. The success of my experiments is unimaginable without Akash's infinite patience to teach and guide me at every step - such a humble person. I am really grateful to Tanay for teaching me the wizardry to make everything better in the experiment. I would also like to thank Fang and Morgan for giving me an opportunity to be part of their awesome tuning project and helping me with the experiments at Fermilab, while I was too busy writing this thesis. Bipul, Matt, Mark and Takumi- I am lucky to have spent countless problem solving sessions with you guys. You helped make my transition to this new country effortless. I have to thank my former roommates - Suhail, Bipul, Aabbhas and Shobhit for keeping me sane and well fed for the past six years, especially during the covid lockdown period.

I am very lucky and fortunate to have the support of family- Mummy, Papa, Jiji. Having missed the opportunity to attend college, my parents instilled the value of education in us at a very early age. I am happy that they cherish their sacrifices and are proud of me. Beyond grateful to my extended family for believing in me and providing me with resources for the best education. The most important person, my best friend, my life partner - Neeti.

I cannot imagine how incomplete I would be without her. She has taught me so much about the finer details of life, that matter the most. Her strength, care and continued support help me navigate the ups and downs with ease. She makes me a better person and I am grateful to have found the “architect” of my life.

Abstract

One of the most profound mysteries in the fundamental physics which has puzzled scientists for almost a century is the nature of dark matter. It is hypothesized to makes up 25% of the universe's energy density, however, a direct detection of the dark matter remains hypothetical so far. Due to the strict constraints placed by experimental null results on heavier particles (GeV) such as WIMPS, axions and hidden photons have emerged as a leading dark matter candidate. Both are sufficiently low-energy to behave as a coherent wave with macroscopic occupation number (unknown frequency or mass), and on rare occasion convert into a single photon via electro-magnetic interactions with normal matter. Current dark matter experiments operate a microwave cavity held at cryogenic temperature and use a linear amplifier operating near the standard quantum limit (SQL) to measure the signal power. While these amplifiers provide a big boost in the signal-to-noise ratio at sub GHz range, the noise power linearly increases and signal power plummets at higher frequency. In order to make the search tenable, quantum enhanced search combined with new cavity techniques are required to bring down the detector noise and improve the dark matter signal.

In this thesis, I report the development of multiple complimentary techniques using superconducting qubits to speed up the dark matter search. First, we demonstrated a new quantum measurement technique of counting photons generated by the dark matter in a microwave cavity. By measuring only the field amplitude, the qubit is able to evade the SQL. With repeated quantum non-demolition (QND) measurements of the cavity photons and applying a hidden Markov model, we reduce the noise to 15.7 dB below the quantum limit. Based on the measured background we set a new exclusion limit on hidden photon dark matter. Second, using a superconducting qubit to prepare the cavity in a Fock state and stimulate the emission of a photon from dark matter wave. By initializing the cavity in $|n\rangle = 4$ Fock state, we demonstrate a $2.5 \times$ (4.0 dB) improvement in the signal rate, taking into account the detection efficiency. Combining these two results in a 19.7 dB improvement

in signal-to-noise ratio over the conventional detection methods, speeding up the dark matter search by a factor of 10,000. The measured background sets a new exclusion limit on hidden photon search in a previously unexplored mass range. Lastly, we demonstrate a high quality factor photonic bandgap cavity which is compatible with large magnetic field. The measured quality factor is almost 50 times higher than a conventional copper cavity with $Q = 10^4$ at these frequencies and 50% higher than the axion quality factor. A coherent integration of all these will greatly speed up the dark matter search in the future.

Chapter 1

Introduction

Our universe is full of mysteries. Each phenomenon has its own origin story. Each element interacts with its surrounding in a different way. Since the dawn of era, we humans, being curious in nature have explored and formulated theories to explain phenomenon occurring around us. There is numerous evidence from all over the world that the move towards a rational understanding of nature began in the fields of astronomy, optics and mechanics around 10th century BCE onwards. While a certain group of individuals were trying to understand the biological phenomenon occurring on the earth like evolution, others were trying to venture out and observe things outside the earth, in outer space. We have made a lot of progress in our understanding of nature in the past 400-500 years both on and outside the earth, at nanometer and galactic scales. And we have seen major upheavals in physics models since then, from geocentric to heliocentric, ether to vacuum, and classical to quantum. While the history of physics is an interesting topic in itself, let's come back to the modern times and examine where we stand in our understanding of nature and its governing principles.

In the last 50 years or so, we have made tremendous progress to unify various theories which sought to explain all the “elementary” particles known at the time in a consistent framework known as Standard Model (SM) of particle physics. It has undergone intense experimental scrutiny over the years, yet every test has been testament to its success, including the discovery of Higgs boson in 2012, last remaining particle predicted by the SM. However, the “ordinary matter” explained by SM constitutes only 5% of the mass in the universe. According to “standard cosmological model”, the remaining 95% constitutes the Λ CDM, where Λ stands for dark energy and CDM stands for cold dark matter. But, we do not know what either dark energy or dark matter are made of. Current and decades of past astronomical observations do inform us about their presence and how they behave on

galactic and extra-galactic scales. Dark energy appears to be everywhere, behaving like the opposite of gravity. It has been hypothesised to account for the accelerated expansion of the vast region of empty space between galaxy clusters. Any further discussion of dark energy is beyond the scope of this thesis.

On the other hand, we have been able to infer the existence of dark matter only from the gravitational effect it seems to have on visible matter. It does not interact with the electromagnetic force and appears to be uniformly spread throughout galaxies. Observations tell us that we are flying into a headwind of dark matter, which passes through us all the time at about 200 km/s without leaving a trace. Still, it is a subject of immense theoretical and experimental interest because there is a strong evidence that it is non-baryonic (not made of atoms) and thus, could act as a hypothetical extension to the SM. If detected, it would interact very weakly with everything in the SM and would be produced abundantly in the early universe, satisfying all the properties of dark matter. One thing that all the observations don't tell us is the mass of dark matter particle. There are constraints on the mass depending on the model you trust but the parameter space is huge, which makes its search challenging.

Another field which has seen an explosive growth in the last decade is quantum computing and quantum information science. The idea of a quantum computer was first proposed by Richard Feynman and Yuri Manin to simulate things a classical computer could not feasibly do. However, the techniques and technology developed to interact and control these quantum systems is proven to be very useful to probe fundamental physics which are otherwise limited by laws of quantum mechanics. One of the most promising candidates “superconducting qubit” is at the forefront of this computing revolution. It is developed on the circuit-QED platform which is easy to scale and study rich physical systems allowing users full control over the properties of Hamiltonian. These nanometer scale objects form the back-bone of my PhD research and I am really excited to share all the interesting techniques and results obtained during this journey, which would help speed up the dark matter searches in the

microwave frequency range.

I am going to leave you with a few beautiful images captured by some of the most sensitive pieces of equipment ever built, which provide direct evidence for the existence of dark matter.

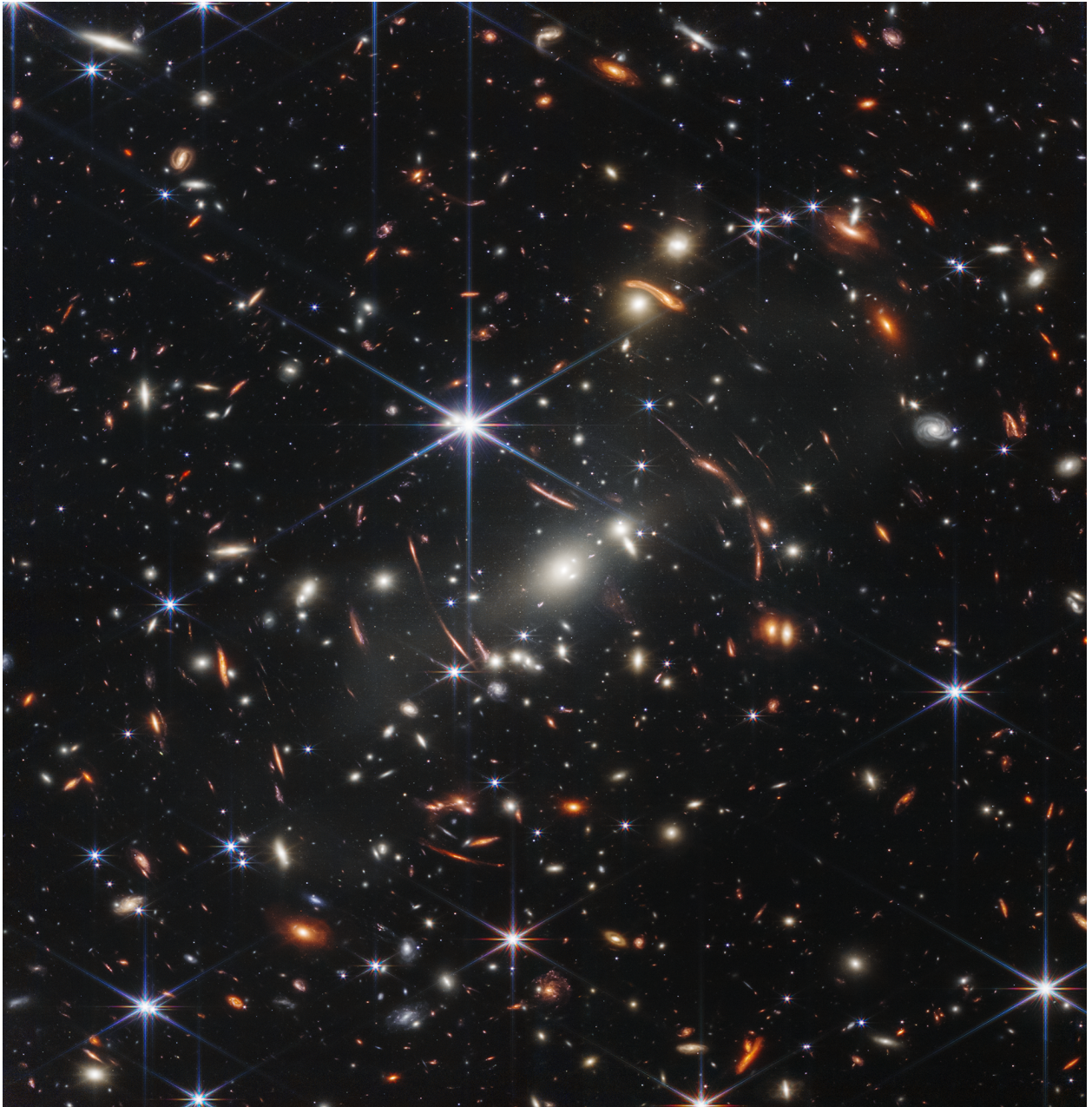


Figure 1.1: **Structure formation in the universe.** Thousands of small galaxies appear across this view. Their colors vary. Some are shades of orange, while others are white. Most appear as fuzzy ovals, but a few have distinct spiral arms. In front of the galaxies are several foreground stars. Most appear blue, and the bright stars have diffraction spikes, forming an eight-pointed star shape. There are also many thin, long, orange arcs (“banana shaped”) that curve around the center of the image which appear at multiple position due to “**Gravitational lensing**”. Dark matter bends the light causing the object to appear multiple times, but it’s the same object. Image credits: NASA JWST.

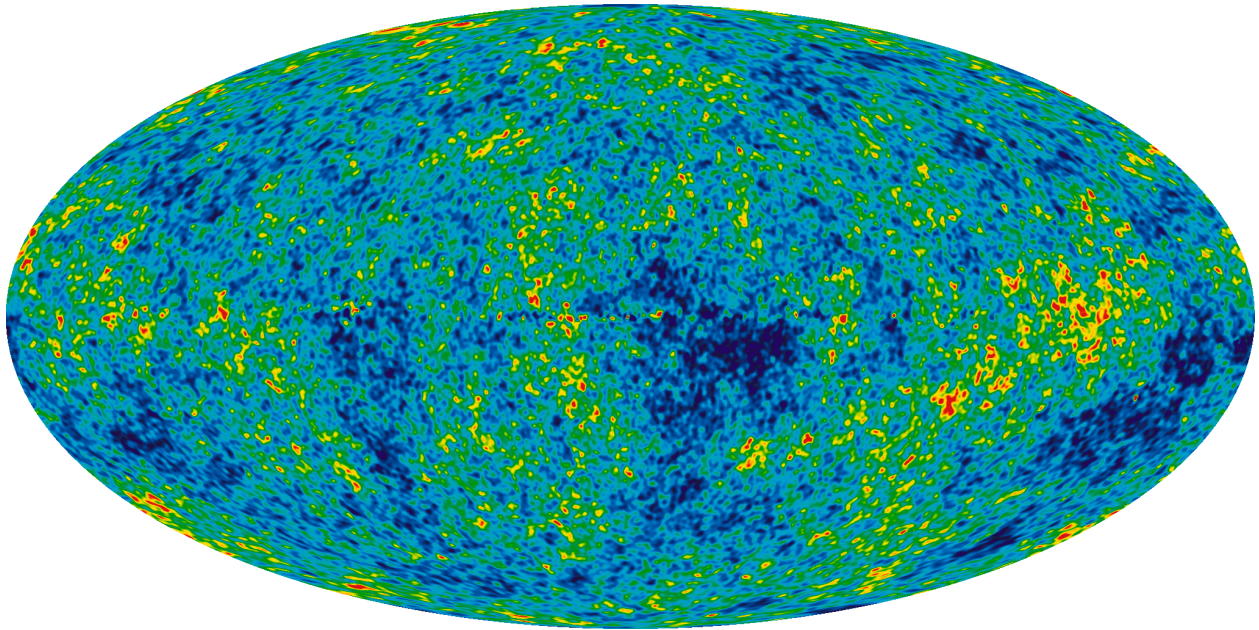


Figure 1.2: **Cosmic microwave background.** The detailed, all-sky picture of the infant universe created from nine years of WMAP data. The image reveals 13.77 billion year old temperature fluctuations (shown as color differences) that correspond to over-densities where gravitational potential wells formed by the dark matter lay the seeds for the formation of galaxies. The signal from the our Galaxy was subtracted using the multi-frequency data. This image shows a temperature range of ± 200 microKelvin. Image credits: NASA / WMAP Science Team.

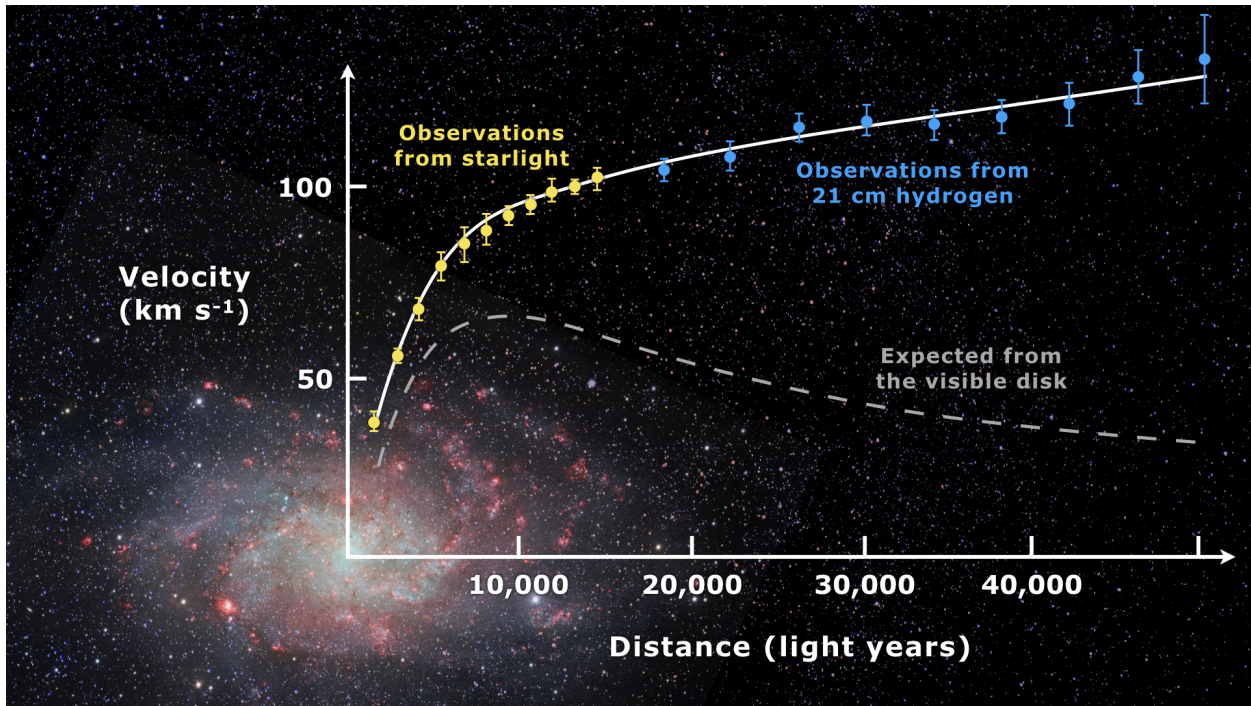


Figure 1.3: **Galaxy rotation curve.** Rotation curve of spiral galaxy Messier 33 (yellow and blue points with error bars), and a predicted one from distribution of the visible matter (gray line). The discrepancy between the two curves can be accounted for by adding a dark matter halo surrounding the galaxy. Image credits: Wikipedia.

1.1 Detecting Dark matter in the lab

Without going into too much detail¹, let me discuss the current state of affairs of the terrestrial dark matter experiments and how we are trying to detect them. We are interested in two well motivated dark matter candidates - **axions** and **hidden photons** which have compelling cosmological origin stories. An axion haloscope consists of an extremely cold microwave cavity, large magnetic field, and a low noise microwave amplifier. If the frequency of the cavity is tuned in resonance with the axion mass then it will convert into a photon with a very small but finite probability. This photon causes an oscillating EM field inside the cavity and the power coming out is amplified using an amplifier before the digitized signal is displayed. For a typical set of experimental parameters at 5 GHz, the expected signal power $P_{sig} \sim 5 \times 10^{-24} \text{W}$! In comparison, the total noise power of a cavity in a dilution refrigerator with a physical temperature of $T \sim 60 \text{ mK}$ is $P_N \sim 10^{-20} \text{W}$. It is larger than P_{sig} by a factor of 10^3 . This signal-to-noise ratio (SNR) plummets as we move to search for axions at higher frequencies. It is mainly due to three reasons:

1. **Noise power** keeps on increasing linearly with the frequency, overwhelming the signal.
2. **Detector volume** shrinks to meet the resonance condition ($V \propto \nu^{-3}$).
3. **Q-factor** decreases at higher frequency due to anomalous skin depth effect.

1.2 Thesis Overview

In this thesis, I am going to demonstrate how we can use superconducting qubits and photonic bandgap cavities to overcome the challenges mentioned above. It is an attempt to describe how a simple device such as a qubit brings quantum advantage to dark matter experiments. I have tried to keep the discussion informal at times to not bore the readers with too much details but I will try to include relevant references whenever appropriate. In Chapter 2,

1. Details in Chapter 2.

I describe the motivation for dark matter candidates we are interested in and how they interact via EM force to produce a detectable signal in the lab. Next, I will explain the superconducting devices such as qubits, in particular **transmon** and 3D cavities in Chapter 3. I will describe the interaction between the two and how to operate and characterize the complete Hamiltonian once the device is mounted in a dilution refrigerator. I will also demonstrate how a qubit allows universal control on the cavity, though only to prepare Fock states as a part of this thesis. In Chapter 4, I explain the various sources of noise and how to quantify them in a real experiment to understand their origin and quantify their contributions in the SNR. In particular, I discuss a quantum noise limited amplifier technology made out of superconducting circuit elements and its operation and characterization in a readout chain connected to the qubit. In Chapter 5, I will explain how we can harness the quantum non-demolition interaction to build a single photon counter with false positive counts $1300 \times$ lower than the standard quantum limit (SQL). In Chapter 6, I will discuss the stimulated emission technique by preparing the cavity in a large n -photon Fock state to enhance the signal. I will explain the concept and the experimental protocol to realize this experiment. I will present a successful demonstration of enhancement by preparing cavity in up to $|n\rangle = 4$ Fock state. Later, I characterize the source of background events and conduct a dark matter search for hidden photons and exclude candidates in an unexplored parameter space. In Chapter 7, I will present a novel cavity technique for axion haloscope which has a quality factor $> 10^6$ and is compatible with large magnetic fields. I will briefly discuss the photonic bandgap structures and design consideration for achieving desired performance of an axion detection cavity. New results at cryogenic temperatures are reported with a photonic bandgap haloscope and JPA to conduct an axion search with magnet ramped up to 10 T. In the end, I conclude by putting all the pieces together and how they fit in the grand vision of future dark matter experiments.

Chapter 2

Dark matter and axion cosmology

Having convinced you that dark matter is worth studying, in this chapter, I will describe the two very well motivated candidates which are interesting to us - **axions** and **hidden photons**. Both are sufficiently low-energy to behave as a coherent wave with macroscopic occupation number, and have compelling cosmological origin stories^{1–5}. I will describe their conversion mechanism into photons and how it can be detected in the lab. Next, I will discuss the challenges with current dark matter experiments and how we can overcome them with a collaborative effort called SQuAD.

2.1 Axion and hidden photons

Axion is a classical example of “two birds with stone”, which solves the long standing charge-parity (**Strong CP**) problem in the SM and account for dark matter if produced in the right conditions at the early stages of universe. The strong CP problem refers to the conservation of charge-parity in quantum chromodynamics (QCD) which is a theory of strong forces. The charge-parity violation is allowed in the strong interactions, which would manifests itself as a measurable electric dipole moment (EDM) of the neutron. The degree of CP violation in QCD is proportional to angle θ which sets the scale of neutron EDM to be $\mathcal{O}(1)$. However, current experimental constraints of the neutron EDM indicate that $\theta \leq 10^{-10}$ i.e., QCD is perfectly CP-conserving within one part in ten billion. Also, the violation of CP symmetry is a subject of great theoretical interest because of the observed asymmetry between matter and anti-matter in the universe.

In 1977, theorists Robert Peccei and Helen Quinn^{6,7} proposed a solution to the strong CP problem by postulating θ to be a dynamical field instead of a number. This means adding a new field- the axion field - to the SM that couples to the strong nuclear force in the

same way as θ . In SM, symmetries lead to forces between particles, force “communicates” the symmetry from place to place between particles and, the force is a field. Quantum mechanics associates a particle with every field (e.g., the photon for the EM field). Thus, to add the axion to the SM, we introduce a new symmetry, called the Peccei-Quinn (PQ) symmetry, which is a global axial U(1) symmetry.

Introduction of the PQ symmetry corresponds to introducing a new bosonic field beyond the single Higgs boson of the SM. It is represented by the angular direction of the potential. At the phase transition temperature, where the symmetry is spontaneously broken, a pseudo Nambu-Goldstone^{8,9} is generated. This particle of the spontaneously broken PQ symmetry is the axion^{10,11}. Frank Wilczek named the axion after a brand of laundry detergent because it “cleaned up” a problem.

The hidden photons (HP) have a slightly different origin story. They could be produced after inflationary period, and are allowed to kinetically mix with the photons. It makes their detection possible and would be a viable candidate to constitute the dark matter component in the universe and explain the anisotropies in the CMB spectrum.

2.1.1 Interaction with Axions

The axion does not interact only with quarks and gluons but also with other particles in the SM. However, these interactions must be very weak for the axion to have evaded detection so far. The interaction with photons can be expressed as

$$\mathcal{L} \supset -\frac{1}{4} g_{a\gamma\gamma} a \mathcal{F}_{\mu\nu} \tilde{\mathcal{F}}^{\mu\nu} = g_{a\gamma\gamma} a \mathbf{E} \cdot \mathbf{B} \quad (2.1)$$

where $g_{a\gamma\gamma}$ is the axion’s coupling strength to photons, γ (i.e., to electromagnetism), a represents the axion field, $\mathcal{F}(\tilde{\mathcal{F}})$ is the electromagnetic field strength tensor (and its dual). As a consequence of the addition of axion field, the Maxwell’s equation of electromagnetism

are modified as

$$\begin{aligned}\nabla \cdot \mathbf{E} &= \rho - g_{a\gamma\gamma} \nabla a \cdot \mathbf{B} \\ \nabla \times \mathbf{B} - \dot{\mathbf{E}} &= j + g_{a\gamma\gamma} (\dot{a} \mathbf{B} + \nabla a \times \mathbf{E})\end{aligned}\tag{2.2}$$

where ρ and j are the ordinary charge and current, while the additional terms correspond to the axion-induced charge and current densities, respectively. The spatial coherence length of the oscillation axion field (a) is large because the momentum spread determined by the galactic escape velocity is small, $\Delta v \propto 10^{-3}c$. It is approximately 1 km for 1 μeV , and is inversely proportional to the axion mass. Therefore, $\nabla a \approx 0$ is valid in this experiment, and thus, only the time-dependent current source term is in effect. In 1983, Pierre Sikivie proposed a promising detection technique¹² using this remaining source term, i.e., the axions are converted into photons in the presence of a magnetic field as illustrated in Fig. 2.1.

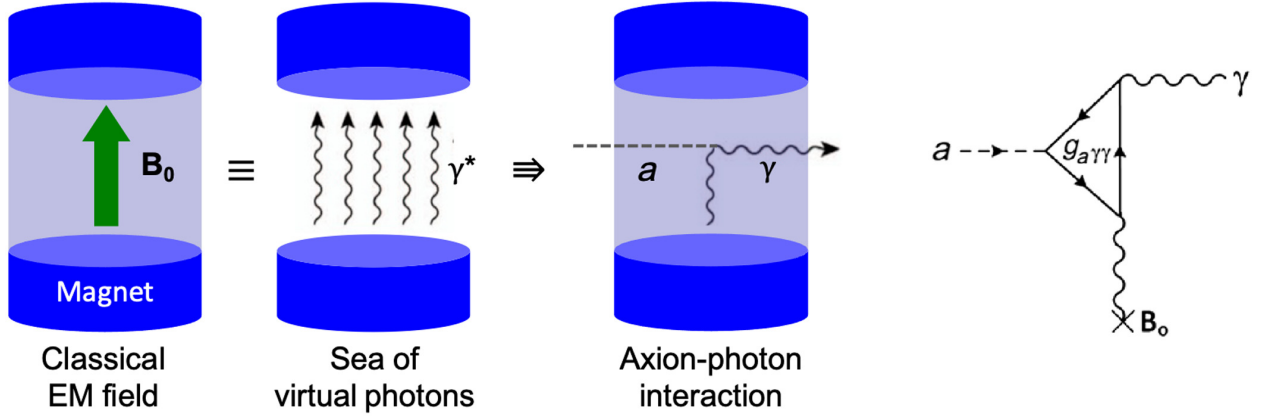


Figure 2.1: **Principle of axion conversion.** A classical strong magnetic field generates a sea of virtual photons with which axions interact to be converted to real photons. The corresponding Feynman diagram is also shown. The axion de Broglie wavelength is much larger than the detector sizes, enabling coherent conversion within the detectors. Image credits: Semertzidis et. al.¹³

Using the fact that $\mathbf{E} = -\frac{\partial \mathbf{A}}{\partial t}$ and integration by parts, the axion current density can be expressed as

$$\mathcal{L}_{ax} \sim \mathbf{J}_{ax} \cdot \mathbf{E} = \frac{\partial}{\partial t} (g_{a\gamma\gamma} a \mathbf{B}_0) \cdot \mathbf{A}\tag{2.3}$$

Assuming the observed dark matter density is composed solely of axions, a classical scalar

field well approximates the axion DM which is very uniform with its energy density stored in harmonic oscillators. Thus, the energy density contained in the axion field is related to the density of dark matter

$$\rho_{DM} = \frac{1}{2} m_a^2 a^2 \quad (2.4)$$

Substituting Eq. 2.4 into Eq. 2.3 and evaluating the time derivative of the oscillating axion field, yields the generated current density in terms of the DM abundance

$$\mathbf{J}_{ax}(t) = g_{a\gamma\gamma} \sqrt{2\rho_{DM}} \mathbf{B}_0 e^{\imath m_a t} \quad (2.5)$$

Eq. 2.3 informs us that in the presence of a large static magnetic field B_0 , a homogeneous oscillating axion field induces an electric field oscillating at the same frequency $\nu_a = m_a c^2/h$, with maximum amplitude

$$E_0 \sim g_{a\gamma\gamma} B_0 a \quad (2.6)$$

2.1.2 Interaction with hidden photons

In this case, the dominant interaction is realized through the kinetic mixing between ordinary photons A^μ and hidden photons A'^μ . The modified Lagrangian is of the form:

$$\mathcal{L}_{HP} \supset -\frac{1}{4}(\mathcal{F}_{\mu\nu} \mathcal{F}^{\mu\nu} + \mathcal{F}'_{\mu\nu} \mathcal{F}'^{\mu\nu}) - J_\mu A^\mu + \frac{1}{2}m_{\gamma'}^2 A'_\mu A'^\mu + \epsilon m_{\gamma'}^2 A_\mu A'^\mu \quad (2.7)$$

where $m_{\gamma'}$ is the mass of hidden photon and ϵ represents the coupling scale between hidden and ordinary photons. All the other relations follows similar to the axion where the current density due to a background of hidden photons can be derived as

$$\mathbf{J}_{HP} = \epsilon m_{\gamma'}^2 \mathbf{A}' \quad (2.8)$$

and, the density of dark matter is related to the magnitude of hidden photon field as

$$\rho_{DM} = \frac{1}{2} m_{\gamma'}^2 A'^2 \quad (2.9)$$

The oscillating effect of the generated current density can be expressed as

$$\mathbf{J}_{HP}(t) = \epsilon m_{\gamma'}^2 \mathbf{A}' = \epsilon m_{\gamma'} \sqrt{2 \rho_{DM}} e^{\iota m_{\gamma'} t} \hat{\mathbf{u}} \quad (2.10)$$

where $\hat{\mathbf{u}}$ represents the spatial dependence of the hidden photon polarization which is imprinted onto the generated current density.

2.1.3 Direction detection of dark matter

In order to detect the low mass particles such as axions and hidden photons, scientists have tried and developed various techniques/experiments such as astrophysical search for axions at CERN Axion Search Telescope (CAST) at CERN, recoil measurements from detectors such as CDMS and XENON100^{14,15} and light shining through wall experiment¹⁶ at DESY, Deutsches Elektronen-Synchrotron.

We are mainly interested in studying the interaction of dark matter fields with the electromagnetic fields. The interaction of both, axion and hidden photon results in an effective current density \mathbf{J}_{DM} which sources an oscillating electro-magnetic field inside a receiver. Currently, there are three experiments around the globe exploiting this interaction - ADMX (Axion Dark Matter eXperiment)¹⁷, HAYSTAC (Haloscope at Yale Sensitive to Axion CDM)¹⁸, CAPP (Center for Axion and Precision Physics Research)¹⁹. A hidden photon search with a superconducting cavity and photon counting technique²⁰ was demonstrated at SQuAD, a joint collaboration between the University of Chicago and Fermilab (also a part of this thesis).

These experiments use a resonant microwave cavity to coherently accumulate a weak signal arising from dark matter fields to photon conversion such that $m_{DM}c^2 = \hbar\omega$. In case

of an axion search, the microwave cavity is submerged in a large superconducting magnet (~ 10 T or higher) as shown in Fig. 2.1. The presence of a large magnetic field prohibits the use of ultra low-loss superconducting cavities and are forced to use lossy copper cavities. There are parallel efforts to develop novel cavity designs with thin layer deposition of high- T_c material on the cavity walls^{21,22}, photonic bandgap cavities made out of sapphire to achieve higher quality factor. Hidden photons do not require a magnetic field and thus, we can use the high quality factor superconducting cavities. Fabrication techniques developed at Fermilab for the accelerator cavities have shown enormous Q-factor in excess of 10^{10} to speed up the hidden photon search tremendously.

The main challenge of the dark matter searches is that the particle mass is an unknown parameter and has to be experimentally determined by scanning a vastly wide mass range. This demands different set of detectors to cover different mass ranges. In this work, we will only focus on the search in microwave range, in particular, 3 – 30GHz.

2.1.4 Expected signal due to dark matter

The interaction between the dark matter field and a microwave cavity can be modeled as a pair of coupled harmonic oscillators. The power transfer between the two is optimal when the dark matter mass is on resonance with the cavity and is enhanced by orders of magnitude given by the cavity quality factor Q_c . In a “haloscope”¹ type experiment, the expected power deposited in the cavity is

$$P_{ax} = (g_{a\gamma\gamma}^2 \frac{\rho_a}{m_a^2})(\frac{\beta}{1+\beta} \omega_c B_0^2 V C_{mnl} Q_L \frac{1}{1 + (2Q_L \Delta\omega_a/\omega_c)^2}) \quad (2.11)$$

where $g_{a\gamma\gamma}$ is the coupling scale, $\beta = 1 - \frac{Q_c}{Q_L}$ is the impedance ratio, C_{mnl} is the form factor, Q_L is the loaded quality factor and $\Delta\omega_a$ is the detuning between the axion and cavity frequency. As search for the dark matter extends to higher frequency the volume of the

1. Haloscope because of the scope for axions in galactic halo

detector must shrink to satisfy the resonance condition. Therefore, the signal power or the expected number of photons scales unfavourably with the frequency, $\bar{n}_{DM} \propto V \propto \lambda^3 = \omega^{-3}$. A similar scaling applies to the hidden photon conversion as well.

For example, an axion search with the microwave cavity (5.965 GHz) used in the present work and given the experimental parameters in typical axion search experiments^{23,18,24,25}, QCD axion models^{26–29} predict a signal with mean photon number of $\bar{n}_{\text{axion}} \sim 10^{-8} - 10^{-5}$ per measurement. For hidden photons, the parameter space is less constrained,^{4,30,31} and the mean photon number per measurement could be $\bar{n}_{\text{HP}} \leq 10^{-1}$ ($\bar{n}_{SQL}^2 \gg \bar{n}_{\text{axion}}, \bar{n}_{\text{HP}}$).

2.1.5 Detection principle

In order to detect the feeble oscillating EM field generated by the DM, a quantum noise limited amplifier is employed to readout the excess power in the microwave cavity. Recent experiments use Josephson Parametric Amplifier (JPA)^{32–35}, where the noise variance is equivalent to fluctuations of an effective background of $\bar{n}_{SQL} = 1$ (see Chapter 3 for a detailed discussion on JPA). It can be operated with a gain of > 20 dB with an instantaneous bandwidth of order 10 MHz. In a coherent detection, the JPA is operated in a phase preserving mode, where both the quadrature of the field are amplified. The figure of merit for a haloscope search experiment is the signal-to-noise ratio given by

$$R = \frac{P_{sig}}{\delta P_N} \quad (2.12)$$

where δP_N is the actual random fluctuations of the noise power within the detection bandwidth. A coherent detection is associated with an intrinsic spectral resolution set by the time over which a measurement is made. According to the Nyquist sampling theorem, a noise limited to a bandwidth $\Delta\nu$ and measured for a time τ is completely represented by $n = 2\Delta\nu\tau$ independent samples. For a Gaussian distribution of the noise voltage within a

2. $\bar{n}_{SQL} = 1$, due to 1/2 photon from the incoming signal mode and 1/2 photon scattered into the output from the idler mode.

bandwidth $\Delta\nu$, we can then write the standard error of the variance³ of voltage distribution as

$$\begin{aligned}\delta P_N &= \sqrt{\frac{2}{n-1} k_B T_{sys} \Delta\nu} \\ &= \frac{k_B T_{sys} \Delta\nu}{\sqrt{\Delta\nu \tau}}\end{aligned}\tag{2.13}$$

where the total noise is modeled as Johnson noise at some effective temperature T_{sys} . Substituting Eq. 2.13 in Eq. 2.12, we obtain the Dicke radiometer equation

$$R = \frac{P_{sig}}{k_B T_{sys}} \sqrt{\frac{\tau}{\Delta\nu}}.\tag{2.14}$$

Assuming the system noise temperature is known, Eq. 2.14 determines the absolute energy scale of the experiment and tells us the time τ required to detect or exclude the dark matter conversion power P_{sig} . Thus, it is very crucial to estimate the system noise temperature with high precision, especially as we move towards using high quality factor cavities such that $\Delta\nu_c \leq \Delta\nu_{DM}$. See Chapter 4 for more careful discussion about various noise sources, their limits and how to quantify them in a real experiment.

2.2 Current Challenges

In this section, I am going to discuss the current challenges faced by dark matter experiments in the microwave frequency range and how we can tackle them.

Quantum limited amplification

Although JPA provides a big boost to the signal-to-noise ratio (SNR) in sub-GHz frequency region but, the noise power proportional to $\hbar\omega$ keeps on increasing at higher frequency searches. Because of the non-commutativity of the two field operators, a simultaneous mea-

3. for large number of samples $n - 1 \approx n$

surement incurs a penalty from the quantum mechanics due to the Heisenberg uncertainty principle. The real and imaginary quadrature of the cavity field can be written in terms of the creation and annihilation operator as

$$\begin{aligned}\hat{\mathbf{I}} &= \frac{\hat{a} + \hat{a}^\dagger}{\sqrt{2}} \\ \hat{\mathbf{Q}} &= \frac{\hat{a} - \hat{a}^\dagger}{\sqrt{2\iota}}\end{aligned}\tag{2.15}$$

Since the field operators contain number operators of a harmonic oscillator which obey commutation relation $[\hat{a}, \hat{a}^\dagger] = 1$, they inherit the same non-commutativity where,

$$\begin{aligned}[\hat{\mathbf{I}}, \hat{\mathbf{Q}}] &= \frac{1}{2\iota} [\hat{a} + \hat{a}^\dagger, \hat{a} - \hat{a}^\dagger] \\ &= \frac{1}{2\iota} ([\hat{a}, \hat{a} - \hat{a}^\dagger] + [\hat{a}^\dagger, \hat{a} - \hat{a}^\dagger]) \\ &= \frac{1}{2\iota} (-[\hat{a}, \hat{a}^\dagger] + [\hat{a}^\dagger, \hat{a}]) \\ &= \frac{1}{2\iota} (-1 - 1) \\ &= \frac{1}{\iota}\end{aligned}\tag{2.16}$$

This non-zero commutation results in an uncertainty relation

$$\Delta\hat{\mathbf{I}} \Delta\hat{\mathbf{Q}} \geq \frac{1}{2}\tag{2.17}$$

which corresponds to a minimum uncertainty of half a photon worth noise added to each measured quadrature. A coherent receiver as mentioned above measures both the quadrature $\hat{\mathbf{I}}$ and $\hat{\mathbf{Q}}$ whereas, a bolometric receiver measures the number operator $\hat{N} = \hat{a}^\dagger \hat{a}$. Quantum noise arises because the quadrature operators do not commute with each other. This added noise overwhelms the signal by multiple orders of magnitude making the dark matter search impossible in a reasonable amount of commissioned time.

Therefore, we developed a novel measurement technique which evades the quantum limit

by avoiding the simultaneous measurement of non-commuting observables of the cavity field (see Chapter 5). The field can equivalently be represented with conjugate variables which follows the same commutation relation, number operator \hat{N} and the phase $\hat{\theta}$. For a dark matter search, information about both the quadrature is not necessary and just counting the number of photons deposited in the cavity is sufficient to classify it a detection event. This results in a distortion of the phase space density where the uncertainty in the amplitude is arbitrarily low at the expense of complete randomization of the phase information.

Plummeting signal power

As mentioned earlier, the signal power which is proportional to the volume of the detector shrinks at higher frequencies to maintain the resonance condition. To overcome this, I developed a stimulated emission technique (see Chapter 6) to enhance the conversion of DM into photons by preparing the cavity in a Fock state.

Anomalous skin depth effect (ASE)

Due to the presence of a large magnetic field required for axion conversion, the current experiments are limited by the quality factor achieved with copper cavities. The dissipation losses in the cavity walls increase at cryogenic temperature and high frequencies due to the ASE. It was first fully described phenomenologically in³⁶ and theoretically in³⁷. Experimentally, it was observed that the mean free path of the conduction electrons becomes larger than the penetration depth of the fields. As a result, only a small fraction of electrons can contribute to conduction, suppressing the effective conductivity at microwave frequencies.

From the classical theory of the skin depth, which tells us that any finite frequency ν , EM fields only penetrate a distance

$$\delta = (\pi \nu \mu \sigma)^{-1/2} \tag{2.18}$$

into a metal with permeability $\mu \approx \mu_0$ and DC conductivity σ . This expression becomes invalid at low temperatures when δ drops below the mean free path of the electrons, $l = (\sigma m_e v_F / n_e e^2)$, where v_F is the metal's Fermi velocity and n_e is its conduction electron density. The suppression in the effective conductivity is of the order $\mathcal{O}(\delta/l)$ thus, $\sigma \rightarrow \gamma(\delta/l)\sigma$ where γ is a numerical factor. Substituting it in Eq. 2.18 we obtain

$$\delta_a = \left(\frac{m_e v_F}{\gamma \pi \nu \mu n_e e^2} \right)^{1/3} \quad (2.19)$$

The quality factor of the cavity is inversely dependent on δ and thus, plugging all the frequency dependencies in Eq. 2.11, we see the rather unfavorable scaling of the axion power conversion with frequency $P_{ax} \propto \nu^{-14/3}$.

Hence, it is important to innovate and develop new fabrication methods to achieve high-Q even in the presence of high magnetic field. One approach that I have embarked upon during this thesis work is to make high-Q cavities using photonic crystals (see Chapter 7). The bandgap protects the fields from reaching the metallic walls, lowering the dissipation losses by orders of magnitude.

2.3 Our Approach

At SQuAD, we have followed the “divide and rule” strategy to develop and demonstrate a solution to each challenge I mentioned above. Our goal is to cohesively integrate all the technologies mentioned in this work as well as others to conduct an axion search with a tuning range of 10% around 12 GHz. In my thesis work, we were immensely benefited by the advancement in superconducting qubit technology geared towards quantum computing applications. We built upon the current research to develop a single photon counter with background counts $1300\times$ lower than the SQL. Using a qubit to prepare quantum state of light in the cavity such as a Fock state, we demonstrate a signal enhancement technique with stimulated emission to speed up the dark matter search. Moreover, inspired by the

nano-photonic cavities, we developed photonic bandgap cavity at microwave frequency to achieve very high quality factor which are compatible with large magnetic field.

Chapter 3

Superconducting devices

Superconductivity was first discovered in 1911 by a graduate student working with Dutch physicist H Kamerlingh-Onnes. While studying the material properties at different temperatures, he observed that the electrical resistance of a mercury wire suddenly dropped by a factor of 20,000 when the wire cooled below a certain temperature. This seemingly-frictionless motion of electrons in a material led to the discovery of a remarkable phenomenon and we named such materials as superconductors. But it was not until 1960s that the scientists were able to mathematically formulate a theory which would explain all the experimental evidences such as field expulsion (Meissner effect), energy gap and interactions of conduction electrons in a cohesive manner. This theory is known as the “BCS theory” named after the trio John Bardeen, Leon Cooper and Bob Schrieffer for which they shared the 1972 Nobel Prize in Physics.

So, how do we use superconductors for quantum bits? Yet, another remarkable phenomenon we haven’t discussed so far is the “quantum tunneling” of electron pairs between two superconducting layers separated by an insulating barrier. This phenomenon known as the “Josephson effect” named after Brian Josephson tells us that a current flows through the “Josephson Junctions” without any loss until a critical current is reached. He also predicted the exact relation between the current and voltage across a junction.

In this chapter, I will describe the practical implementation of “Josephson junctions” and how they have been developed over the past few decades to realize a quantum bit. I will primarily focus on “transmon” qubit and how we can couple it to the field of a microwave cavity to build a photon counting device. Although, I do not explicitly talk about 3D superconducting cavity, it is an integral component to the experiments in this thesis but I will discuss all the characterization methods in this chapter. I refer readers to these references^{38,39} for detailed discussions on the 3D cavity design and fabrication methods.

In the end, I will discuss the principle of operation and design of quantum noise limited amplifiers which use the non-linearity provided by the Josephson junctions.

3.1 Introduction

Josephson junction is a good candidate to make quantum bits because (1) of the low dissipation inherent to superconductors allowing long coherence times (2) complex microwave circuits can be nano-fabricated using integrated-circuit processing techniques thus scaling to a large number of qubits is possible. In order to make a “quantum bit”, we use the non-linearity provided by Josephson junction to lift the degeneracy in a linear oscillator such that the energy levels are no longer equally spaced. We can isolate the first two-levels which constitutes our “Two-level System (TLS)” or an artificial atom as depicted in Fig. 3.1.

Josephson junction consists of two superconducting layers separated by a thin insulating barrier. As described in Landau-Ginzburg theory, the superconducting state on either side of the junction can be expresses by a complex order parameter $\psi = |\psi|e^{i\delta}$. The tunneling of Cooper pairs from superconductor A to superconductor B in response to the phase difference $\delta = \delta_A - \delta_B$ is known as the Josephson effect. The tunneling of charge carrying Cooper pairs manifests at DC as a dissipation-less super current even in the absence of any applied voltage.

For a time dependent δ , the Josephson effect is described by the equations

$$V(t) = \frac{\Phi_0}{2\pi} \frac{\partial\delta}{\partial t}, \quad (3.1)$$

$$I(t) = I_0 \sin(\delta(t)), \quad (3.2)$$

where $\Phi_0 = \frac{h}{2e} = 2 \times 10^{-15} \text{ T m}^2$ is the flux quantum, and I_0 is the critical current of the Josephson junction, which depends on the material properties, geometry and temperature. Comparing Eq. (3.1) to the integral form of Faraday’s law shows that the Josephson phase $(\Phi_0/2\pi)\delta(t)$ behaves formally like a magnetic flux. Using this correspondence and Eq. (3.2),

we can define the Josephson inductance as

$$\begin{aligned} L_J &= \frac{\Phi_0}{2\pi} \frac{\delta(t)}{I(t)} \\ &= \frac{\Phi_0}{2\pi I_0} \frac{\arcsin(I/I_0)}{(I/I_0)} \end{aligned} \quad (3.3)$$

By expanding Eq. (3.3) to second order in (I/I_0) , we obtain

$$L_J = L_0 + \Delta L (I/I_0)^2 \quad (3.4)$$

with $L_0 = \Phi_0/(2\pi I_0)$ and $\Delta L = L_0/6$. The energy stored in the JJ can be computed using Eq. 3.1 and 3.2

$$U = \int IV = E_J(1 - \cos(\delta)) \quad (3.5)$$

where, $E_J = \frac{\Phi_0 I_0}{2\pi}$ is the Josephson energy.

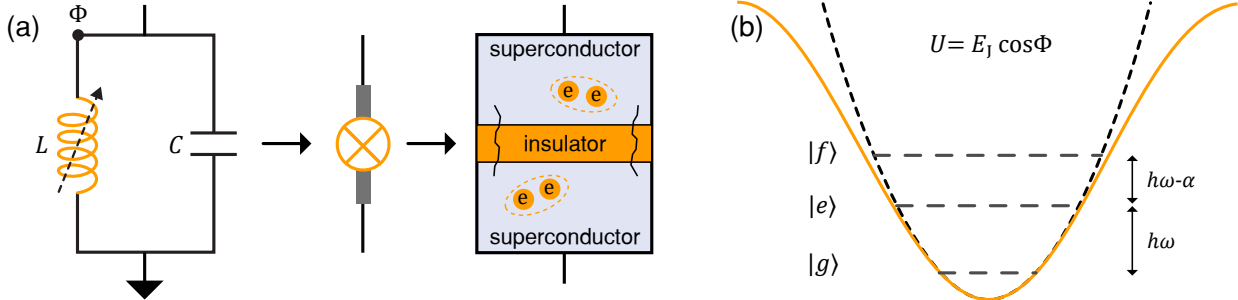


Figure 3.1: **Anharmonic quantum oscillator.** (a) An usual harmonic oscillator consists of a capacitor C and a linear inductor L . A Josephson junction can be modeled as a non-linear inductance represented by the orange cross. It is composed of two superconducting layers separated by a thin insulating layer that allows tunneling of Cooper pairs. This junction is dissipation less at temperatures below the critical temperature of the superconductor. (b) The potential of this circuit is no longer quadratic (dashed line) due to the presence of a non-linear element and is, instead a cosine function (orange). As a result, the energy levels are no longer equally spaced and the energy eigenstates can be addressed individually.

3.2 Non-linear oscillator

There are many types of superconducting circuits which exploit the non-linearity offered by Josephson junction such as flux, phase or charge as the quantum degree of freedom. In the scope of this work, we will focus on a particular type of Josephson junction based device called the transmon⁴⁰. The design of transmon is simple: it is composed of a single junction shunted by a large capacitance. The resultant Hamiltonian resembles like a quantum harmonic oscillator where the conjugate variables follow the usual commutation relation. We can describe the transmon circuit by the simple Hamiltonian⁴⁰

$$\hat{H} = 4E_C(\hat{n} - n_0)^2 + E_J \cos \hat{\delta} \quad (3.6)$$

where \hat{n} and $\hat{\delta}$ are the normalized operators for charge and phase difference across the junction and n_0 is the offset charge. E_C is the charging energy of the capacitor and together with E_J determine all the key features of a transmon. In particular, the transition frequency between the ground, $|g\rangle$ and excited state, $|e\rangle$ scales as $\omega_{\text{ge}} \sim \sqrt{8E_J E_C}$. The best selling point of transmon is its protection against charge noise, fluctuation in n_0 which is achieved by choosing the parameters of transmon such that $1 \ll E_J/E_C < 10^4$. The anharmonicity of the transmon α , difference in transition energies between the two excited states scales with E_C :

$$\alpha = E_{n+1,n} - E_{n,n-1} \simeq -E_C \quad (3.7)$$

This implies that as we increase E_J/E_C to suppress charge noise, we are also inadvertently lowering the anharmonicity of the transmon. A small anharmonicity constrains how fast we can selectively address the individual transition using microwave control drives. Fortunately, while the charge dispersion scales exponentially with E_J/E_C , the α only scales polynomially. This allows us to design devices with good coherence times ($\sim 50 - 200 \mu\text{s}$) and large $\alpha \sim 150 \text{ MHz}$ by appropriately choosing E_J and E_C .

A transmon circuit can be simulated using commercial tools such as **Ansys HFSS** or in

conjunction with open-source community tool such as pyEPR⁴¹ to extract the relevant design parameters. The simple design of a transmon qubit makes it easier to fabricate the device using well-established electron-beam and photon lithographic procedures. These traits make the transmon a favorable choice for many circuit-QED (cQED) experiments as well as the industry efforts to realize a quantum processor which can outperform classical computers.

3.3 Design and Fabrication

Fig. 3.22 shows an optical image of the transmon qubit fabricated in the nano-fabrication facility at PNF, UChicago. Please refer to Akash Dixit's thesis⁴² to read more about the design and fabrication steps involved in achieving the desired device parameters. The devices used in both, the photon counting and stimulated emission experiments were shared with the other quantum computing experiments in the lab.

3.4 Coupling transmon with a microwave cavity

A microwave cavity described by a simple harmonic oscillator Hamiltonian and a transmon qubit are two of the simplest ingredients in cQED toolbox but offer immense possibilities to create and study complex physical systems which are otherwise difficult to find in nature. We are going to study the simplest configuration of a transmon capacitively coupled to a simple resonator. The Jaynes-Cummings Hamiltonian describes the interaction of such a system consisting of the transmon Hamiltonian, that of the resonator and a dipole coupling term that relates the current induced by the oscillating electro-magnetic field in the resonator. The Hamiltonian can be expressed in terms of the number operators of the cavity (\hat{a}) and qubit (σ) as

$$\hat{H}/\hbar = \omega_c \hat{a}^\dagger \hat{a} + \omega_q \frac{\sigma_z}{2} + g (\hat{a} + \hat{a}^\dagger)(\sigma_+ + \sigma_-) \quad (3.8)$$

where ω_c and ω_q are the transition frequencies of the cavity and qubit respectively and g is the dipole coupling between the electric field of the cavity mode and the qubit antenna. It

can be approximated as $g \sim \vec{d} \cdot \vec{E}$ where \vec{d} is the dipole moment of the qubit and \vec{E} is the zero point field of the cavity mode.

In the dispersive limit, meaning the qubit and cavity are far detuned ($\Delta = \omega_c - \omega_q$) and the coupling $\frac{g}{\Delta} \ll 1$, the Jaynes-Cummings Hamiltonian can be investigated using second order perturbation theory to obtain an approximate expression

$$\hat{H}/\hbar \approx \omega_c \hat{a}^\dagger \hat{a} + \omega_q \frac{\sigma_z}{2} - \chi \hat{a}^\dagger \hat{a} \frac{\sigma_z}{2} - \frac{K}{2} \hat{a}^\dagger \hat{a} (\hat{a}^\dagger \hat{a} - 1) \quad (3.9)$$

where K is the non-linearity of the resonator inherited due to its interaction with the transmon. We can infer that the interaction term is dependent only on the number operators $\hat{a}^\dagger \hat{a}$ and σ_z and $\chi = \frac{g^2}{\Delta} \frac{\alpha}{\Delta+\alpha}$. I would like to bring your attention to the key feature of this Hamiltonian, a photon number dependent frequency shift (χ) of the qubit transition as shown in Fig. 3.2. The qubit frequency shifts by an integer multiple of $n \cdot \chi$ dependent on the cavity occupation number.

$$\hat{H}/\hbar \approx \omega_c \hat{a}^\dagger \hat{a} + (\omega_q - \chi \hat{a}^\dagger \hat{a}) \frac{\sigma_z}{2} \quad (3.10)$$

Similarly, we can rewrite this Hamiltonian in the following manner where the cavity frequency shifts depending on the state of the qubit as shown in Fig. 3.3

$$\hat{H}/\hbar \approx (\omega_c - \chi \frac{\sigma_z}{2}) \hat{a}^\dagger \hat{a} + \omega_q \frac{\sigma_z}{2} \quad (3.11)$$

We will take advantage of Eq. 3.10 and Eq. 3.11 to simultaneously couple a transmon qubit to a low-Q ($Q \sim 10^4$) readout cavity for a fast dispersive readout and a high-Q ($Q \geq 10^7$) storage cavity for storing and retrieving the quantum information.

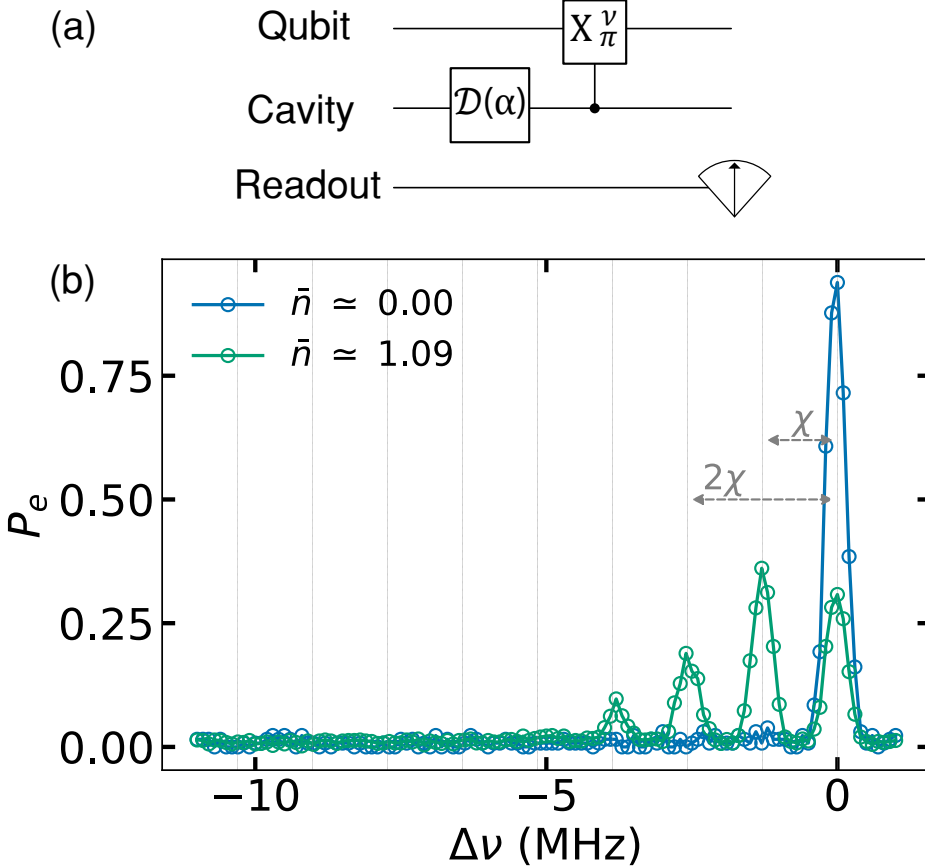


Figure 3.2: **Photon number dependent frequency shift.** (a) Experimental sequence describing the spectroscopy measurement of the transmon after displacing the cavity with a mean photon number of zero and one. (b) In the presence of cavity photons, dispersive coupling shifts the $|g\rangle \rightarrow |e\rangle$ transition frequency down by integer multiples of χ , as shown by the grey arrows. By fitting a Poisson distribution, we can estimate the mean photon number of a coherent state in the cavity.

3.5 Coupling to the outside world

In order to perform operations on these sample, we couple them to the outside world via input and output signal lines. In case of 3D qubit-cavity modules, we have been using SMA flange mounts as a dipole antennae shown in Fig. 3.4, whose coupling can be conveniently set by the pin location and the length. There can be more than one coupling pins to control each component individually. The coupling quality factor Q_c is measured and set at the room temperature as per the desired rate of operation. For example, in order to quickly readout the transmon state, we set the coupling port on the readout cavity such that the

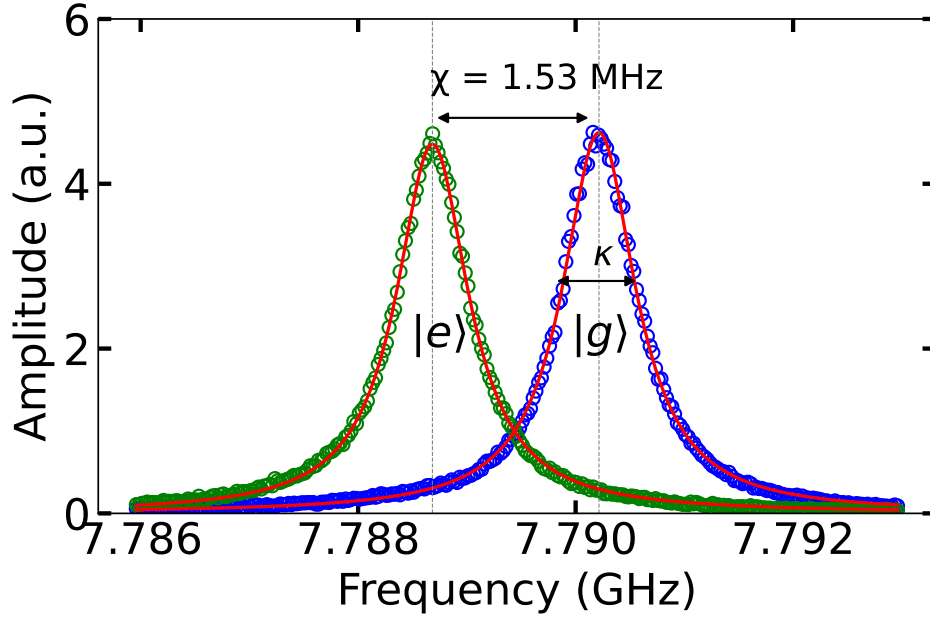


Figure 3.3: **State dependent frequency shift.** Spectroscopy measurement of the resonator cavity when the qubit is prepared in $|g\rangle$ and $|e\rangle$ state before probing the resonator. The χ shift is greater than the κ of the resonator which allows fast and efficient readout. The demodulated signal is very well approximated with a Lorentzian function (red) to obtain an estimate of the frequency and the linewidth κ .

$Q_c \ll Q_i$ ¹. On the other hand, for a storage cavity we set $Q_c > Q_i$ to prevent the thermal photons from leaking in and corrupting the quantum state but at the same time allowing sufficient delivery of power to manipulate the qubit and cavity states at a reasonable rate. The Hamiltonian of a drive on a mode a can be described as:

$$\mathcal{H}_{drive} = \omega_a \hat{a}^\dagger \hat{a} + i\epsilon(t) \hat{a} e^{-i\omega t} - i\epsilon^*(t) \hat{a}^\dagger e^{i\omega t} \quad (3.12)$$

where $\epsilon(t)$ is the time dependent drive amplitude.

3.5.1 Microwave control electronics

The microwave signals required to control the sample with arbitrary phase and amplitude control are sourced from a heterodyne setup, consisting of digital-to-analog converters

1. We need to ensure that the qubit or storage cavity lifetime is not Purcell limited by the readout decay rate.

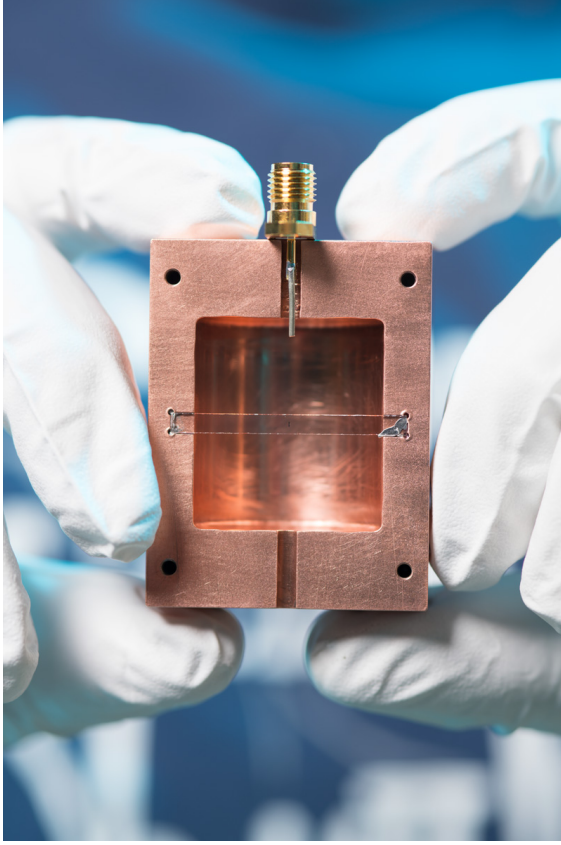


Figure 3.4: **SMA dipole antenna for input-output control.** A 3D copper cavity coupled to a transmon qubit fabricated on a sapphire chip in the middle. The SMA dipole antenna mounted on the top couples the system to the outside world. Courtesy: Reidar Hahn

(DACs), local oscillators (LOs) and IQ mixers. DACs provide the capability to generate an arbitrary waveform centered around an intermediate frequency (IF) $\omega_{\text{IF}} = -250 \text{ MHz}$ to 250 MHz , with up to 500 MHz bandwidth. The IF tone is then up-converted with an IQ mixer (Marki MMIQ-0218LXPC or MMIQ-0416L) using a continuous wave (CW) microwave LO (Keysight MXG or SignalCore SC5511A). We suppress the LO leakage and unwanted side-bands as a by-product of the mixing process by calibrating the gain and phase offset values of the DAC channels such that their relative power is at least 40 dB below the main peak. The signals are further filtered with either a band-pass or a low-pass filter at room temperature and further attenuated in the dilution refrigerator as shown in Fig. 3.5. The attenuators are staggered at different temperature stages to minimize the thermal radiation from higher stages to reach the subsequent stages. If required, additional low-noise amplifiers

are added to the control drives to increase the rate of operations.

QICK

In addition to the commercially available RF electronics solutions, I did get a chance to get involved in the development and testing of custom RF electronics board based on RFSoC technology called QICK (Quantum Instrumentation Control Kit)⁴³. It consists of high frequency DAC channels to directly generate tones up to 6 GHz and ADCs to digitize the readout signal. We tested the new hardware on a transmon qubit and demonstrated that the RF performance of this new hardware is on par with the commercially available expensive equipment. The firmware for this hardware was developed at Fermilab and is freely available on GitHub⁴⁴ for the community to jump-start and develop further as per their requirements. We also added example Jupyter notebooks to guide the users with basic qubit experiments.

3.5.2 Amplification chain

The transmitted signal from readout cavity is amplified by a Josephson Parametric Amplifier operating close to the quantum limit. The amplified signal then goes the High-electron-mobility transistor (HEMT) amplifier at 4 K before reaching the room temperature where a couple of Miteq amplifiers further increase the SNR. We use the same LO and split it twice to use it as a JPA pump to keep the phase delay between the readout and pump tone constant. The RF signal is down-converted using an IQ mixer and the resultant I and Q signals are digitized using a pair of Analog-to-digital converters (ADCs). We do add a pre-amplifier (Mini-Circuit ZX60-P103LN+) in front of the ADC to avoid running into shot-noise/bit-noise issue.

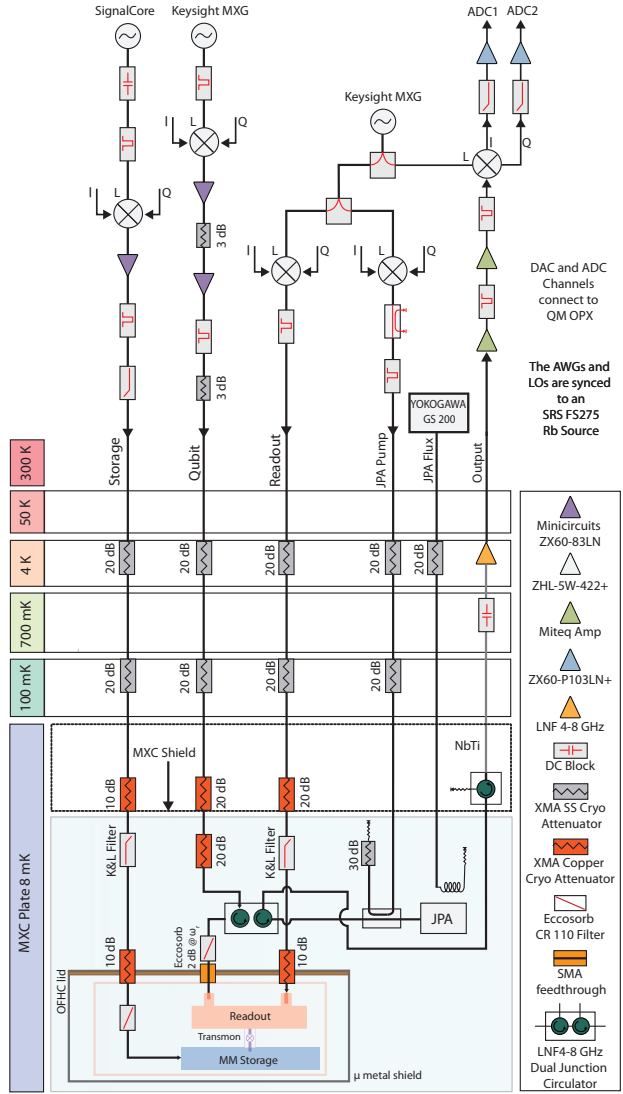


Figure 3.5: **Wiring diagram inside the dilution refrigerator and the room temperature measurement setup.** Quantum Machines (QM) OPX controller was used to generate the arbitrary wave forms (DACs) and digitize the incoming readout signal (ADCs). All the tones are up-converted using IQ modulation. Storage cavity is controlled via a direct port and qubit is controlled by injecting a drive into the strongly coupled port of the readout. Readout signal is injected into the weakly coupled port and, the signal is routed to the JPA using non reciprocal circulator elements. The amplified signal is routed to the HEMT for further amplification and the signal is then mixed down to 100 MHz IF, further amplified, and finally digitized. All the RF lines are heavily filtered with homemade eccosorb filters and attenuated to minimize stray radiation from entering the device.

3.6 Qubit readout and characterization

In the previous section, we discussed how the qubit imparts a state dependent shift on the resonator transition frequency. When this shift χ is much larger than the linewidth of the cavity modes, the dispersive shift offers a convenient tool to implement conditional operations between a transmon and a cavity mode⁴⁵. In particular, we could use this frequency shift of low-Q resonator to detect the state of the transmon^{46,47}. Fortunately, this measurement is Quantum Non-demolition (QND)⁴⁸ in nature, meaning the qubit state is not perturbed significantly while probing the transition frequency of resonator with a weak microwave drive. In a later section, I will show the experimental result of the QND-ness of this readout scheme as shown in Fig. 3.10.

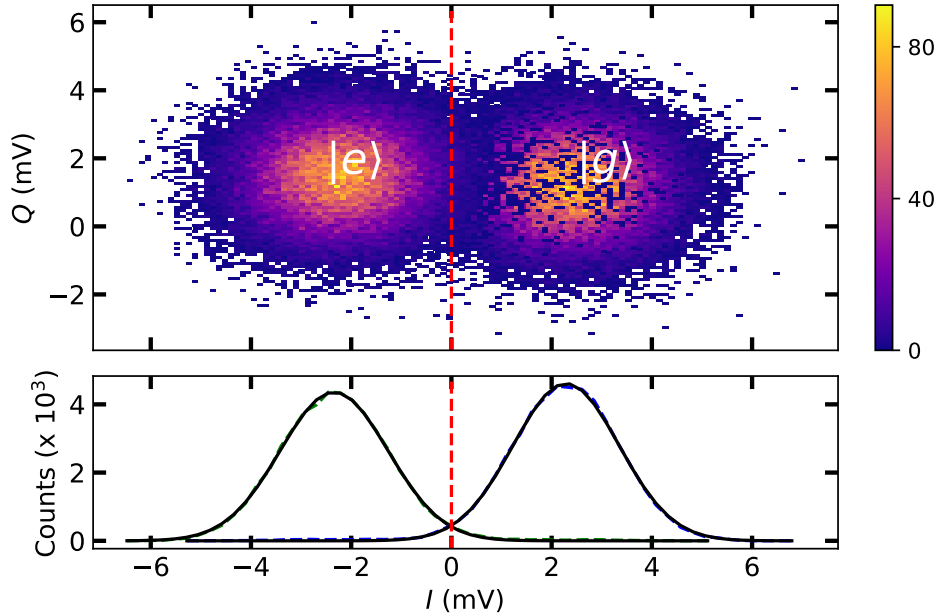


Figure 3.6: **QND readout of the transmon state.** (Top) shows the two quadrature values of the down-converted readout signal for qubit prepared in $|g\rangle$ and $|e\rangle$ state. (Bottom) By fitting a sum of two Gaussian we can estimate the overlap region and assign a fidelity as $F = 97\%$. The red dashed line shows an optimal value of the threshold for tagging a qubit state based on a single shot readout.

Eq. 3.11 tells us that the resonator roughly takes $\frac{1}{\chi}$ time to maximally resolve the two qubit states. However, the information is leaking out of the resonator at the rate κ thus, we can achieve a high-fidelity readout by optimising the design parameter such that

$\chi/\kappa \sim 1$. The decay rate of the readout can be easily controlled by adjusting the coupling to a transmission line. We can improve the SNR of readout chain by amplifying the readout signal at the quantum limit using a Josephson Parametric Amplifier². Fig. 3.6 shows a typical readout histogram with the qubit initialised in $|g\rangle$ and $|e\rangle$. Clearly, single-shot Gaussian blobs are very well separated and we can achieve a readout fidelity of $F = 1 - \frac{1}{2}(P(g|e) + P(e|g)) = 97\%$ with our current device which is likely limited by the thermal excitation of the qubit and the decay of qubit during the readout process. This is a remarkable result feat to achieve with only a mean number of 2 photons in the readout resonator (see Sec. 4.2.3), which would otherwise take $10 - 100$ photons.

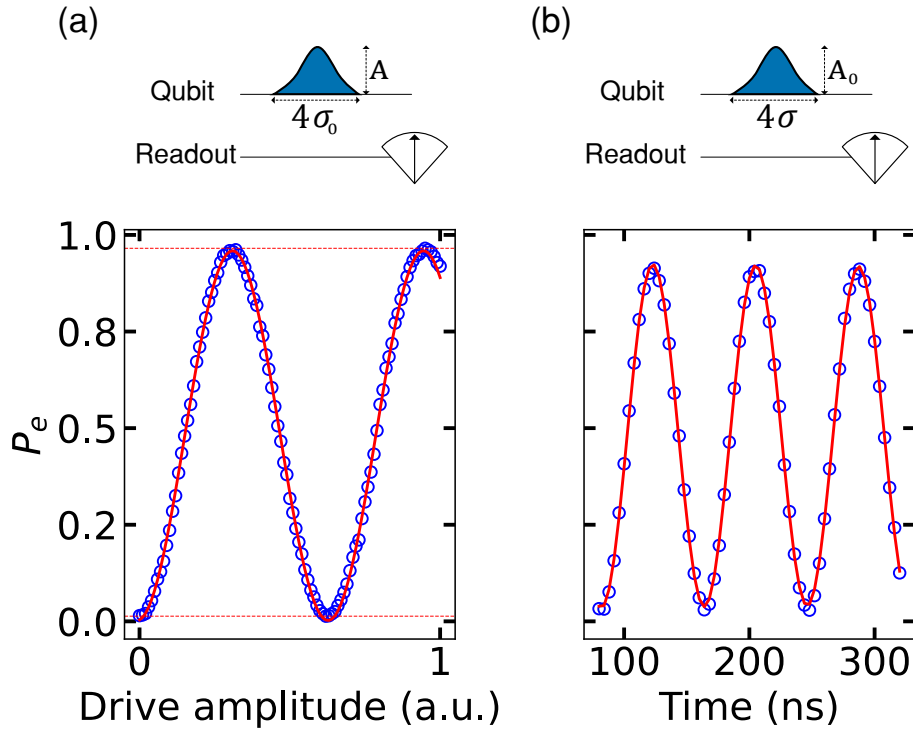


Figure 3.7: **Rabi-flopping experiment of a transmon.** (a) Power/Amplitude Rabi: A Gaussian pulse of fixed length 80 ns ($\sigma_0 = 20$ ns) and variable amplitude (A) is applied to flip the transmon from $|g\rangle$ and $|e\rangle$ state. (b) Time Rabi: Similarly, a constant amplitude pulse (A_0) but varying pulse length (σ) is applied to Rabi-flop the transmon.

With an optimal readout scheme in place, we can now perform a series of basic measurements to determine the key parameters related to transmon. For example, a Rabi-flop

2. I will discuss JPA in detail in a later section.

experiment to estimate the power required to flip the transmon from $|g\rangle$ to $|e\rangle$ state and vice versa (known as π -pulse). There are two ways to calibrate the power and duration of the π -pulse, either fix the duration and vary the power or fix the power and vary the duration as shown in Fig. 3.7. Microwave electronics is very well equipped to handle precise-timing control but suffers from variation in output power due to thermal fluctuations as well as bit-resolution on the DACs. I personally prefer the **power-Rabi** for π -pulse calibration to regularly fine-tune the π -pulse. However, I would like to point out that care must be taken while choosing the pulse length such that the bandwidth (frequency content) of the pulse is $\ll \alpha$ to avoid populating the higher transition levels of the transmon. We typically use Gaussian shaped pulse to keep the bandwidth³ small.

After π -pulse calibration, we can perform a transmon lifetime (T_1) experiment, where we first excite the qubit from $|g\rangle$ to $|e\rangle$ and monitor its decay back to ground state after a variable wait time as shown in Fig. 3.8 (a). The coherence of a transmon (T_2) is measured using a Ramsey sequence which consists of two $\pi/2$ -pulses separated by a variable delay time. In practice, the phase of the second $\pi/2$ -pulse is advanced to intentionally induce oscillations such that the resultant oscillations can be fit to estimate the detuning between the drive tone and the transmon resonance frequency as shown in Fig. 3.8 (b).

After characterizing the first two levels of a transmon, we could potentially use the third energy level to perform certain useful manipulations such as qubit temperature measurement, quickly reset the transmon using $f0 - g1$ side-bands etc. Since we know that the $|e\rangle \rightarrow |f\rangle$ transition occurs at a different frequency from that of $|g\rangle \rightarrow |e\rangle$, we can simply apply the same techniques discussed above but with the drive frequency centered around ω_{ef} instead. For example, we can perform a Rabi-flop experiment between $|e\rangle$ and $|f\rangle$ state using the protocol described in Fig. 3.9 where we first excite the transmon from $|g\rangle \rightarrow |e\rangle$ and then send a drive tone with variable amplitude to excite the transmon from $|e\rangle$ to $|f\rangle$. Similarly, we can perform a Ramsey measurement between $|e\rangle$ and $|f\rangle$ state and determine its coherence

3. Bandwidth of a Gaussian pulse with standard deviation σ is given by, $\Delta\nu \approx \frac{0.44}{\sigma}$

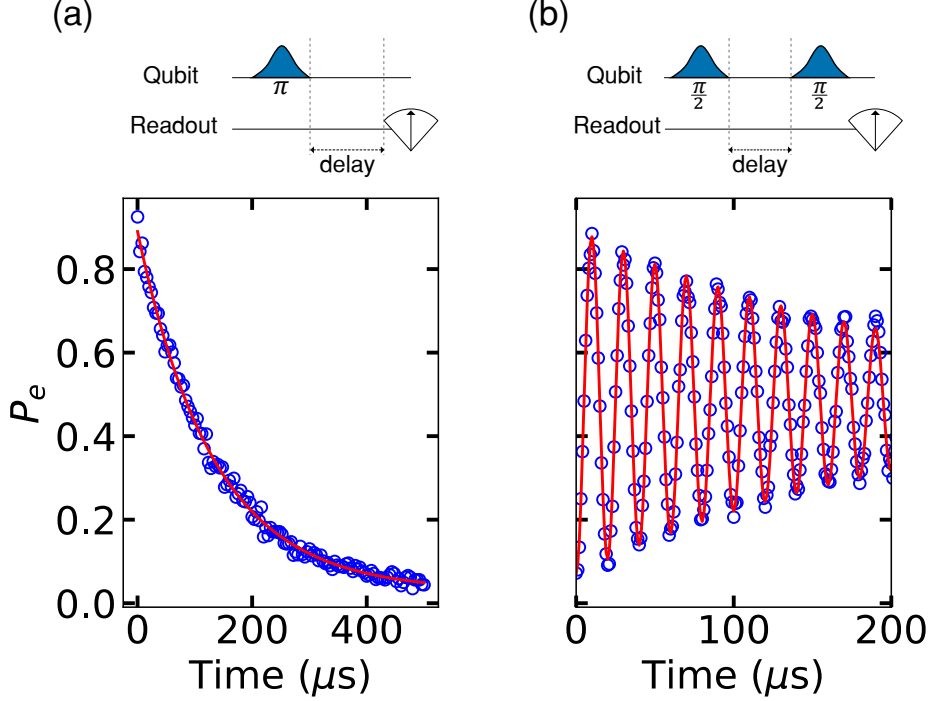


Figure 3.8: Qubit lifetime and dephasing time measurement. (a) T_1 measurement by sending a π -pulse to excite the transmon to $|e\rangle$ state and monitor its decay as a function of variable wait time. By fitting an exponential function, we extract the $T_1 = 120\text{ }\mu\text{s}$. (b) T_2 measurement with a Ramsey experiment. The sequence consists of two $\pi/2$ -pulse separated by a variable delay time. The envelope of the measured oscillations informs the $T_2 \sim 200 - 230\text{ }\mu\text{s}$ and its frequency provides us the detuning between the drive and the transmon resonance frequency. In this case, we intentionally introduced a 60 kHz synthetic detuning.

properties.

We use this Rabi protocol to measure the ambient excited state population of the transmon in its steady state⁴⁹. The measurement consists of two power-Rabi experiments described as follows: (1) we flip the qubit from $|g\rangle$ state to $|f\rangle$ level by sending π_{ge} followed by a π_{ef} to obtain blue curve in Fig. 3.9 (2) we directly send a π_{ef} pulse and expect the transmon to excite to $|f\rangle$ state iff the qubit started in the $|e\rangle$ state. We fit the two data curves with a decaying sinusoidal function to extract the relative amplitudes such that $r = \frac{P(|e\rangle)}{P(|g\rangle)}$. Note that we apply a calibrated π_{ge} pulse at the end so we can use the state discriminator described earlier. Assuming the qubit temperature is low enough that only the first two levels are occupied gives $P(|g\rangle) + P(|e\rangle) = 1$. Combining these two yields the excited state

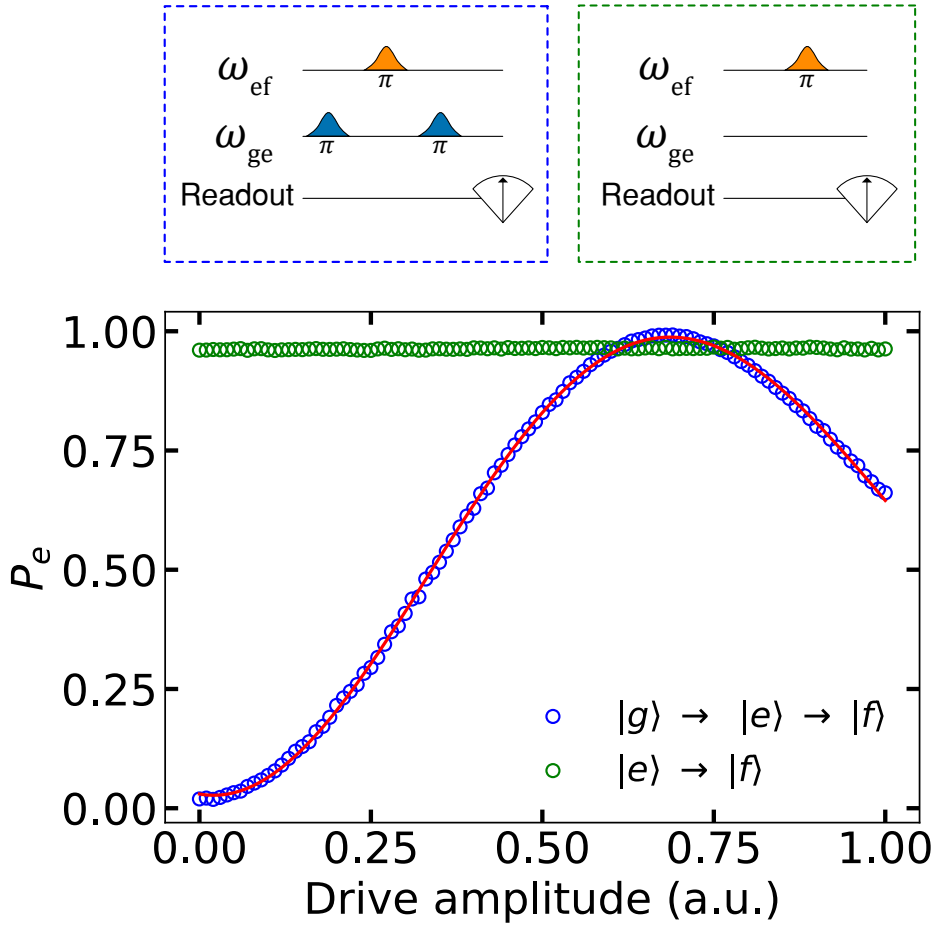


Figure 3.9: **Qubit temperature measurement** Blue: ef Rabi-flopping experiment of a transmon. The transmon is first excited from $|g\rangle$ to $|e\rangle$ state followed by another Gaussian pulse centered around ω_{ef} with varied amplitude (orange pulse) plotted on the x-axis and y-axis corresponds to the measured probability of the qubit in the $|g\rangle$ state; a second π_{ge} pulse is applied to measure the qubit in either $|g\rangle$ or $|e\rangle$ state. Green: $|e\rangle$ to $|f\rangle$ Rabi-flop experiment without initializing the transmon in $|e\rangle$ state.

population $\bar{n}_q = P(|e\rangle) = \frac{r}{r+1}$. Using Fermi-Dirac distribution, we can relate the effective temperature of the transmon to the ratio of ground and excited population

$$r = \frac{P(|e\rangle)}{P(|g\rangle)} = e^{\frac{-\hbar\omega_{ge}}{k_B T}} \quad (3.13)$$

$$\Rightarrow T_q = \frac{\hbar\omega_{ge}}{k_B \ln r} \quad (3.14)$$

where ω_{ge} is the transmon transition frequency. However, this method is reliable only if the excited population is of the order of a few 1 – 5% such that the oscillations are large enough to fit. In the current device, the oscillations are negligible and we couldn't find a reliable fit to extract the excited population. Based on the statistical fluctuations in the amplitude, we set an upper bound on the excited population to be < 1% or equivalently $T_q < 50$ mK.

QNDness of qubit-readout

In a dispersive interaction, we assume that the measurement of qubit does not perturb the state i.e. it is a quantum non-demolition (QND) measurement or in other words, does not induce additional relaxation in the qubit state. However, a recent study has shown that parity measurements, while highly QND, can induce a small amount of additional relaxation⁵⁰. Hence, in order to estimate the same, but, in the context of repeated qubit measurements, we follow the method described in⁵⁰, where we perform a qubit T_1 experiment interleaved with varying number of readout pulse during the delay time. In that experiment, the total relaxation rate was modeled as a combination of the bare qubit lifetime τ_q and a demolition probability p_d associated with each dispersive readout. In Fig. 3.10, we show the extracted total decay time (τ_{tot}) and demolition probability $p_d = 0.6\%$ as shown by the fit. In other words, a single number resolved qubit measurement is 99.4% QND.

3.7 Cavity state control and measurement

The very first measurement includes probing the cavity with a continuous-wave (CW) source such as a Network Analyzer (NA) to determine the resonance frequency of the cavity. However, in some cases, there may not be a direct port connected to the storage cavity. In those cases, we immediately move to pulsed measurements to characterize the cavity parameters accurately by probing the transmon and the readout.

In section 3.4, we discussed the transmon-cavity Hamiltonian and the effect of coupling on

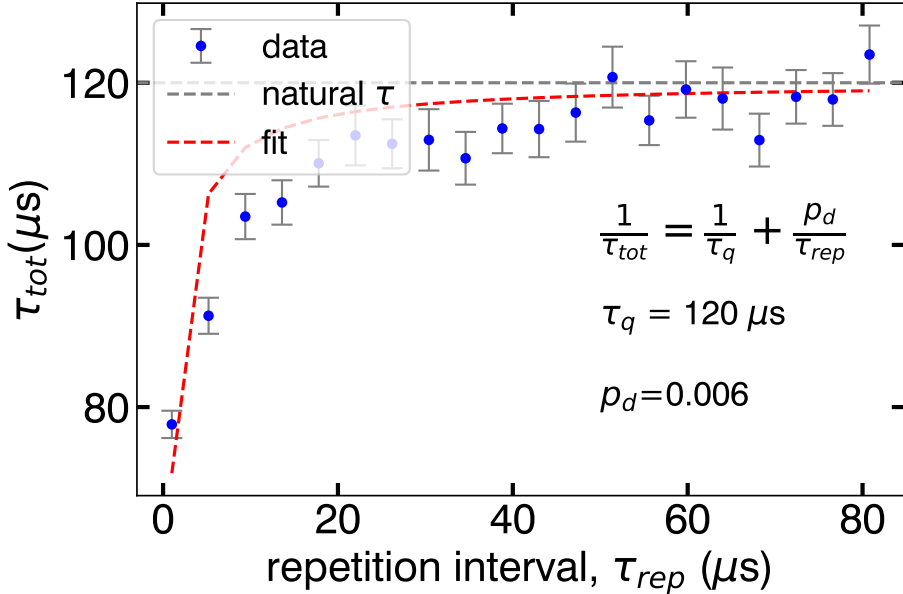


Figure 3.10: **QNDness of qubit measurement.** Qubit cavity T_1 measurements were performed with repeated readout pulses interleaved during the delay time with a variable repetition interval time τ_{rep} . The extracted total decay time was fit to a model $1/\tau_{tot} = 1/\tau_q + p_d/\tau_{rep}$. From the fit (red line), we infer a demolition probability per readout of $p_d = 0.6\%$ corresponding to a QNDness of 99.4%, which is a bit lower than reported for a parity protocol⁵⁰. The natural decay time of the qubit $\tau_s = 120 \mu\text{s}$ is indicated by a dashed grey line.

the transmon frequency shift as a function of the number of photons in the cavity. In Fig. 3.2, we performed a simple number-splitting experiment where we probe the population in each Fock state using a number-selective π -pulse on the transmon, using it as a counter. I must point out that this type of spectroscopy measurement does not reveal any phase information of the quantum state stored in the cavity. In order to obtain complete information (both the quadrature), it is useful to measure the Wigner function of the cavity state. It relates the expectation values of the photon number parity operator $\hat{P} = e^{i\pi\hat{a}^\dagger\hat{a}}$ of a cavity state after it is coherently displaced with amplitude β . The Wigner function for a state given by density matrix ρ is

$$W(\beta) = \frac{2}{\pi} \text{Tr}(\hat{D}^\dagger(\beta) \rho \hat{D}(\beta) \hat{P}) \quad (3.15)$$

where $\hat{P} = e^{i\pi\hat{a}^\dagger\hat{a}}$ is the photon number parity operator. By measuring the Wigner function

or the parity at various points, we can reconstruct the density matrix within a truncated Hilbert space. It contains complete information of the quantum state⁵¹ and non-classical correlations present in the cavity state. However, we will learn that we do not really need this phase information for any of the experiments discussed in this thesis, nonetheless, remains a powerful tool to confirm the quantum nature of the prepared states.

A classical electromagnetic drive acting on a linear resonator populates it with a coherent state and we can describe this action by a displacement operator $\hat{\mathcal{D}}(\alpha)$

$$\hat{\mathcal{D}}(\alpha) = e^{\alpha^* \hat{a} - \alpha \hat{a}^\dagger}. \quad (3.16)$$

The evolution of such states can be visualized by the periodic oscillation of a simple pendulum in the phase space with radius given by $|\alpha|$. Mathematically, we can describe a coherent state α as an infinite superposition of Fock states weighted by a Poisson distribution

$$|\alpha\rangle = e^{-|\alpha|^2/2} \sum_{n=0}^{\infty} \frac{\alpha^n}{\sqrt{n!}} |n\rangle. \quad (3.17)$$

Mapping photon number to parity measurement

In order to determine the number of photons in the cavity, we could either use a number resolved- π pulse (as shown in Fig. 3.2) or perform a parity measurement as depicted in Fig. 3.11. Experimentally, it is implemented by a simple Ramsey pulse sequence on the transmon. It starts with a $\pi/2$ pulse to bring the transmon in a superposition of $|g\rangle$ and $|e\rangle$. During the evolution, the cavity and transmon becomes entangled at a rate χ , resulting in a precession of superposition state around the Bloch sphere at a rate $n \cdot \chi$, where n is the number of photons in the cavity⁴. By waiting for a time π/χ , the transmon would acquire a phase $2n\pi$ for even number of photons and $(2n+1)\pi$ for odd number of photons, pointing

4. The same can be said about the precession of each Fock state $|n\rangle$ around the Bloch sphere with a rate $n\chi$. This is essentially a controlled-phase gate on each cavity photon conditioned on the transmon state, described by $C_\pi = \hat{I} \otimes |g\rangle\langle g| + e^{-i\pi\hat{n}} \otimes |e\rangle\langle e|$.

them along opposite directions on the equator of the Bloch sphere. A $-\pi/2$ pulse on the qubit maps the parity information to either $|g\rangle$ and $|e\rangle$ state of the transmon respectively. For a dark matter search, the expected mean photon number $\bar{n} \ll 1$ thus, it is sufficient to perform a single measurement (1 bit of information) to find out if there is a photon in the cavity or not⁵.

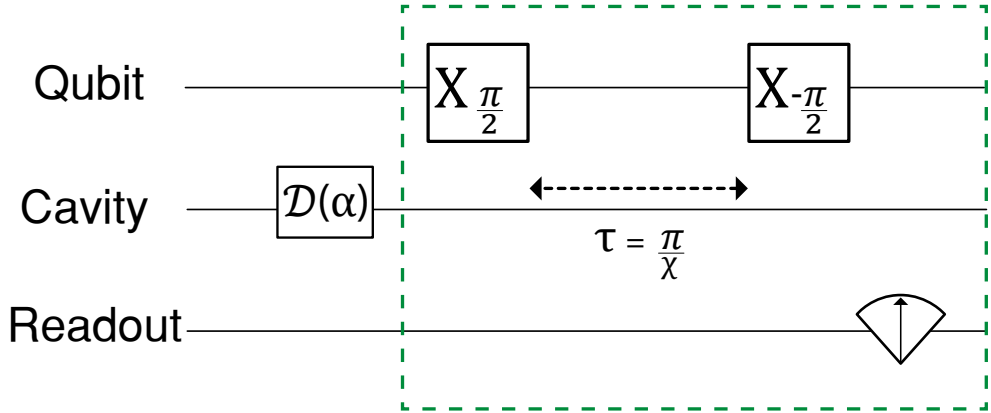


Figure 3.11: **Photon number parity measurement.** The experimental protocol to measure the Wigner function of a cavity state. The sequence consists of two $\pi/2$ pulses separated by a delay time π/χ which maps the number of photons on the qubit state.

Coherence measurements

In order to demonstrate the exceptional coherence properties of 3D superconducting cavities, let's measure the energy relaxation time T_1 , of the cavity by observing the decay of a coherent state in the cavity. We first displace the cavity state by a coherent state $\bar{n}_0 = |\alpha_0|^2 \gg 1$ and probe the probability of it being in the ground state after a variable delay time. A resolved qubit π -pulse centered at the ground state peak is used to infer the cavity state if it has relaxed back to vacuum. The pulse sequence and phase space representation of the cavity

5. Of course, one would need to perform a binary search to distinguish photon states upto $|n\rangle$, which takes $\log_2 n$ steps.

state is depicted in Fig. 3.12 and has the following functional form^{51,38}:

$$P_e(t) \propto e^{-|\alpha|^2 \exp(-\kappa t)} \quad (3.18)$$

where κ is the characteristic decay constant associated with the energy relaxation of the cavity state. The double exponential form requires some care choosing $\alpha_0 \geq 3$ to displace the cavity sufficiently high that the $P(t = 0) \sim 0$ for some time. This helps to easily separate the two distinct curvatures. By fitting the data, we extract the decay constant $\kappa = 757 \pm 7$ Hz which corresponds to a cavity lifetime $T_1 = \frac{1}{\kappa} = 1.33 \pm 0.01$ ms.

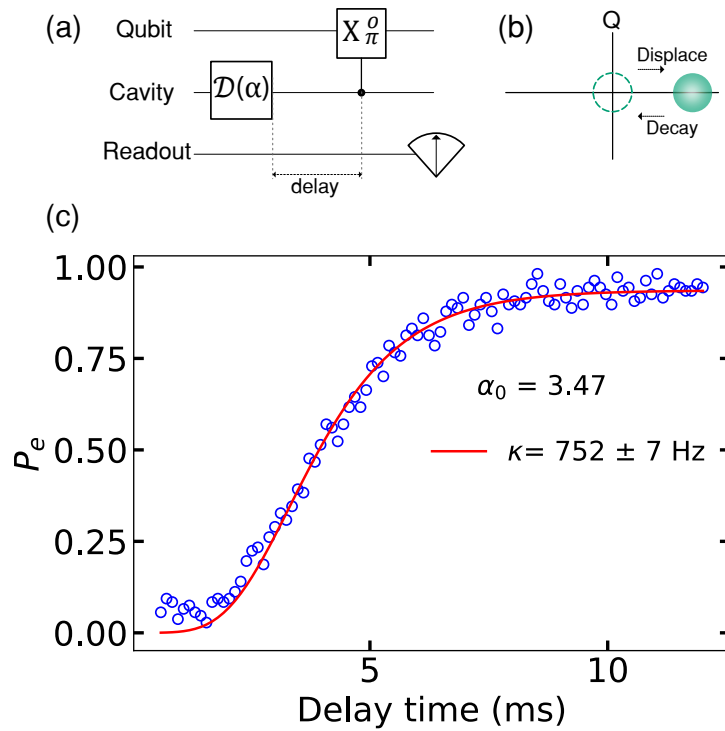


Figure 3.12: **Storage lifetime T_1 measurement with a coherent state.** (a) The experimental sequence to measure the storage cavity lifetime. It consists of a large cavity displacement followed by a variable delay. The cavity state is measured using a number selective π -pulse which excites the qubit only if the cavity has relaxed back to its ground state. (b) Representation of the cavity state evolution in phase-space after a delay time relaxing back to the ground state. (c) Measured qubit excitation probability as a function of the delay time. At first, the signal is flat because the cavity is still far from the origin since $\alpha_0 \gg 1$. For longer delay time, the curve is again flat since the vacuum state is equilibrium. The time duration that separated these two flat regions gives κ for sufficiently large displaced state. The data is fit to Eq. 3.18 to extract χ which results in a lifetime of 1.33 ± 0.01 ms.

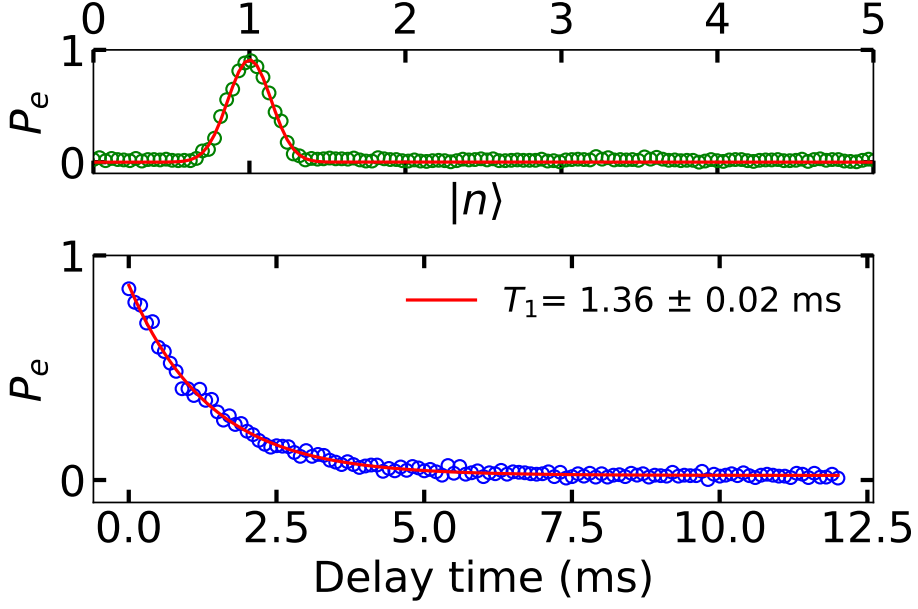


Figure 3.13: Storage lifetime T_1 measurement with a Fock state. (a) The experimental sequence to measure the storage cavity lifetime after preparing the cavity in a $|1\rangle$ Fock state using optimal control pulses. It is measured using a number selective π -pulse centered at the $|n\rangle = 1$ peak which excites the qubit only if the cavity has not relaxed back to its ground state (b) Qubit spectroscopy with a resolved π -pulse reveals a single peak corresponding to $|n\rangle = 1$ Fock state validating the cavity state prepared by OCT pulses. The x-axis is normalized with the χ shift to display the basis Fock states. (c) Measured qubit excitation probability as a function of the delay time. The data is fit to an exponential decay which gives a lifetime of $1.36 \pm 0.02 \text{ ms}$.

Additionally, we could verify that the T_1 decay follows a simple exponential by preparing the cavity in $|1\rangle$ Fock state as shown in Fig. 3.13 (b). We could either use Selective-on Number Arbitrary Phase (SNAP) gates^{52–54} or Optimal Control pulses (OCT)^{55,56} to create non-classical states in the cavity. As shown in Fig. 3.13, the cavity is prepared in $|n\rangle = 1$ Fock state using the OCT pulses. A qubit spectroscopy performed with a resolved π -pulse⁶ reveals a single peak which is centered at the frequency shift equal to χ confirming the successful preparation. The protocol for conducting a T_1 experiment remains similar afterwards where a variable delay is introduced before measuring the cavity state by exciting the qubit with a resolved π -pulse centered at the $|n\rangle = 1$ peak. As expected, a single

6. For a resolved π -pulse, I use a 3000 ns ($\sigma = 750 \text{ ns}$) long Gaussian pulse such that the bandwidth is much smaller than the χ shift.

exponential is observed in the qubit excitation probability P_e with a time constant within the uncertainty of measurements of coherent states. There is a trade-off between the two measurement techniques - coherent states are easier (Fock state are harder) to prepare whereas the decay signal from Fock state is easier (coherent decays with double exponential) to interpret. However, it is reassuring to obtain the two types of measurements and check that the $T_1 = 1.36 \pm 0.02$ ms is in good agreement with the classical energy decay rate of a coherent state.

Compared to their 2D counterpart, 3D cavities are also far superior to preserve the phase coherence of quantum states. Similar to the transmon coherence measurement, we can perform a Ramsey type experiment to determine the phase coherence of the quantum memories. The experiment starts with the cavity prepared in a superposition of $|0\rangle$ and $|1\rangle$ Fock states followed by a variable time delay before probing the cavity state. The cavity is then displaced back towards the origin with a displacement $\alpha_1 = \alpha_0 e^{j\omega t}$ such that the phase coherence is revealed in the sinusoidal oscillations of the subsequent T_2 experiment. There are multiple ways to prepare the cavity in a superposition state: SNAP (Fig. 3.14 (a)), OCT pulses or a careful preparation of a coherent state such that only $|0\rangle$ and $|1\rangle$ (Fig. 3.14 (b)) are populated. This measurement also helps in accurately determining the resonance frequency of the cavity at sub kHz range.

Correction to the χ shift

In Eq. 3.9, we neglected the higher order terms in the dispersive interaction which are only relevant at higher occupation number in the resonator. However, as we will learn later their contributions start to matter and cannot be neglected any further. One of the dominant terms which we should measure and correct for is second order correction to the dispersive shift, χ' , which relates the photon number (n) dependent shift as

$$\chi(n) = n \chi + \frac{1}{2}(n * (n - 1)) \chi'. \quad (3.19)$$

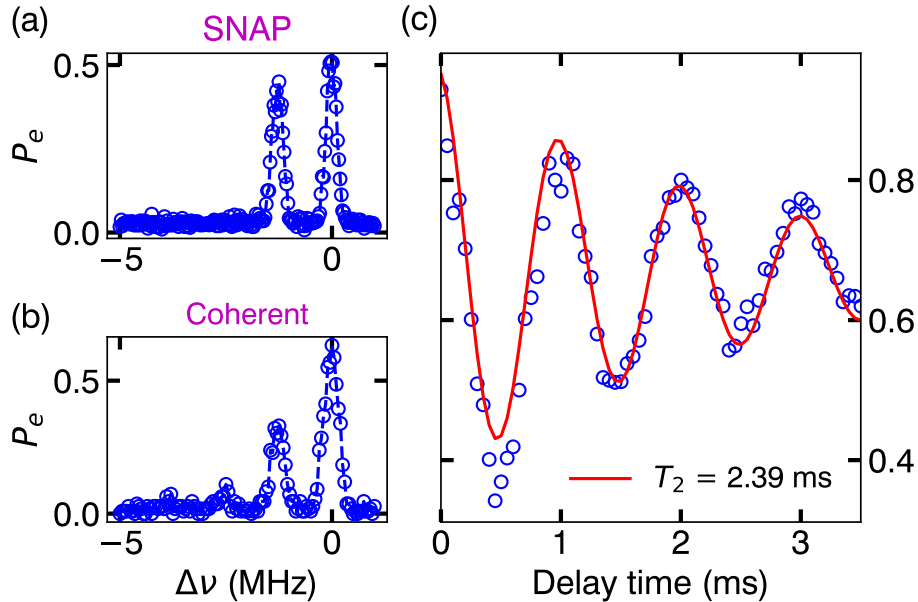


Figure 3.14: Storage coherence T_2 measurement. The experimental sequence to measure the storage cavity coherence. (a) Qubit spectroscopy revealing cavity prepared in an equal superposition of $|0\rangle$ and $|1\rangle$ using SNAP sequence. It is composed of a combination of displacement drives $\alpha = \{0.56, -0.24\}$ interleaved with a selective 2π rotation on the transmon. The cavity is then left to evolve for a variable time delay before giving a final displacement of $\alpha_1 = \alpha_0 e^{j\omega t}$, where ω is the intentional detuning (1 kHz) introduced in the software. (b) Qubit spectroscopy of the cavity prepared in a superposition of $|0\rangle$ and $|1\rangle$ using a displacement drive, but with unequal occupation probabilities. (c) Measured qubit excitation probability as a function of the delay time. The data is fit to extract a coherence time T_2 of 2.39 ms.

To measure the correction term, we displace the cavity with a large displacement $|\alpha| \sim 3$ such that the effect is pronounced at higher photon numbers. Soon after that, a qubit spectroscopy is performed with a resolved π -pulse. The resultant cavity probability distribution is fitted to a sum of Gaussian functions to extract the transition frequency corresponding to each Fock state $\nu_{q,n}$ as shown in Fig. 3.15. The measured frequencies are then fitted to Eq. 3.19 to extract $\chi = 1267 \pm 8$ kHz and $\chi' = 7.3 \pm 5.9$ kHz.

Cavity Kerr non-linearity

The anharmonicities of the cavity (k) and transmon (α) differ by orders of magnitude and therefore, require very different characterization methods. To measure this, we perform an

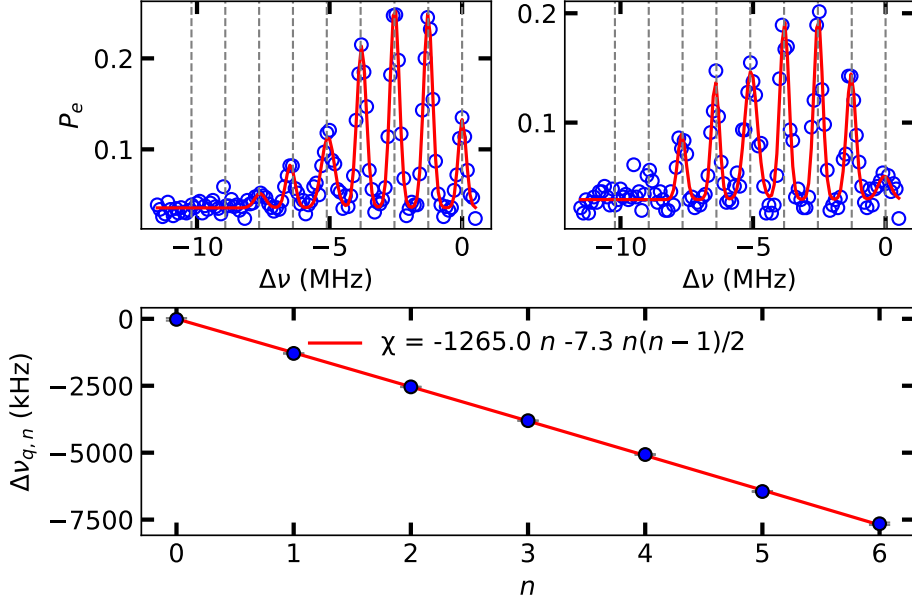


Figure 3.15: **Qubit-cavity dispersive shift measurement.** The dispersive shift χ and its second order correction χ' are determined from qubit spectroscopy experiments with several different displacements (top).The probability distribution is fit to a sum of Gaussian and the resulting number dependent frequencies are fit to a quadratic model.

extension of the cavity Ramsey sequence where in addition to scanning the delay time, the cavity displacement α is also scanned. Although the value may be negligibly small, the n^2 scaling with respect to the photon number will induce sensitivity to k when higher photon number states are occupied in the resonator. Following the functional form from Supp. III of Ref.³⁹, the measured data is fit using the model

$$P_e(t) = \left| e^{-\alpha^2} \sum_n \frac{1}{n!} \alpha^{2n} e^{-itn(\omega+kn/2)} \right|^2 \quad (3.20)$$

to extract $k/2\pi = 20 \pm 1$ kHz.

With these basic measurements to characterize the complete Hamiltonian in place, we can determine the cavity parameters and coherence properties for conducting desired experiments. Next, I will discuss another important feature of the dispersive coupling, that is an otherwise linear oscillator inherits non-linearity which is sufficient to prepare any quantum states in a superconducting cavity and perform universal control on it. I will mainly focus

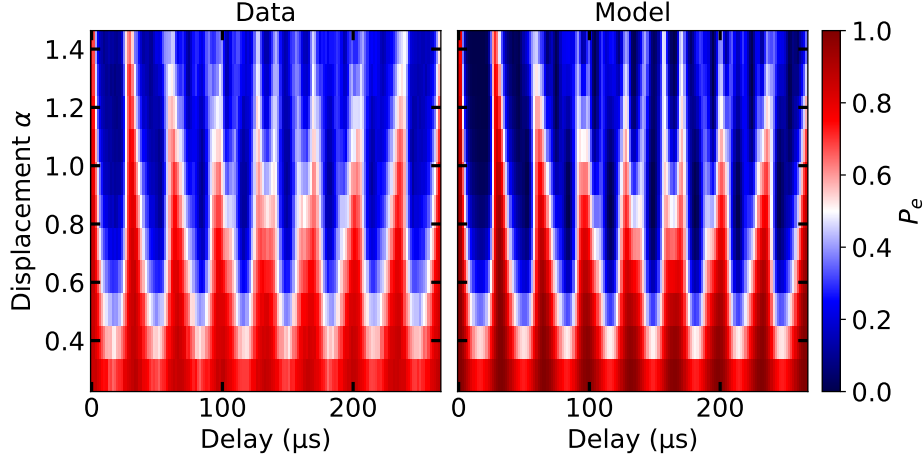


Figure 3.16: **Cavity Kerr non-linearity measurement.** Cavity Ramsey sequence performed in Fig. 3.14 with added variation of the displacement amplitude. The Kerr non-linearity can be determined by fitting to Eq. 3.20 which corresponds to the bending of the curve seen above.

on two methods.

3.7.1 Selective-on Number Arbitrary Phase (SNAP) gate

Let's first look at how the SNAP gate allows for universal control over a harmonic oscillator by making active use of the dispersive interaction. A SNAP gate consists of a qubit drive which forms a closed trajectory on its Bloch sphere such that the enclosed area imparts a Berry phase⁵⁷ on the system $|g\rangle \rightarrow e^{i\phi}|g\rangle$. The induced phase is different from the more familiar dynamic phase since the cyclic change of the qubit state is adiabatic i.e. the duration of the drive pulse is long. In other words the qubit drive is weak compared to χ . The evolution of the qubit is conditioned on the Fock state of the resonator, taking $|g, n\rangle \rightarrow e^{i\phi}|g, n\rangle$. Thus, the phase accumulation is differential between different Fock states implying number dependent Berry phase. By interleaving cavity displacement drives with SNAP gates, we can build quantum states in the oscillator by interfering differential phases. For instance, a single SNAP gate and two displacement drives on the oscillator is sufficient to create an $|n\rangle = 1$ Fock state in the cavity.

We can gain intuition for the protocol by considering a qubit trajectory that is along a

single axis, e.g. a 2π pulse along the qubit's x-axis which accumulates a π phase shift on the state. Therefore, if the pulse is number selective on the m^{th} Fock state then the amplitude C_m will change its sign. The next displacement will mix the neighbouring Fock states, which may now be out of phase and therefore interfere non-trivially. In practice, the displacement amplitudes are numerically optimized to maximize the fidelity of the final state⁵⁴. Let's look at the combined application of these gates to create a Fock state. First, a displacement of $\hat{D}(1.14)$ on the oscillator creates a coherent state in the cavity that has

$$|\Psi\rangle_c = 0.522|0\rangle + 0.595|1\rangle + 0.480|2\rangle \\ 0.316|3\rangle + 0.180|4\rangle + \mathcal{O}(0.1)[\geq 5]. \quad (3.21)$$

The resolved π -pulse imparts a Berry phase $\phi = 2\pi$ on the $|0\rangle$ state, leaving the cavity state in

$$|\Psi\rangle_c = -0.522|0\rangle + 0.595|1\rangle + 0.480|2\rangle \\ 0.316|3\rangle + 0.180|4\rangle + \mathcal{O}(0.1)[\geq 5]. \quad (3.22)$$

A final cavity displacement of $\mathcal{D}(-0.56)$ takes the cavity to

$$|\Psi\rangle_c = -0.048|0\rangle + 0.990|1\rangle + 0.003|2\rangle \\ 0.133|3\rangle + 0.002|4\rangle + \mathcal{O}(0.01)[\geq 5] \quad (3.23)$$

resulting in a sequence that can prepare the $|n\rangle = 1$ Fock state with probability $P_1 = 0.98$. However, in practice, SNAP does not prepare a perfect $|n\rangle$ Fock state. During the number selective qubit rotation which lasts for a duration $\sim \frac{1}{\chi}$, the cavity and qubit are completely entangled which can be comparable to the decay rates of the system. For our device, the qubit's coherence time in the memory experiment was observed to be $T_{2,q} = 50\text{ }\mu\text{s}$, while the duration of SNAP gate was chosen to be $T_{gate} = 3\text{ }\mu\text{s}$. A naive estimation of fidelity $\mathcal{F} \sim e^{-T_{gate}/T_{2,q}}$ would predict approximately 92% (check once) of the cavity to be prepared

in the correct Fock state.

We experimentally test the SNAP gates to prepare $|1\rangle$ and $|2\rangle$ Fock states as shown in Fig. 3.17. A qubit spectroscopy with a resolved π -pulse is performed to measure the fidelity of the SNAP preparation step. While the cavity is mostly in $|1\rangle$ Fock state, fitting qubit spectroscopy to normalized Gaussian distribution under each peaks determines the population of each Fock state (P_n) such that $P_0 = 5.3 \pm 0.1\%$, $P_1 = 87.6 \pm 0.1\%$, $P_2 = 3.4 \pm 0.1\%$ and all the other states below the noise level of our detection. We observe leakages to neighboring Fock state due to imperfect interference caused by unwanted phase accumulation by the cavity state and imperfect SNAP gate. By tuning the phase of the cavity displacement drives we can reduce the leakage and improve the fidelity. However, I would not recommend it, as is not a deterministic procedure and results in a wastage of time. Recent results have shown further improvements in the preparation fidelity by numerically optimizing the SNAP gate in the presence of systemic errors⁵⁸.

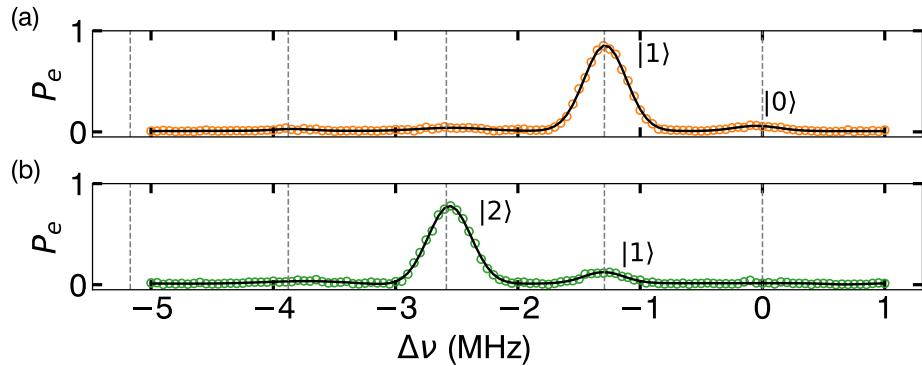


Figure 3.17: Examples of SNAP sequences to prepare Fock states in the cavity. Resolved qubit spectroscopy after the application of SNAP gates interleaved between a series of optimal cavity displacements. (a) Two displacement pulses on the cavity are separated by a 3 μ s long single number-selective 2π rotation that takes $|g, 0\rangle \rightarrow e^{i\pi} |g, 0\rangle$ via a geometric phase. The qubit spectroscopy reveals the result of this preparation step with cavity mostly prepared in $|1\rangle$, $P_1 = 87.6 \pm 0.1\%$ and the neighboring Fock states occupying $P_0 = 5.3 \pm 0.1\%$, $P_2 = 3.4 \pm 0.1\%$, (b) Three displacement pulses on the cavity interleaved by two number-selective 2π rotation that takes $|g, 0\rangle \rightarrow e^{i\pi} |g, 0\rangle$ and $|g, 1\rangle \rightarrow e^{i\pi} |g, 1\rangle$ as shown on the left. Fitting a qubit spectroscopy reveals the population of each Fock state as $P_1 = 11.3 \pm 0.1\%$, $P_2 = 81.3 \pm 0.1\%$, $P_3 = 7.4 \pm 0.1\%$.

Although the SNAP gates are intuitive to follow and easier to implement, their duration

to prepare higher Fock state doesn't scale favorably for our needs. To create a $|n\rangle$ Fock state, the sequence consists of a total of $2n + 1$ operations, including n resolved π -pulses. For instance, preparation of $|2\rangle$ Fock state would take roughly 7 μs which introduces at least 7% error due to qubit decay itself. However, it is easier to implement them and measure the cavity parameters.

3.7.2 Numerical optimisation methods to create quantum states

We can also accomplish universal control by considering the time-dependent Hamiltonian in the presence of classical control fields. Both for solid state⁵⁹ as well as cQED systems^{55,56}, it has been demonstrated that numerical optimization procedures can faithfully solve the inversion problem of finding the optimal control pulses to prepare any non-classical state. In our lab, a Gradient Ascent Pulse Engineering (GRAPE) method based package was developed by Nelson et al.⁵⁵ and is used to efficiently compute the qubit-cavity control pulses, $\xi(t)$ to transfer the system from quantum state A to B . Unlike SNAP gates to prepare Fock state, where the intended operation can be decomposed into a set of individual gate sequences, in a state transfer method, we may not necessarily find an equivalent decomposition of gates. In some sense, it acts as a black box.

For our qubit-cavity system, we assume that the Hamiltonian can be written in the following form:

$$\mathcal{H}(\vec{\xi}(t)) = \mathcal{H}_0 + \sum_k \xi_k(t) \mathcal{H}_k \quad (3.24)$$

and our goal is to synthesize the time-dependent control field envelopes $\vec{\xi}(t)$. The success of GRAPE crucially depends on the accurate model of the system, thus, it is very important that all the terms in the Hamiltonian are accurately measured in the experiments. We include the correction terms up to second order for both qubit and cavity to capture most of the physics.

Constraints in the optimization routine

The optimization problem we are trying to solve is generally under-determined, i.e. there are many solutions $\vec{\xi}(t)$ which achieve equally high fidelities. Thus, we can add additional terms to the optimization cost function which provides an optimal solution against several other requirements. Without going into the actual implementation in the code, a few of them that I implemented are discussed below,

1. **Pulse amplitude:** The output power of the AWG is limited, this sets the maximum amplitude for the pulse $\xi(t) \leq \xi_{max}$ for all t . Of course, we can increase the power by additional amplifier but it introduces noise and non-linearity in the dispersion relation.
2. **Pulse bandwidth:** There are multiple reasons why we might want to constrain the bandwidth of a pulse. The AWGs have a maximum available bandwidth but more importantly the mixer calibration and power variation is effected at large detunings from resonance, causing non-linearities in the transfer function.
3. **Intermediate photon number:** The computational Hilbert space to solve the optimization problem grows exponentially with the number of levels considered in the cavity number operator \hat{a} . Thus, due to finite computing memory we are forced to truncate the photon number up to n_{tr} such that the dynamics relevant for the desired state transfer occurs within the $|0\rangle, |1\rangle, \dots, |n_{tr} - 1\rangle$ subspace.

Once it returns a set of optimized control signals we can implement the complete in-phase/quadrature (IQ) modulated microwave drives centered at the qubit (cavity) resonance frequencies using arbitrary wave generators (AWGs). As an example shown in Fig. 3.19, we start with a qubit and cavity mode in their respective ground states and apply OCT pulses to transfer the state from $|g, 0\rangle \rightarrow |g, n\rangle$. We then perform a Wigner tomography of the resulting state to reconstruct the complete density matrix. The timescale for the duration of these operations scales with $1/\chi$ and the fidelity of state transfer is ultimately limited by the coherence time of the qubit.

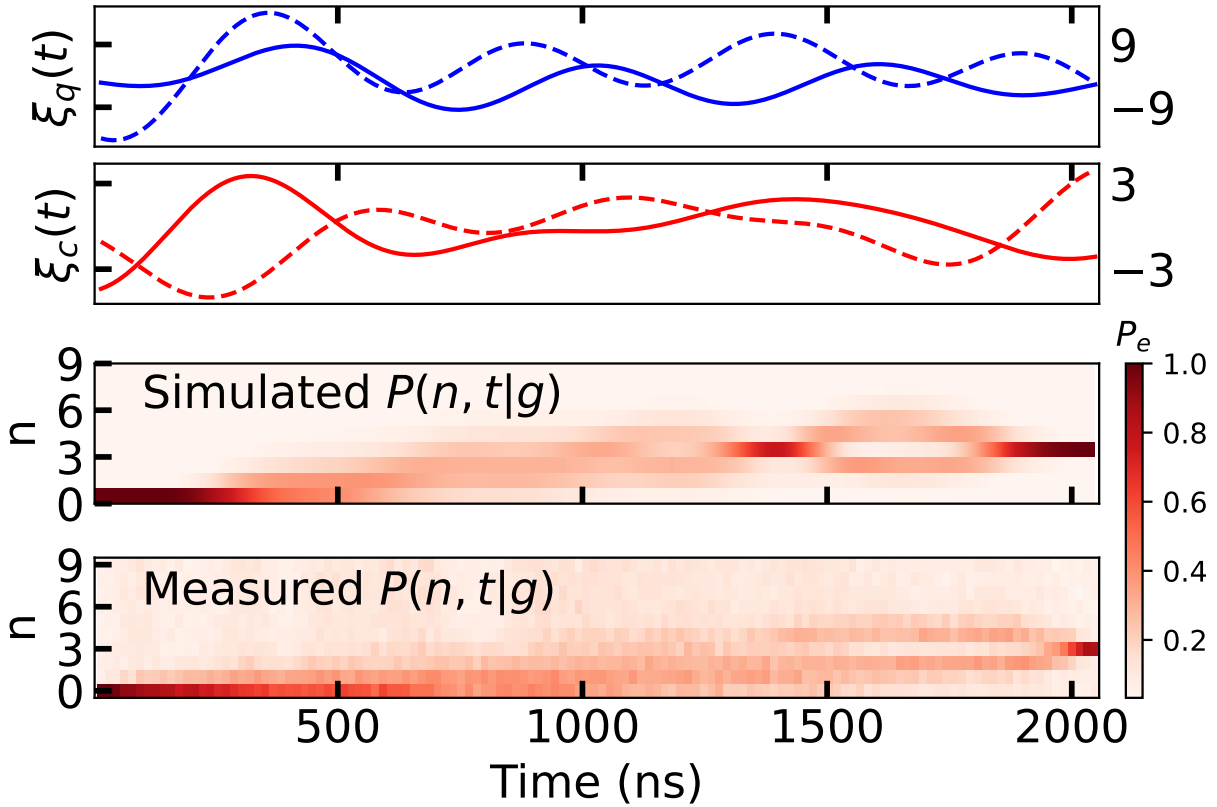


Figure 3.18: **Cavity dynamics under OCT pulses.** (L) Simulated cavity state evolution using simulation tool QuTip. The cavity explores higher photon number during the course before converging to the target state. (R) Measured cavity state in the experiment where the dynamics follows the simulation closely. The qubit spectroscopy reveals a single peak confirming the preparation of $|n\rangle = 3$ Fock state.

Comparing simulations to experiments

Before we experimentally test these OCT pulses, we can check their performance using simulation tool QuTip^{60,61} and observe the dynamics of the cavity as it evolves in time. In Fig 3.18, I show the simulated and measured trajectory of the cavity state under the application of OCT pulses to prepare $|n\rangle = 3$ Fock state. We can verify that (a) higher Fock states are occupied during the state transfer (b) the trajectory converges to the target state. By comparing the peak value w.r.t to the $|0\rangle$ peak, we estimate the preparation fidelity to be 88%.

It is worth noting that not all OCT pulses work as intended and there is a feedback loop

which helped me collect a set of pulses which showed reasonable performance on the real device. I would recommend readers to refer Philip Reinhold's thesis⁶² which goes over the debugging in a systematic manner. A few minor convention problems that I would like to address here are - it is very easy to forget a factor of 2π here and there, so once must be consistent in the definition of the drive Hamiltonian as defined in the OCT package and the actual experimental implementation. Second, make sure that the drive Hamiltonian has the correct phase between the real and imaginary components, for e.g. $\hat{a} + \hat{a}^\dagger$ or $\hat{a} - \hat{a}^\dagger$. In order to truly achieve very high preparation fidelity a closed-loop optimization would be ideal but the long memory lifetimes of the cavity makes it infeasible.

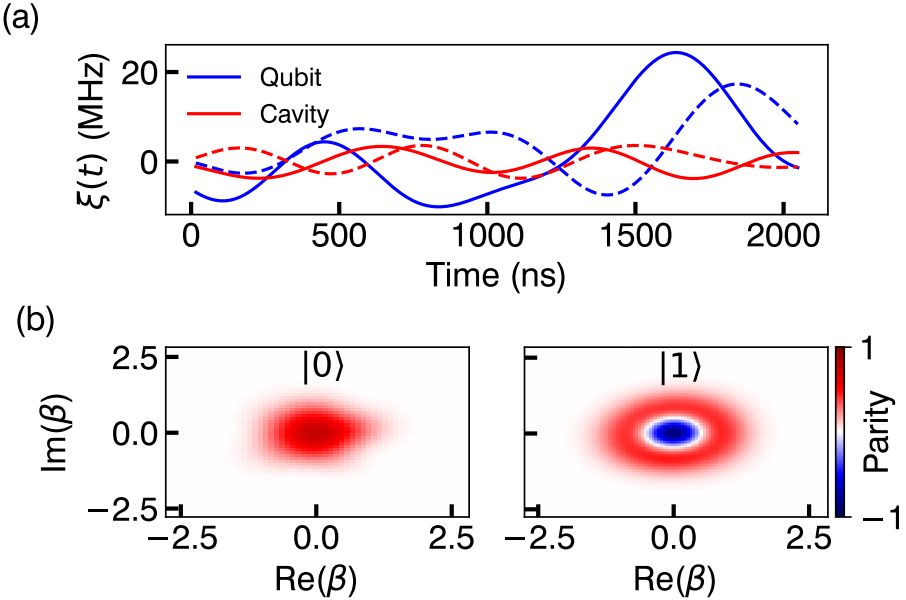


Figure 3.19: **Example of an OCT pulse to prepare Fock states.** (a) A set of optimal control pulses simultaneously driving the qubit and cavity to implement a non-trivial state transfer from a vacuum state $|n\rangle = 0$ to $|n\rangle = 1$ Fock state. Solid and dashed lines represent the in-phase and quadrature-phase component respectively of the control fields. (b) Wigner tomography is performed before and after the application of OCT pulses. It measures the parity after displacing the resultant state with an amplitude β . The left plot corresponds to the vacuum state of the cavity with a blob centered at the origin. On the right, it has a -1 value at the origin since $|n\rangle = 1$ is an odd parity state. Its radial symmetry indicates the lack of a well-defined phase for single Fock states.

We compare the Fock state preparation fidelity from spectroscopy distribution (see Fig. 3.13) to density matrix reconstruction method which are in good agreement for $|1\rangle$ Fock

state. We extract the fidelity of the state preparation from density matrix reconstruction and qubit spectroscopy both giving $P_1 = 94 \pm 1\%$. The major sources of error are imperfect DAC calibration, uncertainty in χ measurement and qubit being left in $|e\rangle$ at the end of the OCT sequence. Higher order correction to the Hamiltonian terms start to dominate as we prepare higher Fock state and the GRAPE method does populate the higher excited levels of the cavity as seen in Fig. 3.18.

QNDness of repeated number resolved qubit measurements

In an earlier section, I discussed the QNDness of a dispersive measurement of the qubit state. Similarly, for the storage cavity which is dispersively coupled to the transmon, we assume that the measurement of cavity state via a parity or number resolved π -pulse does not perturb the state i.e. it is a quantum non-demolition (QND) measurement or in other words, does not induce additional relaxation in the cavity mode. However, in order to confirm the same, but, in the context of number resolved qubit measurement, we follow the method described in⁵⁰, where we perform a cavity T_1 experiment interleaved with varying number of repeated number resolved qubit measurements during the delay time. In that experiment, the total relaxation rate was modeled as a combination of the bare storage lifetime τ_s and a demolition probability p_d associated with each qubit measurement. In Fig. 3.20, we show the extracted total decay time (τ_{tot}) and demolition probability $p_d = 2.6 \pm 0.02\%$ as shown by the fit. In other words, a single number resolved qubit measurement is 97.4% QND. For $|n\rangle = 2$, we measure the demolition probability $p_d = 4 \pm 0.04\%$, higher by a factor of 2. The measured demolition probabilities are listed in Table 3.1. This is an important measurement and will be very relevant when we write down the HMM analysis for the stimulated emission experiment. Interestingly though, we do not observe any additional loss in the cavity state if the number resolved π -pulse is off-resonant.

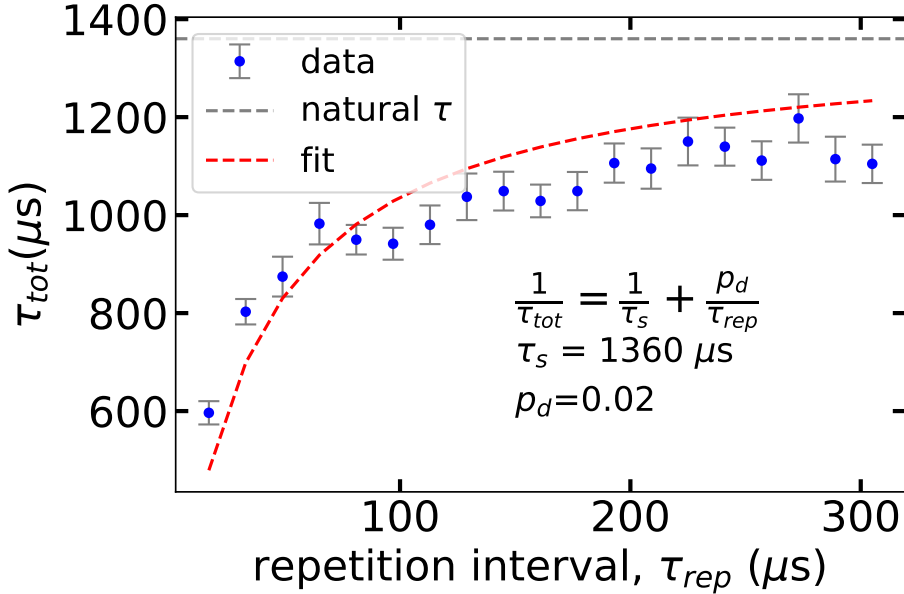


Figure 3.20: **QNDness of storage cavity measurement.** Storage cavity T_1 measurements were performed with repeated number resolved qubit measurements interleaved during the delay time with a variable repetition interval time τ_{rep} . The extracted total decay time was fit to a model $1/\tau_{tot} = 1/\tau_s + p_d/\tau_{rep}$. From the fit (red line), we infer a demolition probability per readout of $p_d = 2.6\%$ corresponding to a QNDness of 97.4%, which is a bit lower than reported for a parity protocol⁵⁰. The natural decay time of the storage $\tau_s = 1360 \mu s$ is indicated by a dashed grey line.

| $ n\rangle$ | $\tau_s(\mu s)$ | p_d | σ_{p_d} |
|-------------|-----------------|-------|----------------|
| $ 1\rangle$ | 1360 | 0.026 | 0.002 |
| $ 2\rangle$ | 660 | 0.040 | 0.004 |
| $ 3\rangle$ | 527 | 0.10 | 0.05 |
| $ 4\rangle$ | 319 | 0.074 | 0.012 |

Table 3.1: **Cavity state demolition probability.** Measured lifetime of the different Fock states and their fitted demolition probability with error bars. p_d can be approximated with a linear dependence on n .

3.8 Josephson Parametric Amplifier

Another device which has found very useful application of the non-linearity provided by the Josephson junction is a Josephson Parametric Amplifier or JPA for short. For detailed and rigorous demonstrations of JPA, I refer the reader to^{63,64,34}.

3.8.1 principle of operation

In a simple harmonic oscillator, the phenomenon of parametric gain may be achieved by modulating one of the parameters which governs its resonance frequency ω_0 periodically in time. The source of energy required for this modulation is provided by the “pump”, and the oscillator when operating in this regime is called a parametric amplifier. The underlying principle of parametric gain is the energy transfer between the pump and Fourier components of the oscillator’s motion with fixed phase relationships to the modulation. In a degenerate amplifier, where the signal (ω_s) and idler frequencies (ω_i) are the same, the component of oscillations in phase with the pump (ω_p) is linearly amplified while the orthogonal component is de-amplified. The frequencies of the pump, signal and idler follows energy conservation relationship wherein, the JPA could be operated in a “four-wave mixing” mode (charge-pump) or “three-wave mixing” mode (flux pump). In a four-wave process, the frequencies follow the relationship,

$$\omega_p + \omega_p = \omega_s + \omega_i, \quad (3.25)$$

whereas, in the case of a three wave mixing process,

$$\omega_p = \omega_s + \omega_i, \quad (3.26)$$

In other words, two pump photons mixes in a four-wave mixing process, whereas, in a three-wave mixing process a single pump photon is split into one signal and one idler photon. The JPAs used in my experiments operate in the degenerate mode and thus, I will restrict my focus to the JPAs where parametric gain is obtained using Eq. (3.4) and Eq. 3.25, with a pump tone close to its resonance frequency, ω_0 .

A parametric amplifier consists of electrical elements such as an inductor L and a capacitance C connected in parallel such that the resultant Hamiltonian is of the form

$$H = \frac{1}{2}CV^2 + \frac{1}{2}LI^2, \quad (3.27)$$

where $\omega_0 = 1\sqrt{LC}$. The parametric process is realized by modulating the inductance of Josephson junction. Recall Eq. 3.3 where, $L_J = L_0 + \Delta L(I/I_0)^2$, and by modulating the current I with a sufficiently intense pump tone at ω_0 will create the desired $2\omega_0$ modulation of the inductance to achieve parametric gain. Such a drive results in a four-wave mixing process.

In practice, the JPA has several important advantages. First, by fabricating the whole device out of a superconductor, we get a low loss device which makes it easy to realize a design in which the only noise added by a JPA operating in phase-insensitive mode (check it for phase sensitive) is the input noise at the image frequency. A second advantage is the tunability: there exists an intimate relationship between the Josephson phase and the magnetic flux which causes the quantization of the net magnetic flux through a superconducting loop. This implies that a SQUID loop (a pair of JJ connected in parallel with superconducting leads) acts like a single JJ with an effective critical current

$$I_0^S \approx 2I_0 \left| \cos\left(\frac{\pi\Phi}{\Phi_0}\right) \right| \quad (3.28)$$

where Φ is the magnetic flux threading the SQUID loop⁶⁵. We can exploit Eq. (3.28) in a different way and use SQUIDs instead of Josephson junctions in the design of a JPA. Application of a DC flux adjusts L_J and thus the resonant frequency, making the JPA flux-tunable. However, due to the intrinsically resonant nature of a parametric amplifier, the operating bandwidth is generally narrow (10s of MHz) but sufficient for most readout applications. Moreover, the flux tunability allows seamless integration of JPAs, greatly benefiting the haloscope type search.

3.8.2 Design and Fabrication

The schematic of a JPA is shown in Fig. 3.21, it is a lumped element single-port resonator comprising an interdigitated capacitor C, an array of N=4 SQUIDs, and a small capacitor

C_c to couple to a 50Ω transmission line. We closely followed the design philosophy from³⁵ to keep the design simple and reliable.

The JPA functions in a reflection mode as indicated by the single port. In order to minimize the loss, the JPA is always over-coupled to the transmission line, and the Q-factor is determined by the coupling capacitor C_c . The resonance frequency of this circuit is given

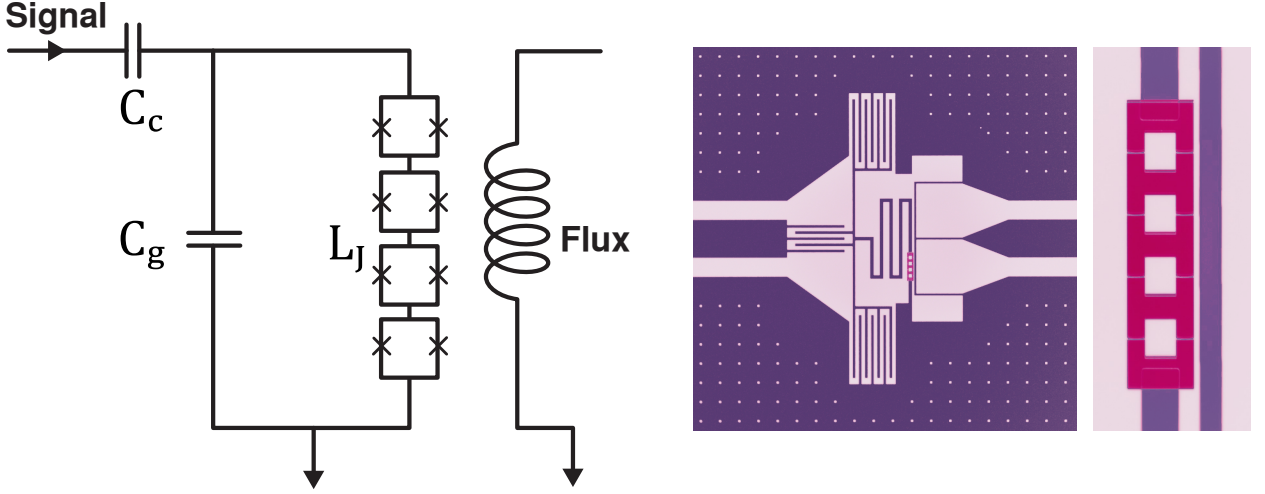


Figure 3.21: **Schematic of a JPA circuit.** (Left) A circuit diagram representing the elements in a JPA device. It consists of a coupling capacitor (C_c) which is over-coupled to the transmission line. The signal enters and exits through the same port after amplification. The resonator consists of a fixed capacitor (C_g) in parallel to tunable inductor (L_J) formed by a series of SQUID loops. The SQUID loops are inductively coupled to an on-chip flux bias line which carries DC current to tune the resonance frequency. (Right) Microscopic image of the fabricated device. A 50Ω transmission line carrying the signal, capacitively coupled to the LC circuit. A magnified image of the SQUID array is shown to the right. A waffled surrounding superconducting ground plane is patterned to pin magnetic flux vortices in place and isolate the SQUID array.

by $\omega_J = 1/\sqrt{(L_J + L_0)(C_g + C_c)}$, where L_0 is geometric (linear) inductance (approx. $10 \text{ pH}\mu\text{m}^{-1}$). We perform finite-element electromagnetic simulations in HFSS tool to estimate and optimize the circuit parameters to achieve a maximum target frequency (at $\Phi_0 = 0$). The device is fabricated on a $7 \text{ mm} \times 7 \text{ mm} \times 0.43 \text{ mm}$ Sapphire chip coated with a 75 nm thick Nb metal as the base layer. Photo-lithography tool (Heidelberg MLA150) was used to pattern the large structures followed by an electron-beam lithography (Raith) to pattern the Josephson junctions. The SQUIDS were fabricated with a double-angle evaporation

technique using Plassys tool. Finally, the resistance of a single SQUID junction is measured at room temperature to infer the expected L_J given by Ambegaokar–Baratoff formula⁶⁶. For a maximum frequency of 13.2 GHz, we chose $C_g = 0.196 \text{ pF}$, $C_c = 0.03 \text{ pF}$, $L_0 = 0.4 \text{ nH}$ and $L_J = 0.24 \text{ nH}$, corresponding to room temperature resistance of 70Ω per SQUID loop. The desired chip is mounted in a copper sample box which routes the signal and flux bias via SMA port as shown in Fig. 3.22. It also helps thermalize the chip and shield it from blackbody radiation emitted by higher temperature stages of the dilution refrigerator.

I had designed a simple copper box shown in Fig. (3.22) to characterize the JPA at miliKelvin temperature. The two SMA pins carry the signal and pump (left) whereas the one on the right carry the DC flux bias to tune the frequency. The JPA chip itself is finally coupled to the SMA ports through wirebonds and care must be taken to reduce the loss as much as possible.

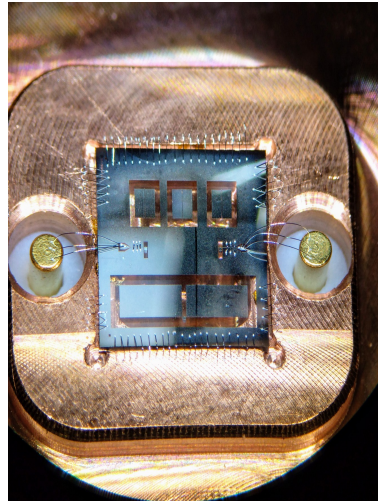


Figure 3.22: **JPA in a box.** (a) Microscope image of a JPA chip mounted inside a copper box. Two SMA ports wirebonded for routing signal and flux bias to the device.

3.8.3 Test and Characterization

The JPA characterization involves checking the flux response, finding optimal bias point, measuring the gain profile and noise performance. To characterize the flux response of a JPA, we supply current to an on-chip flux bias line (See Fig. 3.21) using a low-noise voltage

supply (YOKOGAWA GS200) and measure the phase response of the resonator using a Vector Network Analyzer (VNA). The current applied to the on-chip flux line induces an effective flux which threads the SQUID loop and thus, varying the current changes the effective L_J (Eq. (3.4)) which tunes the resonant frequency as shown in Fig. 3.23.

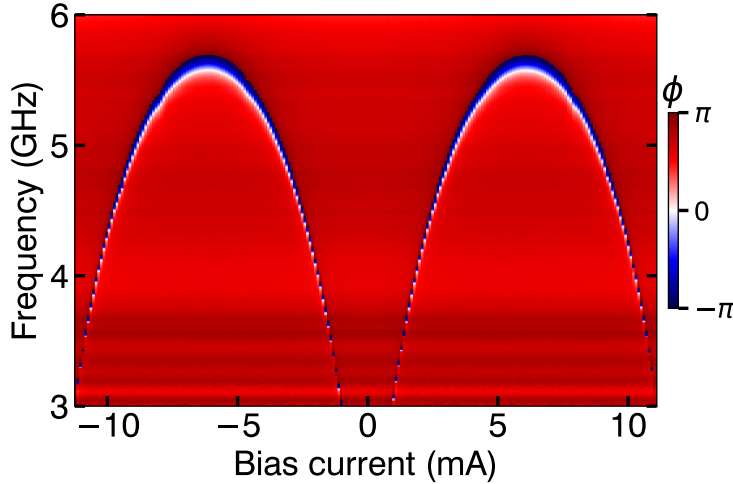


Figure 3.23: **Flux-scan of the JPA resonance frequency.** $\omega_J/2\pi$ vs. bias current $I_\Phi \propto \Phi$. In an ideal lossless case, the JPA will not show any features in the magnitude response but in phase as shown above.

Using Fig. 3.23 as a reference, we can now bias the JPA to the desired frequency and start optimizing the gain profile. We use the charge drive (four-wave mixing) to pump the JPA. The biasing procedure starts with setting the resonator frequency, typically 200 MHz higher than the pump frequency ($\omega_J \sim \omega_p + 2\pi \times 200$ MHz). While the pump tone is off, we record the transfer function of the full signal path and use it as a reference. Next, the pump power is slowly increased to achieve 3 – 5 dB of gain around the pump frequency. The pump power is slowly adjusted to obtain a maximum gain curve. We then adjust the flux bias to further increase the detuning and achieve a larger gain profile. These two knobs of increasing the detuning and pump power are iteratively turned until a maximum gain of 20 dB is achieved at the pump frequency. Fig. 3.24 shows a typical gain curve, fitted to a Lorentzian function with a 3 dB bandwidth of 10 MHz. In the next chapter, I will explain how we can use the dispersive interaction between the readout and the transmon to estimate

the noise performance of a JPA.

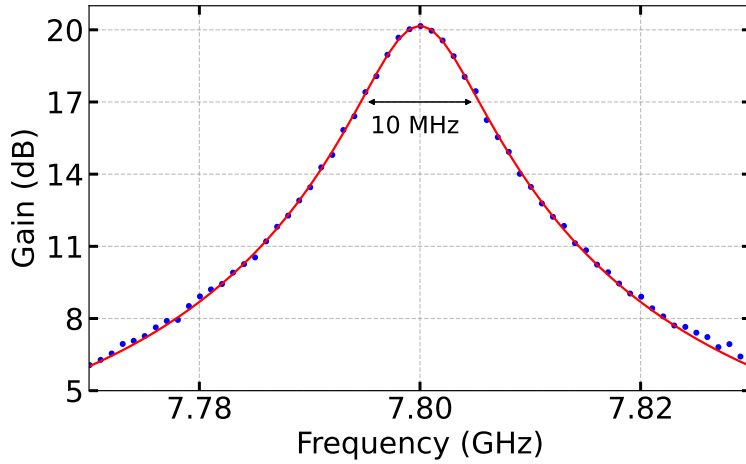


Figure 3.24: **Measured gain of the JPA.** Gain profile of the JPA as a function of the signal frequency. The exact curve gain is well approximated by a Lorentzian function (red) to extract the 3 dB bandwidth, $\Delta\nu_J = 10$ MHz.

Chapter 4

Noise temperature measurement

Microwave signals originating from a resonator in a cryogenic environment is at least an order of magnitude lower than the noise level associated with the measurement. Hence, detection of such weak signals is a primary task in the field of quantum technology. These microwave resonators operate at miliKelvin bath temperatures in order to reduce the thermal occupation of a resonator. It is thus essential to amplify the signal adding as little noise as possible. However, quantum mechanics imposes constraint on the minimum amount of noise that an amplifier must add to satisfy the Heisenberg uncertainty principle^{67,32}. While amplifiers based on the conventional semiconductor technology add much more noise, ultra-low noise amplifiers have been developed exploiting the non-linearity of Josephson junctions. Josephson Parametric Amplifiers (JPAs) are widely used in the circuit-QED field to achieve single shot readout of the qubit state without averaging. JPAs are also deployed in dark matter haloscope experiments like ADMX, HAYSTAC to measure the axion conversion power coming out of a tunable microwave cavity. One of the most important parameter which determines the success of a haloscope search as defined by Eq. 2.14 is the total noise N_{sys} . Therefore, it is critical to study and estimate the noise performance of readout chains performing such sensitive measurements.

An amplifier is rated by its power gain (G , amplification factor), bandwidth ($\Delta\nu$, frequency band over which it amplifies) and noise temperature (T_N , added noise). The noise performance can be expressed as a noise temperature, i.e., the noise added by an amplifier to a signal that is equivalent to that of a matched resistor of thermodynamic temperature T . In this chapter, I will begin with a discussion of the noise added in an amplification process and explain the lower limits imposed by quantum mechanics. Next, I will discuss common methods to measure the noise temperature of a RF chain. In particular, I will describe the procedure to calibrate the noise temperature of a JPA using a qubit as a primary

thermometer.

4.1 Sources of noise and their limits

Noise is a complimentary parcel provided by the nature while observing any phenomenon. We, as humans, have studied and developed sophisticated tools to suppress unwanted noise and unravel the useful information. A quick example is noise-cancelling headphones which suppresses the unwanted pulse tube noise as I write this section while sitting in the lab. From a scientific perspective, we classify classical noise arising in electrical circuits into two: (a) Shot noise and (b) Johnson noise. In 1918, a German physicist Walter Schottky identified and formulated a theory of “tube-noise” - a fluctuation in the current caused by the granularity of the discrete charges composing it. One decade later, Johnson and Nyquist studied a different type of noise- one caused by the thermal fluctuations of stationary charge carriers.

For cavity based experiments, the Johnson (thermal) noise is always present and associated with the resistance of the cavity walls. At finite temperature, the thermal motion of electrons causes power dissipation in an imperfect conductor, and these fluctuating currents imply the presence of fluctuating electromagnetic fields inside the cavity volume. Using a simple thought experiment, Robert Dicke showed that the voltage noise on an antenna receiving blackbody radiation is completely equivalent to the Johnson noise of a matched load at the same temperature⁶⁸. Thus, we can write the noise power dissipated in any bandwidth $\Delta\nu$ as,

$$P = k_B T \Delta\nu \quad (4.1)$$

resulting in a power spectral density of

$$S(\nu) = k_B T \quad (4.2)$$

The independence of noise spectral density with frequency is valid under the condition

that $k_B T \gg h\nu$ and should be modified to account for the quantum effects at low temperature to

$$S(\nu) = \frac{h\nu}{2} \coth \frac{h\nu}{k_B T} \quad (4.3)$$

using the fluctuation-dissipation theorem⁶⁹. In the Rayleigh-Jeans limit ($k_B T \gg h\nu$), one can recover Eq. (4.2) by approximating $\coth x \approx 1/x$ for small x . However, in the Wein limit $k_B T \ll h\nu$, where quantum effects are prominent and setting $\coth x \approx 1$, for large x , we find

$$S(\nu) = \frac{1}{2} h\nu \quad (4.4)$$

This corresponds to half-a-photon worth of noise originating from the zero-point fluctuations (ZPF) of an electromagnetic field. In a later section, we will see how it manifests in real measurements and limits our measurement capabilities.

Based on our discussion so far, we can write the most general expression for the system noise temperature of a haloscope at physical temperature T coupled to a coherent receiver,

$$k_B T_{sys} = h\nu N_{sys} = h\nu \left(\frac{1}{e^{h\nu/k_B T} - 1} + \frac{1}{2} + N_A \right) \quad (4.5)$$

The first term on the RHS represents the actual **thermal noise**, which is proportional to the average number of blackbody photons inside the cavity at physical temperature T . The second terms is **quantum noise** associated with the ZPF (Eq. 4.4) of the fluctuating field. The last term N_A corresponds to the total added **input noise** by the amplifier itself.

At sufficiently low temperatures, $k_B T \ll h\nu$, the thermal occupation is exponentially suppressed and quantum effects dominate. Thus, the total noise is independent of the physical temperature T . Quantum noise arises from the fact that the two quadrature amplitudes we are trying to measure do not commute with the Hamiltonian, and have to pay a hefty penalty for such coherent detection. Unfortunately, quantum mechanics takes its price not once (in second term) but twice. So far, we have ignored the third term representing the total added noise N_A , which is the sum of thermal and ZPF noise of the idler mode. The output

of a linear amplifier is just the input signal multiplied by gain $G \gg 1$. The energy required for amplification is provided by some source, and thus, the amplifier mixes the signal and idler into the same output port, coupling noise to the output signal.

The total output noise power of an amplifier connected to an impedance-matched source with an effective temperature T_0 is given by,

$$P_{out} = Gk_B(T_0 + T_A)\Delta\nu \quad (4.6)$$

where, T_A is the noise added by an amplifier and can be interpreted as the increase in noise temperature of the source impedance during the amplification process. It should be noted that this additional noise would have to be present at the input of an ideal noiseless amplifier with gain G to reproduce the noise we actually observe at the real amplifier's output. In case of a JPA, it can be thought of as the temperature of the idler mode.

In a cascaded chain of linear amplifiers, each with gain G_i and noise temperature T_{A_i} , it is easy to see that the output noise of the preceding stage acts as the input noise for the following amplifier and thus, the net input-inferred added noise of the chain will be

$$N_A = N_{A_1} + \frac{1}{G_1}N_{A_2} + \frac{1}{G_1G_2}N_{A_3} + \dots \quad (4.7)$$

From Eq. (4.7), we can infer that the noise performance of the full receiver chain is determined by first amplifier, provided it has sufficiently high gain G_1 . Now, we may naively think that with a careful design of an amplifier we can make the added noise arbitrarily small, however, Haus and Caves proved³² that a phase-sensitive linear amplifier must contribute

$$N_A \geq 1/2 \quad (4.8)$$

noise quanta to the output signal. In this section, we learnt that the input quantum noise

and the Haus-Caves theorem together imply the **Standard Quantum Limit (SQL)**

$$N_{sys} \geq 1 \quad (4.9)$$

which may be parameterized in the temperature units as

$$T_{SQL} = (h/k_B)\nu_c \sim 480\text{mK} \quad (4.10)$$

for $\nu_c \sim 10\text{GHz}$. Other factor which we have not discussed but will effect the total noise performance of the receiver chain is the transmission loss between the device and a pre-amplifier. We ought to reduce this loss by keeping the RF path short and must be taken into consideration while designing either a haloscope or a qubit-based readout.

This summarizes our discussion about the sources of noise and the limits posed by quantum mechanics. In the next section, I will briefly describe the various methods used to determine the noise temperature of a linear amplifier. I will particularly focus on how a narrow-band accurate microwave power calibration can be implemented using the ac Stark shift of a qubit to measure the noise temperature of a JPA.

4.2 Calibration of noise temperature

There are various methods developed to estimate the noise performance of a microwave amplifier chain. In this section, I will discuss their implementation, complexities and challenges associated with each.

4.2.1 Y-factor method (Hot-cold load method)

As the name suggests, we place an impedance matched resistor with a “hot” temperature T_H as the input noise source of an amplifier and the amplified output noise N_H is recorded

using a spectrum analyzer in a specified bandwidth¹. A heater is attached to this hot-load such that it's temperature can be controlled by applying current to it. We then repeat the previous step at a vastly different temperature T_C corresponding to Johnson-noise N_C . Y-factor is defined as the ratio of the output noise powers $Y=N_H/N_C$ and can be used to the calculate the noise temperature of the amplifier with the following equation:

$$T_A = \frac{T_H - Y T_C}{Y - 1} \quad (4.11)$$

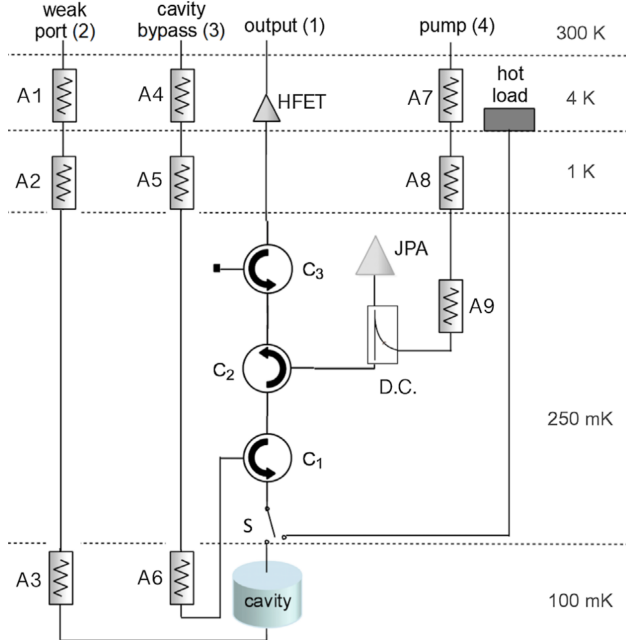


Figure 4.1: Wiring diagram for a Y-factor measurement. Schematic of a noise source with heater to measure gain and noise of the output chain. The hot load is thermally anchored to a higher temperature stage to prevent the heat from raising the temperature of mixing chamber. A switch bypasses the cavity to route the noise generated by hot load whose temperature is varied by varying the current on a heater attached to it. The output power is then digitized with a spectrum analyzer. Image credits: ADMX

One can build a microwave cryogenic noise source using a well characterized resistor^{70,71} or purchase a commercial one from BlueFors⁷². Before we move on, I should also mention a few technical challenges associated with the Y-factor method: **(1)** impedance mismatch

1. The resolution bandwidth is chosen such that the noise floor is at least 20 dB below the measured background.

between the hot and cold source signal pathways could lead to systematic errors, (2) uncertainty of the temperature values could lead to fitting errors in the regime where the amplifier noise temperature is lower than the cold load, (3) poor thermalization of the load resistor could lead to over-estimation of the calculated noise temperature (4) ensure that the noise power is sufficiently below the critical power of a JPA otherwise, it may lead to significant variation in the gain or even unstable performance.

I built an analysis tool for the ADMX using hot-cold load method to calibrate the system noise temperature as well estimate the attenuation in the signal path between the cavity and the JPA. This study also helped us examine the effect of magnetic field on the noise performance of high-electron-mobility transistor (HEMT) amplifiers used at the second stage. The tools and results are used to set axion sensitivity limits since then^{73,23,17}.

4.2.2 Primary thermometer

In the previous section, we discussed how uncertainty in a secondary thermometer could lead to imprecise estimation of noise temperature. Thus, it is desirable to have a primary thermometer whose temperature is related to other measurable quantities through a known physical law. This eliminates the need for initial calibration and the possibility of calibration drift in the sensor under varied conditions. Almost all of the thermometers used in our lab are secondary, meaning they are either pre-calibrated by a vendor or calibrated in our lab using some primary thermometer. One such device called a **Shot Noise Thermometer (SNT)**⁷⁴ is based on the electrical noise across a tunnel junction which is “related to the voltage across the junction by a relative noise measurement with only the use of electron charge, Boltzmann’s constant, and the assumption that electrons in a metal obey Fermi-Dirac statistics”.

The shot noise tunnel junction is based on a regular Josephson junction formed by Al – AlO_x – Al with nominal resistance 50Ω such that it is impedance matched to the microwave electronics. A local permanent magnet is added to keep the aluminum in a nor-

mal metal state at the miliKelvin temperatures. In theory, we could use any normal metal but in practice, I believe it is difficult to make 50Ω resistors whose resistance will stay close to this value even below 1 K.

In general, the amplifier has a frequency-dependent gain $G(\nu)$ and noise temperature ($T_{sys}(\nu)$) and we can fit the total noise power⁷⁴ to

$$P(V, \nu) = G(\nu) k_B \Delta\nu \left[T_{sys}(\nu) + \frac{1}{2} \left(\frac{eV + h\nu}{2k_B} \right) \coth \left(\frac{eV + h\nu}{2k_B T} \right) + \frac{1}{2} \left(\frac{eV - h\nu}{2k_B} \right) \coth \left(\frac{eV - h\nu}{2k_B T} \right) \right] \quad (4.12)$$

where V is the voltage applied to the SNT and ν is the frequency at which the power is measured in a bandwidth $\Delta\nu$. As shown in Fig. 4.2, the fit determines gain G , system noise temperature T_{sys} and system temperature T . In the high voltage limit, tEq. 4.12 results in

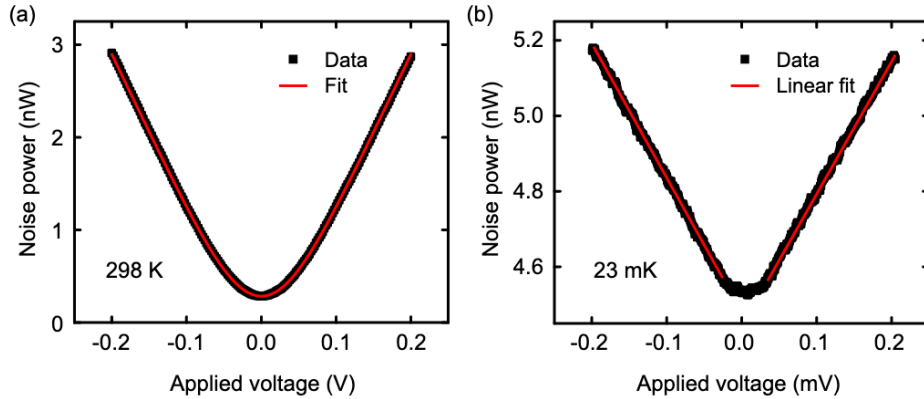


Figure 4.2: **Response of a SNT as a function of applied voltage.** (a) Output noise power (black squares) of the amplification chain at room temperature (298 K). The red curve corresponds to the fit of the data to Eq. 4.12. (b) Similar response at low temperature (23 mK). Linear fits described by Eq. 4.13 can be used to extract gain and system noise temperature. Figure adapted from Tanay Roy's thesis⁷⁵.

a linear relation between the output power and frequency given by

$$P(V, \nu) = G(\nu) k_B \Delta\nu \left(T_{sys}(\nu) + \frac{e|V|}{2k_B} \right). \quad (4.13)$$

We can extract $G(\nu)$ and $T_{sys}(\nu)$ by fitting a linear curve. Before we move on, I would like

to point out a few considerations while integrating SNT with a microwave receiver chain

- Achieving $50\ \Omega$ impedance is non-trivial in junction fabrication and as explained earlier, any differences would introduce systematic uncertainties.
- In many applications, the output noise power of SNT is found to saturate the JPAs thus, a well thermalized attenuator before the amplifier input may be helpful.
- The SNT junction is very sensitive to electro-static discharge (ESD) and thus, requires very careful handling.

In summary, the simple calibration routine and accurate measurement of the receiver chain is a strong selling point to implement the SNTs. I would like to take this opportunity and thank Joe Aumentado (NIST) for graciously offering SNT to characterize our microwave chains.

4.2.3 Qubit as a thermometer

In the discussions so far, we have used broadband noise sources as an input-noise source to an amplifier but in most applications, we are only interested in the noise performance of our receiver chain in a narrow-band. In this section, I will describe a narrow-band power calibrator comprising a superconducting qubit dispersively coupled to a readout resonator. We implemented this method following^{76–78} which is widely used in the superconducting qubit industry.

I would refer the reader to section 3.4 and just highlight the interaction between a transmon dispersively coupled to a readout cavity: photon number dependent shift in the qubit frequency, given by $\Delta\nu = \bar{n}_r \times \chi_{q,r}$. We can perform a Ramsey interferometry experiment to accurately determine the shift in qubit frequency and thus, infer the mean photon occupation in the readout. Given the stability of qubit transition frequency and also the microwave sources, we can easily achieve ppm resolution in frequency which makes the uncertainties if not smaller, comparable to the SNT.

1-Photon calibration

We perform a Ramsey type experiment where we introduce a readout pulse with varying amplitude (normalized to the actual readout amplitude) during the wait period in-between two $\pi/2$ pulses. The shortest wait period is chosen such that the readout cavity reaches its steady state, in this case $\tau_{min} \geq 2T_{1,r}$. As expected, we see the Ramsey oscillations smear out as we inject more photons in the readout Fig. 4.3. By fitting an exponential decay function with an oscillating term we can extract the shift in qubit frequency and the dephasing time, T_2^* . The shift in the qubit frequency is related to the photon number as:

$$\Delta\nu = \chi_{q,r} \bar{n} = \chi_{q,r} (\lambda A^2) \quad (4.14)$$

where, λ is a proportionality constant between the applied amplitude and the photon number. The additional dephasing is given by the rate

$$\Gamma_n = \frac{8 \bar{n} \kappa \chi_{q,r}^2}{\kappa^2 + 4\chi_{q,r}^2} \quad (4.15)$$

where κ and $\chi_{q,r}$ can be inferred from Fig. 3.3. From Fig. 4.4 (b) we estimate the mean photon number in the readout, $\bar{n}_r = 2.17 \pm 0.05$, which implies that we perform our high-fidelity single-shot qubit readout with approximately 2 photons.

We play a continuous readout tone and record the noise power on a spectrum analyzer with a resolution bandwidth (RBW) B . The signal-to-noise ratio (SNR) is given by,

$$SNR = \frac{S}{N} = \frac{\bar{n}_r h \nu \kappa}{k_B T_{sys} B} \quad (4.16)$$

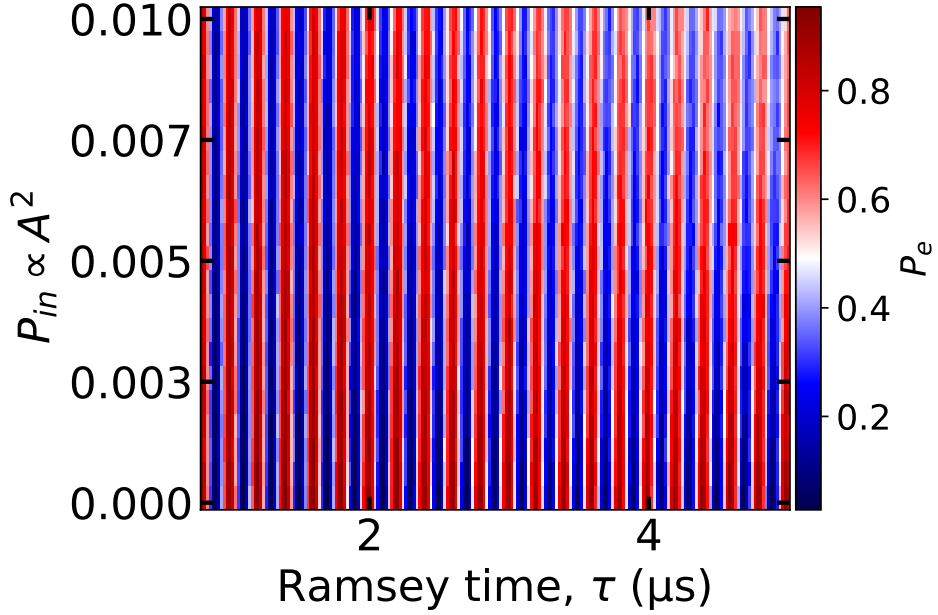


Figure 4.3: **Qubit Ramsey as a function of the input readout power.** The x-axis corresponds to the delay time between two $\pi/2$ pulses during which a readout pulse is played with an amplitude, A corresponding to the y-axis. At high input power, the oscillations start to fade away. Using square-law equation, the input power $P_{in} \propto A^2$ is proportional to the mean photon number \bar{n}_r .

Eq. 4.16 implies

$$T_{sys} = \frac{2.17 * (6.626 \times 10^{-34}) * (7.7894 \times 10^9) * \frac{1}{233*10^{-9}}}{(1.38 \times 10^{-23}) * (10 \times 10^3) * 10^{\frac{SNR}{10}}} = 3.27 \text{ K} \quad (4.17)$$

The estimated T_{sys} seems reasonable assuming the quoted noise temperature of 2 K by the manufacturer (Low-Noise Factory). It implies that there is approx. 3 dB of loss between the readout port at MXC stage and the LNF amplifier at 4 K stage. There are 3 circulators in-between which contributes at least 3×0.4 dB of loss and additional losses arising due to short normal metal RF cables. Now, we can use this estimated system noise temperature and record the improvement in $SNR_i = (S_{on}/N_{on})/(S_{off}/N_{off})$ after we turn the JPA on.

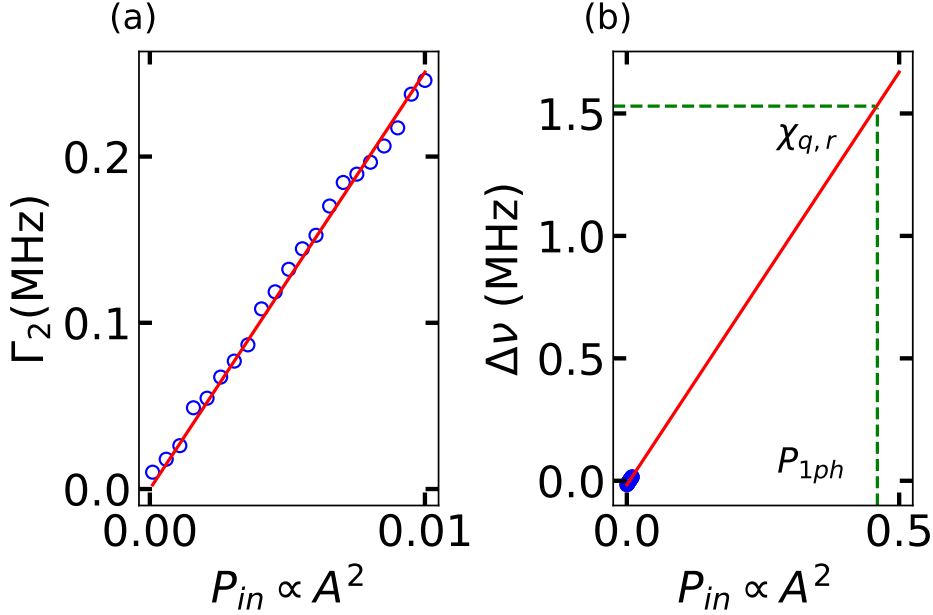


Figure 4.4: **1-Photon amplitude.** (a) Dephasing rate as a function of the input readout power. The curve is fit to Eq. 4.15 to extract the scale factor λ . Notice that the fitted line passes through origin implying that the residual population in the readout is approaching zero. (b) Shift in qubit frequency as a function of the input readout power. The horizontal green dashed line represents the shift, $\chi_{q,r}$ we expect for $\bar{n} \sim 1$ and the vertical dashed line corresponds to 1-photon input power as given by the fit.

The noise temperature of the JPA can be computed from the following expression:

$$\begin{aligned} T_N^{JPA}(\nu) &= T_{sys}(\nu) \left[\frac{1}{SNR_i(\nu)} - \frac{1}{G_{JPA}(\nu)} \right] \\ &= T_{sys}^{JPA}(\nu) - \frac{T_{sys}(\nu)}{G_{JPA}(\nu)} \end{aligned} \quad (4.18)$$

where $G_{JPA} = S_{on}/S_{off}$ is the gain of the JPA. We can quickly check that Eq. 4.18 follows Eq. 4.7 and we infer the total system noise temperature with JPA on as $T_{sys}^{JPA}(\nu)$. From Fig. 4.5, we can compute the gain when the JPA is on vs off to be ~ 14.34 dB and the improvement in SNR to be roughly 5.76 dB. Using Eq. 4.18 and plugging the computed quantities, we estimate the noise temperature of the JPA to be 0.771 K. The quantum limited noise at 7.789 GHz is roughly 360 mK, which implies our JPA is operating at roughly 50% efficiency.

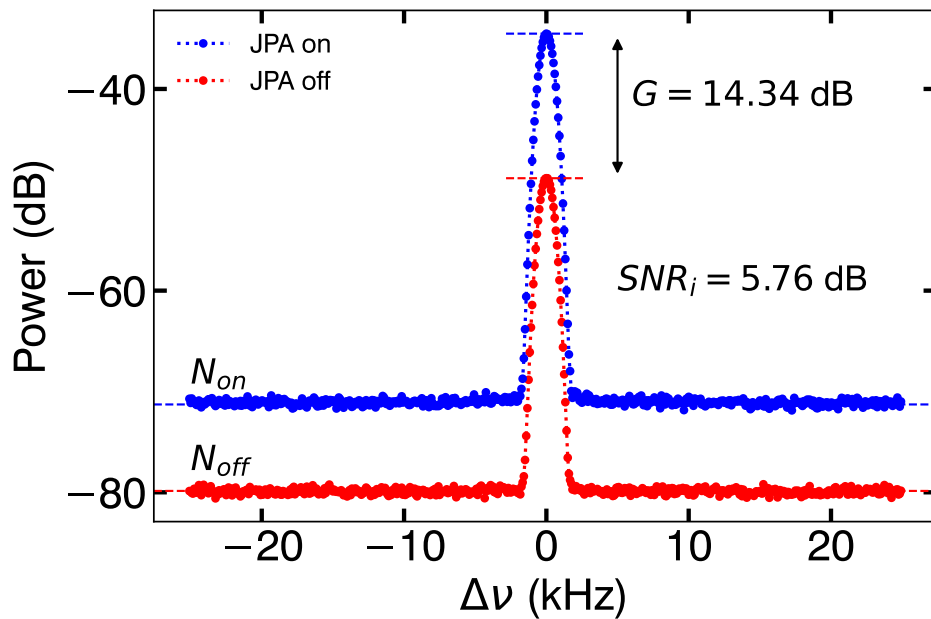


Figure 4.5: **SNR improvement with JPA added to the readout chain.** Plotting the measured power as a function of the detuning from the readout resonator frequency with the JPA on vs off. The JPA is biased at 14 dB gain to optimize the qubit readout fidelity.

Chapter 5

Single Photon Counter

In the last chapter, we discussed how the frequency of a transmon shifts depending on the number of photon present in a resonator. In the present chapter, I will describe how we can build a photon counter which is resilient to errors caused by the external environment. Next, I will discuss an application of such a low-background detector to search for hidden photons with an unprecedented sensitivity. In the end, I will discuss the optimizations I have implemented on the RF measurement chain to drastically improve our readout SNR and the duty cycle of the photon counting protocol. Parts of this chapter are adapted from^{20,42}.

5.1 Meet the device

The photon counting device consists of a transmon cavity which is dispersively coupled to a high-Q storage cavity and low-Q readout cavity as shown in Fig. 5.1. The entire cavity is machined out of a 6N (99.9999%) monolithic aluminum block using a flute¹ method developed in our lab³⁹. This method ensures exceptionally low-dissipation seam-loss and one can easily achieve internal Q-factor $\gtrsim 100$ Million ($T_1^s \sim 10$ ms).

I will refer the reader to excellent resources for designing cQED components and skip the details here but mention key considerations to keep in mind while designing a photon counter type device.

1. **Interaction rate:** sets the time to detect the photon but also limits the lifetime via Purcell⁷⁹ decay. Thus, a balance is necessary for optimal application use.
2. **Frequency hierarchy:** In order to isolate the qubit from external environment, the qubit frequency is designed to be below the fundamental modes of both the storage and the readout.

1. Because of the hole pattern resemblance to a flute.

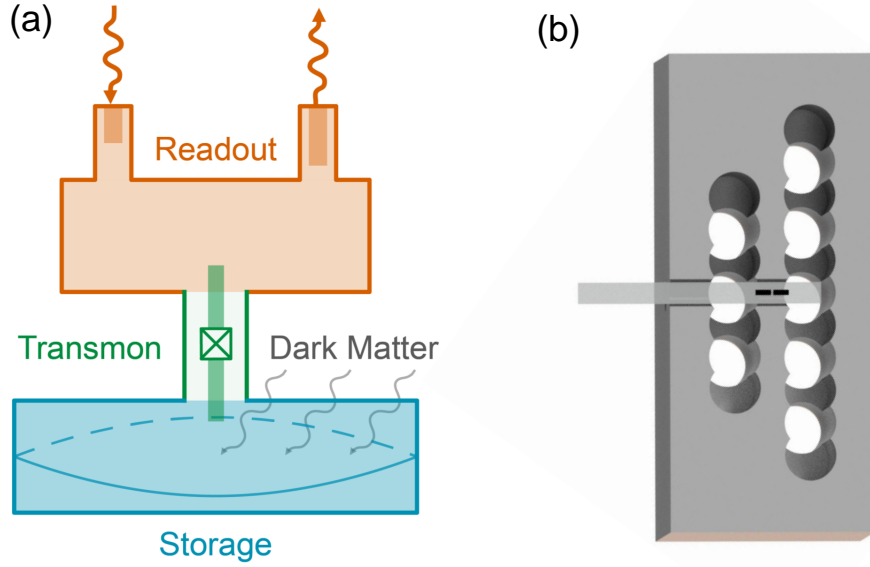


Figure 5.1: **Photon counting device.** The transmon is simultaneously coupled to a high-Q storage cavity and low-Q readout cavity. The storage cavity sources the dark matter photon and the readout cavity measures the state of the transmon. (b) 3D render of the design which is machined using a CNC machine and a transmon qubit fabricated on a sapphire chip.

3. **Fast readout:** The readout cavity is strongly coupled to the transmission line for a fast qubit measurement and thus, a dominant source of noise. An effective rf-filtering scheme must be developed to suppress any radiation from leaking in.

5.2 Quantum Non-demolition interaction

In section 3.6, I briefly mentioned that the dispersive interaction between the qubit and cavity is QND, meaning that the qubit state is unperturbed during the act of measurement. Similarly, the cavity state is left unchanged during operations on the transmon. If we stare at Eq. 3.9, we realize that the interaction term ($\chi \hat{a}^\dagger \hat{a} \frac{\sigma_z}{2}$) commutes with the bare Hamiltonian of the cavity ($\omega_c \hat{a}^\dagger \hat{a}$) and the qubit ($\omega_q \frac{\sigma_z}{2}$). The act of cavity state measurement due to interaction with a qubit collapses/projects the cavity to a Fock state, without absorbing or

destroying the cavity state. And hence, we can measure the resultant cavity state multiple times.

Ideally, a parity measurement tells us the presence of a photon in the cavity. However, the measurement is corrupted due to various possible errors that could result in inefficiencies or worse, false positive detection. The errors are caused by spurious qubit excitation, decay and dephasing, cavity decay and incorrect readout signal. In a typical transmon-cavity system, these errors occur with probabilities of the order $0.1 - 5\%$ which is much greater than the potential dark matter signal induced probability. We take advantage of the QND interaction in order to mitigate the effect of these errors on detector inefficiency and false positive probability.

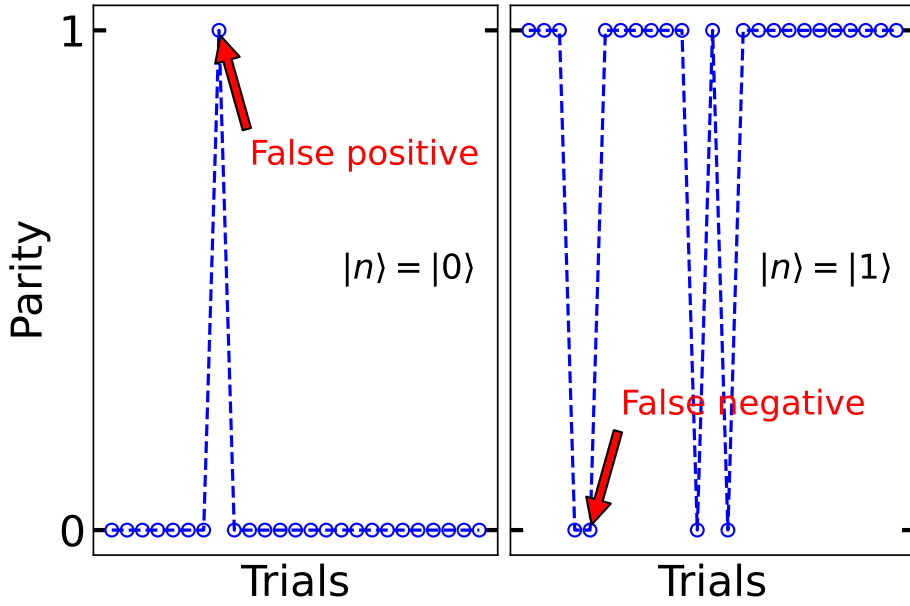


Figure 5.2: **Spurious parity jumps.** (Left) shows the measured parity when there is no photon in the cavity and a false positive event where the parity changes to 1. (Right) measured parity when the cavity is prepared in $|n\rangle = |1\rangle$ Fock state with few jumps to 0 leading to inefficient detection.

5.3 Repeated measurement protocol

The repeated parity measurement protocol is depicted in Fig. 5.3s. It starts with adding a coherent state $|\alpha\rangle$ in the storage cavity followed by a set of repeated parity sequences with a delay between each measurement. The delay is important to let the readout resonator relax back to its steady state otherwise it may cause the qubit resonance frequency to shift and thus, the next $\pi/2$ pulse will be erroneous.

Each experiment comprises of $N + 1 = 31$ parity measurements returning a readout sequence $(\mathcal{R}_1, \mathcal{R}_\infty, \dots, \mathcal{R}_N)$ which is fed into a Bayesian analysis^{80–82} to reconstruct the initial state of the storage cavity.

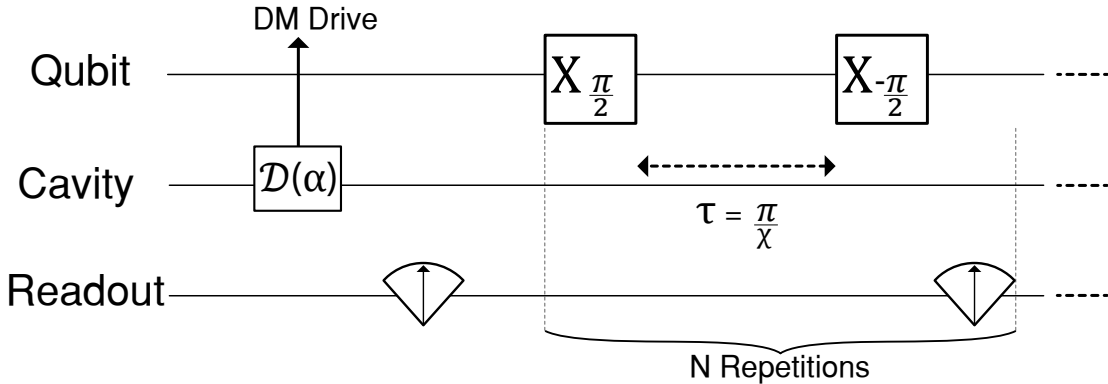


Figure 5.3: **Photon counting protocol.** Repeated parity measurement protocol with cavity prepared in a coherent state. It consists of injecting a variable number of mean photons in the cavity followed by repeated parity measurement of the photons using a transmon qubit. The parity sequence consists of two $\pi/2$ pulse separated by a time $\tau = \pi/\chi$ followed by a qubit readout.

5.4 Hidden Markov Model Analysis

We developed a Hidden Markov Model (HMM) to reconstruct the cavity state at the beginning of the experimental sequence. This analysis tracks all the possible transmon and cavity states and their imperfect measurements that would result in the observed readout sequence. It consists of hidden states, their signatures, transitions between hidden states, and emission of hidden states. In our case, the hidden state refers to the joint qubit and cavity states

which are measured via the readout signal. For the photon counting experiment, we are interested in cavity states² $n \in [0, 1]$ and qubit states $q \in [g, e]$ so the possible hidden states are $\mathcal{S} \in [0g, 1g, 0e, 1e]$. Similarly, the observed qubit state due to imperfect readout is given by $\mathcal{R} \in [\mathcal{G}, \mathcal{E}]$.

Now, let's discuss the components of the HMM namely the “transition matrix” T and the “emission matrix” E which describes the possible evolution of the joint qubit-cavity state (\mathcal{S}) between successive measurements and the possible readout outcomes for a given qubit-cavity state respectively. The transition matrix is written as below

$$T = \begin{bmatrix} |0g\rangle & |1g\rangle & |0e\rangle & |1e\rangle \\ \begin{bmatrix} P_{00}P_{gg} & P_{00}P_{ge} & P_{01}P_{ge} & P_{01}P_{gg} \\ P_{00}P_{eg} & P_{00}P_{ee} & P_{01}P_{ee} & P_{01}P_{eg} \\ P_{10}P_{gg} & P_{10}P_{ge} & P_{11}P_{ge} & P_{11}P_{gg} \\ P_{10}P_{eg} & P_{10}P_{ee} & P_{11}P_{ee} & P_{11}P_{eg} \end{bmatrix} & |0g\rangle \\ |01\rangle \\ |1g\rangle \\ |1e\rangle \end{bmatrix} \quad (5.1)$$

where the probability of a hidden state $\mathcal{S}_i \rightarrow \mathcal{S}_{i+1}$ is given by $T_{\mathcal{S}_i, \mathcal{S}_{i+1}}$.

1. Cavity transitions: There are two processes that can change the cavity state between successive measurements: decay and heating³. Each measurement of the cavity projects it into a number state and in between two measurements, the cavity state evolves for a time, $t_m = 10 \mu\text{s}$.

- Cavity decay: Over the course of t_m the probability of cavity to decay from $|1\rangle \rightarrow |0\rangle$ is given by $P_{10} = 1 - e^{-t_m/T_1^s}$, where T_1^s is the cavity decay time.
- Cavity heating: The probability of spontaneous cavity heating $|0\rangle \rightarrow |1\rangle$ toward the steady state population, \bar{n}_c , is given by $P_{01} = \bar{n}_c(1 - e^{-t_m/T_1^s})$.

2. We will generalise this in Chapter 6 for higher Fock states.

3. We have not included cavity dephasing (or coherence) as it is not relevant for the HMM analysis since the cavity is only in a number state, which has no definite phase due to the number-phase uncertainty relation.

The remaining two terms P_{00} and P_{11} correspond to events where cavity state remains unchanged such that the pairwise sum adds to 1 ($P_{00} + P_{01} = 1$).

2. **Qubit transitions:** There are three process that can result in a qubit error: decay, dephasing and heating.

- Qubit decay: The qubit state may decay from $|e\rangle \rightarrow |g\rangle$ with a probability $P_{eg}^\downarrow = 1 - e^{-t_m/T_1^q}$, where T_1^q is the qubit decay time.
- Qubit dephasing: The qubit state may dephase though only during the parity wait time $t_p = 380\text{ ns}$ thus, $P^\phi = 1 - e^{-t_p/T_2^q}$, where T_2^q is the qubit dephasing time and $t_p \ll T_2^q$.
- Qubit heating: Spontaneous heating $|g\rangle \rightarrow |1\rangle$ to the steady state qubit population \bar{n}_q occurs with a probability $P_{ge}^\uparrow = \bar{n}_q(1 - e^{-t_m/T_1^q})$.

The transition matrix covers all these processes in $P_{ge} = P_{ge}^\uparrow + P^\phi$ and $P_{eg} = P_{eg}^\downarrow + P^\phi$. As before, P_{gg} and P_{ee} corresponds to events where qubit state remains unchanged such that their pairwise sum adds to 1 ($P_{gg} + P_{ge} = 1$).

In sections 3.6 and 3.7, we discussed the qubit and cavity characterization experiments we can perform to measure the decay time (T_1^q, T_1^c), coherence time $T_{2,q}^\phi, T_{2,c}^\phi$ and the steady state population \bar{n}_q . Using the numbers we obtained, let's evaluate the elements of the transition matrix

$$T = \begin{bmatrix} |0g\rangle & |1g\rangle & |0e\rangle & |1e\rangle \\ \begin{bmatrix} 0.989 & 0.011 & 0 & 0 \\ 0.094 & 0.906 & 0 & 0 \\ 0.018 & 1.94 \times 10^{-4} & 0.011 & 0.971 \\ 1.71 \times 10^{-3} & 0.0164 & 0.889 & 0.093 \end{bmatrix} & \begin{matrix} |0g\rangle \\ |01\rangle \\ |1g\rangle \\ |1e\rangle \end{matrix} \end{bmatrix} \quad (5.2)$$

The emission matrix captures the probability to observe a signal \mathcal{R} given the qubit-cavity

state is \mathcal{S} . It is represented by a 2×4 matrix for two possible readout signals where $[F_{g\mathcal{G}}, F_{e\mathcal{E}}]$ gives the probability of obtaining the correct readout and $[F_{g\mathcal{E}}, F_{e\mathcal{G}}]$ gives the probability due to readout errors which is indistinguishable from state change errors.

$$E = \frac{1}{2} \begin{bmatrix} F_{g\mathcal{G}} & F_{g\mathcal{E}} \\ F_{e\mathcal{G}} & F_{e\mathcal{E}} \\ F_{g\mathcal{G}} & F_{g\mathcal{E}} \\ F_{e\mathcal{G}} & F_{e\mathcal{E}} \end{bmatrix} \begin{array}{l} |0g\rangle \\ |0e\rangle \\ |1g\rangle \\ |1e\rangle \end{array} \quad (5.3)$$

Note that there is a factor of $1/2$ in front of the matrix, this is due to the fact that readout is independent of the cavity state. For example, $F_{g\mathcal{G}} = P(\mathcal{G}|g) = P(\mathcal{G}|g0) + P(\mathcal{G}|g1)$. And since the readout state remains unchanged by the cavity state, $P(\mathcal{G}|g0) = P(\mathcal{G}|g1)$ such that $P(\mathcal{G}|g) = 2P(\mathcal{G}|g0)$ and thus, $E_{|g0\rangle, \mathcal{G}} = \frac{1}{2}F_{g\mathcal{G}}$.

Now going back to section 3.6 and Fig. 3.6 we can estimate the elements in the emission matrix. The resulting single shot data is fitted to a sum of Gaussian distribution to obtain a confusion matrix described below.

$$\begin{bmatrix} |g\rangle & |e\rangle \\ \begin{bmatrix} 0.976 & 0.024 \\ 0.030 & 0.970 \end{bmatrix} & \begin{array}{l} \mathcal{G} \\ \mathcal{E} \end{array} \end{bmatrix} \quad (5.4)$$

There are two main sources of error contributing to the readout infidelity: spurious qubit transitions and voltage fluctuations from readout amplification chain. It is important to decouple the two and only include the readout errors due to voltage fluctuations while evaluating the emission matrix. To do so, we compute the readout infidelity by subtracting the qubit error probabilities during the $1\mu s$ readout window due to the qubit decay ($[1 - e^{-1\mu s/T_1^q}] = 8 \times 10^{-3}$) or heating ($\bar{n}_q[1 - e^{-1\mu s/T_1^q}] = 8 \times 10^{-5}$) from the total measured

error during the readout. However, these values are within one sigma and we can evaluate the elements of the emission matrix based on the confusion matrix to be $F_{gG} = 97.6 \pm 0.1\%$ and $F_{eE} = 97.0 \pm 0.1\%$.

$$E = \frac{1}{2} \begin{bmatrix} 0.976 & 0.022 \\ 0.030 & 0.970 \\ 0.976 & 0.022 \\ 0.030 & 0.970 \end{bmatrix} \begin{array}{l} |0g\rangle \\ |0e\rangle \\ |1g\rangle \\ |1e\rangle \end{array} \quad (5.5)$$

It is an important task to accurately fill out the transition and emission matrices which forms the core of HMM analysis. The qubit, cavity and readout parameters measured independently are summarized below.

| Device Parameter | Value |
|----------------------------------|---|
| Qubit frequency | $\omega_q = 2\pi \times 4.961 \text{ GHz}$ |
| Qubit anharmonicity | $\alpha_q = -143.2 \text{ MHz}$ |
| Qubit decay time | $T_1^q = 115 \pm 10 \mu\text{s}$ |
| Qubit dephasing time | $T_2^q = 160 \pm 10 \mu\text{s}$ |
| Qubit echo time | $T_2^e = 220 \pm 20 \mu\text{s}$ |
| Qubit residual occupation | $\bar{n}_q = 2 \pm 1 \times 10^{-2}$ |
| Storage frequency | $\omega_s = 2\pi \times 5.965 \text{ GHz}$ |
| Storage decay time | $T_1^s = 1360 \pm 23 \mu\text{s}$ |
| Storage dephasing time | $T_2^s = 2390 \pm 286 \mu\text{s}$ |
| Storage-Qubit Stark shift | $2\chi = -2\pi \times 1.285 \text{ MHz}$ |
| Storage residual occupation | $\bar{n}_c = 6.3 \pm 0.3 \times 10^{-3}$ |
| Readout frequency | $\omega_r = 2\pi \times 7.790 \text{ GHz}$ |
| Readout $ e\rangle$ shift | $2\chi_r^e = -2\pi \times 1.53 \text{ MHz}$ |
| Readout fidelity ($ g\rangle$) | $F_{gG} = 97.6 \pm 0.1\%$ |
| Readout fidelity ($ e\rangle$) | $F_{eE} = 97.0 \pm 0.1\%$ |

Table 5.1: **Device parameters.** Measured qubit, storage, and readout cavity parameters. These independently measured values are necessary to determine for the transition and emission matrices. This enables the hidden Markov model to capture the behavior of the system during the measurement sequence.

5.5 Reconstructing the cavity state

As mentioned earlier, HMM analysis provides us a tool to compute the cavity state probabilities at the beginning of the measurement sequence. It involves tracking all the possible paths that the joint qubit-cavity states may take such that their imperfect measurement would result in the observed readout sequence $(\mathcal{R}_0, \mathcal{R}_1, \dots, \mathcal{R}_N)$. The probability is mathematically represented in Eq. 5.6 which uses an efficient backward algorithm as described in Appendix D⁴².

$$P(n_0) = \sum_{S_0 \in [|n_0,g\rangle, |n_0,e\rangle]} \sum_{S_1} \dots \sum_{S_N} E_{S_0, \mathcal{R}_0} T_{S_0, S_1} E_{S_1, \mathcal{R}_1} \dots T_{S_{N-1}, S_N} E_{S_N, \mathcal{R}_N} \quad (5.6)$$

We can understand this complicated expression as follows: (1) The inner set of N sums of the qubit-cavity states S_i account for all the various possible state changes as well as the emissions during each observation. (2) Since the goal of reconstruction is to determine the initial cavity state, we need an additional sum over the two possible qubit states. Let's consider an example where the readout changes from \mathcal{G} to \mathcal{E} . In this simple case, we can count the number of possible process which could have resulted in this measured sequence as shown in Fig. 5.4 and their associated probabilities. There are three possible scenarios (with probability): correct detection of a photon in the cavity ($P_{11}P_{gg}F_{e\mathcal{E}}/2$), a qubit heating event ($P_{00}P_{ge}F_{e\mathcal{E}}/2$) or (c) a plain readout error ($P_{00}P_{gg}F_{g\mathcal{E}}/2$).

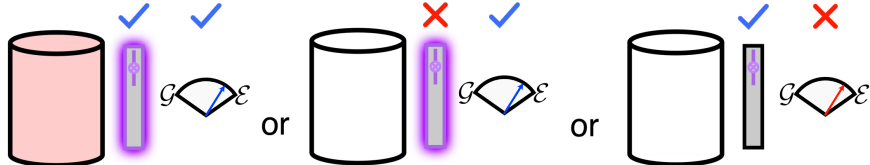


Figure 5.4: **State reconstruction scenarios.** The cavity state reconstruction accounts for all the possible processes that would result in the measured emission sequence. For example, a measured sequence of $\mathcal{G} \rightarrow \mathcal{E}$ could come from three possible scenarios shown above: a photon in the cavity, spurious qubit heating, or readout error. Image adapted from Akash Dixit's thesis⁴².

5.6 Likelihood test

For a given sequence of observed readouts, we can use Eq. 5.6 to compute the probabilities corresponding to zero ($P(n_0 = 0)$) or one photons ($P(n_0 = 1)$) in the cavity. We devise a likelihood ratio test to determine the initial cavity state.

$$\lambda = \frac{P(n_0 = 1)}{P(n_0 = 0)} \quad (5.7)$$

The likelihood ratio λ helps us discriminate between the two possibilities. If $\lambda < \lambda_{thresh}$, we can infer the cavity has no photons in the cavity and vice-versa. For example, a likelihood ratio of $\lambda = 1$ indicates that the cavity is equally likely to have zero or one photons. Thus, in order to gain more confidence a large likelihood ratio is required and this sets the false positive probability due to detector errors. We can decrease the detector based false positive probability (δ_{det}) by increasing the threshold for detection as

$$\delta_{det} = \frac{1}{\lambda_{thresh} + 1} \quad (5.8)$$

However, there is a price to be paid in lower detection efficiency as the threshold is set high. This cost is acceptable for two reasons: the false positives are exponentially suppressed with more measurements and it is safer to be conservative and falsely discover the dark matter due to spurious errors.

5.7 Testing the HMM with real events

So far I have described the internal workings of HMM, how we can reconstruct the cavity state and set a threshold to set off a detection event. In this section, I am going to demonstrate the effectiveness of repeated measurement protocol in exponentially suppressing false positive events with only linear increase in the number of parity measurements.

5.7.1 No photon in the cavity

In these experiments, we let the cavity relax for almost 5 cavity lifetimes such that it reaches its steady state and then start recording \mathcal{G} over 30 repeated parity measurements. The readout sequence is shown in Fig. 5.5 where we see observe no state change, indicating the absence of a photon in the cavity. We can check that the reconstructed probabilities reflect the same with $P(n_0) < 0.01$ after 30 measurements.

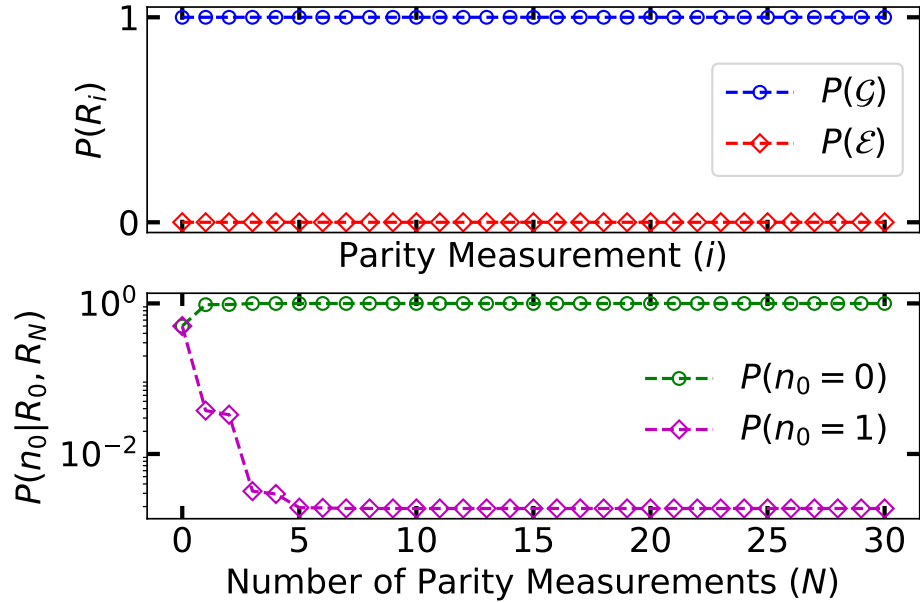


Figure 5.5: **Zero cavity photon.** (Top) Observed readout sequence \mathcal{G} indicating no change in the state of qubit. (Bottom) Reconstructed probabilities of the initial cavity state as a function of the number of parity measurements included in the HMM analysis.

5.7.2 One photon in the cavity

This is an interesting one where we do inject a photon in the cavity and record 30 repeated parity measurements as shown in Fig. 5.6. The qubit state successfully flips between \mathcal{G} and \mathcal{E} as expected indicating the presence of a photon in the cavity. I would like to highlight two features in the reconstructed probabilities of the initial cavity state: firstly, we are able to detect a positive event with a very high likelihood ratio even in the presence of a few spurious detector errors (3^{rd} and 9^{th} measurement), demonstrating robustness. Second, the

false positive probability ($P(n_0)$) exponentially decreases with only linear increase in the number of parity measurements. The probability of a series of detector errors conspiring to produce the observed readout sequence is $P(n_0 = 0) < 10^{-20}$.

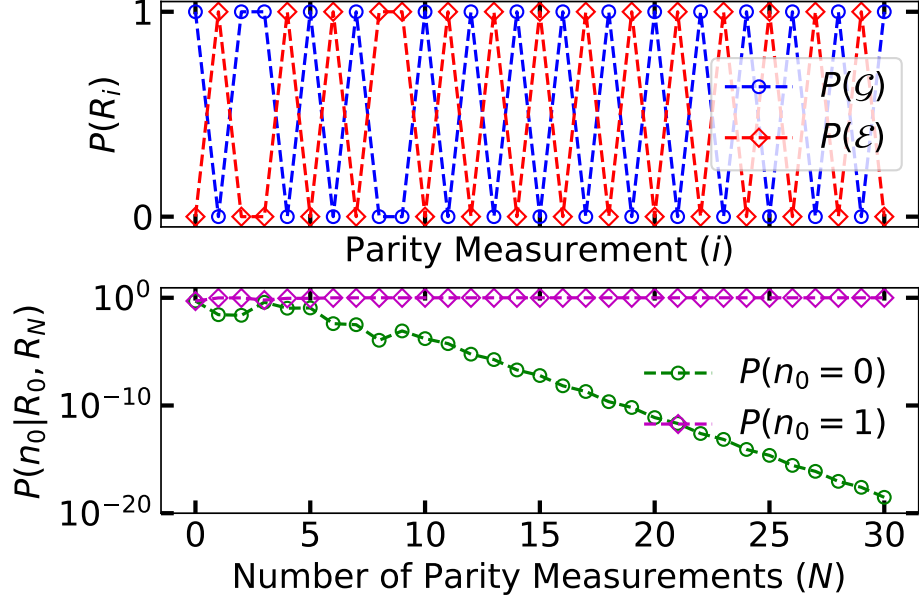


Figure 5.6: **One cavity photon.** (Top) Observed readout sequence \mathcal{G} flipping back and forth indicating the presence of a photon. (Bottom) Reconstructed probabilities of the initial cavity state as a function of the number of parity measurements included in the HMM analysis. The false positive probability exponentially decreases with only linear increase in the number of measurements.

5.8 Detector Characterization

In order to implement this qubit based photon counter for sensitive applications, it is necessary to characterize the detector's performance with a calibrated coherent photon source. We evaluate the detector performance by injecting a calibrate photon population into the cavity and counting them using the procedure described in section 3.7 and 5.7.

For each calibrated injected mean photon population \bar{n}_{inj} , we perform a series of 30 repeated parity measurements and reconstruct the initial cavity state probability using the HMM analysis. A likelihood ratio is computed for these probabilities and compared against

a variable threshold to determine the positive events (presence of a photon in the cavity). The measured photon probability \bar{n}_{meas} for each \bar{n}_{inj} is computed by taking a ratio of the number of photons counted with the total number of measurements performed.

We expect the number of measured photons to grow linearly as a function of the injected photon number and thus can write a relation described by the functional form:

$$\bar{n}_{meas} = \eta \bar{n}_{inj} + \delta \quad (5.9)$$

where η is the detection efficiency and δ is the detector dark count. As shown in Fig. 5.7, for any fixed threshold ($\lambda_{thresh} = 10^8$) we can fit the measured and injected photon probabilities to Eq. 5.9 and extract the detector efficiency and dark counts probability. Although it may seem that we can reduce the false positive probability to arbitrarily small

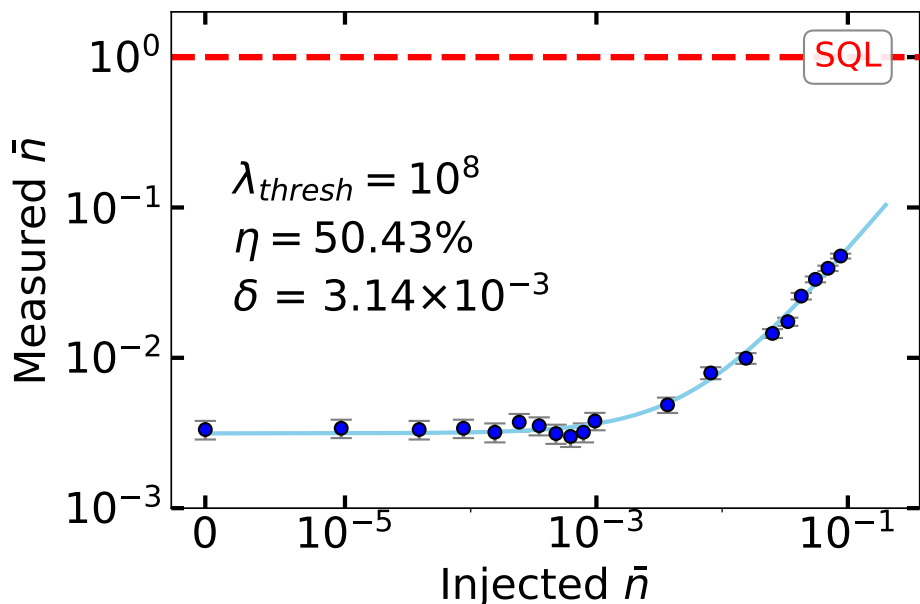


Figure 5.7: Photon counter characterization. Starting with a cavity in its steady state, a variable displacement is applied followed by 30 repeated parity measurements. The resulting readout sequence is analyzed with the HMM and a likelihood ratio is applied to determine the measured cavity population. Detector efficiency (η) and false positive probability (δ) are determined from the fit. The dashed red line corresponds to the standard quantum limit (SQL) which results in the noise-equivalent of one photon occupation³². We have demonstrated detection capabilities of a single mode photon population with sub-SQL sensitivity.

value by choosing a larger likelihood ratio, the efficiency of the detection also plummets down (see 5.8 (a)) and start missing real photon events. Thus, it is crucial to choose a reasonable threshold such that we operate in the regime of background dominated false positives. One way could be to plot the efficiency corrected false positive probability as a function of the threshold as shown in Fig. 5.8 (b). Initially δ/η decreases as the threshold is increased, indicating a suppression of detector based false positives but eventually reaches a steady state value of $\bar{n}_s = 6.23 \pm 0.30 \times 10^{-3}$ even as the threshold is increased. This tells us that the events being measured are not due to a series of detector based errors but rather a background of real photons populating the cavity. Hence, operating the detector with a $\lambda_{thresh} = 10^8$ is sufficient to suppress the detector based errors below the measured backgrounds. It essentially means that at most 1 out of 10^8 events could be due to detector based errors.

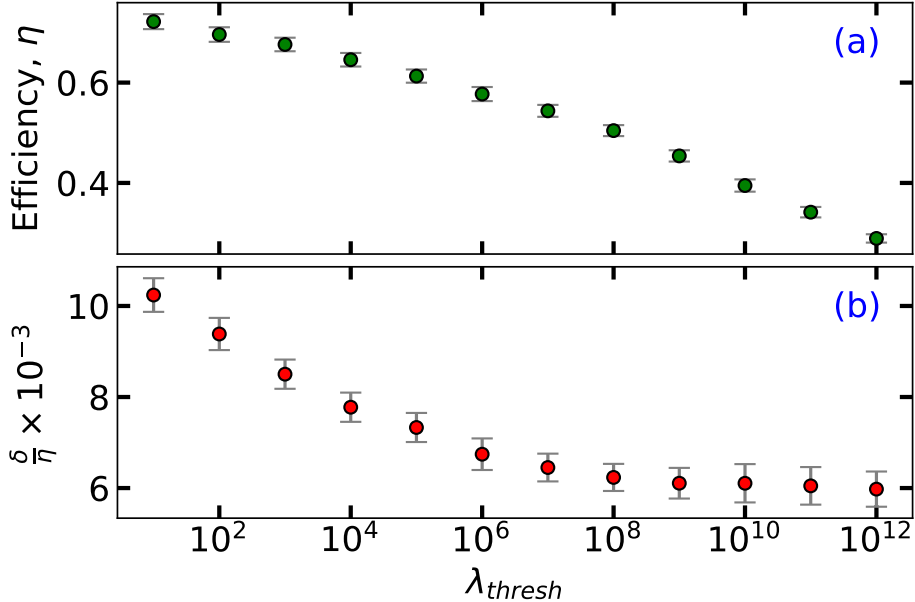


Figure 5.8: **Detector efficiency and false positive probability.** (a) Detector efficiency monotonically falls off as a function of λ_{thresh} and the tolerance for qubit based errors is reduced. (b) Efficiency corrected false positive probability (δ/η) decreases with increasing threshold but asymptotes at higher thresholds, indicating detector errors are no longer dominant contribution to the total detector false positive probability.

We can convince ourselves that these events are real photons by plotting histogram of the

likelihood ratio for two different \bar{n}_{inj} as shown in Fig. 5.9. The likelihood ratios for events where the injected photon number is low are comparable to the events when a significant number of photons are injected. This clearly indicates that such events are highly unlikely due to detector errors and are correctly detected cavity photons.

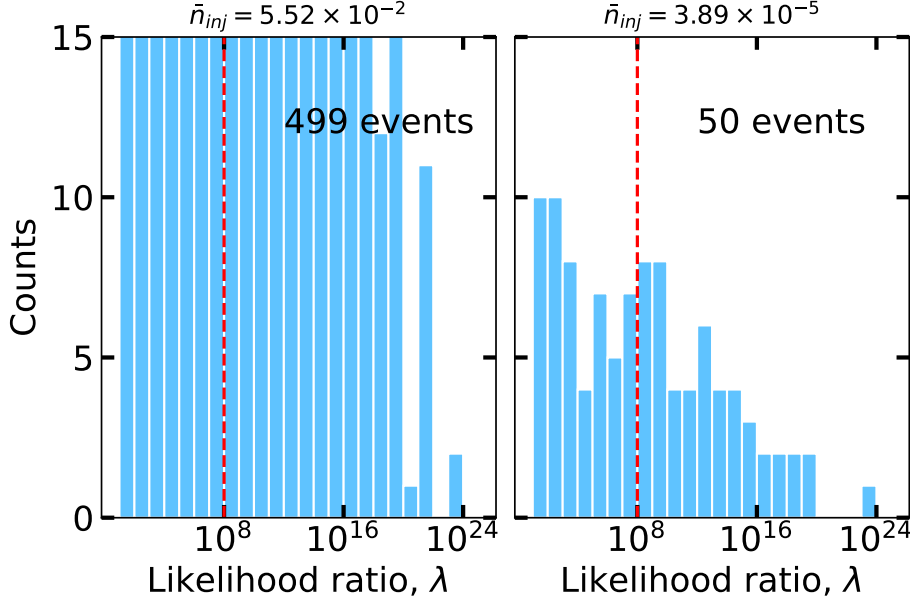


Figure 5.9: **Histogram of events.** Likelihood ratios of all events for two different injected mean photon numbers is plotted. The y-axis is cut-off at 15 counts to view the rare events at high likelihood ratio and red dashed line corresponds to $\lambda_{thresh} = 10^8$ used in the analysis shown in Fig. 5.7. The total number of events which crossed the λ_{thresh} is mentioned on the plot. For low injected photon numbers, it is clearly evident that detection events with high likelihood ratio is from a background occupying the storage cavity rather than detector based false positives.

5.9 Metrological Gain

By counting photons with repeated parity measurements and applying a Markov model based analysis, we demonstrate single photon detection with background shot noise reduced to $-10 \log_{10} \sqrt{\bar{n}_c} = 11.0 \pm 0.1$ dB below the SQL. In Fig. 5.10, I show the qubit based photon counting implemented on two samples (namely Picollo and Multimode) and their associated metrological gain as compared to trapped ions, Bose-Einstein condensates, and cold atom

systems. With this capability to detect background events much below the SQL, we have developed a quantum sensing which can be applied for dark matter search as we will learn shortly.

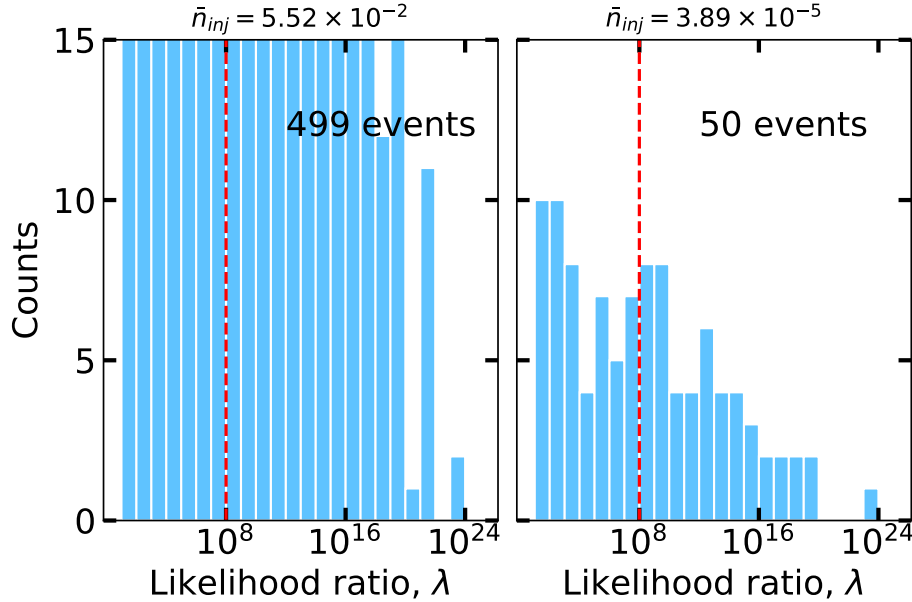


Figure 5.10: **Metrological gain literature survey.** Replace the image.

| Qubit based Photon Counting | | |
|------------------------------|-----------------|-------------------|
| Sample or Run | Frequency (GHz) | Gain |
| Picollo (Run1) ²⁰ | 6.011 | 15.7 ± 0.9 dB |
| Picollo (Run2) | AX | ALA |
| Multimode (Run3) | 5.956 | 11.0 ± 0.1 dB |

Table 5.2: Metrological gain with qubit based photon counting with multiple samples at different frequencies.

5.10 Mysterious Background Photons

With photon counting technique summarized in Table 5.2, we demonstrated detection of signal photons free of detector errors, leaving only background photons as the primary source of detector false positives. In order to further increase the sensitivity of the photon counter, we need to identify and mitigate the background sources.

One quick thing to check is the effective temperature of the observed background photon population and compare it to the physical temperature of the cavity. The observed photon population $\bar{n}_s = 6.23 \pm 0.30 \times 10^{-3}$ corresponds to a photon temperature of 56.38 ± 0.01 mK⁴, whereas the physical temperature of the base plate reads 8 mK, indicating the sample is coupled to extraneous baths.

There are various potential sources of cavity photons that constitute the measured background. I will summarize two possibilities here - direct absorption of photons and indirect excitation due to coupling to hot sub-systems. For detailed discussions, I would encourage the reader to refer^{42, 39}.

1. **Direction absorption of photons:** The measured effective temperature of the photons in the cavity is much greater than the operating temperature of the dilution refrigerator. This led us to believe that the radiation is somehow leaking and coupling to the cavity mode. It could be due the poorly thermalized cryogenic components, black-body radiation from higher temperature stages, back-propagation of amplifier noise or insufficient attenuation on the microwave lines.

While assembling the microwave lines in the fridge, I designed the breakout clamps such that there was no direct path for the radiation to reach the sample (light-tight) and ensured that all the microwave components were directly screwed to a copper plate for better thermalization. We also added a mixing chamber (MXC) radiation shield to

4. The observed background photon population is much higher than our previous work reported in²⁰ mainly due to the addition of a direction transmission line coupled to the storage cavity and we suspect radiation leaking via the port.

further isolate the sample from blackbody radiation as shown in the Fig. 5.11. These changes made noticeable difference in the qubit thermal population and the coherence times as summarized in Fig.

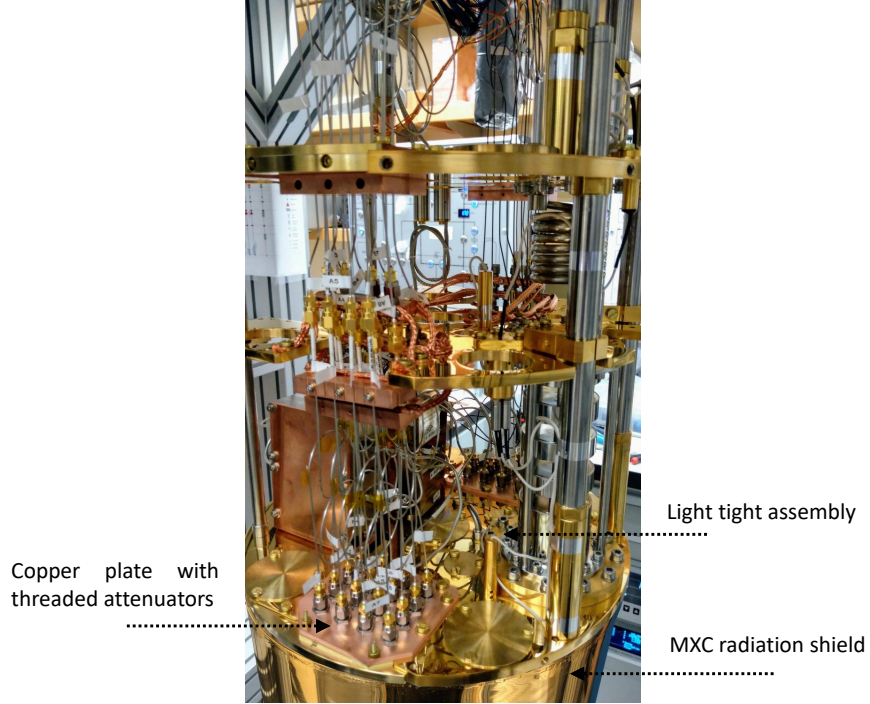


Figure 5.11: **Microwave lines assembly in a dilution refrigerator.** Signal carrying microwave lines with a combination of attenuators to shield the samples from room temperature radiation directly reaching the MXC stage. 60-80 dB of attenuation is added on the input line between 300K and 8mK stages to suppress any stray photons from leaking in. All the unused holes on the MXC plates are sealed with screws to ensure light tightness. The MXC shield prevents the blackbody radiation from higher temperature stages to impinge on the sample.

2. Quasi-particle induced photons: The coupling between the cavity mode and transmon results in hybridization of the states of the two systems. In the dispersive limit, the dressed eigenstates of qubit $|\tilde{e}\rangle$ and cavity $|\tilde{1}\rangle$ can be represented in terms of the bare eigenstates as

$$\begin{aligned} |\tilde{e}\rangle &= \sin(\theta) |g, 1\rangle + \cos(\theta) |e, 0\rangle \\ |\tilde{1}\rangle &= \cos(\theta) |g, 1\rangle - \sin(\theta) |e, 0\rangle \end{aligned} \tag{5.10}$$

where θ is the mixing angle between the two systems and is determined by their coupling strength g and the detuning Δ . Using Eq. 5.10 and trigonometric identities, we obtain $\tan 2\theta = \frac{2g}{\Delta}$ and the overlap $|\langle \tilde{1} | e, 0 \rangle|^2 = \sin^2 \theta = 7.68 \times 10^{-3}$. Qubit heating events from quasi-particle tunneling excites the qubit in its bare basis with a probability \bar{n}_q thus, a qubit excitation could manifest as a cavity photon with the probability $\bar{n}_s^q = \bar{n}_q \times \sin^2 \theta \leq 7.68 \times 10^{-5}$. This contribution is much smaller compared to the observed residual cavity occupation, ruling out this mechanism as the possible source.

5.11 Hidden Photon Search

Using the qubit based photon counting technique, we have demonstrated an unprecedented sensitivity towards background photons which can be applied to conduct a narrow-band hidden photon search. As mentioned earlier, this detector is ideally suited for a hidden search due to the absence of a large static magnetic field. We can exclude a previously unexplored region of the hidden photon parameter space and set sensitivity limits on the interaction between hidden photons with normal matter. In this section, I report the results from our publication²⁰, however, the analysis is exactly the same for a similar search with a different set of device parameters discussed earlier.

5.11.1 Search protocol with photon counting

In a traditional dark matter haloscope search experiment, the signal is always building up inside the microwave cavity. However, we cannot perform a continuous search with photon counting protocol as the process of repeatedly measuring the cavity state with a qubit Zeno suppress further buildup of the signal in the cavity⁸³. Thus, while the photon is counted, the dark matter signal does not accumulate, effecting the duty cycle of the experiment.

The cavity integrates the signal over its lifetime $T_1^s = 546 \mu\text{s}$ and the photon counting

consists of $N = 30$ repeated parity measurements each taking $t_m = 10\text{ }\mu\text{s}$, totaling $300\text{ }\mu\text{s}$. This corresponds to a duty cycle of $\frac{T_1^s}{T_1^s + N*t_m} = 65\%$. In this run, we collected 15,141 independent sequences for a total search time of 12.81 s of which 8.33 s is the signal integration.

5.11.2 Computing the expected signal rate

The dark matter wave on resonance with the cavity mode ($m_{DM} c^2 = \hbar\omega_c$) will coherently build up the electric field and deposit photons at a rate given by

$$\frac{dN_{HP}}{dt} = \frac{U/\omega_s}{T_{int}} = \frac{1}{2} \frac{E^2 V}{\omega_s} \frac{1}{T_{int}} \quad (5.11)$$

where U is the steady state stored energy and T_{int} is the integration time. In the photon counting case, we let the integration time equals one coherence time of the cavity, $T_{int} = T_1^s = \frac{\omega_s}{Q_s}$. The dark matter sources a space-filling current density which induces a electric field response in the cavity oscillating at the frequency equal to the dark matter mass. Through the Maxwell source equation we can relate the electric field and current density as

$$\begin{aligned} -\frac{\partial E(t)}{\partial t} &= J_{DM} \\ -\frac{\partial E_0 e^{imt}}{\partial t} &= J_{DM} \\ -mE(t) &= J_{DM} \\ E(t) &= -\frac{J_{DM}}{m} \end{aligned} \quad (5.12)$$

The dark matter wave coherently builds up signal inside the cavity which linearly increases with the integration time T_{int} until it reaches the coherence time of the dark matter wave T_1^{DM} (corresponding to $Q_{DM} = 10^6$). However, if the cavity coherence time is greater than T_1^{DM} , the storage cavity continues to accumulate the signal with a randomized phase every dark matter coherent time. This leads to $\frac{Q_s}{Q_{DM}}$ incoherent displacements within a single cavity lifetime resulting in a random walk of cavity displacements which is $\sqrt{\frac{Q_s}{Q_{DM}}}$ times

larger than a single dark matter wave induced displacement. The random walk enhancement motivates us to make the detection cavities with as high Q as possible.

For hidden photons, the current density J_{DM} is set by the mixing parameter ϵ , field amplitude A' and mass $m_{\gamma'}$. These are in turn related to the observed dark matter density ρ_{DM} if we assume all the dark matter in the universe comprises of hidden photons,

$$J_{HP}^2 = \epsilon^2 m_{\gamma'}^4 A'^2 = 2\epsilon^2 m_{\gamma'}^4 \rho_{DM} \quad (5.13)$$

where the observed dark mater density $\rho_{DM} = 0.4 \text{GeV/cm}^3 = 2\pi \times 9.67 \times 10^{23} \text{GHz/cm}^3$.

Another factor which sets the expected signal rate is called the geometric overlap factor between the cavity mode and the dark matter G . It is computed according to the expression written below,

$$G = \frac{1}{3} \frac{\left| \int dV E_z \right|^2}{V \int dV |E_z|^2} \quad (5.14)$$

For a simple rectangular (pill-box) or right cylindrical cavity design, we can analytically compute the expression based on the electric field profile ⁵ of the desired mode⁴². The geometric factor for a lowest order mode of the rectangular cavity turns out to be $\frac{2^6}{\pi^4}$ and 0.69 for a TM₀₁₀ type mode in the right cylindrical cavity. The polarization of the hidden photon dark matter \mathbf{u} is randomly oriented every dark matter coherence time and results in alignments with the electric field of the cavity only 1/3 of the time. Thus, the form factor $G = \frac{1}{3} \frac{2^6}{\pi^4}$.

Considering all these contributions, we can write down the final expression for the number of expected photon deposited in the storage cavity during the integration time $T_1^s = \frac{Q_s}{\omega_s}$

$$\begin{aligned} \frac{dN_{HP}}{dt} &= \frac{1}{2} \frac{(-J_{DM} \frac{Q_{DM}}{m})^2 V}{\omega_s} \frac{\omega_s}{Q_s} \frac{Q_s}{Q_{DM}} \\ \frac{dN_{HP}}{dt} &= \epsilon^2 \rho_{DM} Q_{DM} G V \end{aligned} \quad (5.15)$$

⁵. $\mathbf{E} = E_0 \sin(\frac{\pi x}{L}) \sin(\frac{\pi y}{w}) \mathbf{z}$ for a rectangular cavity and $\mathbf{E} = E_0 J_0(\frac{2.405}{R}) \mathbf{z}$ for a cylindrical cavity where $J_0(x)$ is the zero-order Bessel function.

The photon rate for a total number of $N_{meas} = 15000$ trials over an integration time of $T_s^1 \times N_{meas} = 20.4$ s yields the expected number of deposited photons given by,

$$N_{HP} = \frac{dN_{HP}}{dt} \times T_1^s \times N_{meas} = \epsilon^2 \rho_{DM} Q_{DM} G V \frac{Q_s}{\omega_s} N_{meas} \quad (5.16)$$

5.11.3 Calculating 90% confidence limit

| Expt. Parameter | Θ | σ_Θ |
|--------------------------|----------------------------|-----------------------------------|
| Quantum efficiency | $\eta = 0.409$ | $\sigma_\eta = 0.055$ |
| Storage cavity frequency | $\omega_s = 6.011$ GHz | $\sigma_{\omega_s} = 205$ Hz |
| Storage quality factor | $Q_s = 2.06 \times 10^7$ | $\sigma_{Q_s} = 8.69 \times 10^5$ |
| Storage cavity volume | $V = 11.8$ cm ³ | $\sigma_V = 0.2$ cm ³ |
| Storage form factor | $G = 0.22$ | $\sigma_G = 0.003$ |

Table 5.3: **Photon counting experimental parameters.** Systematic uncertainties of physical parameters in the experiment must be incorporated in determining the excluded hidden photon mixing angle ϵ . The uncertainty in the quantum efficiency is determined in the main text from fitting the relation between the measured and injected photon population at a detection threshold of $\lambda_{thresh} = 10^5$. The storage cavity frequency uncertainty is obtained by Ramsey interferometry. The quality factor of the cavity is given by $Q_s = \omega_s T_1^s$ so the uncertainty is calculated as $\sigma_{Q_s}^2 = (\omega_s \sigma_{T_1^s})^2 + (T_1^s \sigma_{\omega_s})^2$. The volume uncertainty is estimated by assuming machining tolerances of 0.005 inches in each dimension. The form a factor uncertainty is estimated from assuming 1% error in the simulated structure. Of the experimental quantities, the efficiency has largest fractional uncertainty (13%), though the statistical fluctuations of the observed counts still dominate (33%).

By counting single photons when the applied drive population less than the background population (\bar{n}_c) we perform a hidden photon search. We count $N = 9$ background photons in $N_{meas} = 15,141$ measurements. We determine the hidden photon mixing angle ϵ that can be excluded at the 90% confidence level by computing the probability that the signal could result in less than or equal to 9 photons measured ($N \leq 9$) with less than 10% probability. In each measurement a photon is counted or not so the signal is described by a binomial distribution with probability set by the expected number of deposited photons as calculated in Eqn. 5.16. The systematic uncertainties of the various experimentally determined quantities in Eqn. 5.16 are treated as nuisance parameters⁸⁴ with an assumed Gaussian distribution of

mean Θ and standard deviation σ_Θ as shown in Table 5.3. We marginalize over the nuisance parameters⁸⁵ and compute the cumulative probability shown in Eqn. 5.17.

$$P(\leq N) = \int_0^\infty \prod_i d\Theta'_i \frac{e^{-(\Theta_i - \Theta'_i)^2/2\sigma_{\Theta_i}^2}}{\sqrt{2\pi}\sigma_{\Theta_i}} \sum_{k=0}^N \frac{N_{\text{meas}}!}{k!(N_{\text{meas}} - k)!} \\ \times \left(\frac{\eta' \epsilon^2 \rho_{\text{DM}} Q_{\text{DM}} Q'_s G' V'}{\omega'_s} \right)^k \\ \times \left(1 - \frac{\eta' \epsilon^2 \rho_{\text{DM}} Q_{\text{DM}} Q'_s G' V'}{\omega'_s} \right)^{N_{\text{meas}} - k} \quad (5.17)$$

For a given hidden photon candidate, a cumulative probability of < 0.1 implies that candidate has less than 10% chance of producing the observed signal, thereby excluding such a candidate with 90% confidence. This leads us to exclude, with 90% confidence, hidden photon candidates with $\epsilon^{90\%} > 1.68 \times 10^{-15}$ as seen in Fig. 5.12

5.11.4 Hidden photon parameter space exclusion

Single photon counting with repeated parity measurements is sensitive to a wide range of candidates in the parameter space of hidden photon mass ($m_{\gamma'}$) and kinetic mixing angle (ϵ). To determine the sensitivity of the detector to a particular candidate, there are two considerations: the photon number dependent shift of the qubit transition as a function of the hidden photon mass, and the probability that a candidate would result in the measurement of a photon with probability larger than excluded. The photon population excluded as the 90% confidence level is computed using the excluded mixing angle $\epsilon^{90\%}$ and Eqn. 5.16 as $\bar{n}_{\text{HP}}^{90\%} = \frac{N_{\text{HP}}^{90\%}}{N_{\text{meas}}} = 2.42 \times 10^{-3}$.

The photon dependent shift of the qubit transition as a function of the frequency of an external drive is determined in Gambetta et. al.⁷⁷ to be $2\chi + \omega_c - \omega_{\gamma'}$ where $\hbar\omega_{\gamma'} = m_{\gamma'}c^2$. The efficiency of an individual parity measurement for a photon dependent shift that is incommensurate with the nominal shift 2χ is given by $\eta_{\text{parity}} = |\frac{1}{2}(e^{i\pi(2\chi+\omega_c-\omega_{\gamma'})/2\chi} - 1)|^2$ (Fig. 5.13). The effect of an inefficient parity measurement is modeled as a higher probability

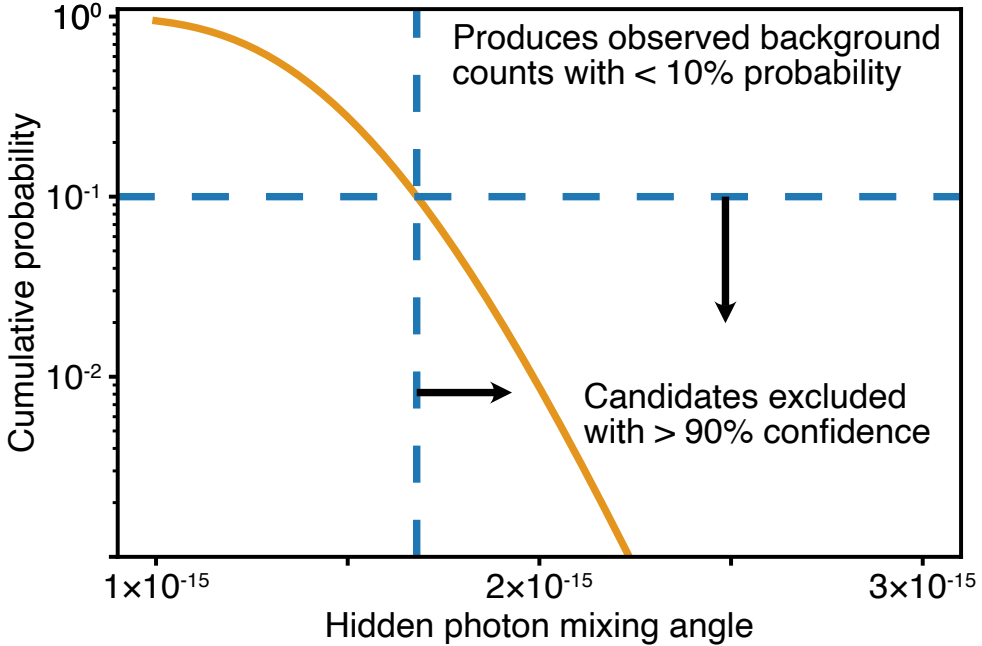


Figure 5.12: **Cumulative probability of hidden photon candidate producing observed signal.** Regions where the cumulative probability falls below 0.1 are ruled out as potential hidden photon candidates with 90% confidence. The minimum mixing angle that can be excluded with 90% confidence is 1.68×10^{-15} .

of qubit error in the hidden Markov model. The data is then reanalyzed and the efficiency of detection in the presence of the additional error is extracted (Fig. 5.13).

We note that for large detunings of the external drive, the shifted qubit transition frequency is out of the band of the resolved- π pulses used in the photon number measurement. The pulse shapes are Gaussian with $\sigma = 750$ ns. This constrains the maximum addressable dark matter detuning from the cavity. A hidden photon candidate that could result in more detector counts than background counts is only possible if the population of the odd number states of the cavity state (P_{odd}) induced by the hidden photon is larger than the excluded hidden photon probability ($\bar{n}_{\text{HP}}^{90\%}$). To calculate this P_{odd} we again follow Gambetta et. al.⁷⁷.

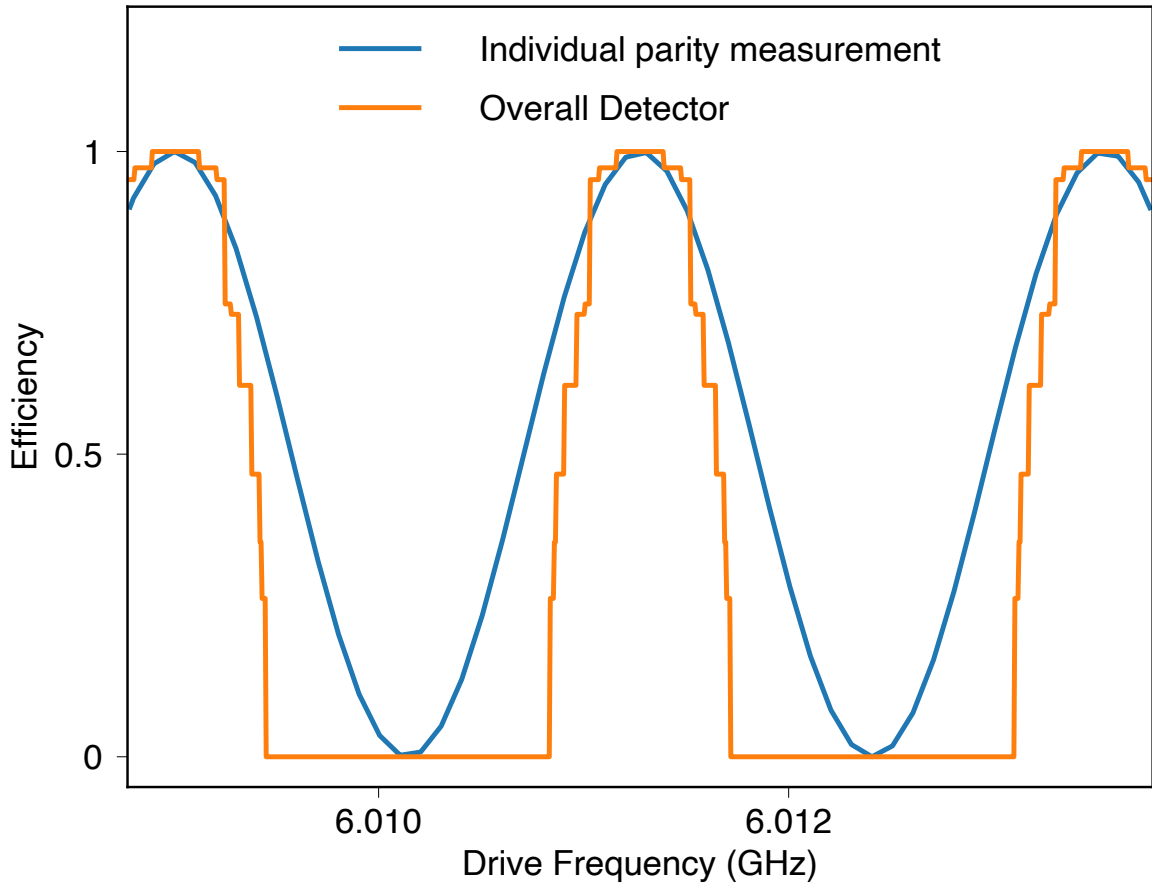


Figure 5.13: **Parity measurement and detector efficiency.** The efficiency of an individual parity measurement (blue) is sinusoidal in the frequency of the hidden photon induced drive $\omega_{\gamma'}$. The detector is a series of 30 repeated parity measurements and operates with an efficiency shown in orange.

$$P_{\text{odd}} = \frac{1}{\pi} \sum_{k=0}^{\infty} \text{Re} \left(\frac{\frac{1}{(2k+1)!} (-A)^{2k+1} e^A}{2(2\pi/T_2^{q,\text{echo}} + \Gamma_m) + (2k+1)2\pi/T_1^c} \right) \quad (5.18)$$

where $A = D \frac{\pi/T_1^c - i\chi - i(\omega_c - \omega_{\gamma'})}{\pi/T_1^c + i\chi + i(\omega_c - \omega_{\gamma'})}$ and $\Gamma_m = D \frac{\pi}{T_1^c}$ with the distinguishability $D = \frac{2(n_- + n_+)\chi^2}{(\pi/T_1^c)^2 + \chi^2 + (\omega_c - \omega_{\gamma'})^2}$. n_- and n_+ are related to the drive strength (n_{drive}) in units of photons: $n_{\pm} = \frac{n_{\text{drive}}(\pi/T_1^c)^2}{(\pi/T_1^c)^2 + (\omega_c - \omega_{\gamma'} \pm \chi)^2}$. At a given hidden photon mass, we calculate all n_{drive} such that $P_{\text{odd}} \geq \bar{n}_{\text{HP}}^{90\%}$.

We note that for external drives with large amplitudes, the shifted qubit transition frequency will be out of the band of the $\sigma = 6$ ns Gaussian $\pi/2$ pulses used in the parity

measurement. This constrains the maximum addressable dark matter induced photon occupation.

By combining the detector efficiency with the n_{drive} such that $P_{\text{odd}} \geq \bar{n}_{\text{HP}}^{90\%}$, we determine all n_{drive} to which the repeated parity measurements are sensitive enough to detect and exclude (Fig. 5.14). Using Eq. 5.16 we convert the excluded n_{drive} to a region of excluded hidden photon mixing angle (ϵ).

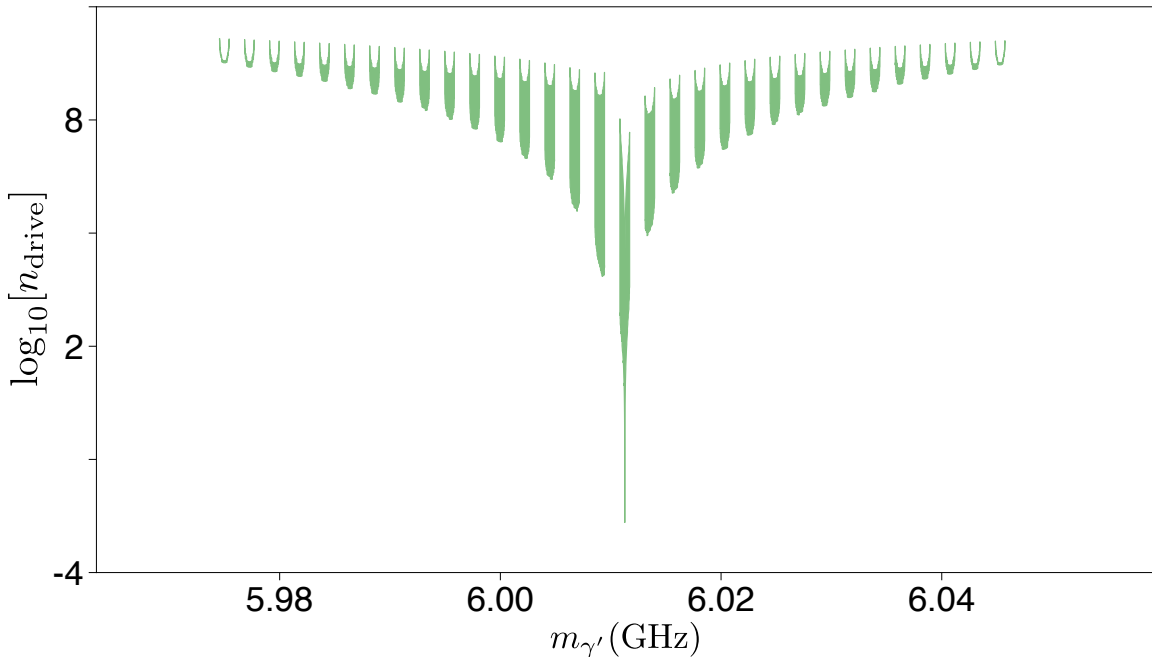


Figure 5.14: **Excluded n_{drive} as a function of $\omega_{\gamma'}$.** The shaded region indicates n_{drive} induced by the hidden photon that result in $P_{\text{odd}} \geq \bar{n}_{\text{HP}}^{90\%}$ that are detectable and are therefore excluded as possible candidates.

The above calculations assume an infinitely narrow dark matter line. To obtain the excluded region of the hidden photon kinetic mixing angle, we must account for the lineshape of the dark matter⁸⁶. We convolve the dark matter lineshape, characterized by $Q_{\text{DM}} \sim 10^6$, with the region shown in Fig. 5.14 to obtain the excluded ϵ shown in the main text.

We note that the storage cavity contains an infinite set of discrete resonances each with a unique coupling to the dark matter. We focus only on the lowest order mode that is

specifically designed to couple to the qubit. In principle, the interactions between any modes and the dark matter could result in additional sensitivity to the hidden photon. This would require the mode of interest to have a sufficiently large geometric form factor as well as a resolvable photon number dependent qubit shift. Future dark matter searches could employ structures with multiple resonances to enable multiple simultaneous searches³⁹.

5.12 Measurement optimization

Since we reported our first photon counter results, I have made significant improvements in optimizing our measurement and calibration protocols. In this section, I am going to discuss them in detail and describe their impact on the overall efficiency of the detector and duty cycle.

5.12.1 Josephson Parametric Amplifier

In order to dramatically increase our single-shot readout fidelity, I developed the JPAs in our lab under the guidance of Dr. Tanay Roy. We tried and tested a couple of different approaches to realize JPAs which would give a reasonable amount of gain (20 dB) and a near quantum limit efficiency. Our first approach was inspired by Tanay's PhD work⁸⁷ to build an impedance engineered parametric amplifier which would result in amplification over a large band-width. However, after a couple of iterations, we realized that the fabrication step involving the deposition of parallel plate capacitor wasn't reliable , resulting in unstable gain profiles.

So, we decided to try a simple JPA design⁸⁸ based on lumped circuit-QED elements. I discussed the operation of a JPA in sec. 3.8.1 and how we can bias it to achieve an optimal gain at the signal frequency. However, it is possible that one may have to tune the parameters a little bit and bias the JPA such that the qubit readout fidelity is maximized but at a lower gain. Following the procedure we achieved a single-shot qubit readout fidelity

of 97% approaching the decay limit as shown in Fig. 3.6. This improved our repeated QND measurement protocol in multiple ways:

1. **Lower readout time:** With a quantum-limited amplifier, we achieved a high fidelity readout with a 1 s readout pulse length compared to 3 s in²⁰. This resulted in a photon counting protocol which is 25% faster.
2. **Lesser number of photons:** More amplification implies improved SNR which means fewer number of photons in the readout collects the same amount of information about the state of the qubit. With the calibration tool I developed in Fig. 4.4, we expect 4× fewer photons in the readout and it reaches the steady state in a short period of time. On an average 2 photons in the readout resonator are sufficient to measure the state of qubit with 97% fidelity. This helped us reduce the wait time between two repeated measurements from 5 s to 1 s decreasing the idle time by further 40%.

5.12.2 Optimal readout shape pulse

Although the JPA reduces the effective number of photons in the readout, it takes a long time for the readout resonator to return to its ground state after the measurement pulse. The residual photons in the readout continue to measure the qubit preventing further high-fidelity operations for a period of 4 – 5 time constants.

For our repeated parity measurements, we would like the resonator to immediately reset to its ground state at the end of the measurement pulse. One experimental technique called Cavity Level Excitation and Reset (CLEAR)⁷⁸ pulse has demonstrated a cavity ring-down almost two times faster than the natural decay. I followed the measurement procedures described in the paper to characterize the readout parameters such as the decay constant, absolute number of photons etc.. I compared the performance of a constant amplitude pulse and an optimal shape readout pulse inspired by⁸⁹. The idea is simple, we could extract the maximum information out of the resonator if we could ring-up the resonator quickly (within

a cavity lifetime) with a pulse shape which matches the spectral features of the resonator itself and ring it down with a similar shape but with a negative amplitude. A typical pulse shape is shown in Fig.5.15 (inset) where we concatenate the optimal pulse by sandwiching a constant amplitude sequence between a ring-up and ring-down sequence. The amplitude of the constant part is kept similar for a fair comparison between the two.

For a fair comparison, we keep the amplitude of the constant part same and check that the readout fidelity is approximately the same.

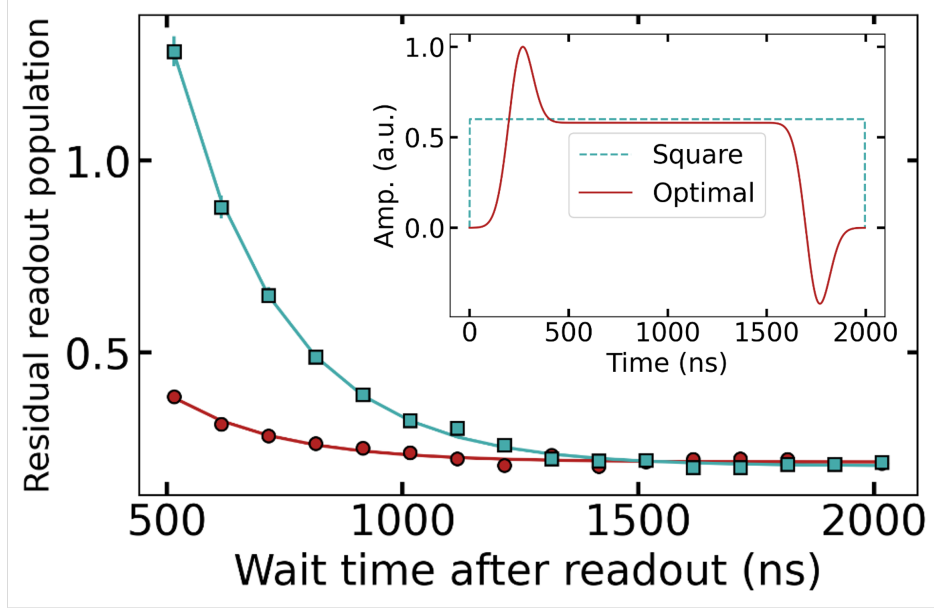


Figure 5.15: **Comparison of readout photon population with different pulse shapes.** [inset] A constant readout pulse (dashed), (solid) optimal readout pulse with a Gaussian rise and fall to quickly ring-up and ring-down the resonator. The duration of these segments are chosen to match the characteristic charging time of the oscillator. [main] Residual photon population in the readout resonator as a function of wait time. The resultant population is fitted to a exponential decay to estimate the initial population and compare the two pulse shapes.

5.12.3 Linear filter/optimal integration weights

In a typical digital down-conversion process, the incoming signal time trace is integrated with an equally-weighted distribution function. However, as shown in Fig. 5.16 we know that the photons leaking out of a resonator do not carry much information (signal) during

the ring-up and ring-down. In other words, we are integrating the time bins which contains more noise compared to the signal degrading the SNR.

There are a couple of methods which can be implemented to tackle this issue. Firstly, use a smaller integration window such that we only digitize the time trace after the resonator reaches its steady state and before it starts to decay (say between 500 – 2500ns). The drawback is that we are loosing useful information and may be a limiting factor for application which require fast readout such as error-correction protocols. Secondly, we could try to learn and optimize the integration weights such that we can maximize the separation between the $|g\rangle$ and $|e\rangle$ trajectories in the I-Q space. This method utilizes the entire time trace and thus, one build non-linear filters to shorten the readout time. We implemented a linear filter using conventional machine learning methods to learn and optimize the integration weights such that the resultant fidelity is maximum. It was implemented on the QM OPX hardware for which the example scripts may be found on their Git repository.

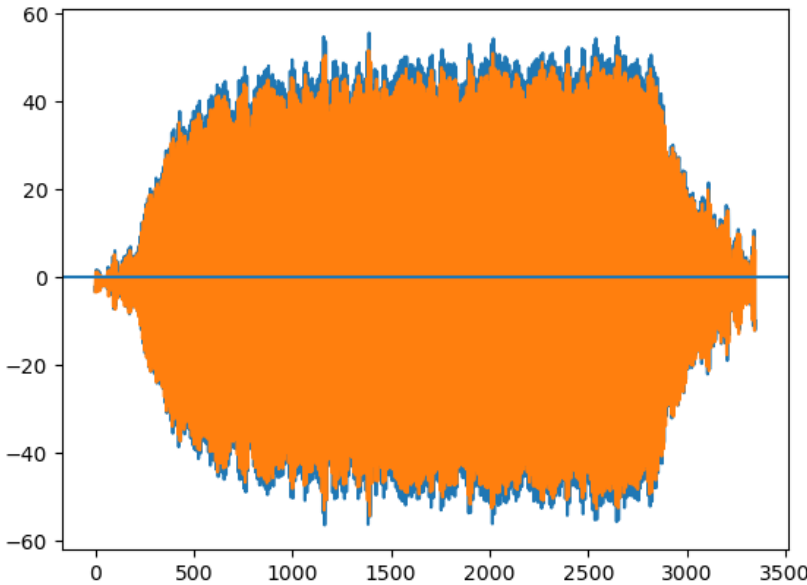


Figure 5.16: Temporal response of the readout cavity. Incoming readout signal at the ADC port showing the two quadrature before digitization. Cavity ring-up in the beginning, then it reaches a steady state followed by a ring-down in the end.

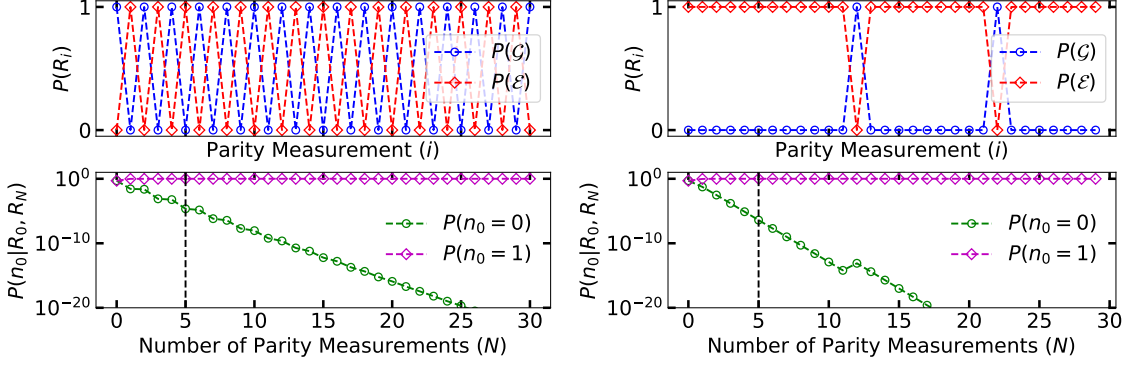


Figure 5.17: **Without and with active reset.** (T-L) Measured readout sequence for a photon in the cavity alternating between \mathcal{G} and \mathcal{E} without the active reset. (B-L) The reconstructed cavity state probability for 1 photon event. The dashed line is shown to compare the false positive probability for a given number of total parity measurements. (T-R) Measured readout sequence with active reset where we measure the qubit mostly in \mathcal{E} indicating a presence of the photon in the cavity. (B-R) shows the reconstructed cavity state probability which keeps going down exponentially. Y-axis limits are set to compare the likelihood ratio in both the cases. Need fewer number of parity measurements to reach a desired a false positive probability.

5.12.4 Active reset of the qubit

Another advantage of a high fidelity qubit readout is the ability to perform active reset. This speeds up all transmon measurements by a factor of $100\times$. Usually, we wait for at least $5 T_1^q \sim 500 \mu\text{s}$ in between two instances to initialize the qubit in the correct state. However, with active reset we can conditionally flip the qubit to a desired state and immediately start the next measurement.

We observe it's biggest impact in the photon counting technique where we reset the qubit from $|e\rangle$ to $|g\rangle$ in-between two repeated parity measurements as shown in Fig. 5.17. The qubit in $|e\rangle$ state has a higher probability to decay and change state ($1 - e^{-t_m/T_1^q}$) compared to a heating events changing the qubit state from $|g\rangle$ to $|e\rangle$ ($\bar{n}_q[1 - e^{-t_m/T_1^q}]$) resulting in fewer detector errors. It implies we need fewer repeated parity measurements to reach the same likelihood ratio, improving the duty cycle of the experiment even further. This does add one additional calibration step and an error probability term in the transition matrix associated with the reset efficiency.

5.13 Summary

In this work, we demonstrated a novel photon counting technique using superconducting qubits with background errors 15.7dB below the SQL. With the measured background, we set a new exclusion limit in the hidden plot frequency point with an unprecedented sensitivity. In addition to this work, I was able to bring down the repeated parity measurement time from 10 μ s to 2.5 μ s with optimized readout hardware and protocols. This factor of 4 speed up is pretty significant for a full-fledged axion search as the cavity coherence times are much shorter and allows us to make enough repeated parity measurements to suppress the detector based false positive probability beyond the SQL.

Chapter 6

Enhancement of weak signal with stimulated emission

In the previous chapter, we discussed how a qubit coupled to a cavity acts as a single photon counter with sensitivity far beyond the reach of conventional detector technologies using quantum limited amplifiers. This chapter focuses on another aspect of the dispersive coupling which allows us to prepare non-classical states in the cavity. I will discuss the physics behind the stimulated emission technique and how we can boost the signal rate to make the dark matter (DM) searches go faster. I will demonstrate how we can initialize the cavity in a Fock state utilizing the non-linearity inherited from the transmon. In the later half, I will present the results demonstrating the enhancement as we go to higher Fock states. Lastly, I will discuss how we conduct a hidden photon search with the measured background events.

6.1 Signal Enhancement with Stimulated Emission

In a conventional dark matter experiment (axion or hidden photon), the signal arises from the spontaneous emission of photons into initially unpopulated (vacuum) cavity mode from the background dark matter wave. As we go to higher frequency searches, the volume of the detector shrinks ($V \propto \lambda^3$) causing the signal rate to drop too low to achieve a desired SNR in a reasonable amount of integration time. One way to boost the signal rate is to prepare the cavity field with large amplitude sine wave which allows the cavity to receive power more easily as given by

$$P_s = \int dV \mathbf{J}_{DM}(x) \cdot \mathbf{E}(x) \quad (6.1)$$

It is analogous to pushing a child on the swing. If the swing is already in motion then it is

easier to transfer/extract power compared to when it's at rest. One needs to provide the push at the correct time (or phase) to transfer energy and keep the swing in motion. However, the dark matter wave arrives at the cavity with an unknown phase which makes it impossible to always match the phase of the cavity field for optimal power transfer. If the correct phase is serendipitously chosen, then the signal rate can be enhanced by a large amount. If the incorrect phase is chosen, then the direction of power flow reverses and the dark matter wave extracts power from the cavity field. It should be noted that even if a correct phase is chosen, one has to deal with the increased Poisson noise from the Glauber coherent state of the cavity wave. This shot noise is a manifestation of the zero-point fluctuation (ZPF) noise of the vacuum limiting our resolution to single photon (SQL) when attempting to detect an increase of the coherent state amplitude (haziness around the blob) as shown in Fig. 6.1.

Instead, we can prepare the cavity in a Fock state with large, but definite occupation number N_{Fock} to enhance the signal rate. The Fock state has no definite phase associated with it (see Fig. 6.1), which makes it equally sensitive to any instantaneous phase of the incoming DM wave. Being a state of definite photon number, the Poisson noise also vanishes. We can model the action of the DM wave on a Fock state as a classical drive which shifts this phase-symmetric state away from the origin in the Wigner phase space. The resultant state comprises both in-phase components which extracted excess power from the DM wave and also out-of-phase components which delivered their power to the DM wave. The stimulated emission process for DM converting into photons is enhanced by a factor of $N_{Fock} + 1$ while the stimulated absorption process is enhanced by a factor of N_{Fock} . From now on-wards, I will discuss the rest of the chapter for an axion like dark matter particle, however, the formalism is equivalent for hidden photons as well.

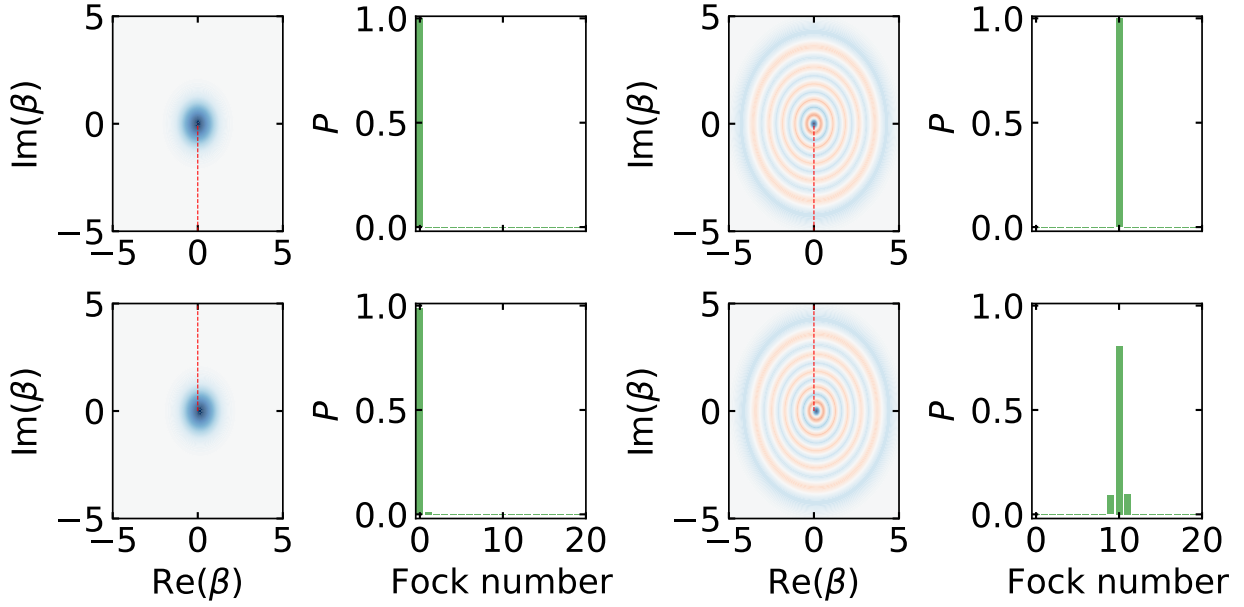


Figure 6.1: Phase-space representation of the cavity state before and after the dark matter wave push. (Left plots) Displacing the cavity initialized in $|0\rangle$ in an arbitrary direction by a small coherent push $\beta_{coh} \ll 1$ results in a small probability $P_{0,1} \propto |\mathcal{M}_{0,1}|^2$ for creating a $|1\rangle$ component by spontaneous emission of a photon from the DM wave. The direction of displacement is determined by the instantaneous phase of the DM wave which is randomized every DM coherence time, but since the initial cavity state is azimuthally symmetric, a displacement in any direction gives the same probability $P_{0,1}$. The red dashed line is shown as a guide to locate the origin w.r.t to the center of the blob. (Right plots) The cavity is initialized in a $|n\rangle = 10$ Fock state which also has an azimuthally symmetric Wigner distribution. Displacing this distribution in an arbitrary direction shifts some part of the distribution to larger radius and other parts to smaller radius. For example, the lower plots shows a displacement of $\beta_{coh} = 0.1$ in the positive $X = Re(\beta)$ direction. The shift to larger radius corresponds to stimulated emission to states with larger photon number, for example $|11\rangle$ while the shift to smaller radius corresponds to stimulated absorption to states with smaller photon number, for example $|9\rangle$. As shown in the histograms, the stimulated enhancement factors ($N_{Fock}+1$) and N_{Fock} give probabilities which satisfy $P_{10,11} = 11 \times P_{0,1}$ and $P_{10,9} = 10 \times P_{0,1}$.

6.1.1 Treating dark matter wave as a classical drive

From the dark matter density we can infer that the dark matter wave has classical occupation number ¹ and thus, can be considered as a classical wave $\theta = \theta_0 \exp(m_{DM}t + \phi_0)$ which drives the cavity mode, similar to what we discussed earlier in section 3.7. ϕ_0 is the

1. The number of dark matter particles contained in a volume of 1cm^3 is roughly given by $\frac{\rho_{DM}V}{m_{DM}} \sim \frac{2\pi \times 9.67 \times 10^{13} \text{GHz}}{6\text{GHz}} \sim 10^{14}$

instantaneous phase of the axion wave and it drifts in value by one radian over the coherence time Q_{DM}/m_{DM} . On time scales shorter than the coherence time, the axion wave can be described as a coherent state and the interaction Hamiltonian integrated over the cavity volume V is given by

$$\mathcal{H}_{int} = g(\vec{B}_0 \cdot \vec{E})\theta V = g\theta(t)B_0\sqrt{Vm_a}(\hat{a}\hat{b}^\dagger + \hat{a}^\dagger\hat{b}) \quad (6.2)$$

where \hat{a} and \hat{b} corresponds to the annihilation operator for cavity and axion field respectively. The action of the axion wave can be modeled as a displacement operator $\hat{\mathcal{D}}(\beta) \equiv e^{\beta^* \hat{a} - \beta \hat{a}^\dagger}$ acting on the cavity state, traditionally prepared in the vacuum state $|N\rangle = 0$. Generally, we look for an spontaneous emission from the axion wave into the cavity mode and strive to measure the operator

$$|\langle N+1 | \hat{\mathcal{D}}(\beta) | N \rangle|^2 \quad (6.3)$$

for $\beta \ll 1$. However, if the cavity is initialized in a large N Fock state, then there will be a large enhancement of this process. In other words, the probability of finding the cavity in $N+1$ Fock state is significantly higher. Using the physics learnt in our quantum mechanics course and a few manipulations, we can prove a few relations to mathematically prove this

$$\begin{aligned} \hat{\mathcal{D}}^\dagger(\beta) \hat{a} \hat{\mathcal{D}}(\beta) &= \hat{a} + \beta \\ \hat{\mathcal{D}}(\beta) |0\rangle &= e^{|\beta|^2/2} e^{\beta^* \hat{a}} e^{\beta \hat{a}^\dagger} \approx (1 + \beta \hat{a}^\dagger) |0\rangle \\ \langle N+1 | \hat{\mathcal{D}}(\beta) | N \rangle &\approx \beta \sqrt{N+1} \end{aligned} \quad (6.4)$$

For a coherence time-limited amplitude transfer and setting $\beta = \beta_{coh}$, the occupation probability of the cavity in $|N+1\rangle$ Fock state grows as

$$|\langle N+1 | \hat{\mathcal{D}}(\beta_{coh}) | N \rangle|^2 = |\beta_{coh}|^2 (N+1) \quad (6.5)$$

Eq. 6.5 tells us that the rate of observing $|N + 1\rangle$ is enhanced by a factor of $N + 1$ relative to the usual spontaneous emission scenario in which the cavity is prepared in the vacuum state with $|N\rangle = 0$. For example, in the single photon counting technique described earlier, the signal would be occasional observance of $|1\rangle$ in the final state and the relative measured probabilities of $|1\rangle$ and $|0\rangle$ would determine the coupling g . Compared to that, cavity initialized in $N > 0$ provides information on g , but with an enhanced signal rate of observing the final state in $|N + 1\rangle$ as depicted in Fig. 6.1.

Now, if only we had a photon counting detector which could distinguish between $|N + 1\rangle$ and $|N\rangle$ Fock states, we would benefit from this technique. But wait, we did discuss such a protocol in Fig. 3.2 where a transmon dispersively coupled to a cavity when probed with a narrow bandwidth pulse resolves the individual Fock states in the cavity. With a number resolved detector and stimulated emission technique, we could drastically enhance the signal rate to a level detectable above the minimum signal shot-noise limited rate and in particular enable search at frequencies above 10 GHz. So, how do we prepare non-classical states in the cavity?

6.2 Preparing Non-classical States in the Cavity

In section 3.7, I discussed how the transmon provides an unique tool set to prepare any quantum state in the cavity. For this experiment, I used a 3D Multimode cavity³⁹ as shown in Fig. 6.2 (a). It consists of a long cavity volume which supports multiple modes in the cavity dispersively coupled to the same transmon qubit. The state of the qubit is readout using a 3D readout cavity. I used the methods previously discussed to prepare Fock states in the cavity namely, SNAP gates and GRAPE generated optimal control pulses. Both the methods utilize the non-linearity imparted by the qubit to perform conditional gates or, state transfer to evolve the qubit-cavity system from $|g, 0\rangle \rightarrow |g, n\rangle$. As discussed earlier, the SNAP method suffers from two issues limiting the maximum achievable fidelity. First, the number of constructed sequences scales as $(2n + 1)$, requiring large number of gates, limiting

operations which are feasible in the presence of decoherence. Second, the constructed model fails to account for the higher order Kerr non-linearity ($\mathcal{H}_{Kerr}/\hbar = K(a^\dagger)^2(a)^2$) in the Hamiltonian, which is non-negligible at higher photon occupation.

For this particular experiment, I pursued the GRAPE method to generate OCT pulses which achieve maximum fidelity. In Fig. 6.2, I demonstrate the creation of Fock states in the cavity up to $|n\rangle = 4$. In principle, we could prepare even higher Fock states, however, at some point due to the enhanced decay of the photon in the Fock states, the photon losses will be comparable to the qubit decay and the two error sources become indistinguishable. The enhancement of decay rate^{90,91} is the consequence of spontaneous enhancement of the emission due to the same enhancement factor which enhances the signal and we can quickly check that by applying annihilation operator on the number state ²

$$\hat{a} |n\rangle = \sqrt{n} |n-1\rangle \quad (6.6)$$

where, the probability of photon loss in the Fock state is enhanced by a factor n .

Estimating the state preparation fidelity

We need a metric to experimentally test the performance of these OCT pulse, such that we can iterate over a small set of parameter space to optimize the performance even further. The fastest and most convenient metric to quantify the fidelity is the qubit spectroscopy with a number selective π -pulse. As I mentioned earlier, Fock states have no definite phase associated with them. Thus, a qubit spectroscopy reveals all the information about the probability distribution of the cavity state. Once we have a set of pulses that satisfies the fidelity criterion, we perform Wigner tomography of the cavity state and demonstrate the key signature of Fock states - concentric rings in the phase space as shown in Fig. 6.2 (b).

2. This is just an intuitive reasoning and not a complete analytic derivation. One must solve the master equation in the presence of dissipation to obtain the complete expression. I would like to clarify that the lifetime of the cavity in a particular Fock state changes but the photon lifetime in the cavity is unaltered.

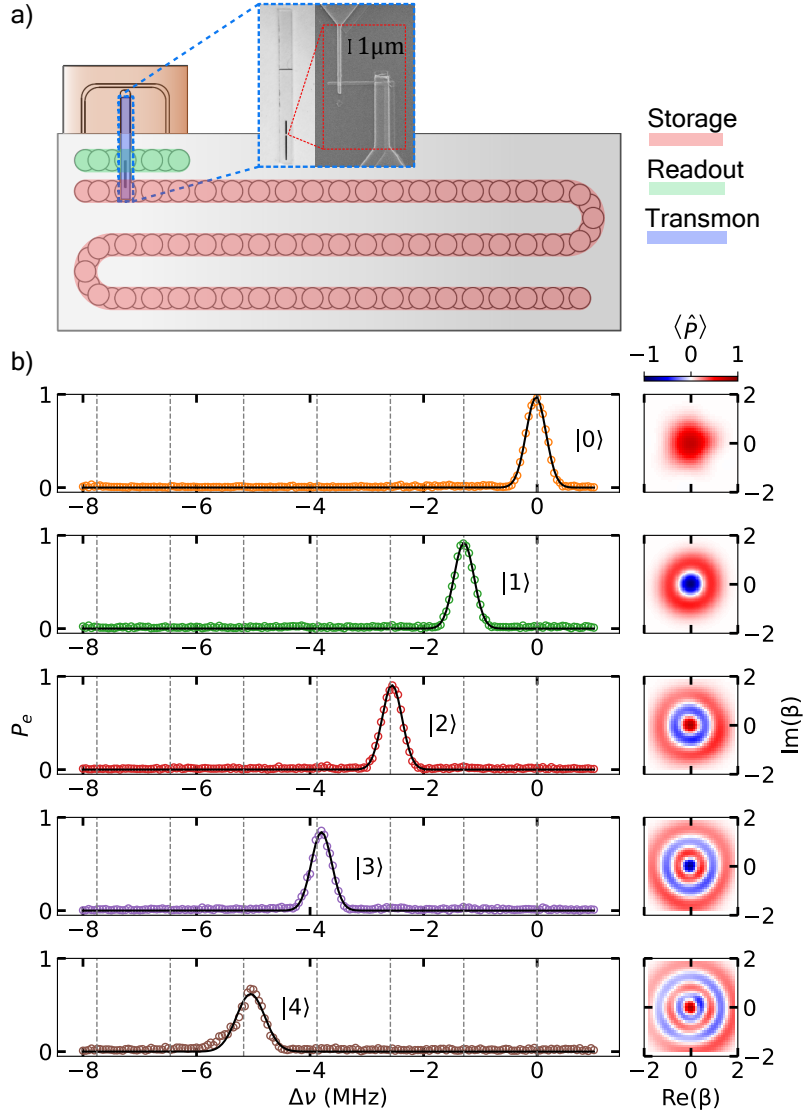


Figure 6.2: Creation of Fock states in the cavity using GRAPE method. (a) A schematic of the multimode flute cavity showing the location of the storage cavity (red), readout cavity (green), and transmon chip with a SEM image of the Josephson junction (blue)³⁹. (b) Characterization of the cavity state using qubit spectroscopy (left) and Wigner tomography (right). Qubit spectroscopy is performed immediately after the OCT pulses, single peak in each probability distribution confirms the creation of correct $|n\rangle$ Fock state. Resultant probability distribution is fitted to a Gaussian to determine the state preparation fidelity. Grey dashed lines correspond to shift in frequency without the correction term. However, the deviation of peak position at higher photon numbers implies the higher order correction is non-negligible. (Right) Wigner tomography is performed by coherently displacing the resultant cavity state in the 2D phase space to map the average parity and thus, reconstruct the cavity state density matrix using Eq. 3.15.

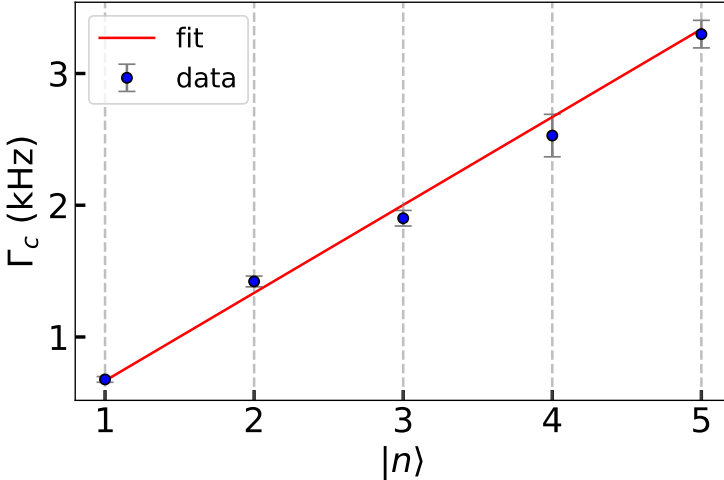


Figure 6.3: **Decay rate of Fock states.** Measured lifetime of the different Fock states prepared in the cavity using OCT pulses. The decay rate is inversely proportional to the lifetime ($\Gamma = 1/T_1$). The curve shows enhancement in the decay rate as a function of the Fock state $|n\rangle$. The linear fit to the data fits well as predicted by⁹⁰, where $T_1^n = T_1/n$.

This verifies our claim that the OCT pulses indeed create the intended Fock states.

While estimating the fidelity, we must account for the error in signal due to qubit decay and readout. One way would be to offset the fitted peak values with the peak value obtained for $|n\rangle = 0$ case. In the case of Wigner tomography, we would modify the parity sequence by flipping the qubit to $|e\rangle$ state before the parity sequence to nullify the error due to qubit heating and decay and collect two measurements to analyze the averaged data.

6.3 Stimulated emission protocol

The stimulated emission protocol is divided into two parts: first part involves the preparation of cavity in a desired Fock state, $|n\rangle$ and the second part involves the detection of cavity in the $|n + 1\rangle$ Fock state. In addition to the Fock state preparation in the first half, we also actively minimize the false positive events, cavity accidentally starting in $|n + 1\rangle$ state. We do so by conditionally flipping the qubit state three times with π -pulses centered at the $(n + 1)$ -shifted peak. If and only if the measurement outcome is a set of $[\mathcal{G}, \mathcal{G}, \mathcal{G}]$ do we proceed ahead with the rest of the protocol. By doing this, we can suppress the false positive

rate below 3%.

At the end of the first part, in a separate experiment we measure the efficiency of the state preparation by measuring the qubit excitation probability with a number resolved π -pulse centered at the $|n\rangle$ peak. The measured fidelities are $P_0 = 95.2 \pm 0.3\%$, $P_1 = 91.2 \pm 0.4\%$, $P_2 = 87.3 \pm 0.5\%$, $P_3 = 81.6 \pm 0.6\%$, $P_4 = 63.6 \pm 0.7\%$. For comparison, a coherent state with mean photon number $\bar{n} = 3$ and post-selection would only result in $P_3 = 22.4\%$. Hence, OCT pulses is an optimal way to prepare Fock state and keep the false positives low.

After the state preparation, we apply a coherent drive to the cavity mimicking a dark matter push to characterize the detector. A series of repeated QND measurements are recorded by performing conditional π -pulses centered at the $(n+1)$ -shifted peak. We then apply the hidden Markov model (HMM) analysis to reconstruct the cavity state probability immediately after applying the coherent drive. The schematic of the experimental protocol is depicted in Fig. 6.4. After a few trial and error, I decided upon the current protocol which is predominantly focused on keeping the false positive errors low.

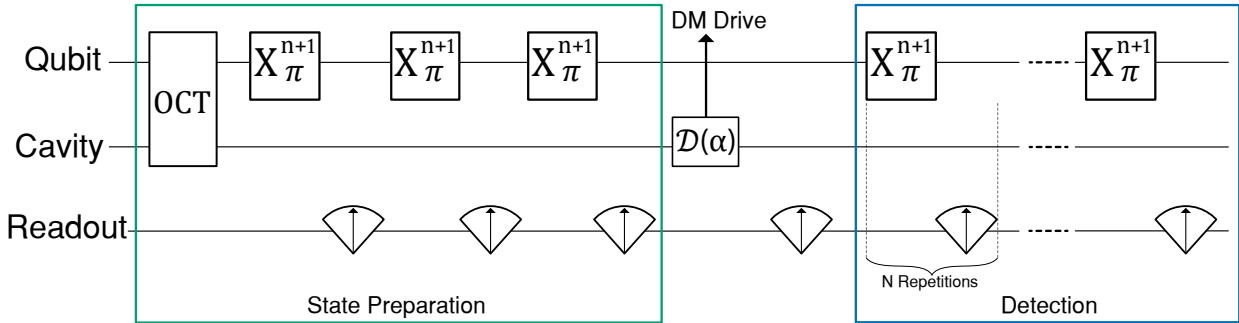


Figure 6.4: **Stimulated emission protocol.** Schematic of the experimental sequence divided into two. The first part involves the Fock state preparation and false positive reduction with conditional π -pulses. If the outcome is positive, the experiment proceeds to the next step, where a coherent displacement on the cavity state mimics a dark matter push. This is followed by a series of 30 repeated measurements with conditional π -pulses centered at $(n+1)$ peak to detect the change in cavity state from $|n\rangle \rightarrow |n+1\rangle$.

Minimizing the false positive probability

One of the most challenging task in designing this experiment is to suppress the false positive probability while keeping the original Fock state intact. In the photon counting experiment, it meant accidentally measuring the cavity in $|1\rangle$ state due to spurious errors. In the stimulated emission case, it would mean the cavity initialized in $|n+1\rangle$ Fock state instead of $|n\rangle$. In order to successfully implement this experiment we desire - high state preparation fidelity with very low false positive probability. Using OCT pulses helps us achieve reasonable Fock state preparation fidelity³, allowing us to develop the other parts of the experiment. Also, we learnt in the previous chapter that detector based errors can be exponentially suppressed by performing repeated QND measurements of the cavity state. Unfortunately, with a single resolved π -pulse centered at n^{th} Fock state, we can only extract one bit of information, either the cavity is in $|n\rangle$ Fock state or not. Thus, we have a choice to make at this point - (1) either perform repeated measurement at $|n\rangle$ to gain more confidence that the cavity initialized in the correct state or, (2) repeatedly probe the $|n+1\rangle$ to suppress any false positive events with a high likelihood ratio.

In the early stage, I focused on probing the target state $|n\rangle$ in the cavity to ensure that the cavity was in the correct state before we proceeded with the rest of the protocol. I performed 10 repeated QND measurements with π -pulses centered at $|n\rangle$ peak and HMM analysis to reconstruct the cavity state probabilities at the end of the first part. The events qualified for detection were post-selected based on the likelihood ratio. This approach didn't work as expected because of the following reasons -

- 10 repeated measurements incurred long wait time for the higher Fock state prone to enhanced decay rates
- Over counting the qualified events where the cavity may not be in the correct Fock state at the end but HMM cannot distinguish it as it takes into account all the previous

3. I will discuss the possible cause of lower fidelity for $|4\rangle$ in a later section.

measurements to assign a likelihood ratio

One year later, we realized it may not be the best approach and decided to follow the second approach where we perform a few conditional checks in real time to ensure that the cavity state didn't jump to $|n + 1\rangle$ and proceed only if the checks are true. During this time, I tested and added new hardware capabilities to perform real time computation needed for such conditional checks. This allowed me to pursue the final stimulated emission protocol and test any other conditional checks if and when required. For example, if we do 4 checks instead of 3 then, we can reduce the false positive probability below 0.1%.

6.3.1 HMM for stimulated emission

We started with the HMM analysis developed for photon counting experiment and modified it to accommodate higher excited states of the cavity. However, given the nature of the readout measurement, we can only answer if the cavity is in a particular Fock state $|n\rangle$ or not $|n'\rangle$ and hence, restrict the cavity state to only change from $|n\rangle$ to either $|n - 1\rangle$ or $|n + 1\rangle$. This assumption is reasonable as the probability to change the photon number by greater than ± 1 is negligible.

The transition matrix which captures the possible changes in qubit and cavity state is different from the photon counting case. Although, the qubit transition probabilities stay the same, the cavity state may change from $|n\rangle \rightarrow |n'\rangle$ via either decay ($|n\rangle \rightarrow |n - 1\rangle$) or excitation ($|n\rangle \rightarrow |n + 1\rangle$) with probabilities $P_{n,n-1} = 1 - e^{-t_m/T_1^n}$ or $P_{n,n+1} = \bar{n}_c[1 - e^{-t_m/T_1^n}]$ respectively. I measured the effect of cavity occupation on the qubit coherence properties and did not see any noticeable change. The lifetime of the cavity is modified due to the enhanced decay of a Fock state ($T_1^n = T_1^s/n$) as compared to the bare lifetime of a coherent state and we account for that in the transition probabilities. In most cases, we assume the interaction between the qubit and cavity to be QND, i.e., the measurement of cavity state by qubit does not perturb the state. However, we have measured the QNDness of this measurement itself (see Fig. 3.20). The measured demolition probability p_D for $|1\rangle$

is 2.6% per measurement. This acts like an additional source of loss to the cavity mode but only when the resolved π -pulse is on resonance with the shifted qubit frequency. Hence, we add this term in the transition matrix. We measured the demolition probability associated with each Fock state as tabulated in Tab. 3.1. To be consistent with the formalism developed for photon counting analysis, the qubit will flip only when π -pulsed at the n -peak and the cavity is in $|n\rangle$.

$$T = \begin{bmatrix} |n'g\rangle & |n'e\rangle & |ng\rangle & |ne\rangle \\ P_{n'n'}P_{gg} & P_{n'n'}P_{ge} & P_{n'n}P_{ge} & P_{n'n}P_{gg} \\ P_{n'n'}P_{eg} & P_{n'n'}P_{ee} & P_{n'n}P_{eg} & P_{n'n}P_{ee} \\ P_{nn'}P_{gg} & P_{nn'}P_{ge} & P_{nn}P_{ge} & P_{nn}P_{gg} \\ P_{nn'}P_{eg} & P_{nn'}P_{ee} & P_{nn}P_{ee} & P_{nn}P_{eg} \end{bmatrix} \begin{matrix} |n'g\rangle \\ |n'e\rangle \\ |ng\rangle \\ |ne\rangle \end{matrix} \quad (6.7)$$

6.3.2 Examples of the HMM in action

We can check the effectiveness of the modified HMM analysis by looking at two example measurement sequences which cross the initial conditional checks after initializing the cavity in $|n\rangle = 1$ Fock state and detecting the cavity state in $|n\rangle = 2$ after the coherent displacement with repeated π -pulses.

No stimulated emission

An example readout sequence is shown in Fig. 6.5, in the case where we do not apply a coherent displacement drive to the cavity state prepared in $|n\rangle = 1$ Fock state. HMM analysis on the observed readout sequence gives reconstructed cavity state probability to be in $|n\rangle = 2$ close to zero.

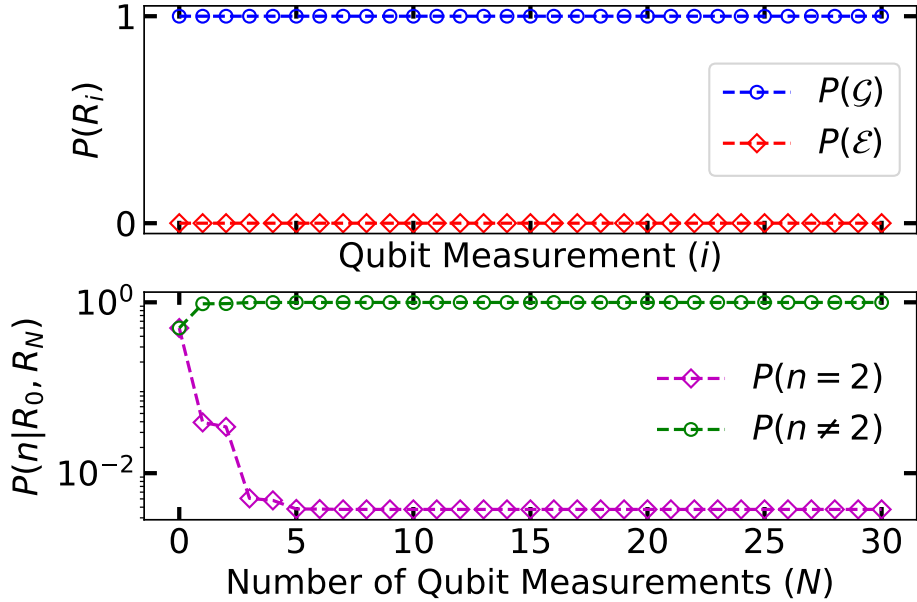


Figure 6.5: No stimulated emission. (Top) Observed readout sequence of repeated qubit measurements with number resolved π -pulses centered at $(n+1)$ peak. (Bottom) Reconstructed cavity state probability to observe the cavity change its state from $|1\rangle \rightarrow |2\rangle$. Clearly, the probability to find the cavity in $|2\rangle$ is low as expected from the readout sequence.

Stimulated emission

On the other hand, when we do apply a coherent displacement on the cavity state prepared in $|n\rangle = 1$ Fock state the observed readout sequence flips back and forth between \mathcal{G} and \mathcal{E} indicating the cavity in $|n\rangle = 2$ Fock state. Reconstructed cavity state probability confirms the stimulated emission with a very high likelihood ratio.

6.3.3 Signature of enhancement with Fock states

In order to characterize the detector after preparing the cavity in a certain Fock state $|n\rangle$, we apply a variable displacement ($\alpha \ll 1$) drive to the cavity and map out the relationship between the injected ($n_{inj} = |\alpha|^2$) and measured photons, performing 30 repeated qubit measurement and applying $\lambda_{thresh} = 10^3$ to discriminate between positive and negative events. This value is informed from the residual cavity occupation $n_{th}^c = 6 \times 10^{-3}$ measured

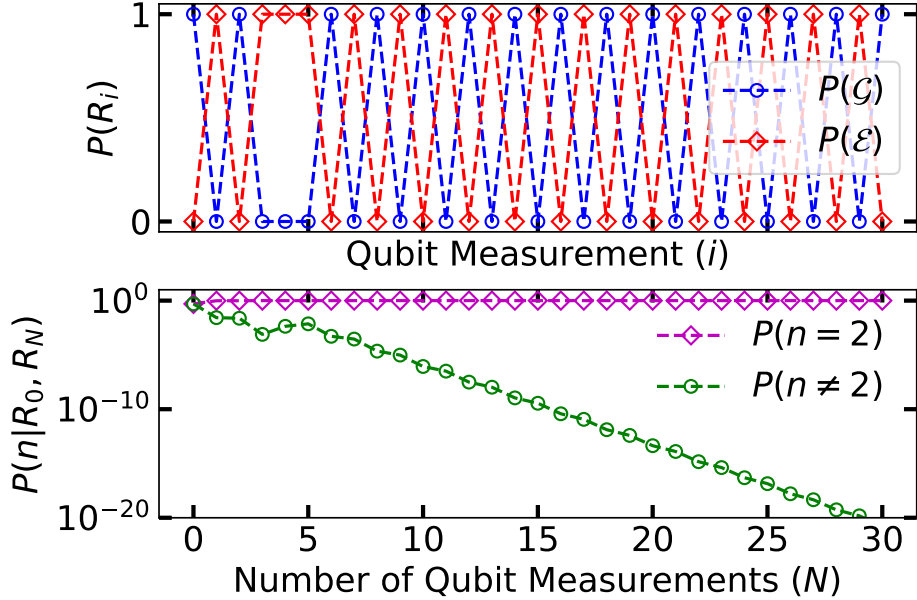


Figure 6.6: **Stimulated emission.** (Top) Observed readout sequence of repeated qubit measurements with number resolved π -pulses centered at $(n+1)$ peak. Successful qubit flip-flop implies the cavity did change its state to go higher Fock state. (Bottom) From reconstructed cavity state probability we can check that the cavity did change its state from $|1\rangle \rightarrow |2\rangle$ with a very high likelihood ratio. The false positive error probability falls off exponentially with the number of measurements included in the analysis and is robust against the presence of a few spurious readout errors.

following the photon counting method described in²⁰(see Fig. 5.8). Detector errors below this value are sub-dominant. For a cavity initialized in $|n\rangle$, the probability of finding the cavity in a Fock state $|l\rangle$ for a complex displacement α is given by the analytical expression⁹²: $P_{nl}(|\alpha|^2) = |\langle l| \hat{D}(\alpha) |n\rangle|^2 = (n! / l!) \alpha^{2(l-n)} e^{-|\alpha|^2} \times \mathcal{L}_n^{l-n}(|\alpha|^2)$ where \mathcal{L}_n^{l-n} is an associated Laguerre polynomial. The resultant data is fit to equation below,

$$n_{meas} = \eta P_{nl}(|\alpha|^2 = n_{inj}) + \delta \quad (6.8)$$

where η is the detection efficiency and δ is false positive probability.

Fig. 6.7 shows the distinct feature of stimulated emission enhancement as we expected, higher number of measured photons for the cavity initialized in higher Fock state. This clearly demonstrates the success of stimulated emission as an enhancement technique for

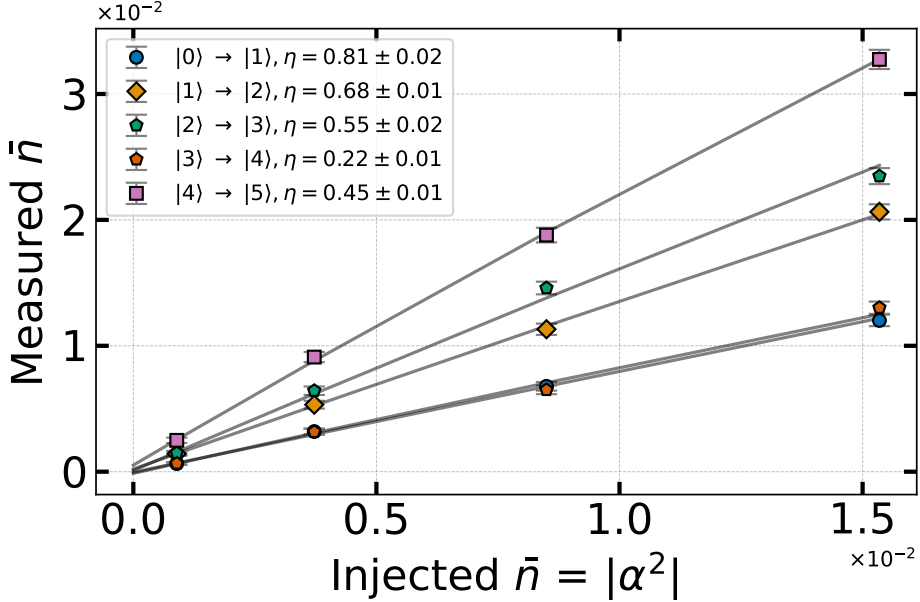


Figure 6.7: **Signature of enhancement.** After initializing the cavity in a Fock state $|n\rangle$, a variable cavity displacement (mock dark matter push), 30 repeated qubit measurements of cavity photon state are performed and a threshold λ_{thresh} is applied to determine the cavity population at $|n+1\rangle$ Fock state. Background events with $\alpha = 0$ are subtracted to compare between different Fock states. $\lambda_{\text{thresh}} = 10^3$ is chosen based on the observed cavity occupation of ($n_{th}^c = 6 \times 10^{-3}$) such that the detector based errors are still sub-dominant. Detector efficiency for each Fock state is determined from the fit and reported in the legend. The monotonic decrease in the efficiency is attributed to - higher decay probability to reach the same false positive probability and demolition probability of the cavity state due to repeated measurements (p_d increase from 0.026 to 0.044). Anomalous behavior in $|3\rangle$ is attributed to the state decaying to nearby modes which are close in the energy level $|q, s, r\rangle$.

weak signals. The detection efficiencies from the fits are mentioned in the plot and the false positive probabilities δ are smaller than 10^{-4} for all Fock states, comparable to the measured residual photon occupation in the cavity. In order to keep the detector based errors the same, we take a toll on the efficiency. To explain this, consider $|n\rangle = 5$ Fock state which is 1.6 times more likely to decay during the repeated measurements protocol to reach the same likelihood as $|n\rangle = 1$. In addition, the higher demolition probability also contributes to the observed difference in efficiency ($0.8/0.4 = 2$). One way to combat is to work with a system with higher Q and lower demolition probability. Weakly coupled qubits in conjunction with ECD technique (Echoed Conditional Displacement)⁹³ could be an attractive solution to prepare

Fock states as well as maintain low demolition probability. A detector with fewer errors caused by thermal population and readout fidelity etc. would certainly help.

Unfortunately, we observe anomalous behavior with $|n\rangle = 3$ data, where the measured counts are lower than expected. We suspect it is due to leakage/cross-talk with a nearby mode which is closer in the energy level. The multiple modes of the cavity and qubit constitute a large number of modes $|q, c\rangle$ in the energy diagram, which causes mode crowding. There is no direct way to investigate the cause but we have identified a couple of transitions which could be facilitated by the always-on interaction of the qubit with all the cavity modes. For example, $|g, 3\rangle$ in Mode#2 is only 10 MHz away from $|e, 2\rangle$ in mode#4, and the difference could have been provided by an on-resonance readout tone. This issue can be easily resolved with a single mode cavity in a future experiment.

In the data plotted above, we did a background calibration by subtracting the total number of counts with the counts observed at $\alpha = 0$ for each Fock state. And I will discuss in the next section how it is justified.

6.4 Hidden photon search

In order to conduct a hidden photon search with the measured counts, I performed a background study varying the dwell time, where the cavity is allowed to integrate the DM signal without applying an external cavity displacement drive. For a coherent signal, we expect the number of counts to increase linearly with dwell time as well as the Fock enhancement factor. The hidden photon signal rate can be written as

$$\frac{dN_{HP}}{dt} = a_0 (n + 1) \tau \quad (6.9)$$

$$N_{HP} = a_0 (n + 1) \tau (N_{trials} \tau) \quad (6.10)$$

where the coupling term $a_0 = m_{HP} \epsilon^2 \rho_{DM} G V$ captures the kinetic mixing term and $N_{trials} \tau$ is the total integration time. However, in the actual experimental conditions,

the measured counts may contain a incoherent term in addition to the Eq. 6.10 such that the measured counts are modified but it won't have the Fock enhancement factor, and yet another term which has counts dependent on the specific state preparation

$$N_{meas} = a_0(n + 1)\tau(N_{trials}\tau) + b(N_{trials}\tau) + c_n N_{trials} \quad (6.11)$$

where a_0 and b and c_n 's are the fit parameters we extract from fitting the measured counts. By performing an ordinary least square (OLS) fit to the measured counts, we extract the fit parameters with their uncertainties tabulated in Table 6.1. The values of fit parameters obtained from performing a Maximum Likelihood Estimate (MLE) were comparable. The large statistical uncertainties on a are probably due to the fact that other two terms dominate the measured counts and fluctuations causing a to swing up and down by a large amount.

| Fitted Parameter | Θ | σ_Θ |
|------------------|------------------------------------|------------------------------------|
| a_0 | $1.858 \times 10^3 \text{ s}^{-2}$ | $7.662 \times 10^5 \text{ s}^{-2}$ |
| b | -7.26 s^{-1} | $4.2 \times 10^1 \text{ s}^{-1}$ |
| c_0 | 3.402×10^{-4} | 4.292×10^{-4} |
| c_1 | 1.419×10^{-3} | 4.0×10^{-4} |
| c_2 | 5.860×10^{-4} | 4.222×10^{-4} |
| c_4 | 7.330×10^{-3} | 6.732×10^{-4} |

Table 6.1: **Fitted parameters.** Statistical uncertainties of the fitted parameters corresponding to each source of background counts. The Fock state with higher background counts have larger c value indicating that the source of counts is related to the state preparation step and thus, it is valid to perform a background subtraction to demonstrate the enhancement technique.

In order to understand the systematic effects, I obtained a distribution of the a_{fit} by fitting the data to simulated data sets generated by sampling b and c_n 's independently assuming a normal distribution and keeping a_0 fixed to a value equal to σ_a . Please note that we are possibly over-estimating the error bars on a_0 as the error-ellipses for b and c 's may be oblique, broadening the distribution while sampling. The procedure was repeated 100,000 times to keep the error probability much below 1%. The resultant distribution is symmetric

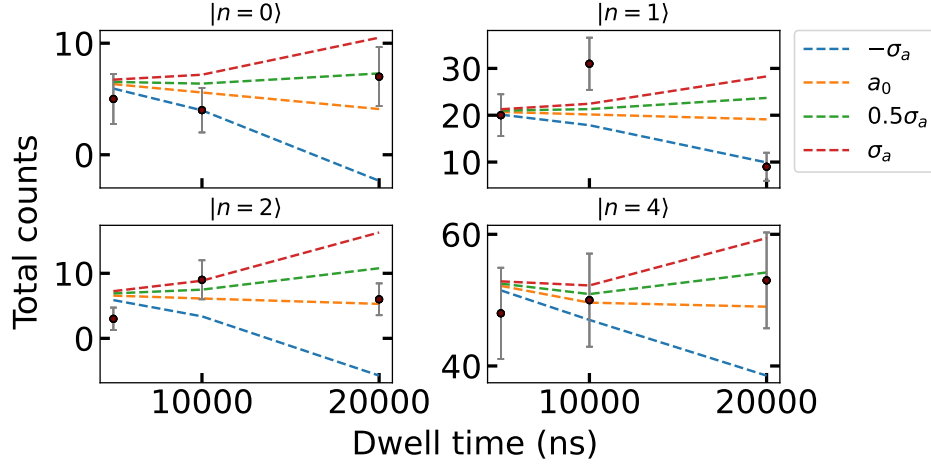


Figure 6.8: **Examples of fit to background counts.** The total number of counts for all trials after preparing the cavity in different Fock states for varied dwell time. The number of counts are then fit to a functional form given in Eq. 6.11 to extract the fit parameters. The dashed line corresponds to different fit values of a_0 to demonstrate that fits work well.

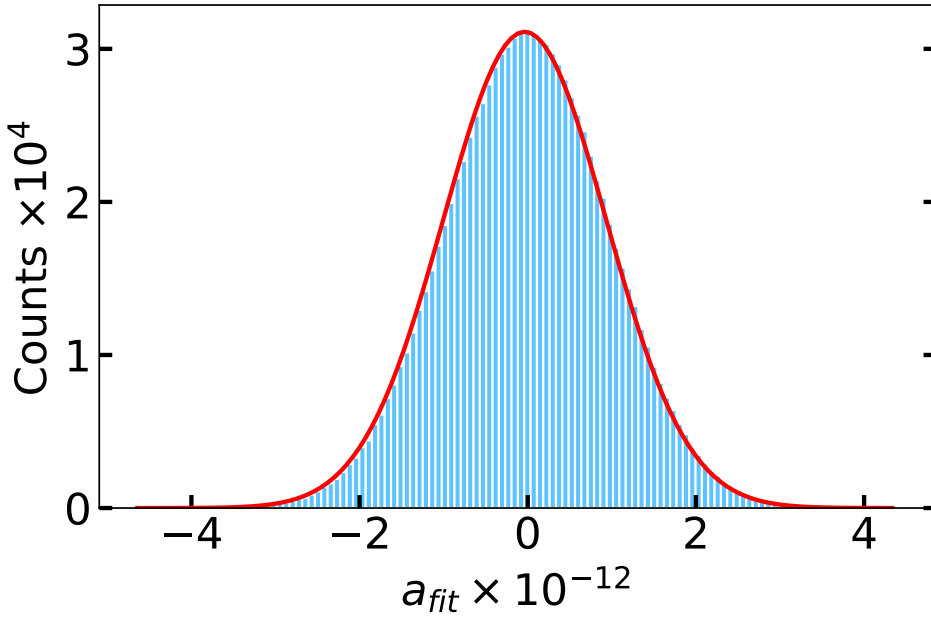


Figure 6.9: **Systematic effects on a_0 .** Observed distribution of a_{fit} with simulated data generated from Gaussian sampling the remaining fit parameters. The simulated data was generated 100,000 times to keep the error probability below 1%. The red line represents a normal distribution fit to the histogram.

about the chosen value of a_0 as shown in Fig. 6.9. It implies that the distribution of the measured value a_0 is also symmetric and we can use the standard deviation to compute the 90% confidence level limit on kinetic mixing angle.

This is a first demonstration of an unique technique which allows us to perform background subtraction without any cavity tuning. In general, a background subtraction is performed in dark matter experiments by tuning the cavity mode frequency and comparing the power levels. However, this option may not be available always and we demonstrate an alternate approach to distinguish between different sources of noise.

6.4.1 Kinetic mixing angle exclusion

For a dark matter candidate on resonance with the cavity frequency ($m_{\text{DM}}c^2 = \hbar\omega_c$), the rate of photons deposited in the cavity prepared in a Fock state $|n\rangle$ by the coherent build up of electric field in time τ is given by³¹:

$$\frac{dN_{\text{HP}}}{dt} = \frac{U/\omega_s}{\tau} = \frac{1}{2} \frac{E^2 V}{\omega_s} \frac{1}{\tau} = \frac{1}{2} J_{\text{DM}}^2 (n+1) \tau^2 \frac{G V}{\omega_s} \frac{1}{\tau} \quad (6.12)$$

The stimulated emission factor appears via the enhancement of magnitude of the electric field generated inside the cavity. The volume of the cavity is $34.5 \times 0.5 \times 2.5 \text{ cm}^3 = 43.13 \text{ cm}^3$. G encompasses the total geometric factor of the particular cavity used in the experiment. This includes a factor of $1/3$ due to the dark matter field polarization being randomly oriented every coherence time. For the lowest order mode of the rectangular cavity coupled to the qubit with $\mathbf{E} = \sin(\frac{\pi x}{l}) \sin(\frac{\pi y}{w}) \mathbf{z}$ the geometric form factor is given by:

$$G = \frac{1}{3} \frac{\left| \int dV E_z \right|^2}{V \int dV |E_z|^2} = \frac{1}{3} \frac{2^6}{\pi^4} \quad (6.13)$$

The hidden photon generated current is set by the density of dark matter in the galaxy $\rho_{\text{DM}} = 0.4 \text{ GeV/cm}^3 = 2\pi \times 9.67 \times 10^{19} \text{ GHz/cm}^3$:

$$J_{\text{DM}}^2 = 2\epsilon^2 m^4 A'^2 = 2\epsilon^2 m^2 \rho_{\text{DM}} \quad (6.14)$$

Substituting Eqn. 6.14 into Eqn. 6.12 yields the signal rate of photons deposited in the cavity by a hidden photon dark matter candidate:

$$\frac{dN_{\text{HP}}}{dt} = (n+1) \epsilon^2 \rho_{\text{DM}} m_{\text{DM}} G V \tau \quad (6.15)$$

We can now compute the kinetic mixing angle from the measured value of a_0 as given by Eq. 6.10. In order to determine the 90% confidence limit on the mixing angle ϵ , we rewrite

$$\epsilon^2 = \frac{a_0}{m_{\text{HP}} G V \rho_{\text{DM}}} \quad (6.16)$$

Using standard error propagation formula, we determine the standard deviation on ϵ given, we have the error estimates for all the parameters tabulated above. The estimated value of $\epsilon_0 = 1.3 \times 10^{-15} \pm 3.30 \times 10^{-13}$, dominated by the error on a_0 . We can now set the 90% confidence limit on the kinetic mixing angle term as $\epsilon^{90\%} = \epsilon_0 + 1.28\sigma_\epsilon = 4.279 \times 10^{-14}$. This leads us to exclude, with 90% confidence, hidden photon with mixing angle $\epsilon^{90\%}$ greater than 4.279×10^{-14} as shown in Fig. 6.10.

| Expt. Parameter | Θ | σ_Θ |
|--------------------------|--------------------------------|-------------------------------------|
| Storage cavity frequency | $\omega_s = 5.965 \text{ GHz}$ | $\sigma_{\omega_s} = 26 \text{ Hz}$ |
| Storage quality factor | $Q_s = 5.11 \times 10^7$ | $\sigma_{Q_s} = 1.4 \times 10^5$ |
| Storage cavity volume | $V = 43.13 \text{ cm}^3$ | $\sigma_V = 1.2 \text{ cm}^3$ |
| Storage form factor | $G = 0.002$ | $\sigma_G = 0.0002$ |

Table 6.2: **Stimulated emission experimental parameters.** Systematic uncertainties of physical parameters in the experiment must be incorporated in determining the excluded hidden photon mixing angle ϵ . The uncertainty in the hidden photon (HP) conversion is determined in the previous section. The storage cavity frequency uncertainty is obtained by Ramsey interferometry. The quality factor of the cavity is given by $Q_s = \omega_s T_1^s$ so the uncertainty is calculated as $\sigma_{Q_s}^2 = (\omega_s \sigma_{T_1^s})^2 + (T_1^s \sigma_{\omega_s})^2$. The volume uncertainty is estimated by assuming machining tolerances of 0.005 inches in each dimension. The form a factor uncertainty is estimated from assuming 1% error in the simulated structure. Of the experimental quantities, the HP conversion has the largest systematic uncertainty.

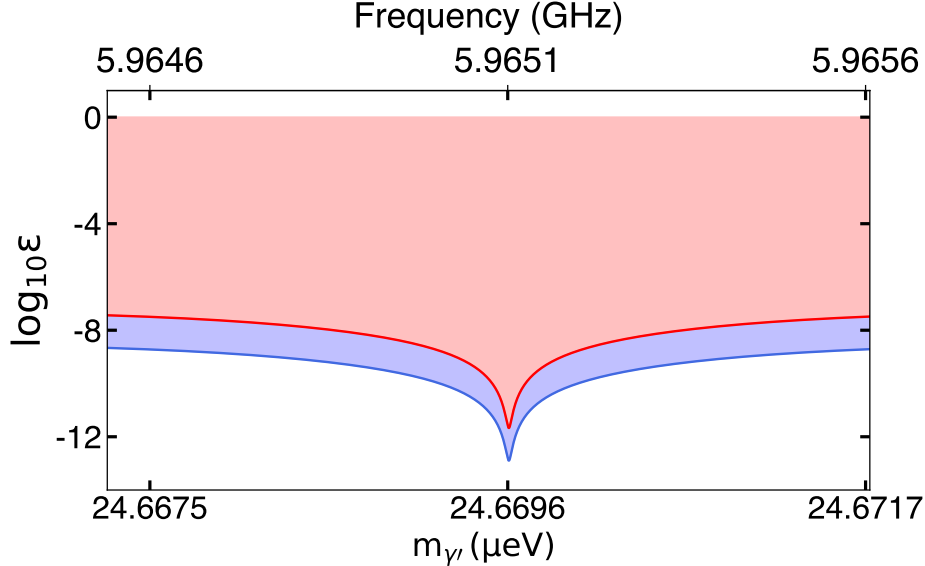


Figure 6.10: **Excluded ϵ with $m_{\gamma'}$.** Shaded regions in the hidden photon parameter space of coupling (ϵ) and mass ($m_{\gamma'}$) are excluded with 90% confidence. The horizontal extent is set by the bandwidth of the number resolved qubit π -pulse which is insensitive to any drive outside the band. The vertical limit is set by the maximum ϵ which would result in hidden photon rate greater than the value which would degrade the fidelity of Fock state preparation significantly. The region between the blue and red curve represents the exclusion with the stimulated emission experiment whereas, the excluded region above the red curve is mainly due to the failure of Fock state preparation which is easily detectable in the experiment.

Maximum allowed kinetic mixing

A hidden photon candidate that could result in more detector counts than background counts is constrained by the cavity occupation number which degrades the fidelity of Fock state preparation in the cavity by a significant amount. In order to estimate the same, the cavity is prepared with varied number of mean photons before applying the OCT pulse. The resultant state is measured with the same procedure as the stimulated emission protocol to compute the fidelity. We observe that the fidelity changes significantly when the mean injected photon number goes above $n_{inj} \geq 0.05$ shown by the red dashed line in Fig. 6.11. The maximum number of photons sourced from the hidden photon which is tolerable before the state preparation is out of control and allows us to perform the stimulated emission experiment. In principle, we can exclude the region all above the red curve due to the failure

of Fock state preparation which is easily detectable in the experiment. In practice, the region above red dashed line is excluded up to $\epsilon \rightarrow \infty$, however, for representational purposes, we plot only up to $\epsilon = 1$.

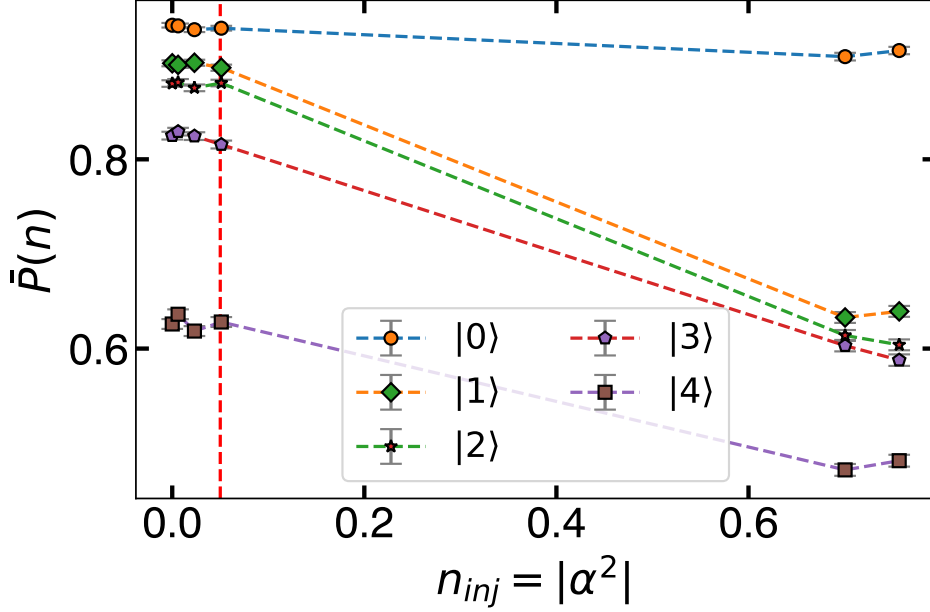


Figure 6.11: **Fock state preparation with non-zero occupation in the cavity.** Measuring the Fock state preparation probability as a function of initializing the cavity with varying occupation before the OCT pulses. Red dashed line corresponds to the maximum tolerable injected number of photons where the fidelity changes significantly.

The sensitivity can be further improved with a cylindrical cavity such that the form-factor is much larger than the current cavity. Lower cavity occupation would definitely help in keeping the background counts low.

6.5 Summary

In summary, we have demonstrated a signal enhancement technique using circuit-QED tools to prepare the cavity in Fock states and to enhance the rate of stimulated photons. It results in a $2.5 \times$ (4 dB) improvement in the signal rate, taking into account the efficiency. We present a first demonstration of an unique method to distinguish between different sources of backgrounds by estimating their individual contributions. The measured contribution due

to a coherent source is converted into hidden photon kinetic mixing angle to set an exclusion limit with an unprecedented sensitivity in an unexplored region. With an optimal cavity design, we could reach even better sensitivity.

Chapter 7

Photonic Bandgap Axion Haloscope

Microwave cavities made out of normal metals are incompatible with large magnetic fields required for dark matter searches, limiting the maximum achievable Q-factors ($Q_c \ll Q_{Dm}$). More importantly, the stimulated emission technique I discussed in the last chapter is dependent on the Q-factor of the cavity to be greater than the dark matter wave. In this chapter, I am going to discuss new fabrication techniques using photonic bandgap material to achieve high Q-factors. Beginning with an introduction to the physics governing photonic bandgap (PBG) and how a defect could localize an EM mode acting as a low-loss cavity. I will describe a few examples which satisfy the cavity requirements for a haloscope experiment. Then, practical implementation of such structures will be discussed, along with their pros and cons. Lastly, I will discuss the final design of a photonic bandgap cavity and low temperature measurements demonstrating its successful implementation.

7.1 Introduction

Advances in semiconductor physics have enabled us to tailor the *electrical* properties of certain materials, thereby initiating the transistor revolution in electronics. It is hard to overstate the impact these advances have had on our society. In late 80's, scientists proposed new ideas where the *optical* properties of a material could be controlled by creating artificial crystal structures. Eli Yablonovitch⁹⁴ and Sajeev John⁹⁵ published two milestone papers on photonic crystals in 1987 opening up an interesting field of research which would revolutionize the optoelectronics industry, doing for light what silicon did for electrons.

7.1.1 What is a Photonic Bandgap (PBG)?

The control of electric currents achieved with the semiconductors such as silicon is dependent on a phenomenon called the bandgap: a range of energies in which the electron is blocked from travelling through the semiconductor. Scientists have produced material with a photonic bandgap- a range of wavelengths of light which is blocked by the material. The analogy between electron-wave propagation in real crystals and the electromagnetic-wave propagation in a multidimensional periodic structure has proven to be a fruitful one. It allows us to manipulate light in addition to electric currents. Photonic crystals occur in nature in the form of structural coloration and animal reflectors as shown in Fig. 7.1.



(a) Opal Armband



(b) Peacock Feathers

Figure 7.1: Natural periodic micro-structures responsible for the iridescent color in stones and feathers. Source: Wikipedia

The existence and properties of an electronic bandgap depend crucially on the type of atoms in the material and their crystal structure - spacing between the atoms and the shape of crystal they form. In the *optical* analogue, atoms or molecules are replaced by macroscopic media with differing dielectric constants, and the periodic potential is replaced by the periodic dielectric function, giving rise to a band structure for photons similar to the electrons in semiconductors.

One of the simplest example of a photonic bandgap material is a multi-layer dielectric structure, such as a quarter-wave stack. It consists of alternating layers of material with different dielectric constants, one you may find in reflective coating on your sunglasses. Light

of a certain wavelength, when incident on such a layered material, is completely reflected. The reason is that the light wave is partially reflected at each interface and, if the spacing is periodic, the multiple reflections of the incident wave will destructively interfere, blocking the wave to propagate in the forward direction. This technique is really useful to produce ultra-high reflectivity mirrors (Bragg mirror) achieving 99.999% or better over a narrow range of wavelengths. If a photonic crystal prohibits the propagation of EM wave of any polarization traveling in any direction for some frequency range then we claim the crystal has a complete photonic bandgap. Typically, a dielectric lattice periodic along three axes shows a complete PBG and we are interested in such structures for dark matter applications.

7.1.2 Why do we need a photonic bandgap?

Before we dig deep into photonic crystals, let me explain a few challenges we face with the current haloscope style cavities and their dominant loss channels. A dark matter detection cavity is a typical right-cylindrical cavity optimized for a TM_{010} mode profile as shown in Fig. 7.2. Due to the presence of a large magnetic field, we cannot use any superconducting cavities and thus, forced to use copper as the outer material. The electric field of a TM mode mainly points along the z-direction which allows the largest coupling $C_{010} = 0.69$ for axion to photon conversion. However, this means that the amplitude of magnetic field at the metal surfaces is maximum, which causes dissipation of the stored energy to the walls. We can separate the contributions due to side-walls (Q_{sw}) and the end-caps (Q_{ec}).

$$1/Q_{tot} = 1/Q_{sw} + 1/Q_{ec} \quad (7.1)$$

For a typical cavity geometry made out of copper, with the help of simulations, we estimate $Q_{sw} \approx 1.15 \times 10^5$ and $Q_{ec} \approx 10^6$. This indicates that the loss on side-walls is a dominant factor. The goal of this exercise is to shape the field distribution such that the amplitude of magnetic field is minimized at the cavity walls and thus, the losses to achieve high-Q.

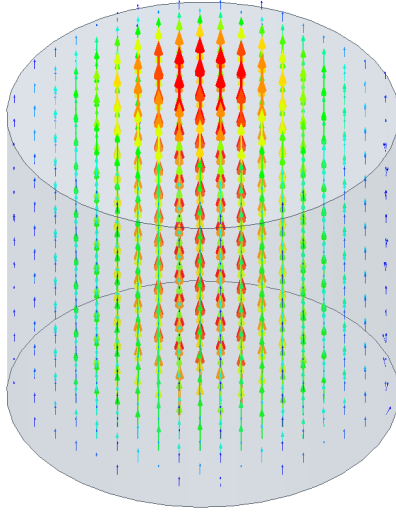


Figure 7.2: **Empty cylindrical cavity.** Electric field profile of a TM_{010} mode with field pointing along the axial direction. The radial distribution follows a Bessel function with an anti-node at the center.

In case you have forgotten, the form factor or coupling ratio C is defined as

$$C_{mnl} = \frac{\left| \int \vec{B} \cdot \vec{E}_{mnl} dV \right|^2}{B_0^2 V \int \epsilon(s) |\vec{E}_{mnl}|^2 dV} \quad (7.2)$$

7.2 Computing the bandgap

The propagation of light in a photonic crystal is governed by the four macroscopic Maxwell equations, which is simplified by the assumption of no sources of light and no free charges or currents. For a 1D quarter wave stack described above, we can still use the wave optics we learnt in our undergraduate class to compute the layer thickness and the bandgap for a given set of materials. However, as the structure complexity grows, numerical calculation is more efficient and accurate to compute the band-structures which is otherwise not feasible with analytical calculations. It is useful to note that the Maxwell equations are linear in frequency and thus, all the computational frameworks initially developed for the optical regime is applicable at microwave frequencies. An useful metric to characterize the PBG which is independent of the scale of the crystal is the gap-midgap ratio, defined as $\frac{\Delta\omega}{\omega_m}$,

where ω_m is the frequency at the middle of the gap. The size of the band-gap is often quoted in percentage and the band diagrams are plotted in dimension less units for both frequency $\omega a/2\pi c$ and wave-vector $ka/2\pi$, where a is the lattice constant.

For a normal incidence at the interface of two materials with refractive indices ($\sqrt{\epsilon}$) n_1 and n_2 and thickness d_1 and $d_2 = a - d_1$ respectively, the gap is maximized when $d_1 n_1 = d_2 n_2$, or equivalently, $d_1 = a n_2 / (n_1 + n_2)$. The gap-midgap ratio between the first two bands is approximately⁹⁶

$$\frac{\Delta\omega}{\omega_m} \approx \frac{\Delta\epsilon}{\epsilon} \frac{\sin(\pi d/a)}{\pi} \quad (7.3)$$

and in this specific case, the midgap frequency can be shown to be

$$\omega_m = \frac{n_1 + n_2}{4n_1 n_2} \frac{2\pi c}{a} \quad (7.4)$$

Using the vacuum wavelength relation $\lambda_m = 2\pi c/\omega_m$, we can check that $d_1 = (1/4)(\lambda_m/n_1)$ and $d_2 = (1/4)(\lambda_m/n_2)$, which means that the individual layers are exactly a quarter wavelength in thickness, thus, the name quarter-wave stack.

7.2.1 Computational tools

There are multiple software tools available in the market which use different methods to solve the EM wave equations in a given geometry. The two most common methods are Finite-Difference Time-Domain (FDTD) and Finite Element Method (FEM). Both have their own strengths and weaknesses, for example, FDTD can cover a wide frequency range in a single simulation run and treat nonlinear material properties in a natural way. On the other hand, FEM can handle any complicated geometry with relative ease. During my research, common software tools using FEM are - **Ansys HFSS**, **Comsol** and for FDTD - **mpb**¹ and **Meep**². For simulating periodic structures, FDTD tools are very efficient in terms of computational

1. <https://github.com/NanoComp/mpb>

2. <https://github.com/NanoComp/meep>

resources as well as time³. Therefore, I computed most of the band structure simulations using `mpb`^{96,97} and the time domain simulations using `Meep`. Both these packages have excellent resources and examples on the web to follow. Let me show you an example of computing the band-structure of a 1D quarter stack formed by alternating layers of $\epsilon_1 = 1$ (air) and $\epsilon_2 = 11.2$ (Sapphire) using `Meep`. Numerically, this structure produces a gap of size 72% for $d_1 = 0.77a$ and $d_2 = 0.23a$ as shown in Fig. 7.3.

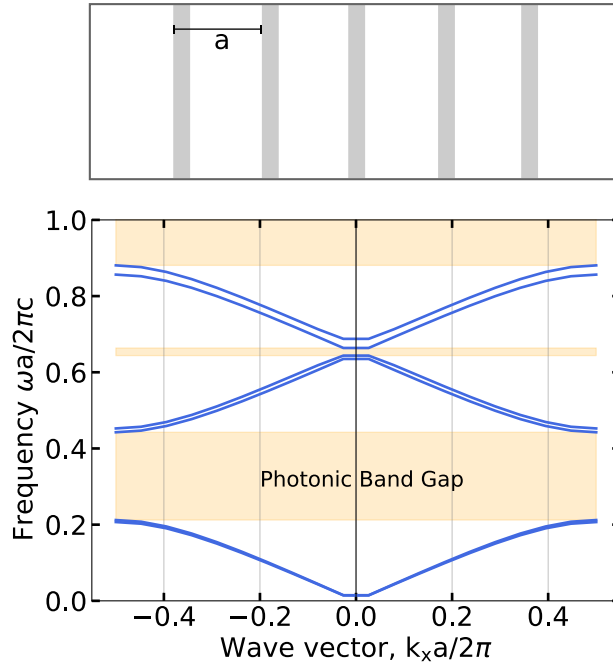


Figure 7.3: **Band structure of a Bragg stack.** (Top) A schematic of Bragg stack depicting alternating layer of dielectric materials. (Bottom) The photonic band-structure of a multi-layer film with lattice constant a and alternating layers of widths equal to quarter wavelengths. The dielectric constant of these alternating layers is $\epsilon_1 = 1$ (air) and $\epsilon_2 = 11.2$ (sapphire).

One of the main advantage using `Meep` is the ability to solve the problem over one lattice period and assign a periodic boundary condition to simulate an infinite crystal. This makes the computation fast without taking too much memory. `Comsol` and `HFSS` also support periodic boundary conditions but require expensive licensing fee. `Meep` is open-source and

3. Also, I got a chance to collaborate with one of the founding fathers, S. G. Johnson who developed the `Meep` package at MIT.

easy to follow with python interface.

7.2.2 Defect as a cavity

So far, we have discussed the band structure of a perfectly periodic system, but what happens if this translational symmetry is broken by a defect? In Fig. 7.3, the shaded region where the bandgap appears, the density of states (number of allowed modes per unit frequency) is zero but modes are allowed to exist if they are evanescent. Thus, defects may allow *localized* modes to exist, if the frequencies lies inside the bandgap. It must exponentially decay once it enters the crystal and the multi-layer films on both sides of the defect behaves like a frequency selective mirror, similar to a Fabry–Pérot cavity as shown in Fig. 7.4.

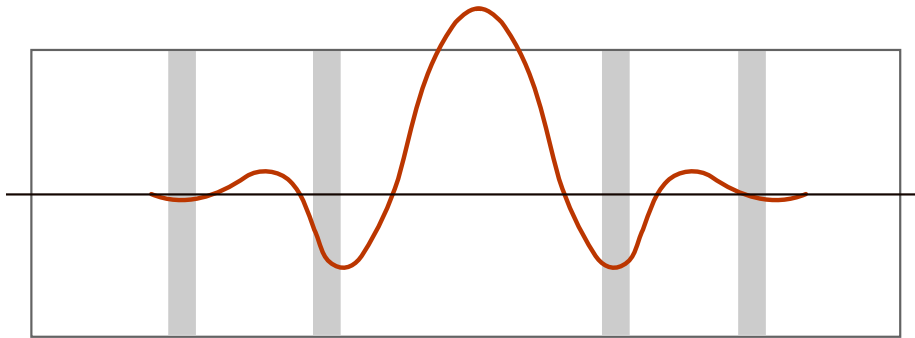


Figure 7.4: Defect in a Bragg stack. A defect created by removing a dielectric layer. The maroon curve represents the electric field associated with the localized mode created inside the bandgap (for on-axis propagation).

In terms of a haloscope experiment, the cavity should have the following properties:

- Finite form-factor $C \Rightarrow TM_{0n0}$ type mode profile is preferred
- High Q-factor
- A large volume, $\mathcal{O}(\lambda^3)$
- Tunable cavity mode is a bonus

This implies that the structure is macroscopic and cannot be fabricated using lithography tools. The material should have a low-loss or equivalently, negligible loss tangent ($\tan \delta$). We will keep requirements in mind before while choosing a photonic crystal lattice.

7.3 Woodpile with an omni-directional bandgap

Following examples from the book, “Molding the flow of light”⁹⁶, I chose the woodpile structure as our subject of interest due to the presence of a complete bandgap. A woodpile (or a log-cabin) structure is a stack of dielectric “logs” with alternating orthogonal orientations. It consists of four-layers arranged in a *ABCD* sequence in which *C* and *D* are the layers with same orientation as *A* and *B*, but are offset by half of the horizontal spacing as shown in Fig. 7.5. The dielectric logs form an FCC lattice stacked in the [001] direction. As I was more familiar with HFSS for EM simulations due to experience with circuit-QED simulations, I spent a considerable time implementing periodic structure simulations which would abruptly terminate due to finite RAM memory issues. A couple of months were spent to optimize the simulation parameters, implementing periodic boundary conditions to avoid simulating large crystal geometries, but, all in vain. Under Steve’s supervision, I was able to setup the simulation of a woodpile structure in Meep and never looked back.

After a detailed literature survey of various dielectric materials, we chose Alumina as our initial prototype test material. It has a large dielectric contrast to give a reasonable bandgap, readily available and low-loss at microwave frequencies with an option to switch to ultra low-loss Sapphire if everything works out. I made a woodpile structure out of Alumina bars with a cross-section of 2.5 mm × 2.5 mm and length 150 mm to fit 15 periods in the horizontal plane (*XY*) plane and 10 periods along the vertical direction (*Z*). To keep uniform lattice spacing between bars, I designed and 3D printed a support structure made out of plastic. It made the assembly convenient and error-free. In order to characterize the properties at room temperature and validate our simulations, we mounted a set of dipole antennae at the two sides as shown in Fig. 7.5 and connected the two ports to a network analyzer. We

measured the forward transfer function S_{21} and saw a clear dip in transmission indicating the presence of a bandgap as shown in Fig. 7.5. The measured bandgap size and frequency range matched very well with the simulation results.

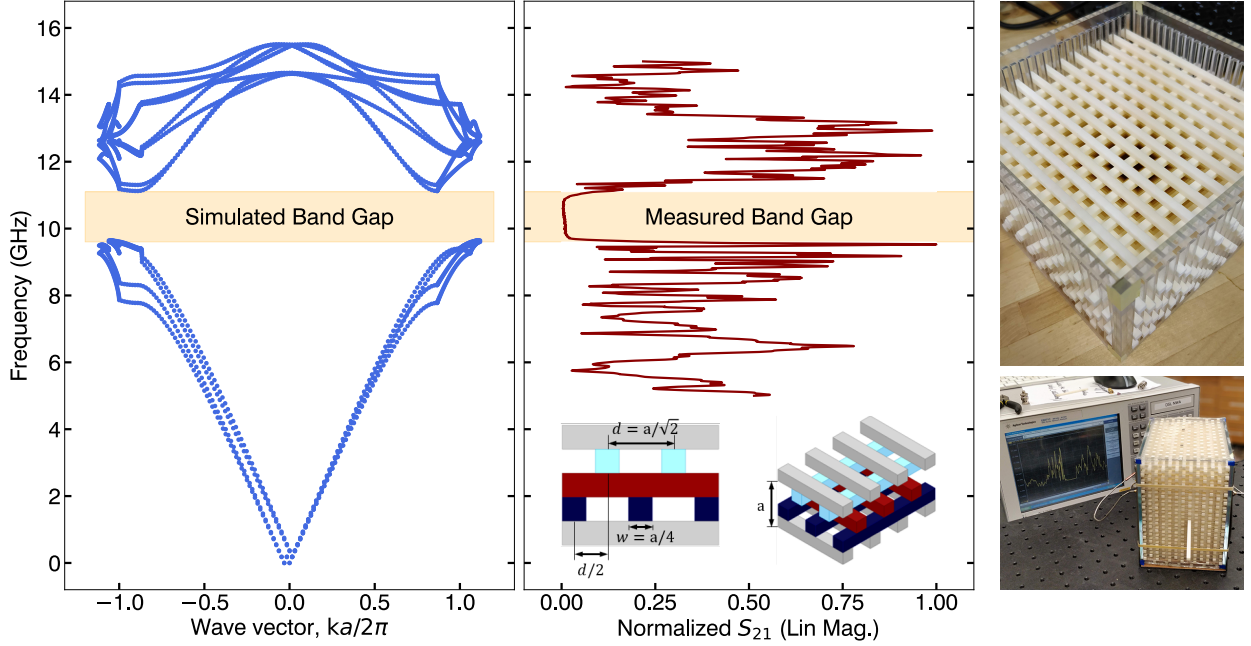


Figure 7.5: **Photonic band-structure of a woodpile structure.** A schematic showing the *ABCD* sequence of dielectric layers. The computed band-structure of a FCC type lattice with 16% omni-directional bandgap. The measured band-structure of a woodpile in the lab showing a forward transfer function S_{21} using a network analyzer. A sharp drop in the transfer function matches very well with the simulated results validating The insert shows an actual log-cabin made out of Alumina bars.

Defect inside a woodpile crystal

Next step, we create a cavity inside this structure. In order to do so, we remove a small section of the log in the middle of the structure forming a point defect. This small defect can be thought of as a rectangular cavity formed by dielectric walls and if the mode of the cavity lies within the bandgap then the field exponentially decays within the crystal forming a localized mode. By varying the size of this defect, we can also tune the frequency of this localized mode. Fig. 7.6 (a) shows the electric field profile of such a mode localized in the defect where most of the EM energy is stored.

One remarkable feature of photonic crystals is that the bandgap is a property of the unit cell and is independent of the number of unit cells. Practical limitations to build and test, lowers the number of periods but as confirmed by Fig. 7.5, the size of the bandgap doesn't change significantly. The effect of a finite number of unit cells is (a) to allow propagation via evanescent modes inside the gap and (b) introduction of defect modes and surface states. Having a small number of cells doesn't change the size of the bandgap, but it does allow significant transmission near the edges of the gap where the decay of the evanescent mode is slow. This leads to dependence of radiation loss on the number of periodic layers surrounding the defect as evident from Fig. 7.6. There are two internal loss channels in the photonic cavities - radiation and material loss. Radiation loss refers to the loss of energy to the nearby surrounding whereas, material loss constitutes scattering of waves at different interfaces and dissipating energy through the phononic modes.

Q-factor of a woodpile cavity

`Meep` computes the time response of a field when a point source placed near the defect tries to excite the resonance mode with a broad frequency range. The ring-down of the field amplitude tells us the decay constant or equivalently, the Q-factor. In order to study the contribution of radiation losses, we set the material losses to zero and vary the number of layers surrounding the defect. As one would expect, the Q exponentially increases with the number of layers, thus, depending on the application we can choose an optimal number of layers such that it's a negligible effect. Using perturbation theory, we can then compute the fraction d of total EM energy stored in the dielectric and estimate the total Q-factor as

$$1/Q_{tot} = 1/Q_{rad} + d \tan \delta \quad (7.5)$$

where d is given by,

$$d = \frac{\int_{V_d} \epsilon(d) \vec{E} \cdot \vec{E} dV}{\int_V \epsilon(s) \vec{E} \cdot \vec{E} dV} \quad (7.6)$$

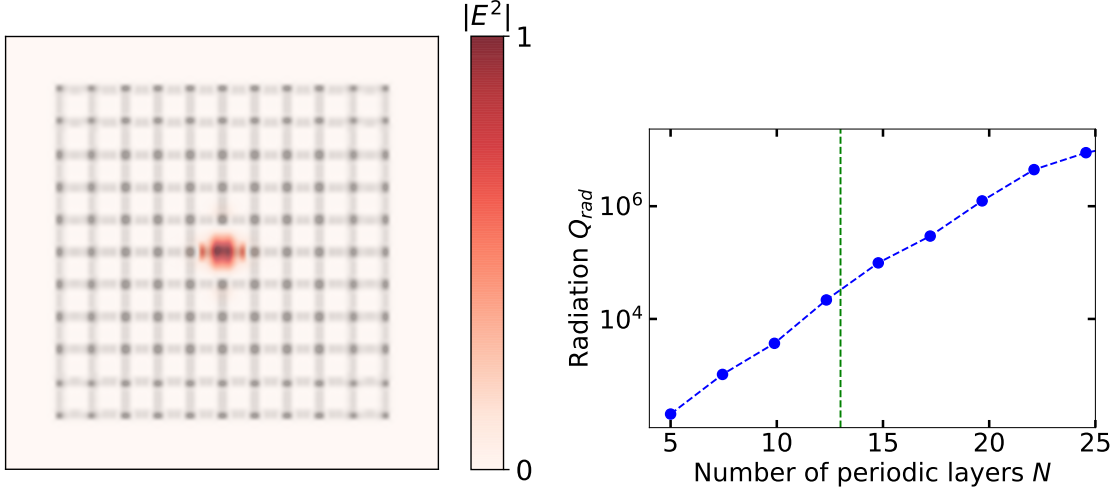


Figure 7.6: **Defect cavity inside a woodpile structure.** (Left) Electric field profile of the mode trapped inside a point defect; grey represents the outline of dielectric logs from a top view (Right) Actual image of the defect created with Alumina logs (c) Exponential increase in radiation Q with the increase in number of layers. Green dashed line corresponds to the number of layers in the actual prototype with an expected $Q_{rad} \approx 2 \times 10^4$.

Cryogenic measurements

After obtaining the desired performance at room temperature, we measure the same at low temperatures. The permittivity of the material ϵ as well as the loss tangent, both change significantly with temperature. The change in ϵ shifts the frequency of the system. The dielectric loss of materials such as Alumina or Sapphire drops by 2 to 4 orders of magnitude as the material cools down and phonons freeze out^{98,99}. On the other hand, the thermal conductivity of dielectric materials also go down, making it difficult to reach thermal equilibrium with the physical surrounding. Hence, it is very crucial to design a prototype such that the entire thermal mass reaches the expected temperature in a reasonable amount of time. For this purpose, I made the entire support structure out of copper and added grooves to position the logs, as well as increase the contact area for better thermalization. Adding copper at the ends also provides reflective boundary condition, enhancing the Q -factor of the cavity. An example of such a prototype is shown in Fig. 7.7. We bolted this cavity to the 1K stage of the dilution refrigerator which has a much larger cooling capacity

than the MXC plate and we expect most of the improvement in Q be visible below 15 K.

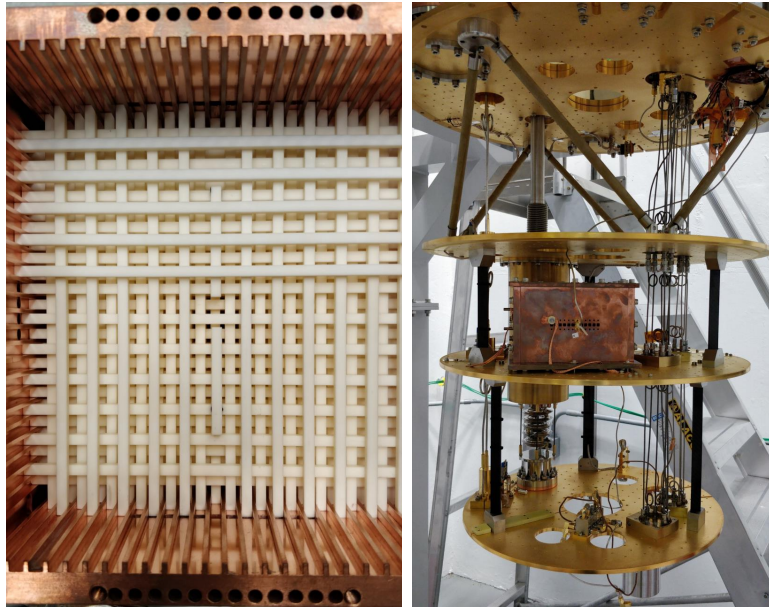


Figure 7.7: **Woodpile cavity for cryogenic measurements.** (Left) Grooves to keep the dielectric bars in place and increase surface area for thermal conduction. (Right) Copper enclosed woodpile cavity mounted to 1K plate of the dilution refrigerator.

While cooling down, I recorded the transfer function of the cavity to track the mode frequency as well as Q. The frequency of the mode shifts higher as the geometry contracts under thermal gradient and the Q-factor improves by a factor of almost 3. The initial results looked promising. The internal quality factor of the cavity mode increased from 15,000 at 300 K to 75,000 at 1 K limited by the losses on metallic walls. Addition of extra periods would make the structure even bigger, which makes it unfit for actual experiment.

Tuning the mode frequency

The results from first prototype were promising and matched our simulation results well. Next, I studied the feasibility of a tuning mechanism to change the frequency of the cavity. The first thing that I tried was to increase the size of the defect along the log, making a longer cavity, thus, decreasing the frequency. However, if we carefully look at the geometry of the

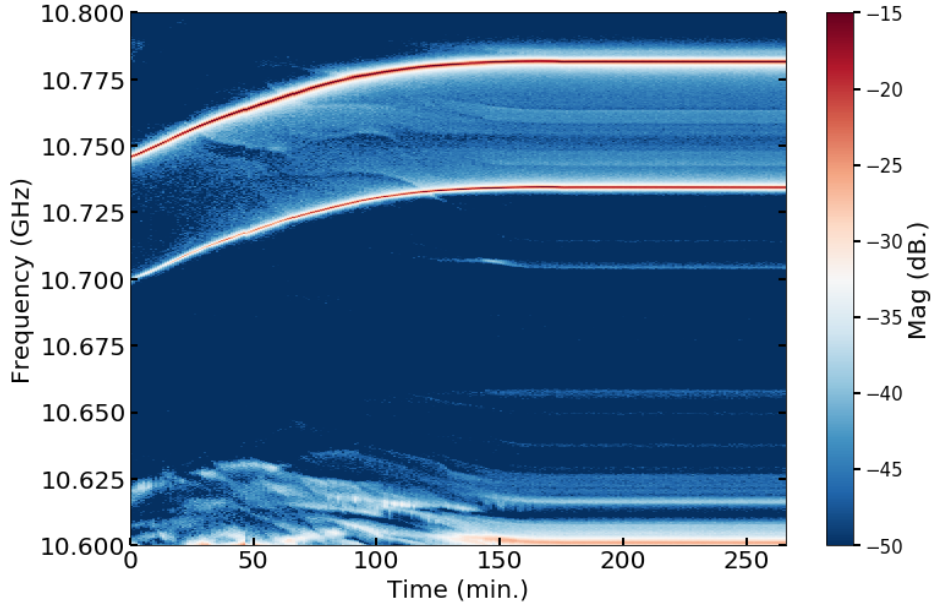


Figure 7.8: **Tracking cavity frequency.** Measurement of the transfer function during the cool-down period. The frequency of the mode increases as expected due to thermal contraction and change in the dielectric constant of alumina bars.

cavity, the second largest dimension is unchanged which means the shift will be minuscule. We verified with the help of simulations that the mode frequency didn't change by more than a percentage, but the radiation Q dropped by a factor of 2. The other way would be to change the size by removing multiple sections as shown in Fig. 7.9. It changes the frequency by a considerable amount, however, at the expense of higher radiation losses. In addition to that, the mechanical tuning of multiple bars is very difficult to control in experimental conditions.

Empirically, mechanical movements at cryogenic temperatures are very difficult to implement and ensure repeatability. Moreover, the size of the crystal required to achieve a $Q \geq 10^5$ is too large to fit inside a 75 mm diameter bore of a 14 T solenoid magnet ordered at Fermilab for axion experiment. I did try to find a low-loss material with a larger dielectric contrast such as Rutile ($\epsilon \sim 100$)^{100,101}, which would shrink the entire geometry by a factor of 3 but couldn't find a vendor to provide the logs as per our requirement. Therefore, after a very detailed study and discussion, we had to look for a different approach/design which

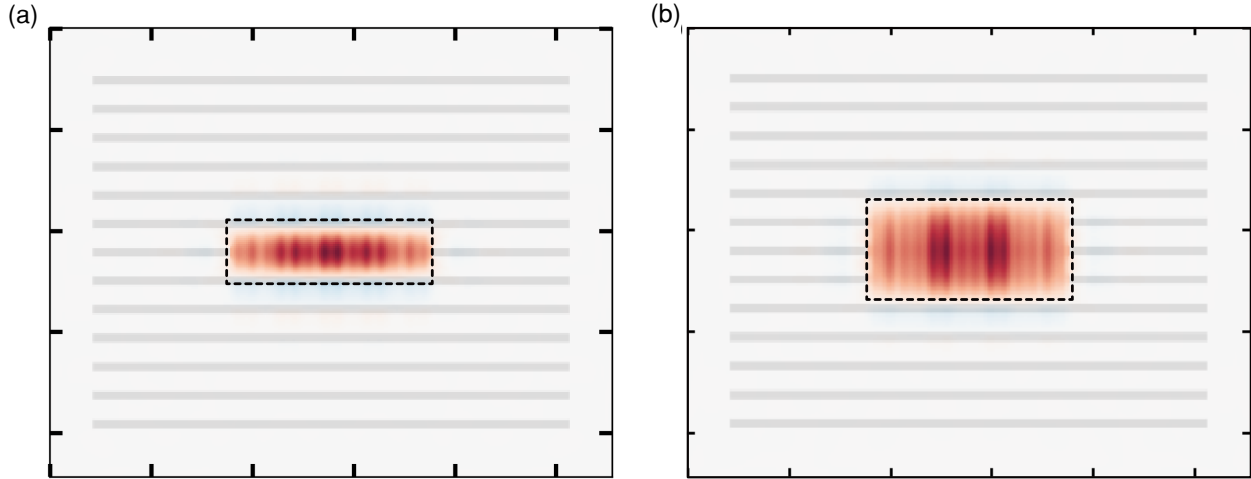


Figure 7.9: Tuning a woodpile defect cavity. (a) The length of the cavity along the bar is increased to tune the mode frequency. (b) A wider cavity volume can be formed by removing multiple sections of the bar which leads to appreciable change in the frequency. Both have radiation Q lower by a factor of 2

would fit inside the magnet and satisfy all the desired properties of an axion cavity.

While I was investigating the woodpile structure, another research group in Italy had tried a triangular lattice of rods¹⁰² to protect the mode in the radial direction. It has a 2D PBG with no protection in the z-direction. Fig. 7.10 shows an example of a triangular lattice with a rod removed from the center. The core acts as a cavity with field mostly pointing along the axial direction. The reported cavity is $Q \approx 3 \times 10^5$ at 4.2 K. However, the form factor takes a hit as the field changes its direction once it crosses the first layer.

However, I could anticipate a few reasons why this design was not pursued further in their work. First, the bandgap size is not large ($\sim 20\%$), requiring more periods to protect the field from reaching side-walls. Second, the number of moving parts (rods) probably makes it difficult to assemble and ensure all the bars are thermalized well.

7.4 Bragg Fiber

The next design that we tried was again based on an example from the book which had been implemented for efficient transport of optical light. “Bragg Fiber” as the name suggests is

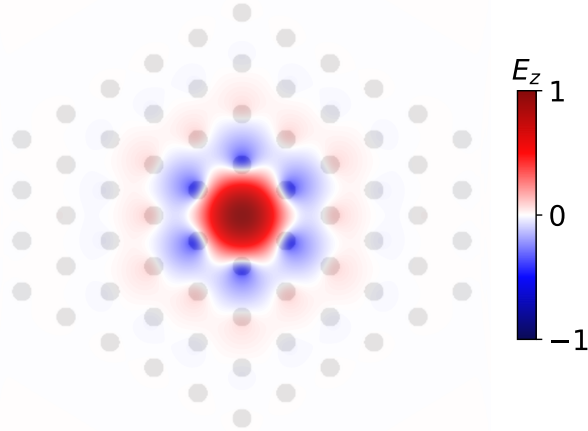


Figure 7.10: **2D triangular lattice with a defect.** A mode localized in the center of a lattice formed by triangular arrangement of dielectric rods (grey circles). A rod from the center is removed to form a defect which acts as a cavity with an electric field profile pointing along the z-direction.

based on the Bragg stack we discussed earlier. Think of it as a 1D stack which is bent to form a cylinder. It was first proposed by Yeh et al.¹⁰³ in 1978. The continuous translation symmetry along the axial direction (Z) and the continuous rotational symmetry in ϕ (the azimuthal angle) means that that the eigenstate can be written in the separable form:

$$\mathbf{H}_{k_z,m} = e^{\imath k_z z + \imath m\phi} \mathbf{h}_{k_z,m}(r), \quad (7.7)$$

which has been reduced to a 1D problem for the radial (r) dependence. It is sufficient to obtain a 1D bandgap in a cylindrical geometry due to conservation of angular momentum m in analogy with quantum mechanics. The flat multi-layer structure exhibits a large bandgap 72% for a air-sapphire layered structure as shown in Fig. 7.3.

In this case, the cavity is formed by removing a few dielectric layers from the middle such that the resulting geometry resembles a hollow core. The radius of the innermost layer determines the mode frequency and can be well approximated with the solution of a metallic cavity. For a TM mode, the solution is given by zero-order Bessel functions such that the resonance frequency for a TM₀₁₀ mode is given by $\omega_n = 2.405R_0/\sqrt{\epsilon\mu}$, where R_0 is the inner

radius. The Bragg cavity was simulated in **Meep** as well as HFSS to verify the field distribution as well as the expected Q. As seen in Fig. 7.11 (b), the field amplitude falls off exponentially away from the center, however, the profile resembles a TM₀₃₀ mode. This was unexpected but it makes sense because the overall radius of the cavity is much larger to support a higher order mode and the dielectric only provides a soft boundary. It lowers the form factor at the expense of a larger detector volume.

As the radiation Q exponentially increases with the number of layers, it requires only a few layers to achieve the desired $Q_{rad} = 10^3$. The field is strongly attenuated per unit layer as the bandgap is larger. We get another factor of enhancement due to the reflective boundary provided by the copper outer layer. The idea of combining the two - a few layers of Bragg fiber combined with a metallic outer wall, to suppress the Ohmic losses but not eliminate them, stems from Miyagi et al.^{104,105}, in the context of minimizing transmission losses at infrared wavelengths.

In order to understand this, let's remind ourselves that Ohmic losses are proportional to the electric field inside the metal, which is what causes the current $\mathbf{J} = \sigma \mathbf{E}$, so the power loss can be written as $P_{loss} \sim \int \mathbf{J} \cdot \mathbf{E} = \int \sigma |\mathbf{E}|^2$. However, for a perfect metal, this is zero ($\mathbf{E} = 0$ inside a perfect conductor).

In order to compute the losses due to finite conductivity, we can use perturbation theory (Chapter 8 Jackson, Eq (8.82)) to first order in the skin depth and write down the expression for power loss on a normal metal surface as

$$P_{loss} = \frac{\mu_{Cu} \omega \delta}{4} \oint_s |H_\phi|^2 ds \quad (7.8)$$

where μ_{cu} is permeability of copper, ω is frequency of the mode, and δ is anomalous skin depth. From fig. 7.11 (b), we can check that the presence of dielectric layers suppresses the magnitude of H_ϕ field reaching the metal surface by a factor of at least 10 compared to an empty copper cavity. And thus, the losses by a factor of 100. We qualitatively estimate

the Ohmic losses using Eq. 7.8 and predict Q-factors due to side-walls $Q_{sw} = 14 \times 10^6$ and end-caps $Q_{ec} = 10^6$. Compared to an empty copper cavity we discussed earlier, the losses on side-walls are down by a factor of 100, making the loss on end-caps the dominant factor. This implies that the bandgap is really effective in shaping the field distribution along the transverse direction.

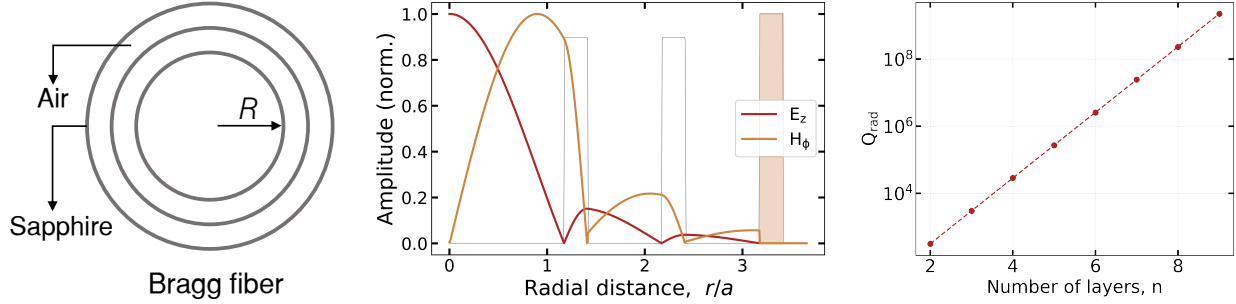


Figure 7.11: **Bragg fiber.** (a) Schematic showing the alternating layers of air and sapphire forming a Bragg fibre. (b) A mode localized in the center with a frequency in the middle of the gap, grey lines showing the dielectric layers and copper metal at the end. Electric and magnetic field profiles resembling TM_{030} with an exponential tail reaching the end. (c) Radiation Q as a function of the number of layers.

7.4.1 Tapered dielectric shells

Now, we need to do the same for end-caps. The Bragg fiber does not exhibit bandgap along the axial direction, but, we can achieve a similar effect as bandgap by introducing a taper profile along the axial direction. As we taper the inner radius, the cutoff frequency for MM mode goes up, and eventually it transitions to an exponentially decaying mode as it passes the operating frequency. It is exactly the same concept as evanescent holes on a flute cavity which prevents the field from leaking out. However, we must practice caution and not taper too rapidly to avoid any scattering into other modes (different propagation constant at the same ω). But if we taper it slowly enough, there is an “adiabatic theorem” (as reviewed in e.g.^{106,107}) the scattering into other modes becomes negligible and you get reflection approaching 100%.

The geometry of the tapered Bragg-fiber is shown in Fig. 7.12 where I parameterize the surface profile to follow a cubic polynomial. I simulated the cavity performance of this geometry varying the height of the taper and the cut-off radius. Based on these results, we decided to choose the height and radius such that the radiation $Q \approx 10^7$. Counter-intuitively, the radiation loss along the axial direction does not decrease monotonically with the height of the taper, instead, increase after a certain height as the taper slowly guides the light outside the cavity. This implies that the taper should have a sharper cut-off to keep the light from leaking out, which also helps to keep the cavity extents limited.

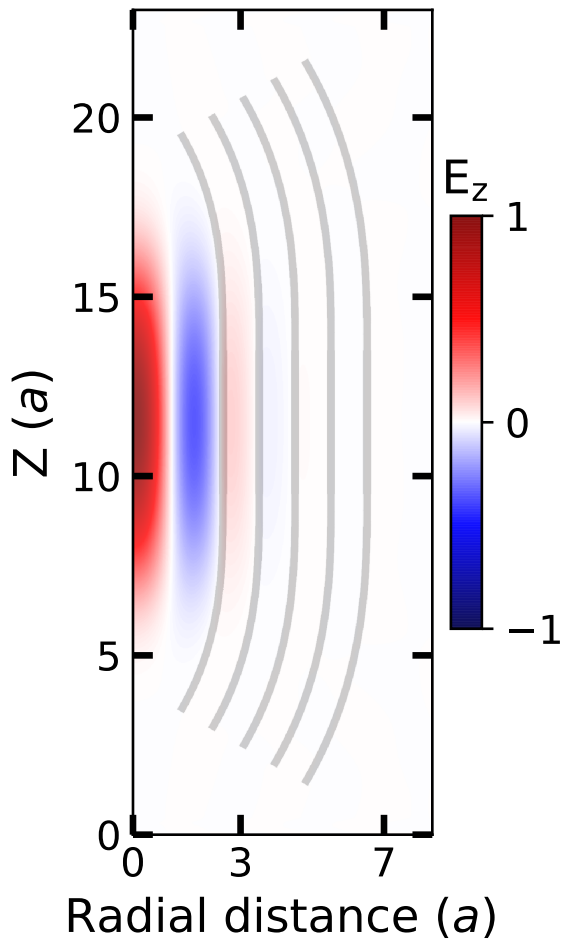


Figure 7.12: **Tapered Bragg fiber.** Electric field profile of a Bragg fiber with tapered ends to prevent the field from reaching the copper end-caps. The magnitude of the field reaching the ends of taper is negligible and the resultant Q-factor is high.

The tapered Bragg fiber cavity meets all the criterion for an axion cavity, however, there

is one little problem. How do we make such a dielectric structure? There are fabrication facilities to 3D print structures out of alumina, zirconia etc. Their method uses additive materials where a binding material is added to the dielectric which diffuses out when the 3D printed ceramic is baked in a kiln. This leads to air cavities in the structure degrading the purity of the material and loss properties. While this is a convenient option, the finished product after sintering is prone to deformation. I had ordered a few straight cylindrical shells to test the geometry and I found the shells elliptical and not circular as per the specifications. We could check the bandgap and Q-factor at room temperature but due to poor loss properties, we couldn't decouple the losses between the metal walls and the dielectric. So, we decided to try out a vendor for sapphire. It is grown in crystalline form which has really low dielectric loss tangent at microwave frequencies and better thermal properties at cryogenic temperatures than alumina. It is relatively easier to procure straight cylindrical shells of any size, surface finish etc. However, free-form machined sapphire like the ones we require is very much in demand, which makes the tapered structures super expensive, about \$100K for one shell. While we were again waiting to find a vendor to build this taper geometry, I used another approach inspired from²¹, where the end-caps are shaped into a cone in the middle to lower the current dissipation at the surfaces. This is a clever approach and solves the issues we have been facing with the fabrication of tapered sapphire shells.

7.4.2 Conical taper in metal end-caps

From fig. 7.11 (b), we can infer that the maximum dissipation occurs in the central region as the magnitude of H_ϕ is maximum. We can minimize the extent of field on the metal surface by blocking the field from reaching it. One way would be to introduce a conical taper in the central region. Smoothly but sharply varying the radius of the cone rapidly changes the cut-off frequency of the hole exponentially suppressing the field at the metal surface. We confirm the same in Fig. 7.13. The magnitude of the electric field reaching the conical

surface is almost an order of magnitude smaller than a cavity with flat end-caps.

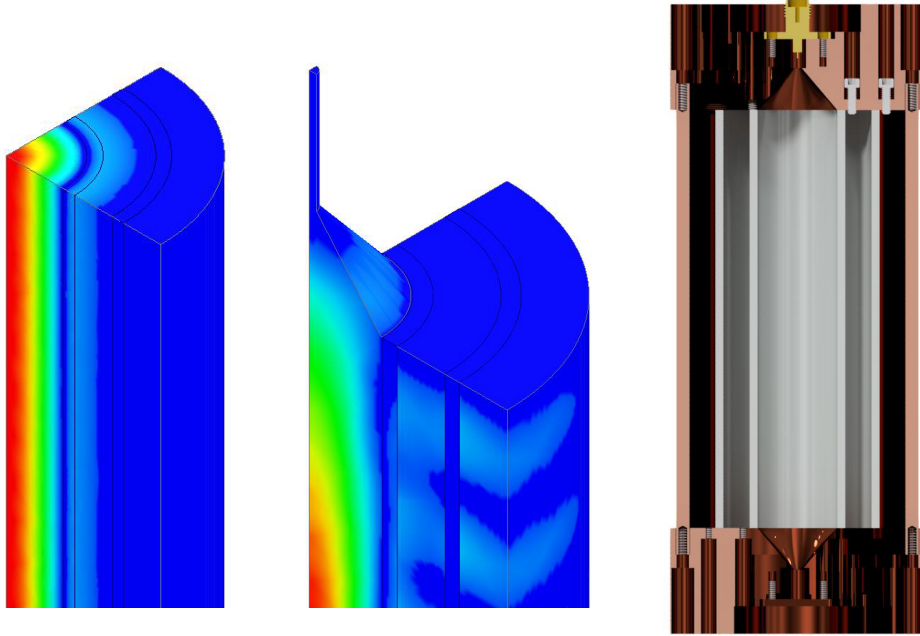


Figure 7.13: Bragg fiber with conical end-caps. (Left) Electric field profile of the Bragg fiber with a flat end-cap as simulated in HFSS. (Middle) Electric field profile with conical taper in copper. The magnitude of the field reaching the ends of taper is negligible and the resultant Q-factor is high. (Right) CAD model of the Bragg fiber cavity with two layers of dielectric shells enclosed in a copper outer layer with conical end-caps and a SMA antenna. PEEK screws are used at the periphery to guide the shells in place.

Design considerations

I performed a parametric sweep varying the upper radius and height of cone to search for an optimal design that maximizes the Q-factor of the cavity. The final design with optimal parameters is simulated in HFSS to estimate the losses due to metal and dielectric. In order to decouple the loss channels, the other channel is set to be lossless by assigning either perfect electric (PEC) boundary condition or setting the $\tan \delta$ to zero. The value of surface conductivity of copper σ_{Cu} used in the simulation has been computed at 12GHz in the anomalous skin depth regime using reference¹⁰⁸. The dielectric shells are grown using the Stephanov method by Rostox-N Ltd (Russia). Due to lack of published data, we use the dielectric loss $\tan \delta \sim 7.2 \times 10^{-6}$ quoted in¹⁰⁹. Most of the material characterization in the

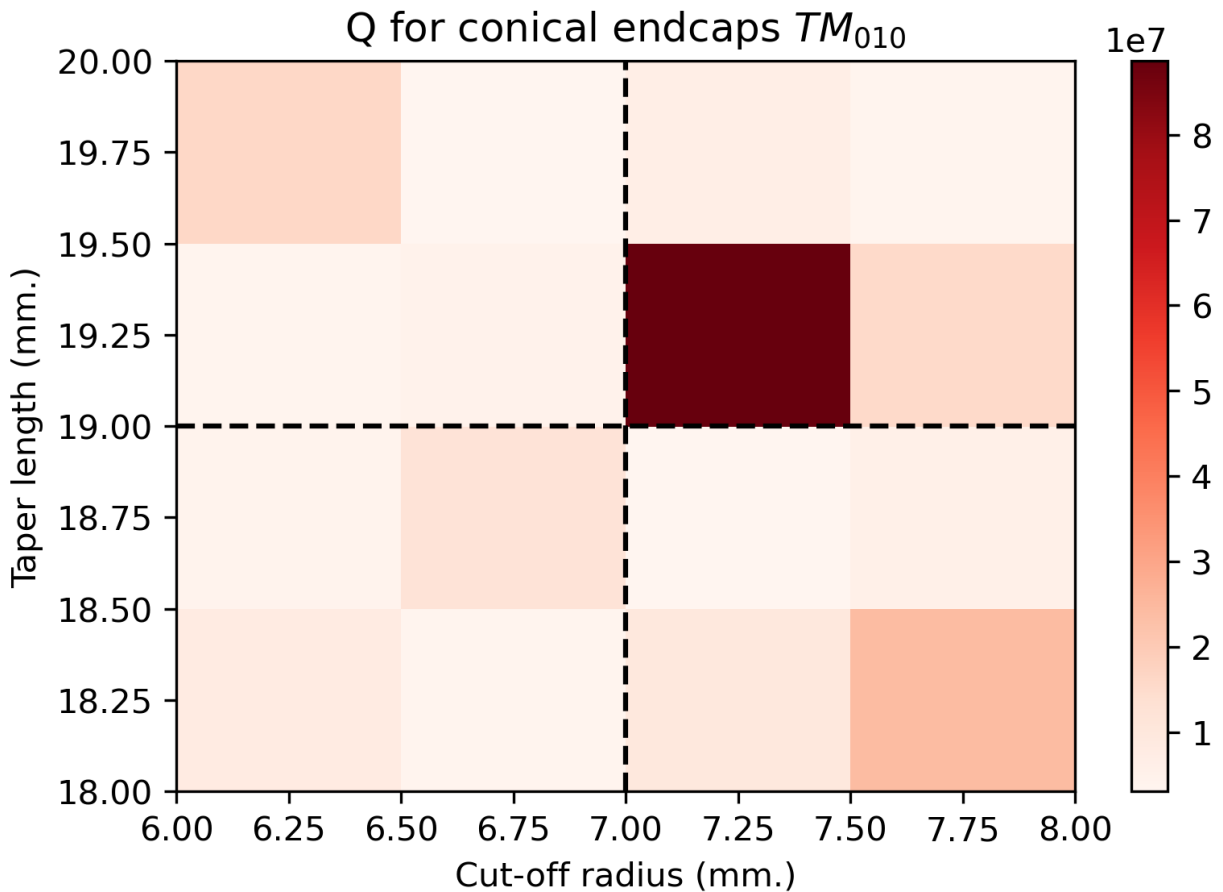


Figure 7.14: **Parametric sweep to determine the optimal cone dimensions.** (Left) CAD model of the Bragg fiber cavity with two layers of dielectric shells enclosed in a copper outer layer with conical end-caps and a SMA antenna. PEEK screws are used at the periphery to guide the shells in place. (Middle) Electric field profile of the Bragg fiber with a flat end-cap. (Right) Electric field profile of the simulated structure in HFSS. The magnitude of the field reaching the ends of taper is negligible and the resultant Q-factor is high.

literature is often conducted up to 4 K, however, we use the same values to compare the measurements performed at 20 mK. Hence, there is some uncertainty associated with the simulation results and we try our best to refine these parameters as per the measured values. Given the short lead time and one experimental demonstration, we decided to use the same vendor to procure the sapphire shells for our first prototype.

In order to hold the shells in place, we use PEEK screws at the periphery. The threaded screws poke out in the field region as shown in Fig. 7.13, however, their contribution to the loss is negligible but sensitive to the penetration inside the cavity volume. Even with a value

of $\tan \delta = 10^{-3}$ for PEEK at room temperature, $Q_{tot} > 10^7$ is obtained with lossless metallic walls and dielectric shells. Putting it all together, the expected $Q_{tot} = 6 \times 10^6$. The volume of the cavity is 204 cm^3 and form factor can only be calculated using HFSS, $C_{030} = 0.062$.

While designing the cavity components, I decided to keep the seams away from the central region, thus, the end-caps attach to the copper tube at the farthest radial point where the field magnitude is minimum. The other design includes slicing the cavity in half along the axial direction. Admittedly, there is still possibility to optimize the seams further to reduce the losses, for example, a knife edge at the seam will ensure light tightness and better design for electroplating. For our first prototype, we ordered out cavity parts CNC machined and electro-polished by an external vendor. I designed and machined a three-legged assembly to hang the cavity from the MXC plate and vertically position it to sit inside the magnet bore such that their centers coincide with each other as shown in Fig. 7.15.

Characterizing the cavity

We measure the resonance frequency of the cavity mode and its quality factor using a Vector Network Analyzer (VNA), recording the reflection (S_{11}) and transmission (S_{21}) transfer functions. First, the empty copper cavity is characterized at room temperature to get an estimate of the copper conductivity at room temperature. It helps us tune the simulation parameters. At 300 K, the measured $Q_{tot} \approx 2 \times 10^3$ corresponds to a surface copper resistivity 0.0213Ω . I then place the sapphire tubes inside the PEEK screw boundary, before enclosing it with the copper outer tube and tightening the end-caps with brass screws. We again measure both S_{11} and S_{21} to extract the internal Q_i and the coupling Q_c as shown in Fig. 7.16 (a). The measured resonance frequency of the cavity $\nu_0 = 12.0083 \text{ GHz}$, which is very close to the designed value of 12 GHz. The internal Quality factor $Q_i = 2.4 \times 10^5$ is lower by a factor of 2 as compared to simulated value. However, due to lack of an independent measurement of the loss tangent of sapphire tubes, it is difficult to draw any conclusions. We can set the coupling Q to the desired value by varying the length of the dipole antenna.

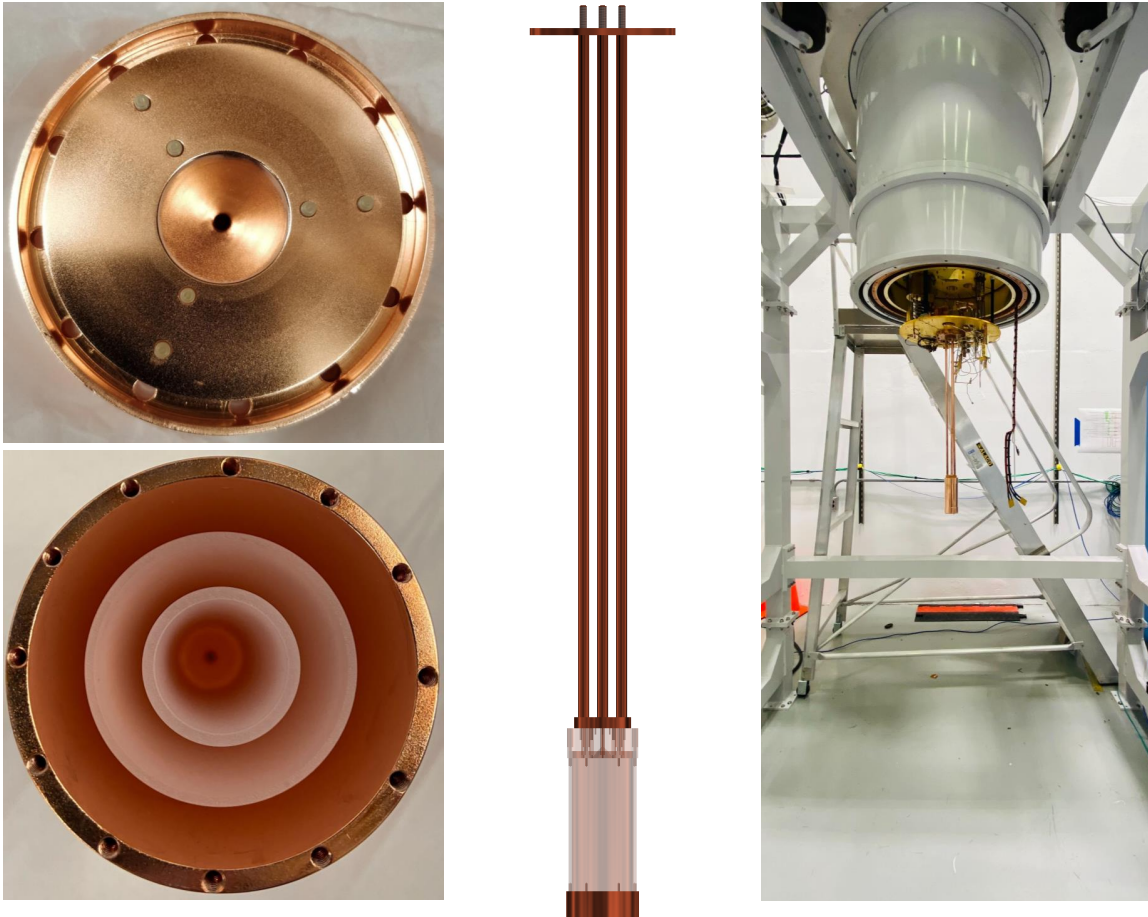


Figure 7.15: **Bragg fiber prototype.** (Left) Fabricated copper end-caps with PEEK screws to guide the shells in place. Top view of the shells mounted inside the copper enclosure. (Middle) CAD assembly of the mounting fixture. The cavity is attached at the bottom of the fixture to correctly position it inside the magnet bore. (Right) The entire assembly is hanging from the MXC plate. Two SMA rf cables are connected to the top and bottom ports to measure both transmission and reflection transfer functions in situ. The bottom port is very weakly coupled $Q_{c1} > 10^8$ and the top port is slightly over coupled at the room temperature such that it is close to critical coupling at low temperature.

The transfer function of the cavity in the reflection is assumed to be

$$S_{11} = \frac{(\kappa_i - (\kappa_c + \iota \gamma)) + \iota(\nu - \nu_0)}{(\kappa_i + (\kappa_c + \iota \gamma)) + \iota(\nu - \nu_0)} \quad (7.9)$$

where $Q_i = \nu_0/2\kappa_i$, $Q_c = \nu_0/2\kappa_c$ and γ is an asymmetry term. In order to measure it accurately, we perform a calibration using Keysight N4691-B E-Cal tool to account for the phase delay and attenuation due to microwave cables. However, at cryogenic temperatures, such

a calibration is not routinely done. It is a reasonable assumption to neglect the variations due to cables as the band of interest is very narrow.

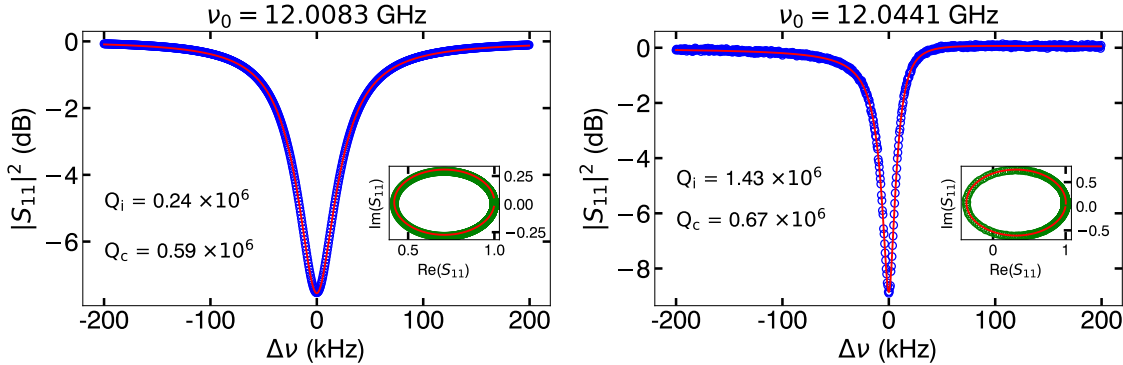


Figure 7.16: **Q-factor measurements.** (Left) Measurement of the reflection transfer function to extract the coupling and internal Q-factor of the cavity at room temperature. Data is fitted (red lines) to the magnitude and phase response to extract $Q_i = 0.24 \times 10^6$ and $Q_c = 0.59 \times 10^6$. This tells us that the cavity is under-coupled at room temperature. We neglect the coupling to the other port as the measured power is below the noise-floor of the VNA. (Right) Measurement at 20mK shows significant improvement in $Q_i = 1.46 \times 10^6$, surpassing the axion Q.

We measure the resonance frequency of the TM₀₃₀ mode cavity once the fridge reaches the base temperature and measure it again after a couple of days. We suspect the dielectric takes longer to thermalize but do not observe a significant change in the cavity parameters over time. It implies that the dielectric shells cool down efficiently in the current configuration. As one would expect, the frequency of the mode is shifted higher by ≈ 40 MHz attributed to the thermal contraction and change in dielectric constant. The measured internal Q-factor of the cavity is $Q_i = 1.46 \times 10^6$. This a very remarkable result for future axion experiments as the cavity Q-factor is officially greater than $Q_a = 10^6$.

The measured Q_i is slightly lower than the expected value by 30%. However, it is good agreement given the uncertainty in material parameters. We did observe radiation leakage outside the cavity, picked up by a bare coax cable with center pin exposed. It could be due to the seam at the end-caps. The other possibility is higher loss tangent of the sapphire as compared to QUAX group¹¹⁰, where the tubes were annealed at very high temperature (1800°C) to relax the internal stresses and remove any contaminants on the surface. We

did try to anneal the tubes in an open-air furnace reaching temperatures up to 1300°C but, didn't see much improvement. The tubes were sonicated in a series of solvents (TAMI)⁴ to remove any organic impurities present on the surface but that also didn't have any positive effect. It is a common procedure in superconducting qubit fabrication using sapphire wafers.

Interestingly though, if the dielectric losses are dominant, we can investigate that by measuring the Q-factor in the presence of a static magnetic field. A majority of the dielectric loss is attributed to two-level systems (TLS) caused by paramagnetic impurities such as Fe³⁺ and Cr³⁺. We could just be unlucky as the absorption lines in these two are reported at 12.03 GHz and 11.45 GHz respectively. In other studies, it has been demonstrated that the Q-factor of superconducting resonators increase as a function of the input power, indicating saturation of such absorptive losses. Fortunately, we can push the electron spin resonances to higher frequency by applying a magnetic field. The evidence for paramagnetic impurities was first reported in whispering-gallery-mode resonators made out of HEMEX sapphire⁹⁹ where the measured loss tan $\delta \sim 10^{-9}$.

I summarize the measured values of cavity parameters at room temperature and cryogenic temperature along with the parameters used in simulations and their corresponding expected values.

Table 7.1: TM₀₃₀ Mode Parameters.

| T(K) | ϵ_r | ρ_{Cu} (Ohm-m) | $\tan \delta$ | ν (GHz) | | $Q_i \cdot 10^6$ | |
|-------|--------------|----------------------|----------------------|-------------|--------|------------------|------|
| 300 K | 11.44 | $1.68 \cdot 10^{-8}$ | $4.87 \cdot 10^{-6}$ | Sim. | Meas. | 0.52 | 0.24 |
| 20 mK | 11.0 | $3.36 \cdot 10^{-9}$ | $1.19 \cdot 10^{-9}$ | 12.005 | 12.008 | 1.86 | 1.43 |

The cavity frequency and quality factor of the mode is very well modeled by the simulations. A cavity with longer height will result in even higher quality factor as the surface-to-volume ratio decreases, easily verified in HFSS. I believe this is a major factor in a higher quality factor demonstrated by the QUAX group.

4. TAMI stands for Toluene, Acetone, Methanol and Isopropanol

Ramping up the magnet

A solenoid magnet with maximum field up to 14 T was used for this test. The Oxford Triton dilution refrigerator was commissioned with this magnet in mind. We can see the giant frame which support the dilution unit in Fig. 7.15 and the magnet is hanging from the still shield which goes up to 4 K. The cavity is vertically positioned in the center of the magnet to minimize any differential forces which may arise if a quench occurs and prevent any permanent damages to the fridge. Due to change in magnetic field, the Eddy currents induced in the conductors gives rise to dissipating power which causes the fridge temperature to rise. In order to minimize this, we keep the ramp rate low and let the fridge temperature come back down and stabilize before recording the cavity transfer function.

The recorded data is fit according to Eq. 7.9 and the extracted cavity parameters are shown in Fig. 7.17. It shows the internal quality factor Q_i improves with the magnetic field before saturating to a value which is about 5% higher, compared to $1.5\times$ improvement reported in¹¹⁰. In recent results¹¹¹, it is reported that the bulk copper undergoes magnetoresistance¹¹² in high-field region, resulting in up to 2% positive change in quality factor. The change in resistivity of copper is quadratic with field and reaches maximum at field strengths greater than 5 T . However, we see a 5% improvement at only 1 T and the trend in Q_i and $\Delta\nu$ follows very well the results presented in¹¹⁰. Hence, we conclude that the improvement observed in Q_i is due to paramagnetic impurities pushed to higher frequencies in the presence of magnetic field. We suspect that the Q_i is limited by the dissipation on copper walls and have not reached the stage where the dielectric loss starts to dominate.

7.5 Tuning the cavity mode

So far, I have discussed the simulations and measurements for a fixed frequency PBG cavity. In a conventional haloscope cavity, a pair of metal or dielectric rods are used to tune the cavity by moving their positions inside the cavity volume as shown in Fig. 7.18. While this

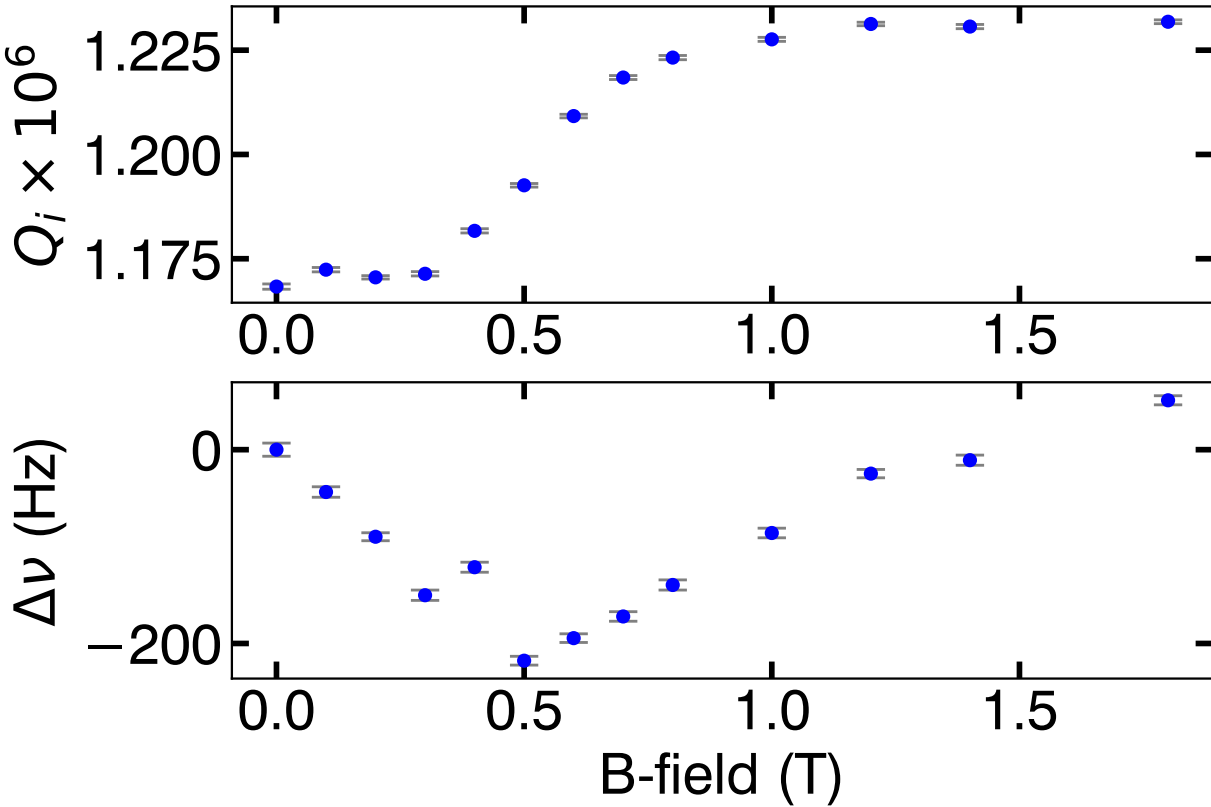


Figure 7.17: **Cavity parameters as a function of magnetic field.** (Top) Internal Q-factor increases with the magnetic field confirming our hypothesis about magnetic impurities in the sapphire crystals. (Bottom) Change in the resonance frequency, agrees well with the QUAX results Fig 4¹¹⁰, dip followed by saturation.

tuning mechanism has proven to be a reliable option, the rods poking the cavity volume, adds an additional loss channel to the cavity mode. Therefore, we need a different method to tune the cavity without degrading the internal quality factor. For the Bragg-fiber cavity, I propose to use a tapered sapphire rod axially piercing the cavity in the center. The mode frequency is tuned by longitudinal motion of the rod. The shape of the rod is tapered to minimize scattering losses occurring at the interface¹¹⁴. In comparison, a straight rod with the same diameter results in degradation of Q by a factor greater than 2. The diameter of the rod is chosen such that the cut-off frequency of the coupling port is higher than the mode frequency to prevent any additional radiation loss. The cavity simulations were performed using COMSOL to study the tuning range and the Q-factor of the cavity as a function of the

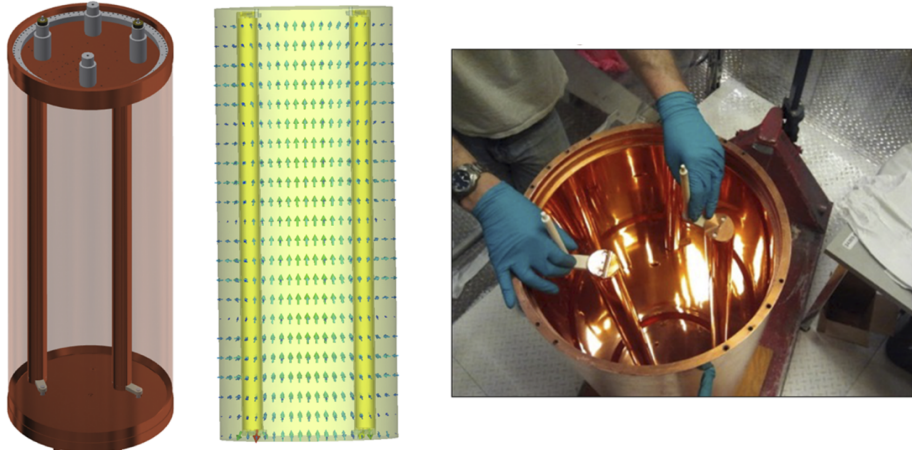


Figure 7.18: ADMX cavity tuning system. The left panel shows a cutaway view of the CAD model. The middle panel represents a computer simulation technology microwave studio simulation of the TM_{010} mode with each of the rods at 116^{deg} from the center. The right panel represents a picture of the system with the top end cap removed showing two 0.05 m diameter tuning rods and their aluminum-oxide ceramic axles.(Image credit: ADMX Technical Paper 2021¹¹³)

rod penetration depth. It has the capability to simulate a 2D slice and use symmetry to simulate the entire geometry with less computation resources.

Introduction of a dielectric rod in the center where the field concentration is high helps us achieve large tuning. This is due to increased participation ratio of the dielectric which pulls down the cavity frequency. Hence, in this configuration as the rod enters further in, the mode frequency decreases as shown in Fig. 7.20. However, the quality factor shows interesting variation dependent on the mode. The one with higher dielectric participation sees increase in quality factor and this could be due to the reduction of losses on the metallic end-caps. From Fig. 7.19 (left) it is evident that the magnitude of the field at the lower end-caps is negligible as compared to the middle plot, resulting in lower dissipation losses and thus, higher Q. We can conclude from this study that a large tuning is possible with multiple potential modes to look for axions.

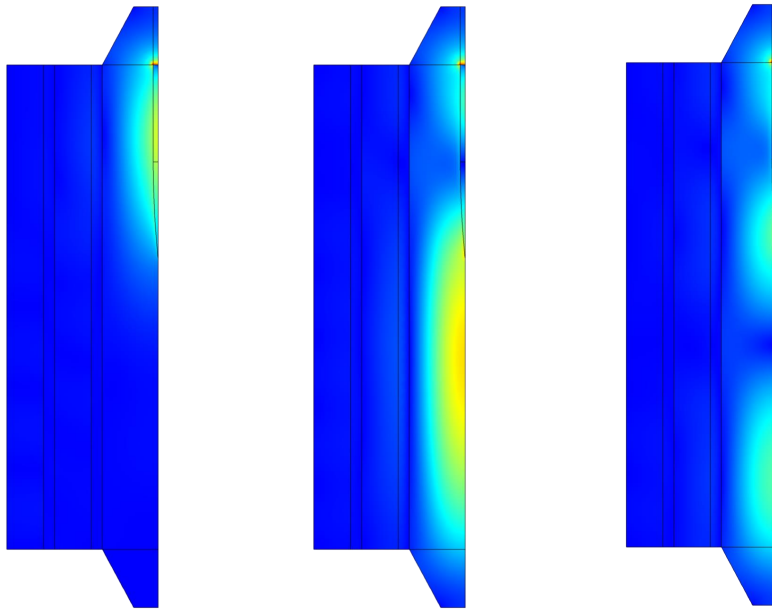


Figure 7.19: **Breaking the radial symmetry to tune the mode.** Electric field profile of the different modes, concentrated in dielectric (left), air (middle) or both (right) with a tuning rod in the center.

7.6 Preparing for science run

After characterizing the first prototype of a photonic haloscope cavity, we started planning to collect science data for a fixed frequency axion experiment. In order to successfully commission a data run we need the following: (1) low noise-amplifier, (2) ADC for signal digitization (3) calibrated noise source.

Low Noise Amplifier

We decided to use JPA as our first stage amplifier. Since we had developed a batch of JPAs for qubit measurement setups, we used the same recipe and changed the junction resistance to reach a maximum frequency close to 12 GHz. A couple of JPAs were tested which reached the desired frequency however, the magnitude response had a lossy feature which was coupled to the resonance frequency of the device. Ideally, it is a loss-less device.

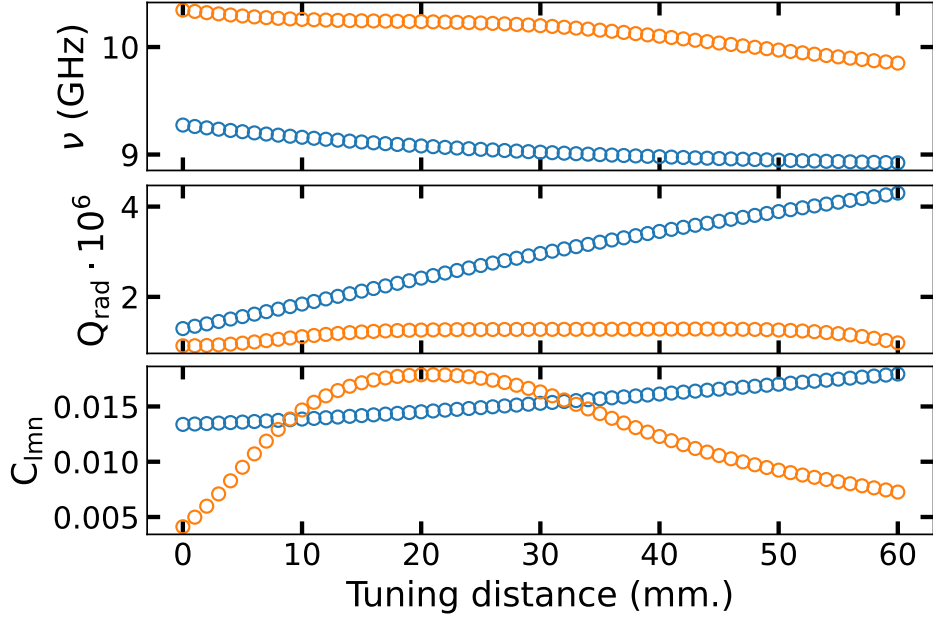


Figure 7.20: **Cavity tuning with a tapered rod.** Modes with quality factor greater than 10^6 are studied with their (Top) resonance frequency (middle) quality factor and (bottom) form factor as a function of the penetration depth of the rod inside the crystal. The higher frequency mode is the one localized in vacuum whereas the other one is concentrated in the tuning rod.

This led us to investigate the design a bit more to understand if any of the device feature is acting as an antenna, radiating energy to the lossy walls. I performed HFSS simulations to check for any box-modes and standing mode resonances associated with the CPW traces. The simulations do not predict any box-modes up to 14 GHz. However, we found a couple of resonances near the operating frequency localized near the input CPW section and the on-chip flux bias line which could be radiating energy into the lossy walls as shown in Fig. 7.21. It is still unclear if that explains the tunability of the lossy feature seen in the experiment. So, we changed the design by shortening the input CPW section and removing the on-chip flux line. An external solenoid coil is attached to the sample holder to flux tune it.

In the next cool-down, we tested the new design and the resonant mode was free from of any loss feature as shown in the flux scan here. Instead, we observed additional flux loops due to flux trapped in either the magnetic shield or the SQUID loops during the cool-down. Fortunately, the feature is far away from the frequency of the cavity mode we are interested

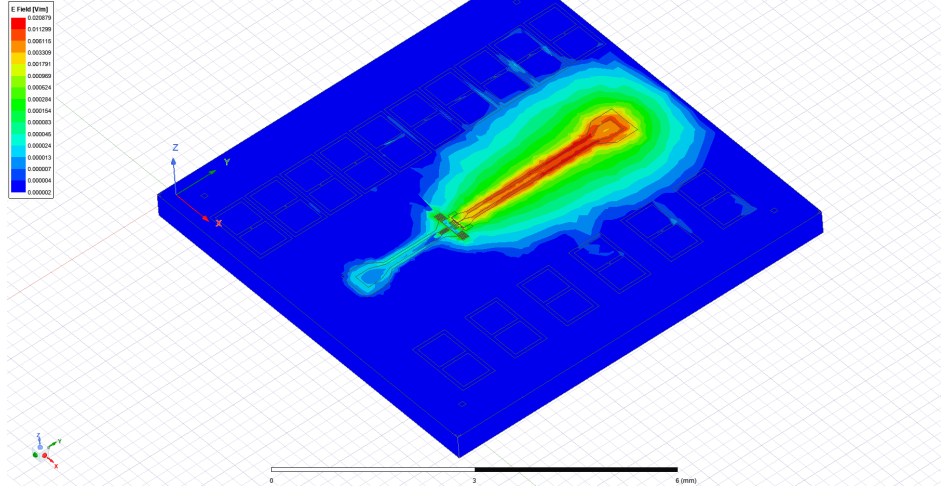


Figure 7.21: FSS Simulation of a JPA chip. Full device chip is simulated in HFSS to debug the lossy mode. The on-chip flux line acts as a resonator with non-zero overlap with the actual device. The frequency of this mode is close to 9 GHz.

in. After biasing the JPA for gain, we obtain a 20 dB gain within a 3 dB bandwidth of 15 MHz. The pump tone is set ~ 500 kHz away from the cavity frequency where we see the optimal improvement in SNR. The maximum improvement in SNR achieved with this device is approximately 10 dB. Assuming the total system noise temperature of the readout chain is dominated by the added noise of HEMT and its physical temperature, we can write the $T_{sys}^{off} = T_{HEMT} + T_{phy} = 3.2\text{ K} + 4\text{ K} = 7.2\text{ K}$.

Using Eq. 4.7 and Eq. 4.18, we can compute the total noise temperature of the output chain when the JPA is turned on. We record the power spectral density at the cavity mode frequency ($\nu_c = 12.044$ GHz), which is off-resonant with the pump tone at ($\nu_p = \nu_c + 500$ kHz). Fig. 7.23, shows the signal, pump and idler tones when the JPA is operational for the case when the magnet is on. By measuring the $SNR_i = 9.93$ dB, the total system noise temperature is estimated to be $T_{sys}^{on} = \frac{7.2\text{ K}}{10^{SNR_i/10}} = 0.730\text{ K}$. The quantum limit at 12 GHz is 576 mK, which implies the amplifier is operating near quantum limit at 88% efficiency.

In order to perform an absolute calibration, we would need a calibrated noise power source such a SNT. We have installed a SNT on another output line to check if it is working

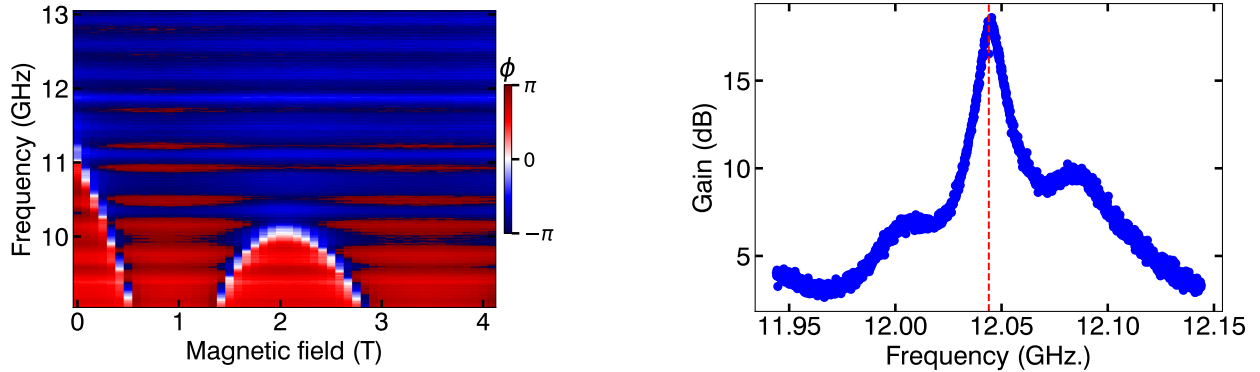


Figure 7.22: **JPA operation with magnet on.** (Left) Phase response of the JPA as the magnet field is ramped up to 5 T. The change in resonance frequency is caused by the residual magnetic field threading the SQUID loop mounted on top of the MXC plate. (Right) Gain profile of the JPA after re-biasing at 5 T magnetic field. The undulations are caused by the reflections in the microwave lines due to slightly longer cable length in the current cool-down.

as expected and add it to the cavity line in a future run.

Magnet ramp

We recorded the phase response of the JPA while ramping up the magnet as shown in Fig. 7.22. From the phase response, we infer that the magnetic field strength is non-negligible above the MXC plate and any sensitive device should be magnetically shielded with Mu-metal cans. After the magnet had reached 5 T, it was set to persistent mode and we re-biased the JPA to obtain a gain profile. Amazingly, the gain response of the JPA was stable and had a peak value of ≈ 17 dB with 3 dB bandwidth of 10 MHz and the noise performance still close to the quantum limit.

Next day, we ramped the magnetic field to 10 T and monitored the phase response of the JPA. It still tuned with an external flux bias and showed gain of ≈ 17 dB with a stable profile. It is a remarkable feat to achieve quantum limited amplification even in the presence of a large magnetic field.

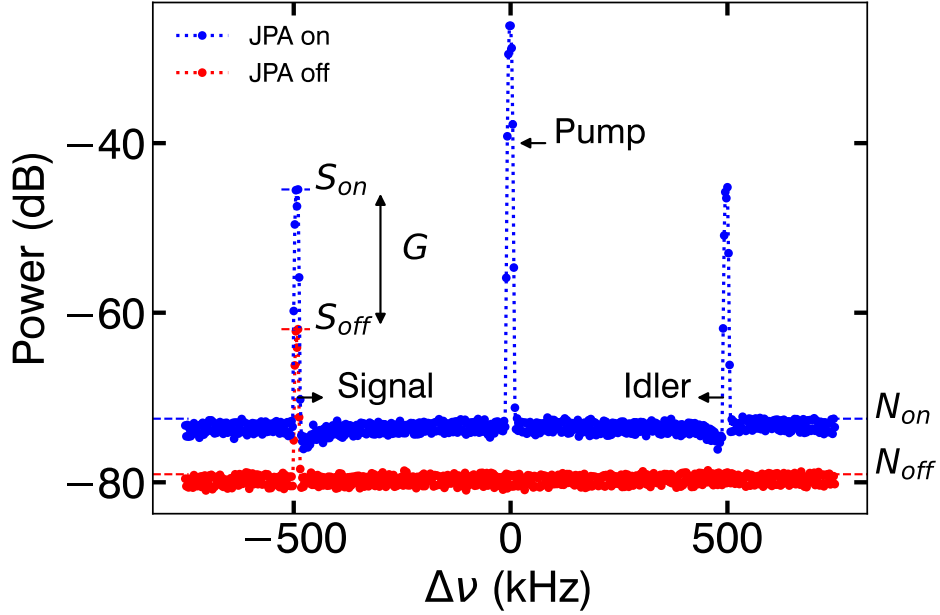


Figure 7.23: **Quantum limited amplification.** Measured power spectral density of the output chain when the JPA is off (Red) and on (blue). The measured gain of the JPA and improvement in SNR at the cavity frequency. The measured gain of the JPA at the signal (cavity) frequency is $G = S_{on} - S_{off} = 16.48 \text{ dB}$ and $SNR_i = 9.93 \text{ dB}$.

Custom electronics

With the help of QICK collaborators, I received a custom FPGA firmware to digitize the signal coming from the cavity and perform Fast Fourier Transform (FFT) on the board itself. It also allows to collect an averaged trace which is very efficient in terms of down time and the memory requirement. We tested the firmware by generating a sinusoidal tone using one of the DACs and feeding it back to the ADC. There are two down-conversion processes implemented in the firmware: the first inside the ADC (running at 1024 MS s^{-1}), which applies a frequency shifting and decimation factor of 8 (BW=128 MHz). This data is then fed into the DDC + CIC block, which allows us to add extra down-conversion by $\sim 30 \text{ mHz}$ resolution with an internal DDS running at this decimated frequency. The output is further filtered and decimated by a factor which can be configured between 1 and 1000. The output samples are then routed into a hardware FFT with a configurable window and fixed length of 65536 samples. This allows to obtain a spectrum with much finer resolution

than the cavity linewidth $\Delta\nu_c \approx 8.5$ kHz.

7.6.1 Projected sensitivity to axions

While we waited for the magnet ramp up, I estimated the integration time required to reach the DFSZ and KSVZ sensitivity with the photon bandgap haloscope based on the measured experimental parameters.

The signal power conversion from axion can be expressed as,

$$P_{ax} = 5.0 \times 10^{-23} \text{W} \left(\frac{C_\gamma}{0.75} \right) \left(\frac{\rho_a}{0.45 \text{GeV cm}^{-3}} \right) \left(\frac{\nu_a}{1 \text{GHz}} \right) \left(\frac{B_0}{10 \text{T}} \right) \left(\frac{V}{30 \text{L}} \right) \left(\frac{G}{0.5} \right) \left(\frac{Q_c}{10^5} \right) \quad (7.10)$$

where C_γ is the model dependent coupling coefficient with a value of -1.92 and 0.75 for the KSVZ and DFSZ model, respectively.

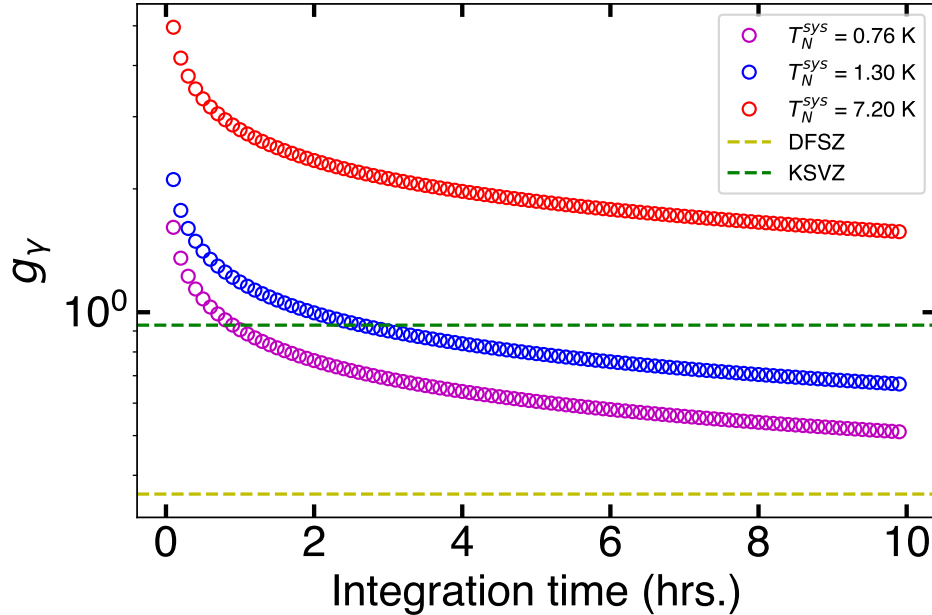


Figure 7.24: **Sensitivity to axion with quantum limited amplifier.** Estimated integration time to reach KSVZ or DFSZ sensitivity with a photonic bandgap haloscope operating in a 14 T magnetic field and varied system noise temperatures. It is a remarkable feat to achieve KSVZ sensitivity with a JPA operating near the quantum limit within an hour long integration period. SNR=2 is assumed to place 90% confidence interval.

7.6.2 Axion data collection

In order to set exclusion limit on the axion coupling with the photonic cavity and quantum limited amplifier, we measure the power spectral density of the noise at the cavity frequency. The incoming signal is down-converted using a LO set at $\nu_{LO} = \nu_c + 10\text{ MHz}$. The down-converted IF signal is amplified and filtered with a narrow band-pass filter before fed into the ADC.

The CIC block of the QICK was set to decimate the signal by another factor of 4 to filter out the noise at frequencies higher than ($|\nu_{IF}| > 32\text{ MHz}$). This gives us a frequency resolution of the FFT to be $\frac{32\text{ MHz}}{2^{16}} = 488\text{ Hz}$, approximately 20 points within the cavity linewidth which is plenty. We plan to collect an averaged trace from the board at a rate of about 1 s^{-1} .

Here is an example of the averaged trace around the cavity frequency. We see a dip at the cavity frequency which is unexpected. There could be multiple reasons why this could happen: (1) there is a hot source in the path which is emitting black body radiation at a temperature greater than the cavity (2) there is a power leakage due to parasitic coupling which is probing the cavity

We are investigating the cause of this leakage and hopefully solve this in the next cool-down.

7.7 Summary

To summarize, we have demonstrated a novel photon bandgap haloscope for axion searched with quality factor roughly $50\times$ that of a copper cavity. The internal quality factor achieved is greater than the intrinsic linewidth of the axion wave, which allows us to implement quantum tricks to enhance the scan rate with techniques discussed in the previous chapters. This is the first experiment in the world to achieve quantum limited amplification at 12 GHz in the presence of a 10 T magnetic field. With lessons learnt in this cool-down we can

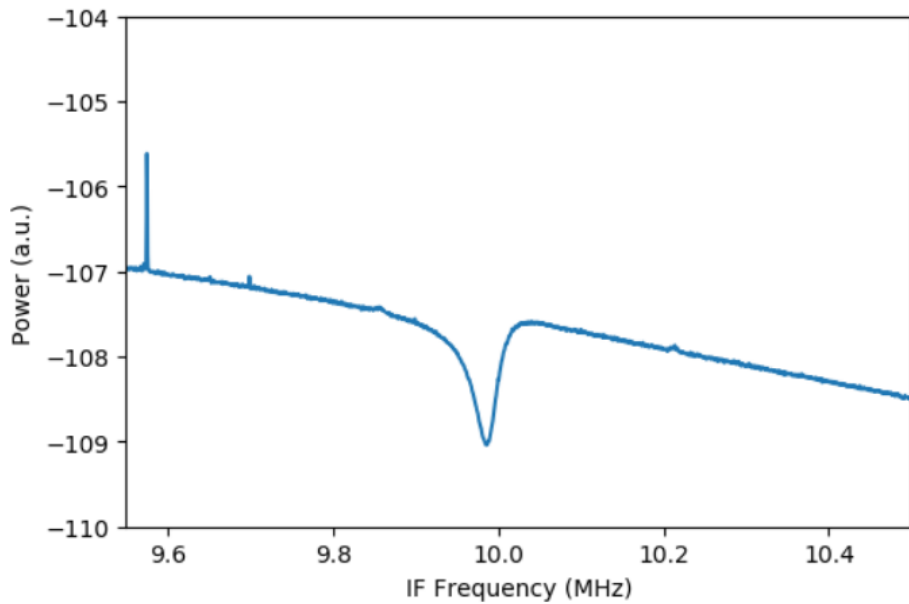


Figure 7.25: **Axion test data.** Digitized power spectrum using the QICKfirmware⁴⁴.

definitely conduct an axion search reaching KSVZ sensitivity within an hour of integration window.

Chapter 8

Future Dark Matter Search

There are two possible dark matter candidates which we are interested in and I believe it is a good approach to first develop the detector technology for hidden photons which doesn't require a magnetic field. It makes the experimental conditions convenient and we are benefited by the high quality factor achieved with superconducting cavities. On the other hand, there are multiple ongoing efforts to conduct an axion search using dielectric cavities made out of sapphire. The higher quality factor allows us to integrate the photon counting and stimulated emission techniques to enhance the SNR even further. Yet another approach which has delivered promising results is the development of cavity coated with thin layer of superconducting material which can be operated in low magnetic field region. The reduction in signal power can be compensated by the drastic increase in quality factor. It will be a rewarding journey for the community to join hands and approach this search cohesively.

8.1 Axion search with qubits

As mentioned earlier, an axion search with a photon counter would drastically increase the scan rate of the experiment, covering an octave in frequency within a day which would have otherwise taken a couple of years with a quantum limited amplifier. However, the presence of a large magnetic field makes this a difficult task to realize in real life. I have demonstrated in this work that photonic bandgap haloscope is a viable option to achieve higher quality factor even in the presence of a large magnetic field. The increased photon lifetime in the cavity allows us to make enough repeated QND measurements to bring down the detector based errors well below the SQL.

There is a recent proposal from our collaborator¹¹⁵ to transfer the photons converted from axions to an auxiliary detection cavity which is far away from the magnetic field.

This concept is called **CEASEFIRE** (Cavity Entanglement And Swapping Experiment For Improved Readout Efficiency), where a non-linear element, coupled to the two modes is used to facilitate the transfer. The modulation of mutual inductance at the difference frequency results in a state-swap at a rate determined by strength of the modulation (or pump), coupling between the cavities and coupler, and non-linearity of the coupler. An experimental demonstration is in works at University of Colorado-Boulder in Lehnert group, and hope to hear interesting results soon.

Moreover, the non-linear coupler allows the transfer of photons between the two cavities even when they are off-resonant. This implies we can operate a tunable axion cavity and use the same detector to cover a finite frequency range by just adjusting the frequency of the pump. The same coupler can also be used to swap and prepare the axion cavity in a Fock state to enhance the signal rate. For a photonic cavity such as one in QUAX¹¹⁰, $|n\rangle = \frac{Q_c}{Q_{DM}} - 1 = 5$ Fock state will be optimal to maximize the SNR. Of course, the actual efficiency of the entire scheme will determine the overall enhancement factor.

8.2 Hidden photon search with a tuner

Absence of a magnetic field in hidden photon search simplifies the experiment significantly. We can use the high quality factor cavities with $Q > 10^{10}$, much larger than the dark matter broadening of $Q = 10^6$. Due to the narrow cavity linewidth and macroscopic occupation number of the dark matter field, we only need to sample the dark matter a couple of times per linewidth. It means an entire octave in frequency can be covered with only 10^6 tunings.

In a tunable cavity, the QND interaction between the cavity and the qubit is unchanged. We follow the same experimental protocols at each tuning provided the dispersive shift is sufficiently large enough to resolve individual photons and the qubit is far detuned. One such element that we have discussed earlier, a SQUID loop, is capable of tuning the cavity frequency by varying the magnetic flux threading the loop. Fang Zhao and Morgan Lynn are currently measuring a prototype which consists of a SQUID loop (tuner) coupled to the

single photon counter device. The simulations predict a tuning of the order $\mathcal{O}(100 \text{ MHz})$, set by the coupling strength g . It is set such that the cavity photons loss is not significantly enhanced by the presence of a tuner. In addition to this, the hybridization of the tuner and cavity results in a reduction of geometric overlap between the dark matter field and cavity field. On resonance, half of the field resides in the tuner which has no coupling to the dark matter, but, the tuning is worth taking the hit in coupling efficiency.

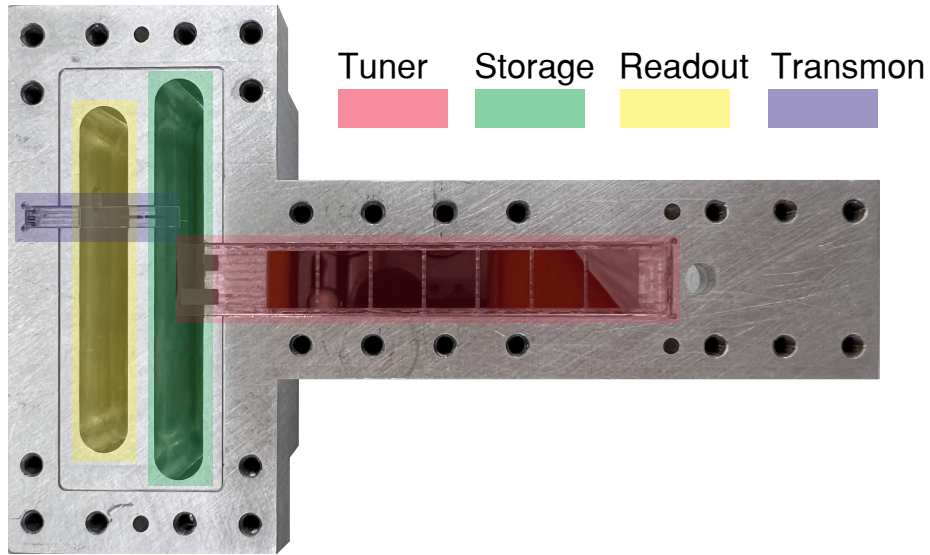


Figure 8.1: Electrical cavity tuning with a Josephson junction. The device consists of two coffin style 3D superconducting cavities, a photon counter transmon qubit and a SQUID loop to tune the storage cavity frequency. All the individual components are labeled. Both, the readout and storage cavity are dispersively coupled to a fixed frequency transmon qubit. The long sapphire chip contains a 3 pole low-pass filter to prevent the storage cavity photons from leaking due to its coupling via the SQUID loop.

8.3 Rydberg atoms as single photon counter

Superconducting qubits are well behaved at frequencies $< 10 \text{ GHz}$, however, going to higher frequencies will be a challenge as the aluminum Josephson junctions are limited by their plasma oscillation frequency to operate only well below 40 GHz . Niobium qubits could in principle operate at higher frequencies though the complicated oxide physics of Niobium make this a difficult material to work with. In contrast, Rydberg atoms do not face these

limitation and could in principle work as single photon sensors at very high frequencies. In fact, the very first demonstration of photon counter was demonstrated in the quantum-optics setup using Rydberg atoms^{51,116}. Another important feature is the possibility of probing the axion cavity with atoms placed directly inside the cavity volume. This work is currently underway at Yale in Maruyama lab.

Chapter 9

Conclusion

SQuAD is an excellent example of a fruitful collaboration between two seemingly disparate fields, coming together to explore new physics. Recent advancements in the quantum information field has paved the way to enable new detector technologies based on the manipulation of laws of quantum mechanics to use them to our advantage.

As the size of quantum processors powered by qubits grows, it is very crucial to understand the errors caused by thermal effects and other background sources. The qubit based photon counting technique demonstrated in this work can be used as a primary thermometer to assess the contamination of quantum information stored in memories^{39,117}. Recently, a couple of experiments investigated the effects of ionizing radiation on the qubit substrate^{118–120}. The absorption of high energy radiation such as γ -rays or cosmic-ray muons generate phonon-mediated quasi-particles causing chip-wide failure. This exchange of ideas and transfer of technology is a two-way street and the qubit community could definitely use the expertise possessed by high energy physicists to mitigate these effects and protect the quantum information encoded on a large array of qubits. For example, experiments are underway at Fermilab to test a multi-qubit chip in a dilution refrigerator situated deep below the ground level to shield it from the ionizing radiations. Moreover, the material research spurred by new cavity fabrication methods will lead to novel materials positively impacting the axion search.

The widespread use of Josephson Parametric Amplifiers made out of superconducting materials has already benefited the dark matter searches in more than one ways^{23,25}. However, the search in GHz frequency range will be nearly impossible without the photon counting based sensors. This technique allows us to evade the limits posed by quantum mechanics and selectively extract the information required to, in principle, conduct a background free search. The qubit based photon counting demonstrated in this work reduces the noise by a

factor > 1000 below the conventional methods. In addition to that, we demonstrated the enhancement of weak signal by preparing Fock states in the cavity utilizing the non-linearity inherited from the qubit. Combining these two, results in a SNR improvement of 19.7dB, speeding up the dark matter search by a factor of 10,000.

The successful demonstration of quantum limited amplification for axion searches at higher frequencies paves the way for current experiments to start exploring this parameter space which can be covered in a reasonable amount of time. There are various other interesting projects which are on-going to cover a wide frequency range utilizing quantum enhanced techniques. And I cannot wait to hear interesting results coming out soon (or even dark matter discovery)! I am very grateful to have been part of this cross-disciplinary research and contribute a few ingredients to the tool-kit. I hope these techniques will be further developed and coherently put together to uncover one of the greatest mysteries of the universe.

References

- [1] Preskill, J., Wise, M. B. & Wilczek, F. Cosmology of the Invisible Axion. *Phys. Lett. B* **120**, 127–132 (1983).
- [2] Abbott, L. & Sikivie, P. A Cosmological Bound on the Invisible Axion. *Phys. Lett. B* **120**, 133–136 (1983).
- [3] Dine, M. & Fischler, W. The Not So Harmless Axion. *Phys. Lett. B* **120**, 137–141 (1983).
- [4] Arias, P. *et al.* Wispy cold dark matter. *Journal of Cosmology and Astroparticle Physics* **2012**, 013–013 (2012).
- [5] Graham, P. W., Mardon, J. & Rajendran, S. Vector dark matter from inflationary fluctuations. *Phys. Rev. D* **93** (2016).
- [6] Peccei, R. D. & Quinn, H. R. Constraints imposed by CP conservation in the presence of pseudoparticles. *Phys. Rev. D* (1977).
- [7] Peccei, R. D. & Quinn, H. R. CP conservation in the presence of pseudoparticles. *Phys. Rev. Lett.* (1977).
- [8] Nambu, Y. Axial vector current conservation in weak interactions. *Physical Review Letters* **4**, 380–382 (1960). URL <https://doi.org/10.1103/physrevlett.4.380>.
- [9] Goldstone, J. Field theories with superconductor solutions. *Il Nuovo Cimento* **19**, 154–164 (1961). URL <https://doi.org/10.1007/bf02812722>.
- [10] Wilczek, F. Problem of strong p and t invariance in the presence of instantons. *Physical Review Letters* **40**, 279–282 (1978). URL <https://doi.org/10.1103/physrevlett.40.279>.
- [11] Weinberg, S. A new light boson? *Physical Review Letters* **40**, 223–226 (1978). URL <https://doi.org/10.1103/physrevlett.40.223>.
- [12] Sikivie, P. Experimental tests of the "invisible" axion. *Physical Review Letters* **51**, 1415–1417 (1983). URL <https://doi.org/10.1103/physrevlett.51.1415>.
- [13] Semertzidis, Y. K. & Youn, S. Axion dark matter: How to see it? *Science Advances* **8** (2022). URL <https://doi.org/10.1126/sciadv.abm9928>.
- [14] Ahmed, Z. *et al.* Search for axions with the CDMS experiment. *Physical Review Letters* **103** (2009). URL <https://doi.org/10.1103/physrevlett.103.141802>.
- [15] Aprile, E. *et al.* First axion results from the XENON100 experiment. *Physical Review D* **90** (2014). URL <https://doi.org/10.1103/physrevd.90.062009>.
- [16] Robilliard, C. *et al.* No "light shining through a wall": Results from a photoregeneration experiment. *Physical Review Letters* **99** (2007). URL <https://doi.org/10.1103/physrevlett.99.190403>.

- [17] Bartram, C. *et al.* Axion dark matter experiment: Run 1b analysis details. *Phys. Rev. D* **103**, 032002 (2021). URL <https://link.aps.org/doi/10.1103/PhysRevD.103.032002>.
- [18] Brubaker, B. M. *et al.* First results from a microwave cavity axion search at 24 μeV . *Phys. Rev. Lett.* **118**, 061302 (2017). URL <https://link.aps.org/doi/10.1103/PhysRevLett.118.061302>.
- [19] Semertzidis, Y. K. *et al.* Axion dark matter research with ibs/capp (2019). 1910.11591v1.
- [20] Dixit, A. V. *et al.* Searching for dark matter with a superconducting qubit. *Physical Review Letters* **126** (2021). URL <https://doi.org/10.1103%2Fphysrevlett.126.141302>.
- [21] Alesini, D. *et al.* Galactic axions search with a superconducting resonant cavity. *Physical Review D* **99** (2019). URL <https://doi.org/10.1103/physrevd.99.101101>.
- [22] Posen, S., Checchin, M., Melnychuk, O. S., Ring, T. & Gonin, I. Measurement of high quality factor superconducting cavities in tesla-scale magnetic fields for dark matter searches (2022). 2201.10733v2.
- [23] Braine, T. *et al.* Extended search for the invisible axion with the axion dark matter experiment. *Phys. Rev. Lett.* **124**, 101303 (2020). URL <https://link.aps.org/doi/10.1103/PhysRevLett.124.101303>.
- [24] Zhong, L. *et al.* Results from phase 1 of the haystac microwave cavity axion experiment. *Phys. Rev. D* **97** (2018).
- [25] Backes, K. M. *et al.* A quantum enhanced search for dark matter axions. *Nature* **590**, 238–242 (2021).
- [26] Dine, M., Fischler, W. & Srednicki, M. A simple solution to the strong CP problem with a harmless axion. *Physics Letters B* **104**, 199–202 (1981).
- [27] Zhitnitsky, A. On Possible Suppression of the Axion Hadron Interactions. (In Russian). *Sov. J. Nucl. Phys.* **31**, 260 (1980).
- [28] Kim, J. E. Weak-interaction singlet and strong CP invariance. *Phys. Rev. Lett.* **43**, 103–107 (1979).
- [29] Shifman, M., Vainshtein, A. & Zakharov, V. Can confinement ensure natural cp invariance of strong interactions? *Nuclear Physics B* **166**, 493–506 (1980).
- [30] Horns, D. *et al.* Searching for wispy cold dark matter with a dish antenna. *Journal of Cosmology and Astroparticle Physics* **2013**, 016–016 (2013).
- [31] Chaudhuri, S. *et al.* Radio for hidden-photon dark matter detection. *Phys. Rev. D* **92** (2015).

- [32] Caves, C. M. Quantum limits on noise in linear amplifiers. *Phys. Rev. D* **26**, 1817–1839 (1982). URL <https://link.aps.org/doi/10.1103/PhysRevD.26.1817>.
- [33] Yamamoto, T. *et al.* Flux-driven josephson parametric amplifier. *Applied Physics Letters* **93**, 042510 (2008). URL <https://doi.org/10.1063/1.2964182>.
- [34] Eichler, C. & Wallraff, A. Controlling the dynamic range of a josephson parametric amplifier. *EPJ Quantum Technology* **1**, 2 (2014). URL <https://doi.org/10.1140/epjqt2>.
- [35] Esposito, Martina *et al.* Development and characterization of a flux-pumped lumped element josephson parametric amplifier. *EPJ Web Conf.* **198**, 00008 (2019). URL <https://doi.org/10.1051/epjconf/201919800008>.
- [36] Pippard, A. B. & Bragg, W. L. The surface impedance of superconductors and normal metals at high frequencies ii. the anomalous skin effect in normal metals. *Proceedings of the Royal Society of London. Series A. Mathematical and Physical Sciences* **191**, 385–399 (1947). URL <https://royalsocietypublishing.org/doi/abs/10.1098/rspa.1947.0122>.
- [37] Reuter, G. E. H., Sondheimer, E. H. & Wilson, A. H. The theory of the anomalous skin effect in metals. *Proceedings of the Royal Society of London. Series A. Mathematical and Physical Sciences* **195**, 336–364 (1948). URL <https://royalsocietypublishing.org/doi/abs/10.1098/rspa.1948.0123>.
- [38] Reagor, M. *et al.* Quantum memory with millisecond coherence in circuit QED. *Physical Review B* **94** (2016). URL <https://doi.org/10.1103%2Fphysrevb.94.014506>.
- [39] Chakram, S. *et al.* Seamless high- q microwave cavities for multimode circuit quantum electrodynamics. *Phys. Rev. Lett.* **127**, 107701 (2021). URL <https://link.aps.org/doi/10.1103/PhysRevLett.127.107701>.
- [40] Koch, J. *et al.* Charge-insensitive qubit design derived from the cooper pair box. *Phys. Rev. A* **76**, 042319 (2007). URL <https://link.aps.org/doi/10.1103/PhysRevA.76.042319>.
- [41] Minev, Z. K. *et al.* Energy-participation quantization of josephson circuits (2021). 2010.00620.
- [42] Dixit, A. V. *SEARCHING FOR DARK MATTER WITH SUPERCONDUCTING QUBITS*. phdthesis, The University of Chicago (2021).
- [43] Stefanazzi, L. *et al.* The QICK (quantum instrumentation control kit): Readout and control for qubits and detectors. *Review of Scientific Instruments* **93**, 044709 (2022). URL <https://doi.org/10.1063/5.0076249>.
- [44] Qick: Quantum instrumentation control kit. URL <https://github.com/openquantumhardware/qick>.

- [45] Schuster, D. I. *et al.* Resolving photon number states in a superconducting circuit. *Nature* **445**, 515–518 (2007). URL <https://doi.org/10.1038%2Fnature05461>.
- [46] Blais, A., Huang, R.-S., Wallraff, A., Girvin, S. M. & Schoelkopf, R. J. Cavity quantum electrodynamics for superconducting electrical circuits: An architecture for quantum computation. *Physical Review A* **69** (2004). URL <https://doi.org/10.1103%2Fphysreva.69.062320>.
- [47] Wallraff, A. *et al.* Strong coupling of a single photon to a superconducting qubit using circuit quantum electrodynamics. *Nature* **431**, 162–167 (2004). URL <https://doi.org/10.1038%2Fnature02851>.
- [48] Johnson, B. R. *et al.* Quantum non-demolition detection of single microwave photons in a circuit. *Nature Physics* **6**, 663–667 (2010). URL <https://doi.org/10.1038%2Fnphys1710>.
- [49] Jin, X. *et al.* Thermal and residual excited-state population in a 3d transmon qubit. *Physical Review Letters* **114** (2015). URL <https://doi.org/10.1103%2Fphysrevlett.114.240501>.
- [50] Sun, L. *et al.* Tracking photon jumps with repeated quantum non-demolition parity measurements. *Nature* **511**, 444–448 (2014). URL <https://doi.org/10.1038%2Fnature13436>.
- [51] Haroche, S. & Raimond, J.-M. *Exploring the Quantum: Atoms, Cavities, and Photons* (Oxford University Press, 2006).
- [52] Krastanov, S. *et al.* Universal control of an oscillator with dispersive coupling to a qubit. *Phys. Rev. A* **92**, 040303 (2015). URL <https://link.aps.org/doi/10.1103/PhysRevA.92.040303>.
- [53] Heeres, R. W. *et al.* Cavity state manipulation using photon-number selective phase gates. *Phys. Rev. Lett.* **115**, 137002 (2015). URL <https://link.aps.org/doi/10.1103/PhysRevLett.115.137002>.
- [54] Fösel, T., Krastanov, S., Marquardt, F. & Jiang, L. Efficient cavity control with snap gates (2020). [2004.14256v1](#).
- [55] Leung, N., Abdelhafez, M., Koch, J. & Schuster, D. Speedup for quantum optimal control from automatic differentiation based on graphics processing units. *Phys. Rev. A* **95**, 042318 (2017). URL <https://link.aps.org/doi/10.1103/PhysRevA.95.042318>.
- [56] Heeres, R. W. *et al.* Implementing a universal gate set on a logical qubit encoded in an oscillator. *Nature Communications* **8** (2017). URL <https://doi.org/10.1038%2Fs41467-017-00045-1>.
- [57] Leek, P. J. *et al.* Observation of berry's phase in a solid-state qubit. *Science* **318**, 1889–1892 (2007). URL <https://doi.org/10.1126%2Fscience.1149858>.

- [58] Kudra, M. *et al.* Robust preparation of wigner-negative states with optimized SNAP-displacement sequences. *PRX Quantum* **3** (2022). URL <https://doi.org/10.1103/2Fprxquantum.3.030301>.
- [59] Khaneja, N., Reiss, T., Kehlet, C., Schulte-Herbrüggen, T. & Glaser, S. J. Optimal control of coupled spin dynamics: design of NMR pulse sequences by gradient ascent algorithms. *Journal of Magnetic Resonance* **172**, 296–305 (2005). URL <https://doi.org/10.1016%2Fj.jmr.2004.11.004>.
- [60] Johansson, J., Nation, P. & Nori, F. QuTiP: An open-source python framework for the dynamics of open quantum systems. *Computer Physics Communications* **183**, 1760–1772 (2012). URL <https://doi.org/10.1016%2Fj.cpc.2012.02.021>.
- [61] Johansson, J., Nation, P. & Nori, F. QuTiP 2: A python framework for the dynamics of open quantum systems. *Computer Physics Communications* **184**, 1234–1240 (2013). URL <https://doi.org/10.1016%2Fj.cpc.2012.11.019>.
- [62] Reinhold, P. *Controlling Error-Correctable Bosonic Qubits*. phdthesis, Yale University (2019).
- [63] Zhou, X. *et al.* High-gain weakly nonlinear flux-modulated josephson parametric amplifier using a squid array. *Phys. Rev. B* **89**, 214517 (2014). URL <https://link.aps.org/doi/10.1103/PhysRevB.89.214517>.
- [64] Wustmann, W. & Shumeiko, V. Parametric resonance in tunable superconducting cavities. *Phys. Rev. B* **87**, 184501 (2013). URL <https://link.aps.org/doi/10.1103/PhysRevB.87.184501>.
- [65] Castellanos-Beltran, M. *Development of a Josephson Parametric Amplifier for the Preparation and Detection of Nonclassical States of Microwave Fields*. Ph.D. thesis, University of Colorado Boulder, Boulder (2010).
- [66] Ambegaokar, V. & Baratoff, A. Tunneling between superconductors. *Phys. Rev. Lett.* **11**, 104–104 (1963). URL <https://link.aps.org/doi/10.1103/PhysRevLett.11.104>.
- [67] Haus, H. A. & Mullen, J. A. Quantum noise in linear amplifiers. *Phys. Rev.* **128**, 2407–2413 (1962). URL <https://link.aps.org/doi/10.1103/PhysRev.128.2407>.
- [68] Dicke, R. H. The Measurement of Thermal Radiation at Microwave Frequencies. *Review of Scientific Instruments* **17**, 268–275 (1946). URL <http://aip.scitation.org/doi/10.1063/1.1770483>.
- [69] Callen, H. B. & Welton, T. A. Irreversibility and generalized noise. *Phys. Rev.* **83**, 34–40 (1951). URL <https://link.aps.org/doi/10.1103/PhysRev.83.34>.
- [70] Cano, J. L., Wade Falk, N. & Gallego-Puyol, J. D. Ultra-wideband chip attenuator for precise noise measurements at cryogenic temperatures. *IEEE Transactions on Microwave Theory and Techniques* **58**, 2504–2510 (2010).

- [71] Yeh, J.-H., LeFebvre, J., Premaratne, S., Wellstood, F. C. & Palmer, B. S. Microwave attenuators for use with quantum devices below 100 mK. *Journal of Applied Physics* **121**, 224501 (2017). URL <https://doi.org/10.1063/2F1.4984894>.
- [72] Simbierowicz, S. *et al.* Characterizing cryogenic amplifiers with a matched temperature-variable noise source. *Review of Scientific Instruments* **92**, 034708 (2021). URL <https://doi.org/10.1063/2F5.0028951>.
- [73] Boutan, C. *et al.* Piezoelectrically tuned multimode cavity search for axion dark matter. *Phys. Rev. Lett.* **121**, 261302 (2018). URL <https://link.aps.org/doi/10.1103/PhysRevLett.121.261302>.
- [74] Dahm, A. J. *et al.* Linewidth of the radiation emitted by a josephson junction. *Phys. Rev. Lett.* **22**, 1416–1420 (1969). URL <https://link.aps.org/doi/10.1103/PhysRevLett.22.1416>.
- [75] Roy, T. *Multimode Superconducting Circuits as Building Blocks for a Programmable Quantum Processor*. phdthesis, Tata Institute of Fundamental Research (2018).
- [76] Schuster, D. I. *et al.* ac stark shift and dephasing of a superconducting qubit strongly coupled to a cavity field. *Phys. Rev. Lett.* **94**, 123602 (2005). URL <https://link.aps.org/doi/10.1103/PhysRevLett.94.123602>.
- [77] Gambetta, J. *et al.* Qubit-photon interactions in a cavity: Measurement-induced dephasing and number splitting. *Physical Review A* **74** (2006). URL <https://doi.org/10.1103/2Fphysreva.74.042318>.
- [78] McClure, D. T. *et al.* Rapid driven reset of a qubit readout resonator. *Phys. Rev. Applied* **5**, 011001 (2016). URL <https://link.aps.org/doi/10.1103/PhysRevApplied.5.011001>.
- [79] Purcell, E. M., Torrey, H. C. & Pound, R. V. Resonance absorption by nuclear magnetic moments in a solid. *Phys. Rev.* **69**, 37–38 (1946). URL <https://link.aps.org/doi/10.1103/PhysRev.69.37>.
- [80] Zheng, H., Silveri, M., Brierley, R. T., Girvin, S. M. & Lehnert, K. W. Accelerating dark-matter axion searches with quantum measurement technology (2016). 1607.02529v2.
- [81] Hann, C. T. *et al.* Robust readout of bosonic qubits in the dispersive coupling regime. *Physical Review A* **98** (2018). URL <https://doi.org/10.1103/2Fphysreva.98.022305>.
- [82] Elder, S. S. *et al.* High-fidelity measurement of qubits encoded in multilevel superconducting circuits. *Physical Review X* **10** (2020). URL <https://doi.org/10.1103/2Fphysrevx.10.011001>.

- [83] Block, E. & Berman, P. R. Quantum zeno effect and quantum zeno paradox in atomic physics. *Physical Review A* **44**, 1466–1472 (1991). URL <https://doi.org/10.1103/2Fphysreva.44.1466>.
- [84] Rolke, W. A., López, A. M. & Conrad, J. Limits and confidence intervals in the presence of nuisance parameters. *Nuclear Instruments and Methods in Physics Research Section A: Accelerators, Spectrometers, Detectors and Associated Equipment* **551**, 493–503 (2005). URL <https://doi.org/10.1016/j.nima.2005.05.068>.
- [85] Conrad, J., Botner, O., Hallgren, A. & de los Heros, C. P. Including systematic uncertainties in confidence interval construction for poisson statistics. *Physical Review D* **67** (2003). URL <https://doi.org/10.1103/physrevd.67.012002>.
- [86] Foster, J. W., Rodd, N. L. & Safdi, B. R. Revealing the dark matter halo with axion direct detection. *Phys. Rev. D* **97** (2018).
- [87] Roy, T. *et al.* Broadband parametric amplification with impedance engineering: Beyond the gain-bandwidth product. *Applied Physics Letters* **107**, 262601 (2015). URL <https://doi.org/10.1063%2F1.4939148>.
- [88] Esposito, M. *et al.* Development and characterization of a flux-pumped lumped element josephson parametric amplifier. *EPJ Web of Conferences* **198**, 00008 (2019). URL <https://doi.org/10.1051%2Fepjconf%2F201919800008>.
- [89] Motzoi, F., Buchmann, L. & DIckel, C. Simple, smooth and fast pulses for dispersive measurements in cavities and quantum networks (2018). [1809.04116v1](#).
- [90] Lu, N. Effects of dissipation on photon statistics and the lifetime of a pure number state. *Physical Review A* **40**, 1707–1708 (1989). URL <https://doi.org/10.1103/2Fphysreva.40.1707>.
- [91] Hofheinz, M. *et al.* Generation of fock states in a superconducting quantum circuit. *Nature* **454**, 310–314 (2008). URL <https://doi.org/10.1038%2Fnature07136>.
- [92] de Oliveira, F. A. M., Kim, M. S., Knight, P. L. & Buek, V. Properties of displaced number states. *Physical Review A* **41**, 2645–2652 (1990). URL <https://doi.org/10.1103%2Fphysreva.41.2645>.
- [93] Eickbusch, A. *et al.* Fast universal control of an oscillator with weak dispersive coupling to a qubit (2021). [2111.06414v2](#).
- [94] Yablonovitch, E. Inhibited spontaneous emission in solid-state physics and electronics. *Physical Review Letters* **58**, 2059–2062 (1987). URL <https://doi.org/10.1103%2Fphysrevlett.58.2059>.
- [95] John, S. Strong localization of photons in certain disordered dielectric superlattices. *Physical Review Letters* **58**, 2486–2489 (1987). URL <https://doi.org/10.1103%2Fphysrevlett.58.2486>.

- [96] Johnson, S., Mekis, A., Fan, S. & Joannopoulos, J. Molding the flow of light. *Computing in Science & Engineering* **3**, 38–47 (2001). URL <https://doi.org/10.1109/5992.963426>.
- [97] Oskooi, A. F. *et al.* Meep: A flexible free-software package for electromagnetic simulations by the FDTD method. *Computer Physics Communications* **181**, 687–702 (2010). URL <https://doi.org/10.1016/j.cpc.2009.11.008>.
- [98] Krupka, J., Derzakowski, K., Tobar, M., Hartnett, J. & Geyer, R. G. Complex permittivity of some ultralow loss dielectric crystals at cryogenic temperatures. *Measurement Science and Technology* **10**, 387–392 (1999). URL <https://doi.org/10.1088/2F0957-0233%2F10%2F5%2F308>.
- [99] Creedon, D. L. *et al.* High q-factor sapphire whispering gallery mode microwave resonator at single photon energies and millikelvin temperatures. *Applied Physics Letters* **98**, 222903 (2011). URL <https://doi.org/10.1063%2F1.3595942>.
- [100] Parker, R. A. Static dielectric constant of rutile (tio_2), 1.6–1060°k. *Phys. Rev.* **124**, 1719–1722 (1961). URL <https://link.aps.org/doi/10.1103/PhysRev.124.1719>.
- [101] Tobar, M. E., Krupka, J., Ivanov, E. N. & Woode, R. A. Anisotropic complex permittivity measurements of mono-crystalline rutile between 10 and 300 k. *Journal of Applied Physics* **83**, 1604–1609 (1998). URL <https://doi.org/10.1063/1.366871>.
- [102] Alesini, D. *et al.* High quality factor photonic cavity for dark matter axion searches. *Review of Scientific Instruments* **91**, 094701 (2020). URL <https://doi.org/10.1063/5.0003878>.
- [103] Yeh, P., Yariv, A. & Marom, E. Theory of bragg fiber. *Journal of the Optical Society of America* **68**, 1196 (1978). URL <https://doi.org/10.1364/josa.68.001196>.
- [104] Miyagi, M., Hongo, A. & Kawakami, S. Transmission characteristics of dielectric-coated metallic waveguide for infrared transmission: Slab waveguide model. *IEEE Journal of Quantum Electronics* **19**, 136–145 (1983). URL <https://doi.org/10.1109/jqe.1983.1071837>.
- [105] Miyagi, M. & Kawakami, S. Design theory of dielectric-coated circular metallic waveguides for infrared transmission. *Journal of Lightwave Technology* **2**, 116–126 (1984). URL <https://doi.org/10.1109/jlt.1984.1073590>.
- [106] Johnson, S. G. *et al.* Adiabatic theorem and continuous coupled-mode theory for efficient taper transitions in photonic crystals. *Physical Review E* **66** (2002). URL <https://doi.org/10.1103/physreve.66.066608>.
- [107] Bienstman, P. *et al.* Taper structures for coupling into photonic crystal slab waveguides. *Journal of the Optical Society of America B* **20**, 1817 (2003). URL <https://doi.org/10.1364/josab.20.001817>.

- [108] Calatroni, S. A Mathematica Notebook for the calculation of the anomalous skin effect in copper (2020). URL <https://cds.cern.ch/record/2718002>.
- [109] Alesini, D. *et al.* Realization of a high quality factor resonator with hollow dielectric cylinders for axion searches. *Nuclear Instruments and Methods in Physics Research Section A: Accelerators, Spectrometers, Detectors and Associated Equipment* **985**, 164641 (2021). URL <https://doi.org/10.1016/j.nima.2020.164641>.
- [110] Vora, R. D. *et al.* A high-q microwave dielectric resonator for axion dark matter haloscopes (2022). [2201.04223v1](#).
- [111] Ahn, S. *et al.* Magnetoresistance in copper at high frequency and high magnetic fields. *Journal of Instrumentation* **12**, P10023–P10023 (2017). URL <https://doi.org/10.1088/1748-0221/12/10/p10023>.
- [112] de Launay, J., Dolecek, R. & Webber, R. Magnetoresistance of copper. *Journal of Physics and Chemistry of Solids* **11**, 37–42 (1959). URL <https://doi.org/10.1016/0022-3697%2859%2990038-1>.
- [113] Khatiwada, R. *et al.* Axion dark matter experiment: Detailed design and operations. *Review of Scientific Instruments* **92**, 124502 (2021). URL <https://doi.org/10.1063/5.0037857>.
- [114] Marcuse, D. THE ASYMMETRIC SLAB WAVEGUIDE. In *Theory of Dielectric Optical Waveguides*, 1–59 (Elsevier, 1991). URL <https://doi.org/10.1016/b978-0-12-470951-5.50007-x>.
- [115] Wurtz, K. *et al.* Cavity entanglement and state swapping to accelerate the search for axion dark matter. *PRX Quantum* **2** (2021). URL <https://doi.org/10.1103/prxquantum.2.040350>.
- [116] Haroche, S. Nobel lecture: Controlling photons in a box and exploring the quantum to classical boundary. *Reviews of Modern Physics* **85**, 1083–1102 (2013). URL <https://doi.org/10.1103/revmodphys.85.1083>.
- [117] Naik, R. K. *et al.* Random access quantum information processors using multimode circuit quantum electrodynamics. *Nature Communications* **8** (2017). URL <https://doi.org/10.1038/s41467-017-02046-6>.
- [118] Vepsäläinen, A. P. *et al.* Impact of ionizing radiation on superconducting qubit coherence. *Nature* **584**, 551–556 (2020). URL <https://doi.org/10.1038/s41586-020-2619-8>.
- [119] McEwen, M. *et al.* Resolving catastrophic error bursts from cosmic rays in large arrays of superconducting qubits. *Nature Physics* **18**, 107–111 (2021). URL <https://doi.org/10.1038/s41567-021-01432-8>.
- [120] Wilen, C. D. *et al.* Correlated charge noise and relaxation errors in superconducting qubits. *Nature* **594**, 369–373 (2021). URL <https://doi.org/10.1038/s41586-021-03557-5>.